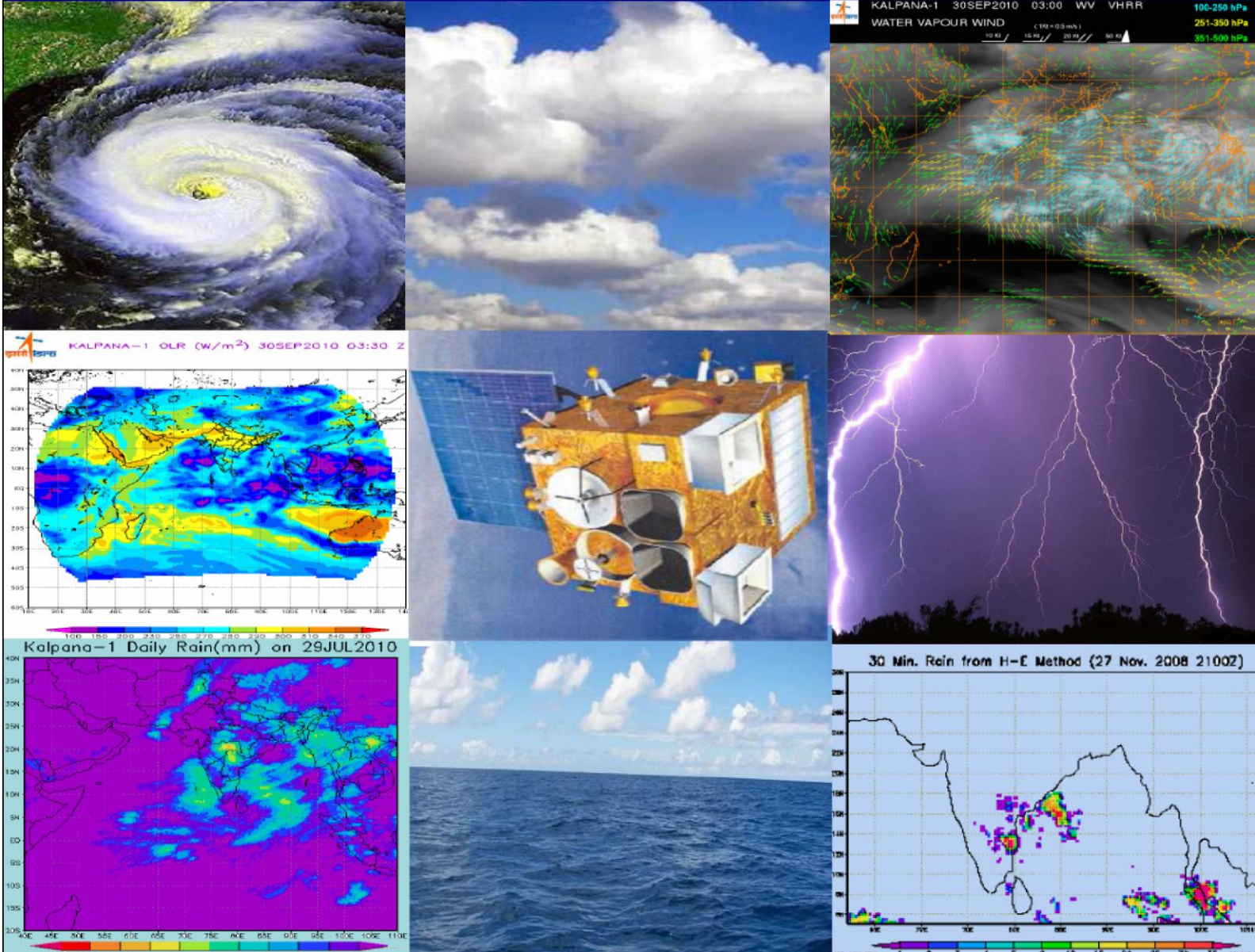


# (MMDRPS Incremental ATBD)

## INSAT-3D

### Algorithm Theoretical Basis Document



November, 2018

**Earth, Ocean, Atmosphere, Planetary Sciences & Applications Area  
Space Applications Centre  
Ahmedabad-380058**



## Table of Contents

1.	Snow-Cover Mapping (SCM) and Fractional Snow Cover (FSC) .....	12
1.1.	Algorithm Configuration Information .....	13
2.2.	Introduction .....	13
1.2.1.	Overview and background .....	14
1.2.2.	Remote Sensing of Snow Cover .....	15
1.2.3.	Objective .....	16
1.3.	Inputs and output data .....	16
1.3.1.	Image and preprocessing data (Dynamic).....	16
1.3.2.	Other Auxillary data and Model Inputs (Static).....	16
1.4.	Algorithm Functional Specifications .....	17
1.4.1.	Overview .....	17
1.4.2.	Theoretical Background .....	18
1.4.3.	Operational Implementation .....	21
1.5.	Outputs .....	22
1.5.1.	Format of the output and the domain .....	22
1.6.	Validation and Error Analysis.....	22
1.6.1.	Field Spectroradiometer data .....	22
1.6.3.	Comparison of INSAT 3D(R) snow maps with AWiFS snow products .....	22
1.7.	Future Scope .....	22
2.	Biomass Burning Emission Product .....	25
2.1.	Algorithm Configuration Information .....	26
2.2.	Introduction .....	26
2.3.	Algorithm Overview .....	27
2.3.1	Algorithm flowchart (FRP approach) .....	28
2.3.2	Domain of operation .....	30
2.3.3	Global scenario .....	30
2.4.	Assumptions and Limitations .....	30
2.5.	Validation .....	31

3.	Land Surface Albedo .....	34
3.1.	Algorithm Configuration Information .....	35
3.2.	Introduction .....	35
3.3.	Theoretical background .....	36
3.4.	Methodology .....	37
3.4.1.	Radiative transfer simulations.....	38
3.4.2.	Generation of narrow to broadband albedo conversion coefficients .....	40
3.4.3.	Calibration of the TOA observations of INSAT-3D Imager sensor .....	40
3.4.4.	Data used and generation of LSA .....	40
3.5.	Results .....	41
3.6.	Summary and Future scope .....	42
4.	Actual Evapotranspiration ( <i>AET</i> ) from INSAT 3D series .....	45
4.1.	Algorithm Configuration Information .....	46
4.2.	Introduction .....	46
4.2.1.	Overview and background .....	47
4.2.2.	Objectives .....	48
4.2.3.	Instrument and characteristics of input products .....	48
4.3.	Inputs .....	49
4.3.1.	Static data.....	49
4.3.2.	Image and pre-processing data (Dynamic) .....	49
4.3.3.	Other auxiliary data and model inputs .....	50
4.4.	Algorithm functional specifications .....	51
4.4.1.	Clear sky Latent heat flux ( $\lambda E_{clr}$ ) .....	51
4.4.2.	Soil heat flux model.....	52
4.5.	LST retrieval under cloudy-sky.....	54
4.5.1.	Daily Evapotranspiration (ET).....	54
4.5.3.	Steps for operational implementation .....	55
4.6.	Outputs .....	56
4.7.	Validation .....	57
4.7.1.	Data required.....	57
4.8.	Sensitivity analysis of STIC model simulated latent heat flux on LST and Albedo.....	57

5.	Net Surface Radiation ( $R_n$ ) from INSAT series of data .....	63
5.1.	Algorithm Configuration Information.....	64
5.2.	Introduction .....	64
5.2.1.	Overview and background .....	65
5.2.2.	Objectives .....	65
5.2.3.	Instrument and characteristics of input products .....	66
5.3.	Inputs.....	66
5.3.1.	Image and pre-processing data (Dynamic) .....	66
5.3.2.	Other auxiliary data and model inputs .....	67
5.3.3.	Operational product of WRF short-range forecast.....	67
5.4.	Algorithm functional specifications .....	68
5.4.1.	Clear sky net surface radiation ( $R_{nclr}$ ) .....	68
5.4.2.	Cloudy sky net surface radiation ( $R_{nclrd}$ ).....	69
5.4.3.	Sensitivity Analysis.....	70
5.4.4.	Steps for operational implementation .....	71
5.5.	Outputs .....	71
5.5.1.	Format of the output and the domain.....	71
5.6.	Validation.....	72
5.6.1.	Data required.....	72
6.	Daily Surface Net Shortwave Radiation over Indian Ocean using half-hourly Outgoing Longwave Radiation Data from Indian Geostationary Satellites .....	76
6.1.	Algorithm configuration information .....	77
6.2.	Introduction .....	77
6.3.	Physical basis of the SWR Algorithm .....	79
6.4.	Formulation of the SWR Algorithm.....	79
6.5.	Algorithm Flow Diagram .....	82
6.6.	Operational Implementation.....	82
7.	Clear Sky Brightness Temperature from INSAT-3D/3DR IMAGER .....	85
7.1.	Algorithm Configuration Information .....	86
7.2.	Background .....	86
7.3.	Objective .....	87

7.4. Inputs .....	87
7.4.1. Image and preprocessing data (dynamic) .....	87
7.5. Algorithm Functional Specifications .....	87
7.5.1. Overview .....	87
7.5.2. Generation of CSBT .....	88
7.5.3. Preparation of latitude-longitude grid.....	88
7.5.4. Averaging of parameters .....	88
7.5.5. Quality indicators.....	89
7.6 Outputs .....	89
7.6.1 Format of the output and the domain.....	89
7.7. Validation.....	89
7.7.1. Data required.....	89
8. Clear-Sky Brightness Temperature Products from INSAT-3D/3DR Sounder .....	91
8.1. Algorithm configuration information .....	92
8.2. Introduction .....	92
8.3. Algorithm Description.....	92
8.3.1. Cloud detection .....	92
8.3.2. Clear-Sky Brightness Temperature computation .....	96
8.4. Outputs .....	97
8.5. Validation.....	98
9. Cloud Top Pressure/Cloud Top Temperature and effective cloud amount from INSAT-3D/3DR IMAGER .....	99
9.1. Algorithm Configuration Information .....	100
9.2. Background .....	100
9.3. Objective .....	101
9.4. Inputs .....	101
9.4.1. Static Data .....	101
9.4.3. Other Auxiliary data and Model Inputs .....	102
9.5. Algorithm Functional Specifications .....	102
9.5.1. Overview .....	102
9.5.2. Infrared Window Channel (WIN) method .....	103

9.5.3. Water Vapor–Infrared Window Intercept Method (H <sub>2</sub> O).....	103
9.5.4. Cloud top height and cloud top temperature from cloud top pressure.....	105
9.5.5. Effective cloud amount.....	105
9.5.6. Radiance bias adjustment.....	105
10. Cloud Top Pressure/Cloud Top Temperature from INSAT-3D/3DR SOUNDER.....	108
10.1. Algorithm Configuration Information .....	109
10.2. Introduction .....	109
10.2.1. Overview and background .....	109
10.2.2. Objective .....	109
10.3. Inputs .....	110
10.3.1. Static Data .....	110
10.3.2. Sounder data (dynamic) .....	110
10.3.3. Other Auxiliary data and Model Inputs .....	110
10.4. Algorithm Functional Specifications.....	111
10.5. Algorithm Theoretical Description.....	112
10.6. Physical Basis of the Cloud Top Pressure/Temperature/Height Algorithm.....	112
10.6.1. CO <sub>2</sub> Slicing: Mid- to High-Level Clouds.....	112
10.6.2. Window Channel method for cloud top pressure for low to mid clouds .....	116
10.7. Cloud top height and cloud top temperature from cloud top pressure .....	116
10.8. Radiance bias adjustment .....	117
11. INSAT-3D Cloud Microphysical Product.....	120
11.1. Algorithm configuration information .....	121
11.2. Introduction .....	121
11.3. Overview and Background .....	121
11.4. Objective.....	122
11.5. Inputs .....	122
11.5.1. Static data .....	122
11.5.2. Dynamic data .....	122
11.5.3. Other Auxillary data and Model Inputs.....	123
11.6. Algorithm Functional Specifications .....	123
11.6.1. Overview .....	123

11.6.2.	Theoretical Background.....	123
11.6.3.	Algorithm Overview .....	124
11.6.4.	Flow Chart .....	125
11.7.	Operational retrieval implementation.....	125
11.8.	Output (over Ocean) .....	126
11.9.	Initial Validation .....	126
11.10.	Limitations.....	127
11.11.	Future work.....	127
12.	5-Day Composite Atmospheric Motion Vectors (AMV).....	129
12.1.	Algorithm Configuration Information.....	130
12.2.	Introduction .....	130
12.3.	Overview and background.....	130
12.4.	Objective.....	131
12.5.	Inputs .....	132
12.5.1.	Retrieved AMVs (Dynamic) .....	132
12.6.	Algorithm Functional Specifications.....	132
12.6.1.	Methodology .....	132
12.6.2.	Operational Implementation .....	132
12.7.	Outputs.....	133
13.	High Resolution Visible Winds (HRVIS).....	134
13.1.	Algorithm Configuration Information.....	135
13.2.	Introduction .....	135
13.2.1.	Overview and background .....	135
13.3.	Inputs .....	136
13.3.1	Static Data.....	136
13.3.2.	Image and preprocessing data (Dynamic).....	136
13.3.3.	Other Auxiliary data and Model Inputs .....	137
13.4.	Algorithm Functional Specifications.....	137
13.4.1.	Tracer selection: .....	137
13.4.2.	Height assignment.....	138
13.4.3.	Tracking .....	139

13.4.4. Wind buffer generation and Quality control .....	140
13.5. Operational Implementation.....	142
13.6. Outputs.....	143
13.6.1. Format of the output and the domain .....	143
13.7. Validation.....	144
13.7.1. Data required.....	144
13.7.2. Methods of validation .....	144
13.8. Technical Issues (Limitations etc.) .....	145
14. Atmospheric Motion Vectors: Staggering.....	149
14.1. Algorithm Configuration Information .....	150
14.2. Introduction .....	150
14.2.1. Overview and background .....	150
14.2.2. Objective .....	151
14.3. Inputs .....	151
14.3.1. Static Data.....	151
14.3.2. Image and pre-processing data (Dynamic) .....	152
14.3.3. Other Auxiliary data and Model Inputs .....	152
14.4. Algorithm Functional Specifications.....	152
14.4.1. Methodology .....	152
14.5. Outputs.....	156
14.6 Validation.....	157
14.6.1. Data required.....	157
14.6.2. Methods of validation .....	157
14.7. Technical Issues (Limitations etc) .....	158
15. Modified GPI and IMSRA method.....	161
15.1. Algorithm Configuration Information .....	162
15.2. INTRODUCTION.....	162
15.2.1 Overview.....	163
15.2.2. Objectives .....	165
15.3. Inputs .....	167
15.3.1. Image and preprocessing data (Dynamic).....	167

15.3.2. Other Auxiliary data and Model Inputs .....	168
15.4. Algorithm Functional Specifications.....	169
15.4.1. Overview:.....	169
15.5 Outputs .....	181
Format of the output.....	182
15.6. Validation.....	182
15.6.1. Data Required: .....	183
15.6.2. Method of Validation: .....	183
15.7. Merged Rain Products (IMSRA and Rain Gauges):.....	184
15.7.1. Major Conclusions .....	185
15.8. Future Scope .....	186
16. MIR Reflectance .....	192
16.1. Algorithm Configuration Information.....	193
16.2. Introduction .....	193
16.2.1. Overview and background .....	193
16.2.2. Objective.....	194
16.3. Inputs .....	194
16.3.1. Static data.....	194
16.3.2 Image and pre-processing data (Dynamic) .....	194
16.4. Algorithm Functional Specifications.....	195
16.4.1. Overview.....	195
16.4.2. Operational retrieval Implementation .....	197
16.5. Outputs .....	197
16.5.1. Format of the output and the domain .....	197
16.6. Validation.....	197
16.6.1. Data required.....	197
16.6.2. Methods of validation .....	198
16.7 Technical issues (limitation etc.) .....	198
16.8 Future Scope .....	198
17. Potential evapotranspiration (PET) from INSAT 3D insolation product and short-range forecasts .....	199

17.1. Algorithm Configuration Information .....	200
17.2. Introduction .....	200
17.2.1. Overview and background.....	201
17.2.2. Objectives.....	202
17.2.3. Instrument and characteristics of input products.....	202
17.3. Inputs .....	205
17.4. Algorithm functional specifications .....	205
17.5. Outputs .....	211
17.6. Validation of INSAT 3D generated daily Potential evapo-transpiration .....	212
17.7. Study of Potential Evapo-transpiration with K1 VHRR data.....	212
17.8. Sources of errors / uncertainties in $ET_o$ estimates and validation issues.....	225
17.9. Future scope of improvement.....	226

## **1. Snow-Cover Mapping (SCM) and Fractional Snow Cover (FSC)**

S. No.	Product Name	Spatial Resolution	Temporal Resolution
1.	Snow-Cover Mapping (SCM)	4 x 4 km <sup>2</sup>	daily
2.	Fractional Snow Cover (FSC)	4 x 4 km <sup>2</sup>	daily

## **1.1. Algorithm Configuration Information**

### **1.1.1. Algorithm Name**

Snow Cover Mapping (SCM) and Fractional Snow Cover (FSC).

(Ref: IMD RFP Sec. 11.9)

### **1.1.2. Algorithm Identifier**

ISRO\_INSAT\_SCM\_A001

### **1.1.3. Algorithm Specification**

Version	Date	Modified by	Description
1.0	28.08.2018	S. K. Singh and Naveen Tripathi	Snow Cover Mapping & Fractional Snow Cover

## **2.2. Introduction**

Algorithms is developed to map snow cover using INSAT 3D(R) Meteorological payload. The snow mapping algorithm uses a grouped-criteria technique using the Normalized Difference Snow Index (NDSI) and other spectral threshold tests to identify snow on a pixel-by-pixel basis, and to map snow cover in dense forests. The NDSI is useful for snow mapping, as snow reflects strongly in the visible region but absorbs in the short-wave IR (SWIR) part of the spectrum. The reflectance of clouds is high in the visible as well as short-wave IR. This characteristic is used to identify and map snow cover. Coarse resolution binary snow product from INSAT 3D imager will be further used to generate fractional snow cover product in synchronous with available high resolution snow cover products.

Validation of the INSAT snow maps will be carried out using snow products of AWIFS data of Resourcesat1/2 and a limited amount of field measurements. In addition, validation will also be carried out using visual interpretation and the MODIS derived snow maps. The accuracy of the snow maps may vary with land-cover type. Hence, the Snow map algorithm has been and will continue to be tested for a variety of land covers. Error estimates have been determined from field measurements for different land covers, and these errors are used to estimate the expected maximum monthly and annual errors in Himalayan snow mapping using the algorithm.

### **1.2.1. Overview and background**

The purpose of the snow-mapping algorithm is to generate Himalayan snow cover product from INSAT 3D(R) data. This algorithm is based on the ratio techniques, which was used successfully to monitor snow using AWIFS data of Resourcesat-1. Daily snow and 10 days snow covered digital map products will be generated.

Snow covers almost 40 per cent of the Earth's land surface during Northern Hemisphere winter. This makes snow albedo and area an important component of the Earth's radiation balance (Foster and Chang, 1993). Large areas in the Himalayas are covered by snow during winter time. Area of snow can change significantly during winter and spring. This can affect stream flow during spring and summer of the rivers originating in the Higher Himalayas. In addition, snow pack ablation is highly sensitive to climatic variation. Increase in atmospheric temperature can influence snowmelt and stream runoff pattern (Kulkarni et al. 2002a). Therefore, mapping of areal extent and reflectance of snow is an important parameter for various climatological and hydrological applications. In addition, extent of snow cover can also be used as an input for avalanche investigation.

Snow was first observed in April 1960 by TIROS-1 satellite in eastern Canada. Since then, the potential for operational satellite-based mapping has been enhanced by the development of higher temporal-frequency and satellite sensors with higher spatial resolution. In addition, satellite sensors with better radiometric resolutions, such as MODIS and AWIFS have been used successfully for snow mapping (Hall et al. 2002; Kulkarni et al. 2006). This is possibly due to distinct spectral reflectance characteristics of snow in visible and short wave infrared region. Information generated from satellite observations has been extensively used for snowmelt runoff modeling (Kulkarni et al. 2002b). Remote sensing technique has been extensively used for snow cover monitoring in the Himalayan region with the help of numerous satellite sensors (Kulkarni and Rathore, 2003). Various analysis techniques as visual, hybrid (Visual and supervised classification) have been used to estimate areal extent of snow cover (Kulkarni and Rathore, 2003). However, major difficulty in snow cover monitoring using automated technique in the Himalayan region is mountain shadow and confusing signature of snow and cloud in the visible and near infrared region. Because of above-mentioned reasons, combination of digital and visual interpretation technique is needed to monitor snow cover. This makes snow cover mapping cumbersome and time consuming. To overcome this problem normalized difference snow index method is developed and discussed in this document. In optical region snow reflectance is higher as compared to other land features as grass, rock and water. However, in SWIR region snow reflectance is lower than rock and vegetation (Kulkarni et al. 2002c). Therefore, snow on satellite images appears white in visible and black in SWIR region. This characteristic has been effectively used to develop Normalized Difference Snow Index (NDSI) for snow cover mapping (Hall et al. 1995).

### **1.2.2. Remote Sensing of Snow Cover**

One of the earliest methods used for snow cover monitoring was visual interpretation. During this investigation Large Format Optical Enlarger was used and investigation was carried out using band 2 of Landsat MSS and IRS LISS-I sensor. The investigation was extensively used for snow cover monitoring in Malan, Tosh and many small basins in the Himalayas (Kulkarni et al. 2004).

This technique was further modified with advancement of Digital Analysis Technique and availability of higher frequency satellite data such as WiFS of IRS and VHRR of NOAA satellite. In this technique, a combination of visual and digital analysis was used. This was necessary because mountain shadows in the months from November to February normally make it difficult to use only digital technique for snow cover delineation. From the month of March mountain shadows are negligible and snow extent can be estimated from supervised classification technique. This technique has been extensively used to map snow cover in Western Himalaya, Baspa and Satluj basins (Kulkarni and Rathore, 2003).

Another major difficulty in snow cover monitoring is cloud cover. It is further compounded due to similar reflectance characteristics of snow and cloud. The discrimination between snow and cloud can be done by using various techniques such as textural analysis, association with shadow and by using multi temporal analysis. In Himalayas and in present investigation, snow/cloud discrimination was done by using texture, where snow shows characteristic mountainous pattern, which cannot be seen when area is cloud covered. In visible and near infrared region reflectance of snow and cloud is very high. Therefore, discrimination between snow and cloud is not possible. This is because of similar reflectance characteristics in this region. In spectral range between 1.55-1.75  $\mu\text{m}$ , 2.1-2.35  $\mu\text{m}$  and 3.55-3.93  $\mu\text{m}$  have shown potential for snow/cloud discrimination. In these bands, snow has lower reflectance than cloud. Spectral region between 1.55-1.75  $\mu\text{m}$  has been successfully used to separate certain types of clouds from snow (Kulkarni et al. 2006).

Reflectance of fresh snow is very high in the visible part of the electromagnetic spectrum, but decreases in the near-IR especially as grain size increases (O'Brien and Munis, 1975; Warren and Wiscombe, 1980; Srinivasulu et al. 2002). In addition, soot from industrial pollution becomes incorporated into the snowpack and this may decrease albedo and enhance snowmelt (Clarke and Noone, 1985; Negi et al. 2006). Both because of natural aging and other factors (e.g. soot or volcanic ash deposition), the reflectance of snow decreases over time. Fresh snow can have a reflectance (integrated over the reflective part of the spectrum) up to about 80 percent but its reflectance may decrease to below 40 percent after snow crystals metamorphose.

Snow, like all natural surfaces, is an anisotropic reflector (Nolin and Liang, 2000). The reflectance from snow is high in the forward direction and is largely specular. While freshly fallen snow can be nearly a Lambertian reflecting surface, as snow metamorphoses the specular component characteristic of forward scattering increases.

### 1.2.3. Objective

The purpose of the snow-mapping algorithm is to generate Himalayan snow cover product from INSAT 3D(R) data. This algorithm is based on Normalised Difference Snow Index method, which was used successfully to monitor snow using AWIFS data of Resourcesat. Daily snow and maximum 10-day snow covered area digital-map products will be generated.

This algorithm will be further modified, with NDVI adopted from other sources and infrared brightness temperature to identify snow in forest covers and identify cloud pixels, respectively.

## 1.3. Inputs and output data

### 1.3.1. Image and preprocessing data (Dynamic)

Parameter	Resolution	Quantization	Accuracy
Radiometric and geometric corrected gray count values Visible (0.52-0.75 $\mu\text{m}$ ) & SWIR (1.55-1.70 $\mu\text{m}$ )	pixel	10 bit	-
Radiometric and geometric corrected gray count values of TIR-1 channel (10.2-11.2 $\mu\text{m}$ )	pixel	10 bit	-
Gray value to brightness temperature conversion table	-	-	0.3 K
Geolocation file	Pixel	-	1 pixel

### 1.3.2. Other Auxillary data and Model Inputs (Static)

Source	Product	Frequency	Role in algorithm	Purpose
Carto/Gtopo	DEM	Once	Mask	Masking low altitude area
Reflectance library using Field observations	Reflectance in visible and SWIR region	As per requirement	NDSI threshold value	Development and validation of algorithm
AWIFS	Snow Cover	5 days	Identification of snow pixel in INSAT grid	Generating fractional snow cover product of INSAT

## **1.4. Algorithm Functional Specifications**

### **1.4.1. Overview**

A grouped-criteria technique incorporating NDSI and threshold-based criterion for the algorithm was selected for the following reasons:

- Sensors with better radiometric resolutions, such as MODIS and AWiFS, have been used for generating the snow products using similar algorithm. (Hall et al., 1995; Kulkarni et al., 2006; Singh et al., 2013; Rathore et al., 2015).
- The technique can map snow under mountain shadow and independent of local solar illumination angle. It makes this algorithm highly suitable for mountainous terrain as Himalayas (Kulkarni et al. 2006).
- INSAT 3D(R) Met payloads has a channel in 1.55 to 1.75  $\mu\text{m}$  with 1 km spatial resolution. Similar channel is not available on GOES satellite. In addition, channel number INSAT 3D(R) 1&2 channels are having 1 km spatial resolution. Therefore, product can be generated at 1 km resolution.
- SWIR reflectance/Brightness temperature will be used to identify certain type of clouds which were not separated using NDSI threshold. Threshold values will be fine-tuned. This will be initially established using Spectral Reflectance library of Space Applications Centre and then sensitivity analysis of INSAT-3D(R) data.
- AWiFS derived snow cover products will be used to estimate snow part in synchronous INSAT pixel to develop approach for estimating fractional snow cover product for INSAT data.

It runs automatically, without human intervention. It is straightforward, computationally frugal, and thus easy for the user to understand exactly how the product is generated.

Snow has strong visible reflectance and strong short-wave IR absorbing characteristics. The Normalized Difference Snow Index (NDSI) is an effective way to distinguish snow from many other surface features. Both sunlit and some shadowed snow is mapped effectively. A similar index for vegetation, the Normalized Difference Vegetation Index (NDVI) has been proven to be effective for monitoring global vegetation conditions throughout the year (Tucker, 1979 and 1986). Additionally, some snow/cloud discrimination is accomplished using the NDSI.

Other promising techniques, such as traditional supervised multispectral classifications, spectral-mixture modeling, or neural-network analyses have not yet been shown to be usable for automatic application at the mountainous region. They are also computationally intensive. Training or the interaction of an interpreter is required for successful application of techniques such as neural-network analysis. These techniques may progress to regional applications and possibly even global application in future years.

In fractional snow cover, presently snow cover products derived using AWIFS data will be used to develop the approach. INSAT derived snow was matched with synchronous AWIFS snow pixels which was used to develop a relationship for snow fraction of INSAT pixel.

#### **1.4.2. Theoretical Background**

##### **1.4.2.1. Snow cover map**

The snow-cover mapping algorithm is designed to identify snow in each 1 km pixel. A regional, daily snow product will be produced. A 10-day composite snow cover product will be generated by compositing successive days of snow cover products. This will yield maximum snow extent for the 10-day period. If a pixel were snow covered on any orbit during that period, then that pixel will be mapped as snow covered even if it were snow-free on all of the other orbits during the 10-day period. Other coverage and persistence statistics will also be included to assist analysis of the data product.

There has been much discussion concerning the optimum composite period for the snow maps (Kulkarni et al, 2006). While weekly composites would correspond with the NOAA/NESDIS maps and the NOHRSC maps, some modelers are interested in longer composition periods, e.g., 7 days to one month. 8-day composites were chosen because this period optimizes the ground coverage from the MODIS instrument. In India, the hydrological data analysis is carried out on 10-daily basis; therefore 10-day composite will be prepared. If a researcher wants to produce a composite product for any period other than a 10-day period, from our daily product, this can be done using the daily data.

##### **1.4.2.2. Normalized Difference Snow Index (NDSI)**

The NDSI is useful for the identification of snow and for separating snow and most cumulus clouds. The NDSI is a measure of the relative magnitude of the characteristic reflectance difference between the visible and short-wave IR reflectance of snow. The NDSI is insensitive to a wide range of illumination conditions (Kulkarni et al. 2006). The NDSI is analogous to the normalized-difference vegetation index (NDVI) (Tucker, 1979 and 1986; Townshend and Tucker, 1984). NDSI can be computed as given below;

$$\text{NDSI} = (\text{Visible}_{\text{INSAT B1}} - \text{SWIR}_{\text{INSAT B2}}) / (\text{Visible}_{\text{INSAT B1}} + \text{SWIR}_{\text{INSAT B2}})$$

Pixels that are approximately 75% or greater covered by snow were found to have NDSI values more than 0.4 in our field investigation at Dhundi test site in Himachal Pradesh (Negi et al. 2006). These NDSI thresholds have been verified from detailed analysis of numerous AWIFS scenes, comparisons with supervised-classification techniques and NDSI technique. (Kulkarni et al, 2004). Pure snow has a high NDSI but NDSI decreases as other features are mixed in a pixel. Snow in mixed pixels has an NDSI that is less than that for pure snow. Pure snow can be distinguished by its high NDSI value (Negi et al. 2006). Since bandwidth of AWIFS band 1 and INSAT 3D(R) imager is different, initially NDSI threshold value will be established using Field Spectral Data

Library of Space Applications Centre (Singh et al. 2005 and Negi et al. 2006). This will be further evaluated during post launch period, by carrying out sensitivity analysis (Kulkarni et al. 2006).

In forested locations, many snow covered pixels have an NDSI lower than 0.4. To correctly classify these forests as snow covered, a lower NDSI threshold is necessary (Negi et al. 2006). NDVI and NDSI will be used together in order to discriminate between snow-free and snow covered forests. Forested pixels have higher NDVI values compared with non-forested pixels. Thus by using the NDSI and NDVI in combination, it is possible to lower the NDSI threshold in forested areas without compromising the algorithm performance for other land covers. Since appropriate bands are not available in INSAT 3D(R) payload, mask will be used from other existing source.

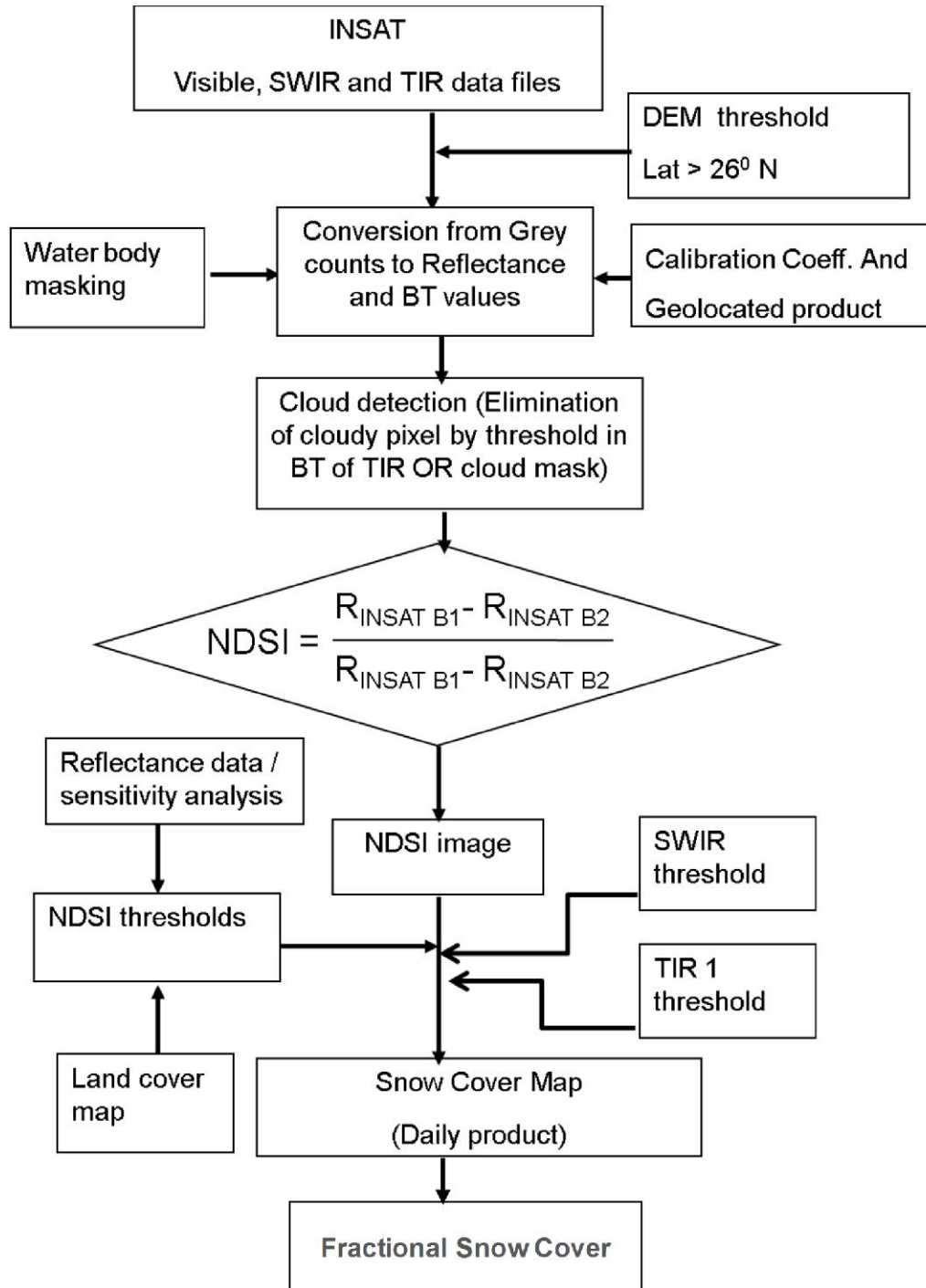
Since water may also have an NDSI 0.4, therefore permanent mask is necessary to separate water from snow.

#### **1.4.2.3. Snow / Cloud Discrimination**

Snow/cloud-discrimination techniques are based on differences between cloud and snow reflectance and emittance characteristics. Clouds are highly variable and may be detected by their generally high reflectance in the visible and near-IR parts of the electromagnetic spectrum (Kulkarni et al. 2002a), whereas the reflectance of snow drops in the short-wave infrared part of the spectrum.

While the NDSI can separate snow from most obscuring clouds, it does not always identify or discriminate optically-thin cirrus clouds from snow. Analyses of AWIFS and MODIS data show that NDSI can map snow under cirrus clouds at least some of the time. Cirrus clouds have high reflectance in SWIR region than snow which requires fine tuning of threshold value and will be used as an additional criterion in present approach. This algorithm will further be improved due to availability of thermal bands in INSAT 3D(R) Met payload. Appropriate brightness temperature threshold will be used to separate cloud from snow (Romanov and Tarpley, 2003) or cloud removal will also be tested using cloud mask product subject to its availability as an additional INSAT 3D(R) derived product. This will be additional criteria than in built criteria of NDSI.

#### 1.4.2.4. Flow Chart



#### **1.4.2.5. Sensitivity analysis to establish NDSI threshold**

In order to establish credible threshold value of NDSI for snow cover mapping, sensitivity tests of individual threshold values were carried out. Sensitivity analysis will be carry out to identify NDSI threshold for INSAT 3D(R) snow products. This threshold value will also be verified using FFC combination for snow covered area identification.

#### **1.4.2.6. Fraction Snow Cover**

Snow binary product of INSAT 3D data, available at coarse resolution, will be used to convert into fractional snow cover which will be helpful to improve the snow cover areal extent based on occupancy of that pixel in terms of actual snow fraction present in respective pixel of INSAT 3D. Synchronous INSAT and high resolution satellite derive NDSI and snow cover product were selected for the winter season. Different months and terrain in Himalayan region was chosen to represent to take care possible scenarios. INSAT derived NDSI and snow pixel was compared with NDSI and snow pixel for high resolution data to develop a relationship between NDSI and snow cover areal extent for coarse and fine resolution datasets. This develop relationship will be used to generate fractional snow cover area for INSAT dataset and will be helpful to improve daily snow cover areal extent from geostationary platform.

### **1.4.3. Operational Implementation**

**Step 1 :** Conversion from gray count to Reflectance and BT:

In this step, the DN values will be converted into Radiance, Reflectance and Brightness temperature using calibration coefficient available with INSAT 3D(R) data. The radiometrically processed data will also be geolocated and this will provide a radiometrically and geometrically corrected product to be used further in algorithm.

**Step 2 :** Cloud elimination

This step includes the cloud screening from the INSAT 3D(R) image. Cloud screening is based on SWIR reflectance/temperature data, or cloud mask product will be used subject to its availability, and this will help to clear cloudy pixels.

**Step 3 :** Generation of NDSI image

Normalized Difference Snow Index will be computed using the normalized ratio of visible and SWIR channel as given below;

$$\text{NDSI} = (R_{\text{INSAT B1}} - R_{\text{INSAT B2}}) / (R_{\text{INSAT B1}} + R_{\text{INSAT B2}})$$

where R is the reflectance of the respective channel.

**Step 4:** Generation of Fractional snow pixel

A developed relationship will be used to convert INSAT 3D coarse resolution pixel into fractional snow cover pixel for the respective pixel.

Accuracy of SCM and FSC is expected to be approximately 90% or better.

## 1.5. Outputs

Parameter	Unit	Min	Max	Accuracy	Resolution
SCM	$4*4 \text{ km}^2$	-	-	-	Pixel level
FSC	$\text{km}^2$	-	-	-	Pixel level

### 1.5.1. Format of the output and the domain

Geolocated Snow cover and fraction snow cover map of INSAT dataset, focusing on Hindu Kush-Karakoram-Himalayan region.

## 1.6. Validation and Error Analysis

### 1.6.1. Field Spectroradiometer data

Field data of snow and other ambient objects will be collected and analyzed for the wavelength bands in INSAT 3DR. These value will be used to verify NDSI threshold to discriminate snow from other existing land cover features.

### 1.6.2. Visual Snow Cover Map

Snow cover pixel will be identified visually and will be verified on automated snow cover product generated using INSAT 3D(R). This may also be extended to visually map snow covers and validate these map with operationally derive snow cover products.

### 1.6.3. Comparison of INSAT 3D(R) snow maps with AWIFS snow products

INSAT-derived snow maps will continue to be compared with snow cover maps generated by AWIFS. In addition, comparisons will be made between MODIS maps. Comparison of Snowmap results with these independently produced snow data sets will allow errors to be identified that will permit us to determine the accuracy of the global maps relative to one another.

## 1.7. Future Scope

This algorithm will be further modified, in conjunction with NDVI (available from AWIFS product or any other source) and infrared brightness temperature to identify snow in forest covers and identify cloud pixels, respectively. INSAT 3D being a coarse resolution satellite, Approach using AWIFS snow products has been developed, however scatterplot shows a spread over different range which could be due to geolocation error. An attempt will also be made using different techniques such as homogeneity test, histogram matching etc. to reduce the scatter due to mismatch

probably arising due to geolocation error. This will further help to improve fractional snow cover product to improve the accuracy of snow cover areal extent.

## References

- Clarke, A.D. and K.J. Noone, 1985. Soot in the Arctic snowpack: a cause for perturbations in radiative transfer. *Atmospheric Environment*, 19, 2045-2053.
- Chaponniere, A., P. Maisongrade, B. Duchemin, L. Hanich, G. Boulet, R. Escadafal and S. Elouaddat, 2005. A combined high and low spatial resolution approach for mapping snow covered areas in the Atlas mountains, *International J. of Remote Sensing*, 26(13), 2755-2777.
- Foster, J. L., and Chang, A. T. C., 1993. Snow Cover. In "Atlas of Satellite Observations Related to Global Change." Eds. R. L. Burney, C. L. Parkinson, and J. L. Foster, 361-370. Cambridge University Press, Cambridge.
- Hall, D.K., G.A. Riggs and V.V. Salomonson, 1995. Development of methods for mapping global snow cover using moderate resolution imaging spectroradiometer data, *Remote Sensing of Environment*, 54, 127-140.
- Hall, D.K., V.V. Salomonson, G.A. Riggs, N. DiGirolamo and K.J. Bayr, 2002, MODIS snow cover products, *Remote Sensing of Environment*, 83, 181-194.
- Kulkarni A. V., S. K. Singh, P. Mathur and V. D. Mishra, 2006. Algorithm to monitor snow cover using AWIFS data of Resourcesat for the Himalayan region, *International J. of Remote Sensing*, 27(12), 2449-2457.
- Kulkarni A. V., P. Mathur, S. K. Singh, B. P. Rathore and N. Thakur, 2004. Remote sensing based techniques for snow cover monitoring for the Himalayan region, Proc. International Symposium on Snow Monitoring and Avalanches, Manali, 399-405.
- Kulkarni, A.V. and B. P. Rathore, 2003. Snow cover monitoring in Baspa basin using IRS WiFS data, *Mausam*, 54(1), 335-34.
- Kulkarni A.V, J. Srinivasulu, S. S. Manjul and P. Mathur, 2002(a). Field based spectral reflectance to develop NDSI method for snow cover monitoring, *Journal of Indian Society of Remote Sensing*, 30 (1 & 2), 73-80.
- Kulkarni A.V, S. S. Randhawa, B. P. Rathore, I. M. Bahuguna and R.K. Sood, 2002(b). A snow and glacier melt runoff model to estimate hydropower potential, *Journal of Indian Society of Remote Sensing* 30 (4), 221-228.
- Kulkarni A.V, P. Mathur, B.P. Rathore, Suja Alex, N. Thakur and Manoj Kumar, 2002(c). Effect of Global warming on snow ablation pattern in the Himalayas, *Current Science*, 83(2), 120-123.
- Negi, H. S., A. V. Kulkarni, R. P. Prajapati, S.K. Singh and J. K. Sharma, 2006. Effect of contamination and mixed objects on snow reflectance using spectroradiometer, *Scientific Report*

number RSAM/SAC/RESIPA/MWRG-GLI/SN25/2006, Space Applications Centre, Ahmedabad, India, 24p.

Nolin, A.W. and S. Liang, 2000. Progress in Bidirectional reflectance modeling and applications for surface particulate media: snow and soils, *Remote Sensing Reviews*, 18, 307-342.

O'Brien, H.W. and R.H. Munis, 1975. Red and near-infrared spectral reflectance of snow. In: Operational Applications of Satellite Snow cover Observations, Ed. A. Rango, NASA SP-391 (Washington, D.C.: NASA), 345-360.

Rathore, B. P., Singh, S. K., Bahuguna, I. M., Brahmbhatt, R. M., Rajawat A. S., Thapliyal, A., Panwar, A. and Ajai (2015). Spatio-temporal variability of snow cover in Alaknanda, Bhagirathi and Yamuna sub-basins, *Uttarakhand Himalaya Current Science*, vol. 108(7), pp 1375-1380.

Romanov P. and Tarpley D. 2003. Automated monitoring of snow cover over south America using GOES imager data. *International J. of Remote Sensing*, 24(5), 1119-1125.

Romanov P., Tarpley D., Gutman G. and Carroll T. 2003. Mapping and monitoring of snow cover fraction over North America, *J. of Geophysical Research*, vol 108, D16, 8619, 14-1to 14-15.

Singh, S. K., H. S. Negi, Babu Govindh Raj K., A. V. Kulkarni and J. K. Sharma, 2005. Spectral reflectance investigations of snow and other objects using ASD radiometer. RSAM/SAC/RESIPA/MWRG-GLI/SN 23/2005, 43p

Singh, S. K., Rathore, B. P, Bahuguna I. M. and Ajai, 2013. Snow cover variability in the Himalayan-Tibetan region. *International journal of Climatology*. DOI:10.1002/joc.3697.

Townshend, J.R.G. and C.J. Tucker, 1984. Objective assessment of Advanced Very High Resolution Radiometer data for land cover mapping, *International J. of Remote Sensing*, 5, 497-504.

Tucker, C.J., 1979. Red and photographic infrared linear combinations for monitoring vegetation, *Remote Sensing of Environment*, 8, 127-150.

Tucker, C.J., 1986. Maximum normalized difference vegetation index images for sub-Saharan Africa for 1983-1985, *International J. of Remote Sensing*, 7, 1383-1384.

## **2. Biomass Burning Emission Product**

S. No.	Product Name	Spatial Resolution	Temporal Resolution
1	BBEP	4 km x 4 km	30 minutes

## **2.1. Algorithm Configuration Information**

### **2.1.1. Algorithm Name**

Biomass burning emission product (BBEP)

### **2.1.2. Algorithm Identifier**

BBEM

### **2.1.3. Algorithm Specification**

Version	Date	Modified by	Description
1.0	June 2018	C. P. Singh	Biomass Burning Emission Product

## **2.2. Introduction**

Near-real-time estimates of biomass burning emissions are crucial for air quality monitoring. This algorithm theoretical basis document (ATBD) provides a description of new fire characterization science product, specifically named as, biomass burning emission product (BBEP) utilizing the INSAT-3D/3DR Imager. The INSAT active fire algorithm is a dynamic multispectral thresholding contextual algorithm that is based on the sensitivity of the 3.9  $\mu\text{m}$  (MIR channel) to high temperature sub-pixel anomalies relative to the less sensitive 10.8  $\mu\text{m}$  (TIR-1 Channel). The current operational version of the INSAT fire product provides information on the location of the fire pixel only. In order to characterize the fire in terms of BBEP further details like estimates of instantaneous sub-pixel fire size, temperature, and radiative power; ecosystem type; and a classification flag needs to be worked out at pixel level. The fire properties are coupled to each other, one cannot calculate an instantaneous fire size without estimating a fire temperature, and fire radiative power (FRP) is a function of size and temperature. The algorithm will work upon accurate estimation of satellite-derived fire radiative power (FRP) for individual fire pixels. The INSAT-3D/3DR satellites observe wildfires at an interval of 15–30 min. Because of the impacts from sensor saturation, thin cloud cover, and background surface, the FRP values will not be continuously observed. The missing observations will be simulated by combining the available instantaneous FRP observations within a day and a set of representative climatological diurnal patterns of FRP for various ecosystems (evergreen forests, semi-evergreen and deciduous forests with their densities like dense, medium and open forests). Finally, the simulated diurnal variation in FRP will be applied to quantify biomass combustion and emissions in individual fire pixels with a latency of 1 day (0300 UTC – 0230 UTC for INSAt-3D & 0315 UTC to 0245 UTC for 3DR; following day). It is expected that near-real-time hourly emissions from BBEP would provide a crucial component for atmospheric and chemical transport modelers to forecast air quality and weather conditions.

### 2.3. Algorithm Overview

Biomass burning emissions can be modeled using four fundamental parameters; burned area, fuel loading (biomass density), the fraction of biomass combustion, and the factors of emissions for trace gases and aerosols. By integrating these parameters, biomass burning emissions can be estimated using the following formula (Seiler and Crutzen, 1980):

Where, E = emissions from biomass burning (kg);

DM = dry fuel mass combusted (kg);

F = factor of consumed biomass that is released as trace gases and smoke particulates

A = burned area ( $\text{km}^2$ );

B = biomass density ( $\text{kg}/\text{km}^2$ );

C = fraction of biomass consumed during a fire event.

This simple model has been widely applied to estimate fire emissions in local, regional, and global scales (Ito and Penner, 2004; Reid et al., 2004; Wiedinmyer et al., 2006; van der Werf et al., 2006; Zhang et al., 2008). The accuracy of the emissions depends strongly on the quality of fuel loading and burned area estimates, which have high uncertainties (Zhang et al., 2008; van der Werf et al., 2010; French et al., 2011). Alternatively, Wooster, 2002 demonstrated a linear relationship between fuel consumption and total emitted fire radiative energy. This is due to the fact that the total amount of energy released per unit mass of dry fuel fully burned is weakly dependent on vegetation types and fuel types, which ranges between 16 and 22 MJ/kg (Lobert and Warnatz, 1993; Whelan, 1995; Trollope et al., 1996; Wooster et al., 2005). Thus, biomass burning emission is linearly linked to fire radiative energy in a simple formula (Wooster, 2002):

$$E = DM \times F = FRE \times \beta \times F = \int_{t_1}^{t_2} FRPdt \times \beta \times F \quad \dots \dots \dots \quad (2)$$

Where; FRP = fire radiative power (MW);

FRE = fire radiative energy (MJ);

$t_1$  and  $t_2$  = beginning and ending time (second) of a fire event;

$\beta$  = biomass combustion rate (kg/MJ)

F = emission factor (g/kg for CO and PM2.5)

FRE represents the combination of total burned area and the dry fuel mass combusted (e.g., live foliage, branches, dead leaf litter, and woody materials) in a given time period, which reduces error sources of parameter measurements comparing with the first approach (eq.1) employing both burned area and fuel loading in the estimates of biomass burning emissions. Thus, the FRP approach will be better to produce BBEP.

### 2.3.1 Algorithm flowchart (FRP approach)

Once a fire is identified, Fire Radiative Power (FRP) estimation algorithm will be applied. FRP is theoretically a function of fire size and fire temperature. It is empirically related to the difference of brightness temperature between a fire pixel and ambient background pixels at the middle infrared (MIR) band (Kaufman et al., 1998). Further, FRP is approximated as the difference of MIR spectral radiances between a fire pixel and ambient background pixels in a linear form (Wooster et al., 2003). The proposed method is based on the assumption that Fire Radiative Power (FRP) is empirically related to the difference of brightness temperature between a fire pixel and ambient background pixels at the middle infrared (MIR) channel. Biomass burning emission will be computed using eq.2 (Wooster, 2002) below:

$$E = \int_{t_1}^{t_2} FRP_{dt} \times \beta \times F$$

$\beta$  is biomass combustion rate (kg/MJ) which is assumed to be a constant. It is  $0.368 \pm 0.015$  kg/MJ based on field controlled experiments regardless of the land surface conditions (Wooster et al., 2005). This coefficient has been accepted for the calculation of biomass burning emissions from MODIS FRP, SEVERI FRP and GOES FRP (Roberts et al., 2009; Ellicott et al., 2009, Zhang et al., 2012), and so this value will be adopted.

$F$  is emission factor (a representative value that is used to represent the quantity of a trace gas or aerosol species released into the atmosphere during a forest fire activity. The value is a function of fuel type and is expressed as the number of kilograms of particulate per ton (or metric ton) of material or fuel. The value for  $F$  will be assigned for each emitted species (CO and PM2.5) with land cover type according to values published in literature (Andreae and Merlet, 2001; Wiedinmyer et al., 2006). Specifically, the emission factors will be assigned to stratified land cover types: e.g. 11.07 g/kg (PM2.5) and 77 g/kg (CO) in forests, 5.6 g/kg (PM2.5) and 84 g/kg (CO) in shrublands, 9.5 g/kg (PM2.5) and 90 g/kg (CO) in grasslands, and 5.7 g/kg (PM2.5) and 70 g/kg (CO) in croplands.

Although INSAT-3D/R satellites observe the surface every 15–30 min, observations of diurnal fires may, to a great extent, be obstructed by the impact factors including cloud cover, canopy cover, heavy fire smoke, heterogeneity of the surface, large pixel size and view angle of satellites, and weak energy release from fire pixels (Giglio et al., 2003; Prins and Menzel, 1992; Roberts et al., 2005; Zhang et al., 2011). Thus, missing FRP observations cause a great amount of gaps in the spatial and temporal distributions. As a result, FRE in a given time period and region is not able to be directly integrated from satellite-observed FRP. To overcome these limitations, the diurnal patterns of FRP need to be reconstructed, which will be done by using a climatological value of FRP between  $t_1$  and  $t_2$  as exemplified in fig.1. Since, we will be giving products only over forests therefore, different forest density classes and forest types will be considered for making efforts in simulating diurnal FRP climatology.

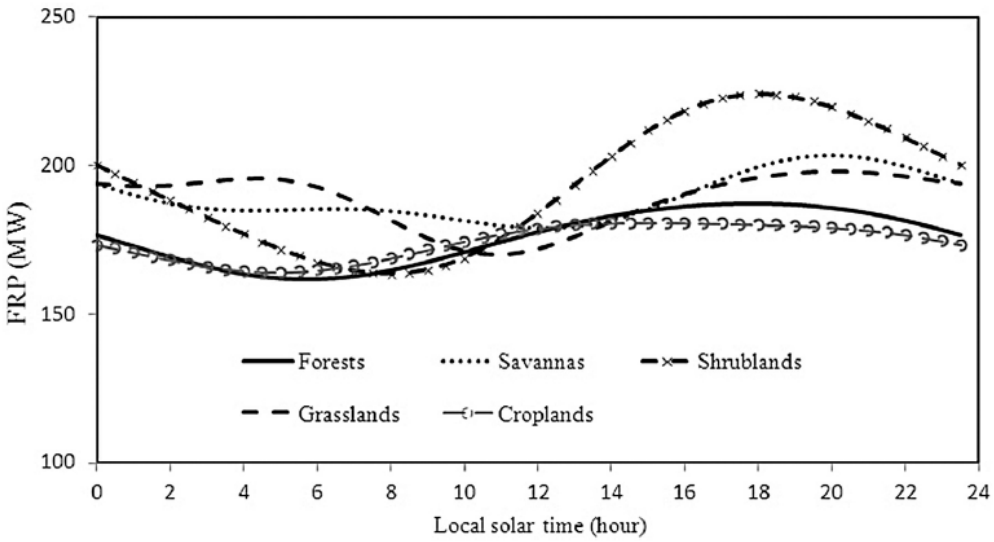


Fig.1. Climatological diurnal FRP (average data from 2002 to 2005) for various ecosystems in North America (Zhang et al., 2012)

To do this, we will adopt the approach that was originally developed to reconstruct diurnal pattern of fire size (Zhang and Kondragunta, 2008; Zhang et al., 2011). The climatological FRP will be calculated for forest types and their density classes, separately. These FRP data in a half-hourly interval will be smoothed using statistical fittings. The offset of shift is determined from the data pairs of the detected FRP for the given fire pixel and the corresponding values in the climatological curve using a least square method. Because fires in a pixel may not last for a very long time and instantaneous fires are not continuously detected due to the impacts from cloud cover, smoke, low severity fires releasing limited fire energy, and other factors (Zhang et al., 2011), the fire duration will be determined by assuming that fire could be extended 2 hours prior and post instantaneous fire detections if the number of the fire detections within a day is more than three times for the same pixel. Otherwise, fire occurrences are based on actual satellite detections. Finally, total FRE will be computed which is the time integral of fire radiative power (FRP) and FRE has correlation between PM 2.5 concentrations and other emissions.

$$FRE = \int_{t_s}^{t_e} FRP dt. \quad \dots \dots \dots \quad (3)$$

where  $t_s$  is the start time of a fire event and  $t_e$  is the end time of the fire pixel.

For a given material one may assert that the total FRE of a fire is directly related to mass consumed by that material's heat of combustion, which can then be related to PM 2.5 and other emissions (Kaufman et al., 1998; Wooster et al., 2003; Roberts et al., 2005).

Because the temporal resolution of INSAT-3D/3DR will range from 15 (together) to 30 min (alone), we will set a minimum time step as 30 min. This means that we will calculate FRE by assuming that a fire can last for at least a half hour if there is one FRP observation. The half-hourly FRE is binned to calculate hourly biomass burning emissions.

In near-real-time monitoring of biomass burning emissions, we will use INSAT-3D/3DR fire products from MMDRPS. The diurnal pattern of FRP will then be simulated for the previous day (0300 UTC – 0230 UTC for INSAT-3D & 0315UTC to 0245UTC for INSAT-3DR) for estimating fire emissions. As a result, the BBEP will be produced with a latency of 1 day. Daily and monthly emissions can be given as the sum of hourly values for a given region and an ecosystem type, separately.

### **2.3.2 Domain of operation**

The domain of application will be kept to  $10^{\circ}$  -  $45^{\circ}$ N,  $45^{\circ}$  -  $105^{\circ}$ E (covering SAARC countries, presently operational Asia\_Mer Sector) and only to forest regions.

### **2.3.3 Global scenario**

FRP approach is adapted by WF\_ABBA in the Cooperative Institute for Meteorological Satellite Studies (CIMSS), University of Wisconsin [Prins et al., 1998; Weaver et al., 2004]. Particularly, the WF\_ABBA V65 detects instantaneous fires in subpixels using infrared bands around 3.9 and 10.7 mm from a network of geostationary satellite instruments that include SEVIRI on board the Meteosat-9, and Imagers on board both GOES and MTSAT. It then derives instantaneous FRP from radiances in single MIR [Wooster et al., 2003]. Further, to minimize false fire detections, the WF\_ABBA uses a temporal filter to exclude the fire pixels that are only detected once within the past 12 h [Schmidt and Prins, 2003]. The WF\_ABBA V65 has been installed in NOAA OSDPD (the Office of Satellite Data Processing and Distribution) to operationally produce FRP from geostationary satellites since late 2009 (<http://satepsanone.nesdis.noaa.gov/pub/FIRE/forPo/>). The NOAA fire product provides detailed information of WF\_ABBA V65 fire detections.

## **2.4. Assumptions and Limitations**

Several assumptions have been made concerning performance estimates. Meteorological satellite instruments are not inherently designed to be able to detect and characterize small sub-pixel hot spots. Therefore, performance of the algorithm will be sensitive to instrument noise and other anomalies. First of all, the output from the equations is no better than the input Imager data. The technique assumes well calibrated Channels that meet current specifications for NedT, co-registration, diffraction, earth location, saturation, etc. It also assumes that sub-pixel detector saturations are flagged and available for application in near real time. If this information is not available, sub-pixel characterization is suspect for both saturated and non-saturated fire pixels. The algorithm assumes that observed radiances are determined by the fire and non-fire portion of the pixel and are only affected by and adjusted for surface emissivity, water vapor attenuation, semi-transparent clouds/smoke, diffraction, and solar reflectivity (3.9  $\mu$ m band – Channel 3 – only).

Each of the above “attenuation” (except clouds/smoke) properties are assumed the same for the fire pixel and background conditions.

## 2.5. Validation

High uncertainty exists in global biomass emissions and accurate validation is currently not possible because of the lack of reliable *in situ* measurement. Therefore, BBEP will be compared with other data sources. We will validate our product with the Global Fire Emissions Database (GFED), Quick Fire Emission Data (QFED), SEVIRI, Himawari & FY-4A and MODIS products. Validation using in-situ measurement using portable instruments will also be attempted.

## References

- Andreae, M. O., and P. Merlet (2001), Emission of trace gases and aerosols from biomass burning, *Global Biogeochem. Cycles*, 15(4), 955–966, doi:10.1029/2000GB001382.
- Dozier, J. (1981), A method for satellite identification of surface temperature fields in subpixel resolution. *Remote Sensing of Environment*, 11, 221-229.
- Ellicott, E., E. Vermote, L. Giglio, and G. Roberts (2009), Estimating biomass consumed from fire using MODIS FRE, *Geophys. Res. Lett.*, 36, L13401, doi:10.1029/2009GL038581.
- French, N. H. F., et al. (2011), Model comparisons for estimating carbon emissions from North American wildland fire, *J. Geophys. Res.*, 116, G00K05, doi:10.1029/2010JG001469.
- Giglio, L., J. D. Kendall, and R. Mack (2003), A multi-year active fire dataset for the tropics derived from the TRMM VIRS, *Int. J. Remote Sens.*, 24, 4505–4525.
- Ito, A., and J. E. Penner (2004), Global estimates of biomass burning emissions based on satellite imagery for the year 2000, *J. Geophys. Res.*, 109, D14S05, doi:10.1029/2003JD004423
- Kaufman, Y. J., Kleidman, R. G., & King, M. D. (1998), SCAR-B fires in the tropics: Properties and remote sensing from EOS-MODIS. *Journal of Geophysical Research*, 103, 31,95531,968.
- Lobert, J., and J. Warnatz (1993), Emissions from the combustion process in vegetation, in *Fire in the Environment: The Ecological, Atmospheric, and Climatic Importance of Vegetation Fires*, Environ. Sci. Res. Rep., vol. 13, edited by P. J. Crutzen and J. G. Goldammer, pp. 15–39, John Wiley, New York.
- Whelan, R. J. (1995), *The Ecology of Fire*, Cambridge Univ. Press, New York.
- Prins, E. M., & Menzel, W. P. (1992), Geostationary satellite detection of biomass burning in South America. *International Journal of Remote Sensing*, 13, 2783-2799.
- Prins, E.M., & Menzel, W. P. (1994), Trends in South American biomass burning detected with the GOES VAS from 1983-1991. *Journal of Geophysical Research*, 99 (D8), 16719-16735.
- Reid, J. S., E. M. Prins, D. L. Westphal, C. C. Schmidt, K. A. Richardson, S. A. Christopher, T. F. Eck, E. A. Reid, C. A. Curtis, and J. P. Hoffman (2004), Real-time monitoring of South American

smoke particle emissions and transport using a coupled remote sensing/box-model approach, *Geophys. Res. Lett.*, 31, L06107, doi:10.1029/2003GL018845.

Roberts, G., M. J. Wooster, and E. Lagoudakis (2009), Annual and diurnal African biomass burning temporal dynamics, *Biogeosciences*, 6, 849–866, doi:10.5194/bg-6-849-2009.

Roberts, G., M. J. Wooster, G. L. W. Perry, N. A. Drake, L.-M. Rebelo, and F. M. Dipotso (2005), Retrieval of biomass combustion rates and totals from fire radiative power observations: Application to southern Africa using geostationary SEVIRI imagery, *J. Geophys. Res.*, 110, D21111, doi:10.1029/2005JD006018.

Seiler, W., and P. J. Crutzen (1980), Estimates of gross and net fluxes of carbon between the biosphere and the atmosphere from biomass burning, *Clim. Change*, 2, 207–247, doi:10.1007/BF00137988.

Trollope, W. S. W., L. A. Trollope, A. L. F. Potgieter, and N. Zambatis (1996), SAFARI-92 characterization of biomass and fire behavior in the small experimental burns in Kruger National Park, *J. Geophys. Res.*, 101, 23,531–23,539, doi:10.1029/96JD00691.

van der Werf, G. R., J. T. Randerson, L. Giglio, G. J. Collatz, M. Mu, P. S. Kasibhatla, D. C. Morton, R. S. DeFries, Y. Jin, and T. T. van Leeuwen (2010), Global fire emissions and the contribution of deforestation, savanna, forest, agricultural, and peat fires (1997–2009), *Atmos. Chem. Phys. Discuss.*, 10, 16,153–16,230, doi:10.5194/acpd-10-16153-2010.

Wiedinmyer, C., B. Quayle, C. Geron, A. Belote, D. McKenzie, X. Zhang, S. O'Neill, and K. K. Wynne (2006), Estimating emissions from fires in North America for air quality modeling, *Atmos. Environ.*, 40, 3419–3432, doi:10.1016/j.atmosenv.2006.02.010.

Wooster, M. J. (2002), Small-scale experimental testing of fire radiative energy for quantifying mass combusted in natural vegetation fires, *Geophys. Res. Lett.*, 29(21), 2027, doi:10.1029/2002GL015487.

Wooster, M. J., B. Zhukov, and D. Oertel (2003), Fire radiative energy for quantitative study of biomass burning: Derivation from the BIRD experimental satellite and comparison to MODIS fire products, *Remote Sens. Environ.*, 86, 83–107.

Wooster, M. J., G. Roberts, G. L. W. Perry, and Y. J. Kaufman (2005), Retrieval of biomass combustion rates and totals from fire radiative power observations: FRP derivation and calibration relationships between biomass consumption and fire radiative energy release, *J. Geophys. Res.*, 110, D24311, doi:10.1029/2005JD006318.

Zhang, X., and S. Kondragunta (2008), Temporal and spatial variability in biomass burned areas across the USA derived from the GOES fire product, *Remote Sens. Environ.*, 112, 2886–2897, doi:10.1016/j.rse.2008.02.006.

Zhang, X., S. Kondragunta, and B. Quayle (2011), Estimation of biomass burned areas using multiple-satellite-observed active fires, IEEE Trans. Geosci. Remote Sens., 49, 4469–4482, doi:10.1109/TGRS.2011.2149535.

Zhang, X., S. Kondragunta, C. Schmidt, and F. Kogan (2008), Near real time monitoring of biomass burning particulate emissions (PM2.5) across contiguous United States using multiple satellite instruments, Atmos. Environ., 42, 6959–6972, doi:10.1016/j.atmosenv.2008.04.060.

Zhang, X., S. Kondragunta, J. Ram, C. Schmidt, and H.-C. Huang (2012), Near-real-time global biomass burning emissions product from geostationary satellite constellation, J. Geophys. Res., 117, D14201, doi:10.1029/2012JD017459.

### **3. Land Surface Albedo**

S. No.	Product Name	Spatial Resolution	Temporal Resolution
1	IMG_LSA	4 km x 4 km	Daily/ 15-day composite

### **3.1. Algorithm Configuration Information**

#### **3.1.1 Algorithm Name**

Land surface albedo

#### **3.1.2. Algorithm Identifier**

IMG\_LSA

#### **3.1.3. Algorithm Specification**

Version	Date	Prepared by	Description
1.0	22.02.2018	Mehul R Pandya	ATBD of broadband land surface albedo from the Imager data of INSAT-3D and INSAT-3DR

### **3.2. Introduction**

Land surface albedo, defined as the fraction of incident solar radiation (0.3–4.0 um) reflected by land surfaces (Dickinson, 1995; Liang, 2004) is one of the most important parameters in general circulation models, hydrology models, numerical weather models, and surface radiation-budget studies. Land surface albedo (LSA) is a key geophysical parameter controlling the energy budget in land-atmosphere interactions (Dickinson, 1983). LSA varies spatially and evolves seasonally based on solar illumination conditions, rainfall, soil moisture, vegetation growth, snow accumulation/melting and anthropogenic activities. Satellite remote sensing can provide a vantage point for estimating land surface albedo at various spectral, spatial, temporal, and angular resolutions. During the last few decades, many satellite-generated albedo products have been derived with varying spatial resolution of 500 m to 20 km. Many researchers across the globe have developed algorithms for various sensors to derive albedo directly from satellite observations. The AVHRR algorithm provides global coverage of albedo products (Strugnell & Lucht, 2001). POLDER and MISR allow researchers to use multi-angular information to obtain a better understanding of surface reflectance anisotropy (Diner et al., 1999; Leroy et al., 1997). The Moderate Resolution Imaging Spectroradiometer (MODIS) albedo product (Schaaf et al., 2002) utilizes multiple spectral bands to derive accurate broadband albedo estimations at both high spatial and high temporal resolutions. Clouds and the Earth's Radiant Energy System (CERES) uses broad shortwave band to derive the planetary albedo (Rutan et al., 2006). With the development and availability of geostationary satellite sensors, many researchers have focused on deriving the diurnal changes of surface albedo based on a much wider range of solar illumination angles, such as the Meteosat/SEVIRI albedo product (Geiger et al., 2008; Pinty et al., 2000).

### **3.3. Theoretical background**

The conventional methods for estimating broadband albedos rely on a series of steps in the processing chain, including atmospheric correction, surface angular modelling, and narrowband-to-broadband albedo conversions. Unfortunately, errors associated with each procedure may be accumulated and significantly impact the accuracy of the final albedo products (Liang, 2003). Uncertainties associated with each procedure may be accumulate and may have bearing on final output.

An alternative scheme developed in the earlier studies (Liang et al., 1999, 2003) linked TOA (top-of-atmosphere) narrowband albedos with three land surface broadband albedos using a feedforward neural network without performing any atmospheric corrections. This idea stems from earlier study (Pinker et al., 1985) that linearly related TOA and surface broadband albedos. Surface broadband albedo depends on surface spectral reflectance as well as atmospheric conditions. TOA observations contain information on both surface reflectance and atmospheric optical properties, which implies that it is possible for us to compute the broadband albedos using TOA narrowband albedos without performing any atmospheric corrections.

Liang et al. (1999) used the MODTRAN model to simulate TOA reflectances under the Lambertian assumption, and they obtained a relationship between MODIS TOA reflectances and broadband albedos by using a neural network method. Liang et al. (2003) used the projection pursuit regression method. However, these two studies did not consider the anisotropy of the land surface. Liang et al. (2005) further improved it for estimating daily land surface albedo of the Greenland ice sheet from MODIS data. They used the discrete ordinates radiative transfer program for a multilayered plane parallel medium to simulate TOA reflectances of snow/ice and then developed the relationship between bidirectional TOA reflectances and broadband albedos using an empirical training method; they divided the solar/view geometry space into angular bins and calculated the regression coefficients of each angular bin using a linear regression method. Qu et al. (2015) have provided detailed review of algorithms for albedo.

Here, we propose to develop a direct-estimation algorithm by employing an atmospheric radiative transfer code to simulate the TOA directional reflectances in the two spectral bands of INSAT-3D Imager located in visible (0.55-0.75 um) and shortwave infrared- SWIR (1.55-1.70 um) wavelengths and also calculate the broadband reflectance in the shortwave band (0.4-2.5 um), and then establishing a relationship between the TOA reflectances and the broadband reflectance using the regression method, which would yield narrow to broadband conversion coefficients.

An approach for estimating land surface broadband albedo from multispectral remote sensing observations is a hybrid approach that combines extensive radiative transfer simulations (physical) with regression methods (statistical). It directly links the TOA radiance or reflectance to surface broadband albedo without performing different processes as per the first approach. Here narrowband-to-broadband spectral conversion by considering the spectral response function of

the sensor in various spectral bands of the instrument is the main step required to derive the albedo. Figure 1 shows the spectral signatures of major surfaces with the relative spectral response (RSR) of INSAT-3D Imager instrument. A weighting factors (Narrow to broad band conversion coefficients) are to be determined with the radiative transfer simulations. This approach has been successfully used to estimate broadband albedo from MODIS data (Liang et al., 2003).

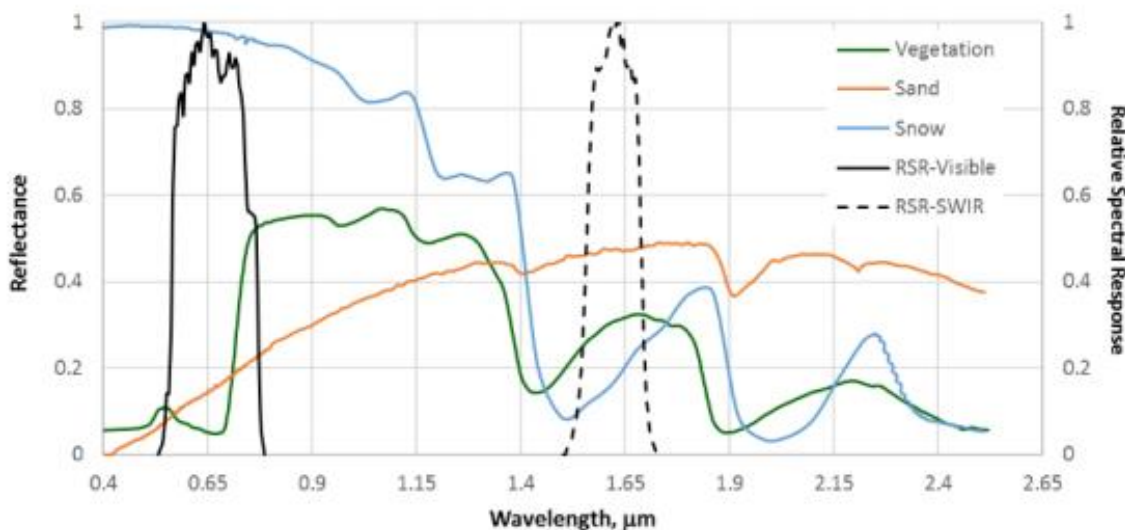


*Figure 1. A typical spectral distribution of the reflectances for vegetation, soil, snow over shortwave solar spectrum range shown with the RSR of two spectral bands: visible (solid line) and SWIR (dashed line) of INSAT-3D Imager instrument.*

### 3.4. Methodology

In the present study, the bidirectional reflectance distribution function (BRDF) is not taken into consideration and the surface is assumed to reflect isotropically (i.e. equally at all angles), so this albedo is referred to as the "diffuse albedo" or the "hemispherical albedo". When the land surface is assumed as lambertian (the reflectance is isotropic from different solar/view angles), the value of Bidirectional Reflectance Factor (BRF) is then equal to the albedo and the surface broadband albedo can be estimated from linear combinations of narrowband albedo (spectral directional reflectance) with different weight coefficients. This method was first proposed by Brest and Goward (1987) and was then applied to different sensors: AVHRR (Saunders, 1990; Russell et al, 1997), Landsat TM (Duguay & Ledrew, 1992; Knap et al, 1999), Meteosat (Valiente et al., 1995) and Visible Infrared Imaging Radiometer Suite (VIIRS) (Liang, 2003). Liang (2001) reviewed the above studies and provided simple conversion coefficients for estimating broadband surface

albedo from a variety of sensors under different atmospheric and surface conditions. The validation results show that the conversion formulae are very accurate with an average residual standard error around 0.02 (Liang et al., 2003).

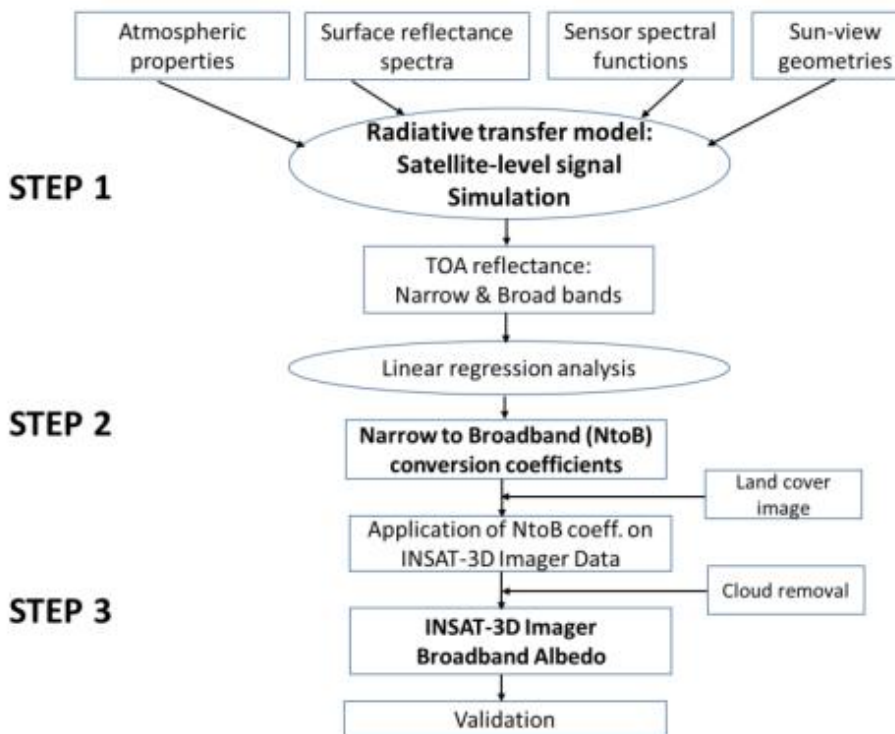


*Figure 2. Algorithm flowchart for direct-retrieval of the broadband albedo from the INSAT-3D Imager data by generating narrow to broadband conversion coefficients*

For the retrieval of broadband albedo in the present study, the basic procedure consists of three major steps as illustrated in figure 2. The first step is to conduct extensive radiative transfer simulations using the 6SV code, the second step is to obtain the narrow to broad band conversion coefficients by linking the simulated TOA reflectance with surface broadband reflectance using linear regression analysis and third step is to apply the narrow to broadband conversion coefficients on the INSAT-3D Imager data to obtain the broadband albedo. Various surface reflectance spectra of different cover types with different atmospheric conditions have been incorporated into the radiative transfer simulations. In this study, attempt has been made to estimate land surface broadband albedos using TOA directional reflectance, instead of TOA spectral albedos. This improvement has in fact greatly simplified this method, since calculating TOA spectral albedo requires TOA angular modelling that might introduce large errors.

### 3.4.1. Radiative transfer simulations

For a given atmospheric and surface condition, we need to compute the directional reflectance at the top of the atmosphere. Assuming the surface is Lambertian, the upwelling

radiance at the TOA can be computed by radiative transfer simulations through 6SV (Second Simulation of a Satellite Signal in the Solar Spectrum – Vector version) code (Vermote et al., 1997). It is critical to use the representative surface reflectance spectra in data simulations. Different surface reflectance spectra covering the spectral range 0.4–2.5 um representing vegetation, sand, water, snow surfaces were interpolated in the study. The simulation outputs include total shortwave albedo and spectral albedos that are calculated by incorporating the sensor spectral response functions.

In the 6SV simulations, varying aerosol optical thickness values corresponding to lower to higher aerosol loadings, continental aerosol model, and tropical atmospheric profile that also represent different water vapor and other gaseous amounts and profiles. The aerosol model used are the defaults in 6SV and atmospheric profiles over Indian region were used in the simulations. For the operational application of this method, more should perhaps be included to represent the variable atmospheric conditions. The upwelling TOA radiance ( $L_\lambda$ ) is further normalized to apparent spectral reflectance ( $\rho_{\text{a}\wedge}$ ) using the expression,

$$\rho_{\text{a}\wedge} = \frac{\pi L_\lambda(\theta_s, \theta_v, \lambda) d^2}{E_0 \cos \theta_s} \quad (1)$$

Where,  $d$  is the Sun-Earth distance in Astronomical Units,  $E_0$  is exo-atmospheric solar irradiance and  $\theta_s$  is the sun zenith angle. Land surface broadband albedo is defined as the ratio of the surface upwelling flux ( $F_u$ ) to the downward flux ( $F_d$ ) (Liang, 2003),

$$\alpha_\wedge(\theta_i; \wedge) = \frac{F_u(\theta_i; \wedge)}{F_d(\theta_i; \wedge)} = \frac{\int_\wedge F_u(\theta_i; \wedge) d\lambda}{\int_\wedge F_d(\theta_i; \wedge) d\lambda} \quad (2)$$

$$\alpha_\wedge(\theta_i; \wedge) = \frac{\int_\wedge F_d(\theta_i; \wedge) \rho(\lambda) d\lambda}{\int_\wedge F_d(\theta_i; \wedge) d\lambda} \quad (3)$$

where  $\wedge$  is denoted to the waveband from wavelength  $\lambda 1$  to wavelength  $\lambda 2$ .  $\wedge \in (\lambda 1, \lambda 2)$ . If  $\wedge \in (0.25, 4\text{um})$  albedo is the total shortwave broadband albedo. The wave range  $\wedge \in (0.4, 0.7\text{um})$  and  $\wedge \in (0.7, 4\text{um})$  correspond to visible and near-infrared (near-IR) albedos, respectively.  $\rho(\lambda)$  is the surface spectral reflectance spectra. One of the major limitations in this simulation study is its assumption of Lambertian surfaces. The major reason is that we do not have a good understanding of the directional reflectance properties of various surface types at the INSAT-3D Imager resolution.

### 3.4.2. Generation of narrow to broadband albedo conversion coefficients

Once the database is created from the simulations described above, the next step is to link TOA reflectance to land surface broadband albedos. This exercise is to be carried out for each of the major land cover types. We used regression analysis to establish the linear relationship (equation 4) between TOA reflectance in two bands of INSAT-3D Imager and LSA and to obtain the arrow to broadband (NtoB) conversion coefficients C0, C1, and C2.

$$\alpha = C_0 + C_1 * \rho_{3D-VIS} + C_2 * \rho_{3D-SWIR} \quad (4)$$

Where  $\alpha$  is the broadband LSA, while  $\rho_{3D-VIS}$  and  $\rho_{3D-SWIR}$  are the TOA reflectances in visible and SWIR bands of INSAT-3D Imager sensor respectively. A set of NtoB coefficients are computed for four major land covers namely, soil, vegetation, water and snow. The physical meaning of the conversion factors C1 and C2 is obvious from equation (4). They quantify the ratio of the reflected radiances within the narrow bands to the reflected radiances for the visible and SWIR broad bands, or the degree of the representativeness of the narrowband reflectance for the broadband reflectance. The conversion coefficients developed from extensive radiative transfer simulations are then would be applied to the INSAT-3D Imager TOA reflectance data.

### 3.4.3. Calibration of the TOA observations of INSAT-3D Imager sensor

It has been observed that the satellite-level signal in two spectral bands of the INSAT-3D Imager instrument significantly underestimate the top-of-atmosphere (TOA) radiance values. This factor severely modulates the LSA computations. An exercise was carried out to compensate this factor of underestimation from a systematic comparison between TOA radiances of INSAT-3D Imager and INSAT-3A CCD and MODIS sensors. After introducing the radiance calibration coefficients equation (4) can be rewritten as,

$$\alpha = C_0 + \beta_1 * C_1 * \rho_{3D-VIS} + \beta_2 * C_2 * \rho_{3D-SWIR} \quad (5)$$

Where  $\beta_1$  and  $\beta_2$  are radiance calibration coefficients of INSAT-3D Imager instrument.

Assuming the multiplication of two coefficients  $\beta_1$  and C1 as new coefficient  $\alpha_1$ ,  $\beta_2$  and C2 as  $\alpha_2$  and C0 as  $\alpha_0$ , equation (5) can be rewritten as,

$$\alpha = \alpha_0 + \alpha_1 * \rho_{3D-VIS} + \alpha_2 * \rho_{3D-SWIR} \quad (6)$$

### 3.4.4. Data used and generation of LSA

Raw digital number data of visible and SWIR bands of INSAT-3D Imager sensor corresponding to 10:30 hrs of 1st of each month of year 2015 was downloaded from the MOSDAC server. The digital number data were converted to the TOA radiances, which was subsequently converted to

the TOA reflectances using equation (1). A cloud mask was devised from two sources, (a) thresholds of INSAT-3D Imager data and (b) MODIS cloud mask. A cloud-free TOA reflectance data was then converted to the LSA using the N to B coefficients generated from the simulation exercise as discussed in previous section. A land over product available from the MODIS sensor was used as a reference for applying land cover-based N to B coefficients.

### 3.5. Results

Monthly broadband LSA maps were derived from the INSAT-3D Imager data representing 1<sup>st</sup> day of each month of the year 2015 using the method discussed in the above section. The broadband LSA was derived at a spatial resolution of 4 km over India and surrounding region. The broadband LSA maps for different months are shown in the figure 3. Visually the spatial patterns and magnitudes of broadband albedo look very reasonable. Majority of the broadband albedo values are in the range of 0.1 to 0.3 representing vegetation and soil pixels. However, desert regions show LSA value greater than 0.3 and ranged between 0.3 to 0.5. While snow covered regions show LSA value greater than 0.4 or 0.5. An error due to clouds still persists even though the cloud mask was applied on the images. Fringe of clouds are seen with very high albedo values, which causes an erroneous albedo value. A better mechanism for removing clouds has to be developed in future.

The assumption of a Lambertian surface is being debated (Liang et al., 2003). The key argument is that the broadband albedo depends on both spectral and angular properties of the land surface. From the validation analysis of the study by Liang et al. (2003), it appeared that an assumption of spectral information dominance over the angular information does not lead to significant errors, which is an important achievement of this study. Overall it can be said that broadband LSA could be successfully computed over India from the INSAT-3D Imager observations.

This is a preliminary study carried out for computing the broadband land surface albedo from the INSAT-3D Imager sensor, however detailed study is underway to establish the proposed method with more simulations involving additional land cover types. There is also a requirement to enhance the cloud removal technique, which will minimize the noise observed in the albedo retrieval. Moreover, issue related to the calibration of INSAT -3D Imager radiance has to be rectified for robust retrieval of the broadband albedo.

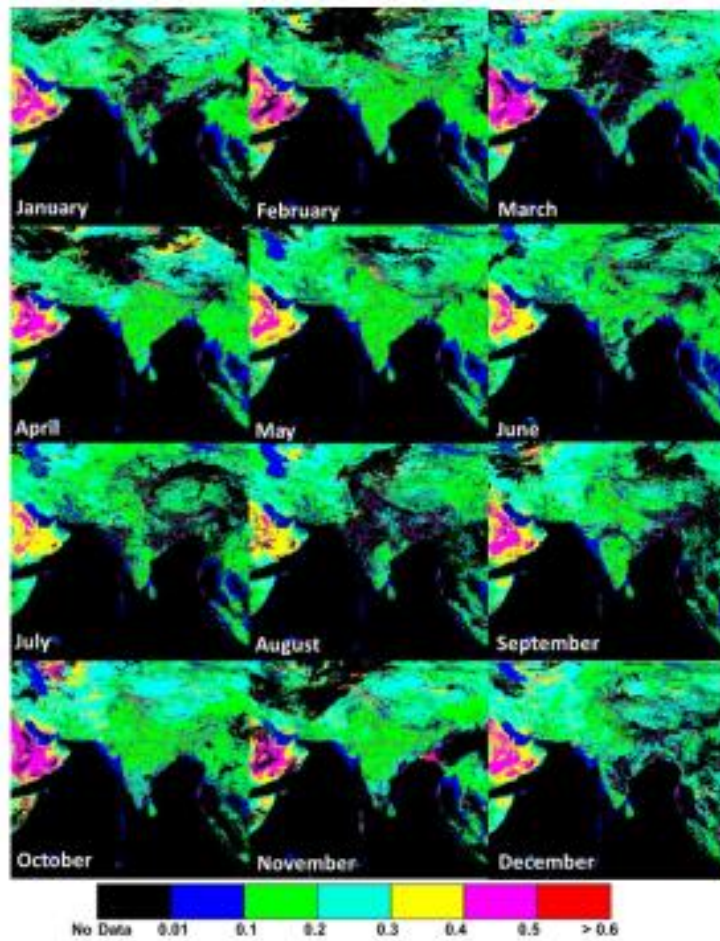


*Figure 3. Broadband albedo derived from INSAT-3D Imager data from the proposed method.*

### 3.6. Summary and Future scope

In this document, we have presented the algorithm theoretical basis (Version 1.0) for the broadband land surface albedo from INSAT-3D Imager dataset. The technique involves development of a direct-estimation of broadband land surface albedo from the observations of the INSAT-3D Imager sensor, which is available from the geostationary platform. Extensive theoretical modelling study was carried out, where an atmospheric radiative transfer model was used to simulate the TOA signals in two broad bands of Imager sensor for diverse land atmospheric scenario. After the simulation exercise was over, a relationship between TOA reflectances and land-surface broadband albedos was developed from the simulation results, which provided a set of conversion coefficients. A separate set of narrow to broadband conversion coefficients for each of the major land covers was generated for INSAT-3D Imager data. Using the proposed method broadband land surface albedo maps were generated over India from the TOA observations of INSAT-3D Imager sensor. Validation of the retrieved albedo will be carried out by comparing it with MODIS albedo products and in-situ albedo measurements. The

preliminary study has provided encouraging results; however, a detailed analysis is underway involving more theoretical simulations and removing the errors due to erroneous cloud mask. Moreover, serious issues related to (1) the calibration of INSAT-3D Imager radiance and (2) cloud cover have to be resolved for robust retrieval of the broadband albedo on routine basis.

## References

- Brest C. and Goward S. (1987), Deriving surface albedo measurements from narrow band satellite data. *Int. J. Remote Sens.* 8, 351–367.
- Dickinson R. E. (1983). Land surface processes and climate surface albedos and energy balance. *Advances in Geophysics*, 25, 305–353.
- Dickinson R. E. (1995), Land processes in climate models, *Rem. Sens. of Env.*, 51, 27–38.
- Diner D. J., Martonchik J. V., Borel C., Gerstl S. A. W., Gordon H. R., Myneni R. B., et al. (1999). Level 2 surface retrieval algorithm theoretical basis document. NASA/JPL, JPL D-11401, Rev. D.
- Duguay C. R., Ledrew E. F. (1992), Estimating surface reflectance and albedo from Landsat-5 thematic mapper over rugged terrain. *Photogramm. Eng. Rem. Sens.*, 58, 551–558.
- Geiger B., Carrer D., Franchisteguy L., Roujean J. L., and Meurey C. (2008). Land surface albedo derived on a daily basis from Meteosat Second Generation observations. *IEEE Transactions on Geoscience and Remote Sensing*, 46, 3841–3856.
- Hartmann D. L., Bretherton C. S., Charlock T. P., Chou M. D., Genio A. Del, Dickinson R. E., Fu R., Houze R. A., King M. D., Lau K. M., Leovy C. B., Sorooshian S., Washburne J., Wielicki B., and Willson R. C. (1999), Radiation, clouds, water vapor, precipitation, and atmospheric circulation,in EOS Science Plan. Greenbelt, MD: NASA, 1999, pp. 39–114.
- Knap W. H., Brock B. W., Oerlemans J., Willis I. C. (1999), Comparison of Landsat TM-derived and ground-based albedos of Haut Glacier D’arolla, Switzerland. *Int. J. Remote Sens.*, 20, 3293–3310.
- Leroy M., Deuze J. L., Breon F. M., Hautecoeur O., Herman M., Buriez J. C., et al. (1997). Retrieval of atmospheric properties and surface bidirectional reflectances over land from POLDER/ADEOS. *Journal of Geophysical Research-Atmospheres*, 102, 17023–17037.
- Liang S. (2001), Narrowband to broadband conversions of land surface albedo I: Algorithms. *Remote Sens. Environ.*, 76, 213–238.
- Liang S. (2003), A direct algorithm for estimating land surface broadband albedos from MODIS imagery. *IEEE Transactions on Geoscience and Remote Sensing*, 41, 136 -145.
- Liang S., Fang H., Kaul M., Tom G. Van Niel, McVicar T. R., Pearlman J. S., Walthall C. L., Daughtry C. S. T., and Huemmrich K. F. (2003). Estimation and Validation of Land

- Surface Broadband Albedos and Leaf Area Index From EO-1 ALI Data. *IEEE Transactions on Geoscience and Remote Sensing*, 41, 1260–1267.
- Liang S. (2004), Quantitative Remote Sensing of Land Surfaces. New York, USA: Wiley, 2004.
- Liang S. (2014), Direct-estimation algorithm for mapping daily land-surface broadband albedo from MODIS data. *IEEE Transactions on Geoscience and Remote Sensing*, 52, 907–919.
- Liang S., Shuey C., Russ A., Fang H., Chen M., Walthall C., Daughtry C., Hunt R. (2003), Narrowband to broadband conversions of land surface albedo: II. Validation. *Remote Sens. Environ.*, 84, 25–41.
- Liang S., Strahler A., and Walthall C. (1999), Retrieval of land surface albedo from satellite observations: A simulation study. *J. Applied Meteorology*, 38, 712–725.
- Liang S., Stroeve J. and Box J. E. (2005), Mapping daily snow/ice shortwave broadband albedo from Moderate Resolution Imaging Spectroradiometer (MODIS): The improved direct retrieval algorithm and validation with Greenland in situ measurement, *J. Geophys. Res.*, 110, D10109.
- Pinker R. T. (1985), Determination of surface albedo from satellite, *Adv. Space Res.*, 5, 333–343.
- Pinty B., Roveda F., Verstraete M. M., Gobron N., Govaerts Y., Martonchik J. V. et al. (2000). Surface albedo retrieval from Meteosat — 1. Theory. *Journal of Geophysical ResearchAtmospheres*, 105, 18099–18112.
- Russell M. J., Nunez M., Chladil M. A., Valiente J. A., LopezBaeza E. (1997), Conversion of nadir, narrowband reflectance in red and near-infrared channels to hemispherical surface albedo. *Remote Sens. Environ.*, 61, 16–23.
- Rutan D., Charlock T., Rose F., Kato S., Zentz, S. and Coleman L., Global surface albedo from CERES/TERRA surface and atmospheric radiation budget (SARB) data product, in Proc. 12th Conf. Atmospheric Radiation., 2006, pp. 10–44.
- Saunders R. W. (1990), The determination of broad band surface albedo from AVHRR visible and near-infrared radiances. *Int. J. Remote Sens.*, 11, 49–67.
- Schaaf C. B., Gao F., Strahle, A. H., Lucht W., Li X. W., Tsang T., et al. (2002). First operational BRDF, albedo nadir reflectance products from MODIS. *Remote Sensing of Environment*, 83, 135–148.
- Strugnell N. C., & Lucht W. (2001). An algorithm to infer continental-scale albedo from AVHRR data, land cover class, and field observations of typical BRDFs. *Journal of Climate*, 4, 1360–1376.
- Qu Y., Liang S., Liu Q., He T., Liu S. and Li X. (2015), Mapping Surface Broadband Albedo from Satellite Observations: A Review of Literatures on Algorithms and Products. *Remote Sensing*, 7, 990–1020.
- Valiente J. A., Nunez M., Lopezbaeza E., Moreno J.F. (1995), Narrow-band to broad-band conversion for Meteosat-visible channel and broad-band albedo using both AVHRR-1 and-2 channels. *Int. J. Remote Sens.*, 16, 1147–1166.

#### **4. Actual Evapotranspiration (*AET*) from INSAT 3D series**

S. No.	Product Name	Spatial Resolution	Temporal Resolution
1	IMG_AET	4 km x 4 km	Daily

## **4.1. Algorithm Configuration Information**

### **4.1.1. Algorithm name**

Actual Evapotranspiration (AET) from INSAT 3D series (EVAPOTRANSPIRATION)

### **4.1.2. Algorithm identifier**

ISRO\_INSAT\_DLY\_ET

### **4.1.3 Algorithm specification**

Version	Date	Prepared by	Description
1.0	19 September 2018	Bimal K. Bhattacharya	Evapotranspiration baseline document

## **4.2. Introduction**

Evapotranspiration (ET) is one of the key variables in hydrological cycle, agricultural drought and crop yield deviation. It is a term used to describe the combined loss of water due to the evaporation largely from soil surface and transpiration from plants. ET is a central process in the climate system and a nexus of water, energy & carbon cycle (Jung et.al. 2010). Land evapotranspiration (ET) is an essential component in global water, energy and carbon cycles, and provides a link between the atmosphere and the Earth's surface (Betts et al., 1996; Jiménez et al., 2011; Tang et al., 2014; Zhang et al., 2012, 2015). It is also an important indicator of hydrologic and heat variations under a changing climate and anthropogenic interference (Brutsaert and Parlange, 1998; Ohmura and Wild, 2002; Wang and Dickinson, 2012). Accurate quantification of ET is thus critical for understanding the hydro-climatologic processes and the interactions of the Earth system (Rodell and Famiglietti, 2002). However, the estimation of large-scale ET from ground-based measurements alone remains challenging due to the sparse network of point observations and the high spatial heterogeneity and temporal variability of ET (Xu and Singh, 2005; Xue et al., 2013). To address this limitation, a number of global ET products have been derived in recent years, including remote sensing-based products (Su, 2002; Muet al., 2007, 2011; Zhang et al., 2009, 2010; Miralles et al., 2011b; Yang et al., 2013). There are many methods mentioned in the literature such as SEBAL (Bastiaanssen 2013), TSEB (Norman & Becker, 1995) and SEBS (Su, 2002). Most of the model uses the operationally available polar/ near-polar orbit satellite datasets such as MODIS, ASTER, LANDSAT have long been utilized for the estimation of ET from field to regional scale. However, the output records suffer from spatial and temporal gaps due to cloud cover and in-frequent image availability based on satellite overpass schedule. However, geostationary satellites, have high temporal resolution continuously measuring several factors related to land surface and the atmosphere over large regional scales. Thus, they have high potential in calculating land surface and water cycle at hourly temporal resolution. This shows the vital role of geostationary satellite in modelling Evapotranspiration on spatial scale. Operational ET

products are available over US and Europe using thermal remote sensing data from geostationary meteorological satellite data such as GOES (Anderson et al, 2007) and MSG-SEVIRI (Hu et al, 2015).

#### 4.2.1. Overview and background

Most of the methods used for modelling evapotranspiration uses energy surface balance framework using thermal infrared remote sensing. This describes the heat and water transfer from land surface to overlying atmosphere within surface layer of Atmospheric Boundary Layer (ABL) :

$$R_n - G = H + \lambda E \quad (1)$$

Where,  $R_n$  is the net surface radiation,  $G$  is the soil heat flux,  $H$  is the sensible heat flux and  $\lambda E$  is the latent heat flux. Remote sensing technique can provide spatial and temporal information of Normalized Difference Vegetation Index (NDVI), Leaf Area Index (LAI), surface albedo, surface emissivity, and radiometric surface temperature, most of which are indispensable to the models and methods that partition the available energy (Li et. al. 2009 , Mauser et.al. 1998). A large number of efforts have been made to incorporate remotely sensed surface temperature in combination with other critical variables, e.g., NDVI and albedo into ET modeling during the past three decades (kala et.al. 2008). It was Penman (Penman 1948) who laid the foundation for relating evapotranspiration to meteorological variables (Allen et.al. 1998). Model simulations or empirical equations requiring meteorological data are the traditional way of estimating evapotranspiration such as gradient method, Bowen ratio method, eddy covariance method, lysimeter method. Malamos et.al. (2015) used PM method to estimate ET on the field scale level while Uddin et.al. (2013) used the Bowen ratio method & EC method to estimate latent heat fluxes. However, because of some practical reasons like diversity in land covers or temporal changes in the landscape, these methods may not represent the evapotranspiration at regional-scale effectively (Zhang et.al. 1995) The most frequently used method for estimating evapotranspiration at present is the Penman-Monteith equation. The energy balance concept and net radiation are used as the principal parameters in most of the remote sensing methods for estimating evapotranspiration (Li et.al. 2002). Till date, several energy balance algorithms are available for calculating ET through remote sensing. such as SEBAL (Bastiaanssen et.al.1998) and SEBS (Su,2002). They are single source model which consider soil and plant as single source. In addition to these, there are dual-source or two-source (soil and vegetation canopy) models, e.g. TSEB (Norman & Becker 1995), SEBI (Menenti & Choudhury 1993) and ALEXI (Anderson, Norman, Diak, kustas & Mecikalski, 1997). Therefore, considering the characteristics and significance of the various ET methods developed over the past decades, precise estimation of ET over regional scale based on the remote sensing technology has become a critical question in ET related studies.

#### **4.2.2. Objectives**

The objectives of this document are:

- (i) To outline the algorithm for the estimation of day-time and daily Evapotranspiration (ET) over land in all-sky conditions
- (ii) To implement the algorithm in IMDPS GPR (Geophysical Parameter Retrieval) chain for automation of ET product generation
- (iii) To describe validation strategy against available *in-situ* measurements and other available satellite-based and reanalysis products.

#### **4.2.3. Instrument and characteristics of input products**

##### **4.2.3.1. Indian geostationary satellite INSAT 3DR**

The Indian National Satellite (INSAT) system is a joint venture of the Department of Space (DOS), Department of Telecommunications (DOT), and India Meteorological Department (IMD). INSAT-3DR carries a multi-spectral Imager (optical radiometer) capable of generating the images of the earth in six wavelength bands significant for meteorological observations, namely, visible (0.55-0.75  $\mu\text{m}$ ), shortwave infrared (1.55-1.68  $\mu\text{m}$ ), middle infrared (3.8-4.1  $\mu\text{m}$ ), water vapor (6.5-7.1  $\mu\text{m}$ ) and two bands in thermal infrared (10.3-11.3  $\mu\text{m}$  & 11.5-12.5  $\mu\text{m}$ ) regions. It also has 19 channel sounder, which is the first such payload to be flown on an ISRO satellite mission. The spatial resolution is 1 km x 1 km for VIS/SWIR band and 4 km x 4 km for thermal IR and 8 km X 8 km bands. The introduction of INSAT Meteorological Data Processing System (IMDPS) (2014) provides both ‘full-globe’ and ‘sector’ data products in all the six bands of imager at half-an-hour interval at 4 km spatial resolution in an automated mode. So, there are maximum 48 acquisitions on a given day. Raw data after reception at each acquisition were corrected for servo, line loss, radiometry, stagger and oversampling removal using the INSAT 3D/3DR data products scheduler. This results into automated generation of co-registered data in each band at Transverse Mercator (TM) projection. The dimension of each band at each acquisition is 1617 rows x 1615 columns for Asia Mercator sector product.

##### **4.2.3.2. Required inputs**

Operational all-sky hourly Net radiation product, sliding monthly noon-time composite of land surface albedo, instantaneous LST from INSAT 3DR

The proposed algorithm for ET will use the INSAT Net radiation hourly product in the MMDRPS operational chain. The net radiation will be computed from daily insolation product at 4 km from INSAT 3D/3DR, proposed operational albedo product from INSAT 3D/3DR, hourly forecast air temperature and relative humidity from WRF model, land surface temperature (LST) from INSAT 3D/3DR, using the surface emissivity obtained from 10 year historical MODIS database or real-time composite NDVI at 1-4 km from other sources (<https://www.eumetsat.int/website/home/Satellites/CurrentSatellites/Meteosat>) for SEVIRI NDVI product for Indian ocean coverage,

National Data Centre, NRSC, Hyderabad for OCM-2 & AWIFS NDVI). The net radiation needs to be made operationally available under clear and cloudy sky conditions to generate latent heat flux and Evapotranspiration (ET).

#### **4.2.3.3. Hourly short-range forecast from WRF**

Weather Research and Forecasting (WRF; [Skamarock et al., 2008](#)) Model version 3.1 is used for All India Short range weather forecast. WRF is a limited area, non-hydrostatic, primitive equation model with multiple options for various physical parameterization schemes. The WRF Model is integrated in a triple domain configuration with a horizontal resolution of 45 km, 15 km and 5 km for the All India, with grid points 260×235, 352×373 and 676×721 in x and y directions for the domains 1, 2 and 3, respectively. The model has 36 vertical levels with the top of the model atmosphere located at 10 hPa. The WRF 3D-Var is used for the assimilation of all available conventional including ISRO-AWS data and satellite observations to improve the model initial conditions. The operational WRF short-range forecasts ([Kumar et al., 2011](#)), available at MOSDAC site used climatological land surface and atmospheric parameters from global database and assimilated all available conventional including ISRO-AWS. The operational forecast is available at finer spatial resolution (~ 5km) at hourly intervals up to 72 hours. Similarly, IMD is also running a WRF model in a double domain configuration with a horizontal resolution of 9 km and 3 km for the RSMC Domain and All India domain respectively. The model has 46 vertical levels with the top of the model atmosphere located at 50 hPa. In this algorithm only temperature and relative humidity at 2-meter height from surface will be used for estimation of ET. For testing the prototype algorithm, SAC WRF forecasts at 5km resolution will be used. However, for operational implementation in MMDRPS, IMD WRF forecasts will be used.

### **4.3. Inputs**

#### **4.3.1. Static data**

Soil textural map and soil moisture constants (Field capacity, Permanent Wilting point, Air-dry water content) are required to be used.

#### **4.3.2. Image and pre-processing data (Dynamic)**

*Table 1*

Parameter	Resolution	Accuracy	Source
Instantaneous Proposed Net Radiation ( $R_n$ ) of Asia Mercator sector	Pixel (4 km x 4 km)	90%	MOSDAC/ MMDRPS
Instantaneous cloud mask	Pixel (4 km x 4 km)	95%	MOSDAC/ MMDRPS

Instantaneous land surface temperature (LST) product of Asia Mercator sector	Pixel (4 km x 4 km)	98-99%	MOSDAC/ MMDRPS
Proposed noon-time sliding monthly composite of land surface albedo of Asia Mercator sector	Pixel (4 km x 4 km)	98-99%	MOSDAC/ MMDRPS

#### 4.3.3. Other auxiliary data and model inputs

Daily land emissivity will be generated from ten-year historical data of MODIS as mentioned in table 2. Real-time availability of monthly sliding composite of NDVI data from other concurrent sources resampled at 4km. Hourly forecast of air temperature at 2m height and relative humidity using high –resolution NWP model (e.g. WRF) as mentioned in Table 3.

*Table 2. Required ancillary data*

Parameters	Source
Daily emissivity from 10-year historical data from MODIS (2008-2018)	<a href="http://modis-atmod.gsfc.nasa.gov">http://modis-atmod.gsfc.nasa.gov</a>
MSG SEVIRI , OCM -2, MODIS NDVI, AWIFS NDVI	<a href="https://www.eumetsat.int/website/home/Satellites/CurrentSatellites/Meteosat">https://www.eumetsat.int/website/home/Satellites/CurrentSatellites/Meteosat</a> , <a href="https://www.eumetsat.int/website/home/Data/Products/Land/index.html">https://www.eumetsat.int/website/home/Data/Products/Land/index.html</a> NDC, NRSC, Hyderabad for OCM-2 & AWIFS NDVI
Soil texture & soil porosity over different LULC	NBSS &LUP, Nagpur digital soil map at 1:250000 scale (to be procured)
Operational hourly forecast output from WRF at $\sim 0.03^\circ / 0.05^\circ$ spatial resolution for the following parameters in ASCII format (latitude, longitude, parameter) 1. Air temperature (K) at 2 m height 2. Humidity (%) at 2m height  The short-range forecasts will be updated every-day at 2pm.	IMD for operationalization / MOSDAC for experimental testing

## 4.4. Algorithm functional specifications

### 4.4.1. Clear sky Latent heat flux ( $\lambda E_{clr}$ )

The Latent heat flux is computed using the equation (2) given by PM equation ([Monteith, 1965](#))

$$\lambda E_{clr} = \frac{s\phi + \rho C_p g_B D_A}{s + \gamma(1 + \frac{g_B}{g_s})} \dots\dots (2)$$

Here,  $\phi$  is net available energy ( $R_n - G$ ),  $\lambda E_{clr}$  is clear sky latent heat flux or evapotranspiration ( $\text{Wm}^{-2}$ ),  $s$  is slope of SVP vs. temperature curve,  $\rho$  is air density ( $\text{kg m}^{-3}$ ),  $\gamma$  is psychometric constant( $\text{hPa K}^{-1}$ ),  $C_p$  is specific heat of air ( $\text{MJ kg}^{-1} \text{K}^{-1}$ ),  $D_A$  is vapor pressure deficit,  $g_B$  is boundary layer conductance ( $\text{ms}^{-1}$ ),  $g_s$  is stomatal (or surface) conductance( $\text{ms}^{-1}$ )

The method used here to compute latent heat flux combines satellite  $T_s$  data (LST) obtained from INSAT 3DR with standard energy balance closure models in order to derive a hybrid closure that does not require the specification of surface to atmosphere conductance terms ([Mallick et.al. 2014](#)). This method is referred to as the Surface Temperature Initiated Closure (STIC). This method can be used by simultaneously solving four state equations as mentioned by ([Mallick et.al. 2014](#)) to estimate latent heat flux. The four internal state equations needs to be solved in iterative manner to compute LE are given below:

$$\Lambda = \frac{2\alpha s}{2s + \gamma(2 + \frac{g_B}{g_s})} \quad (3)$$

$$\Delta T = \frac{e_S - e_A}{\gamma} \left( \frac{1 - \Lambda}{\Lambda} \right) \quad (4)$$

$$g_s = g_B \frac{e_S^* - e_A}{e_S - e_A} \quad (5)$$

$$g_B = \frac{\phi}{\gamma C_p (\Delta T + \frac{e_S - e_A}{\gamma})} \quad (6)$$

Here  $\Lambda$  is the evaporative fraction,  $\Delta T$  is expressed as  $T_s - T_a$  where  $T_a$  ( $^{\circ}\text{C}$ ) is the air temperature and  $T_s$  is land surface temperature ( $^{\circ}\text{C}$ ).  $e_S$  is effective vapour pressure (hPa),  $e_A$  is atmospheric vapour pressure (hPa) at  $T_a$  height of measurement and  $e_S^*$  is saturation vapour pressure at  $T_s$ . The block diagram to compute LE from iterative solution is shown below. In the flow chart (Figure 1),  $T_{SD}$  is the surface dew point temperature ( $^{\circ}\text{C}$ ),  $M$  is moisture availability at surface (0-1)  $T_D$  is dew point temperature ( $^{\circ}\text{C}$ ).

The input needed for computation of  $\lambda E$  mentioned in equation (2) are air temperature ( $T_a$ ), LST ( $T_s$ ), Relative humidity (RH), Net radiation ( $R_n$ ) and soil heat flux (G), For clear sky conditions, hourly Net radiation ( $R_n$ ) product will be used as input. Air temperature and relative humidity will be taken from WRF model at 2m height on hourly scale. LST obtained from INSAT 3DR will be used on-hourly scale as input to this model.

In order to solve net surface available energy,  $\Phi$  ( $=R_n - G$ ) as mentioned in equation (2) and (6) we need to obtain soil heat flux. The soil heat flux can be obtained by two approaches:

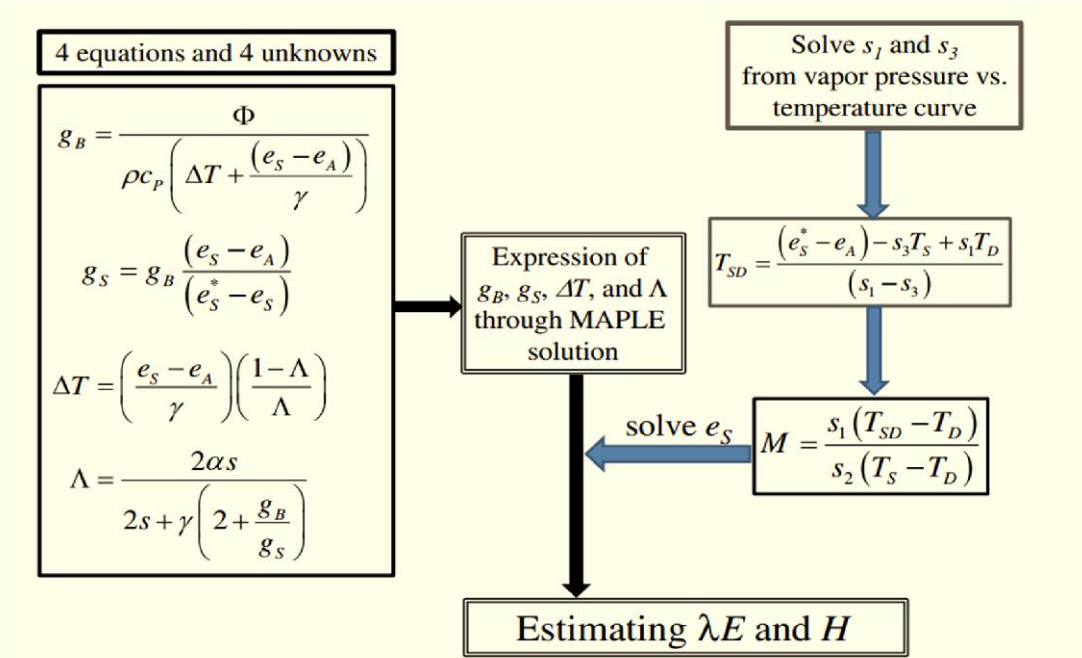


Figure 1: Diagrammatic representation of the core equations used to recover the internal state variables in STIC (Mallick et.al. 2014)

#### 4.4.2. Soil heat flux model

##### Statistical approach

The ratio of daytime soil heat flux and net radiation from AMS measurements over short vegetative systems were found to produce logarithmic relation with INSAT 3A CCD NDVI at 1 km. This relation was used to derive the soil heat flux (Bhattacharya et. al . 2014).

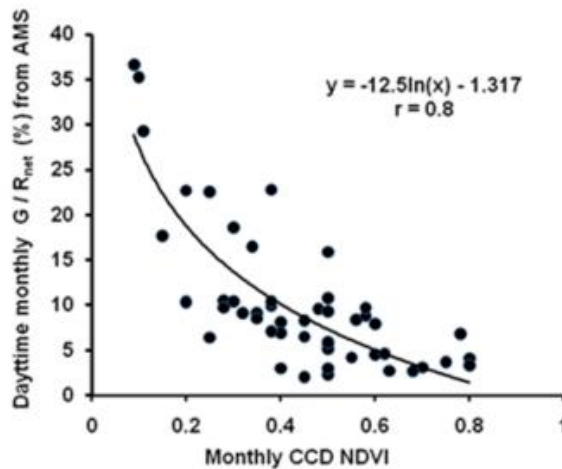


Figure 2: Relationship of net radiation fraction of soil heat flux ( $G$ ) with NDVI

It resulted into a significant correlation coefficient of 0.8. The spread is relatively more which could be due to difference in situ measurement footprints of soil heat flux and net radiation, and INSAT 3A CCD. This function was used to estimate soil heat flux through inversion from regional daytime net radiation and INSAT NDVI.

This relation  $G = -12.5 \ln(NDVI) - 1.317$  will be used to compute the G/R<sub>n</sub> ratio. Using all-sky net radiation product from INSAT 3DR and sliding monthly NDVI composite from other sources, daytime G and net available energy can be computed. Since nighttime soil heat flux is very negligible, daytime G will be scaled to daily 24 hours average G to derive daily  $\phi$ .

#### Thermal inertia-based (TI) physical modelling approach

The physical model for the land surface soil heat flux estimate based on the harmonic analysis of soil surface temperature (HM model) is described by [Murray and Verhoef et.al. \(2007\)](#) as follows:

$$G = \Gamma * ((1 - \frac{1}{2} f_c) * (\sum_1^m A_n \sqrt{n\omega} \sin(n\omega t + \phi_n + \frac{\pi}{4} - \frac{\pi\Delta t}{12})) = \Gamma * J_s \quad (7)$$

where G (W m<sup>-2</sup>) is the at-surface soil heat flux,  $\Gamma$  (J m<sup>-2</sup> K<sup>-1</sup> s<sup>-0.5</sup>) is the soil thermal inertia, M is the total number of harmonics used An is the amplitude of the n'th soil surface temperature (Ts) harmonic,  $\omega$  (rad s<sup>-1</sup>) is the angular frequency, t is the time (s),  $\phi_n$  (rad) is the phase shift of the n'th soil surface temperature harmonic, and Js is the summation of harmonic terms of soil surface temperature.

The parameter soil thermal inertia,  $\Gamma$ , is a key variable for estimating G0 using Eq. (10). Murray and Verhoef adopted the concept of normalized thermal conductivity ([O. Johansen 1977](#)) and developed a physical method to calculate  $\Gamma$  as

$$\tau = \exp [Y (1 - S_r^{Y-\delta})] (\tau_* - \tau_0) + \tau_0 \quad (8)$$

where  $\Gamma$  and  $\Gamma_0$  are the thermal inertia for saturated and air-dry soil (J m<sup>-2</sup> K<sup>-1</sup> s<sup>-0.5</sup>) respectively. Also  $\tau_0 = -1062.4 \Theta_* + 1010.8$  &  $\tau_* = 788.2 (\Theta_*^{-1.29})$ .  $\Theta$  (cm<sup>3</sup> cm<sup>-3</sup>) as soil porosity (equal to the saturated soil moisture content);  $\gamma$  (-) is a parameter depending on soil texture obtained from soil map ;  $S_r$  is the moisture availability at surface obtained moisture availability subroutine from STIC model. For instantaneous observations using satellite data n = 1 and phase  $\phi$  can be taken as 0°.

$$J_s(t) = (1 - \frac{1}{2} f_c) * (A_n \sqrt{n\omega} \sin(n\omega t + \phi_n + \frac{\pi}{4} - \frac{\pi\Delta t}{12})) \quad (9)$$

$\Delta t$  (s) is time offset between the canopy composite temperature and the below-canopy soil surface temperature and is found as 1.5 h in Murray and Verhoef based on their data. With the two boundary values (i.e.,  $\Delta t = 1.5$  h for  $f_c=1$  and  $\Delta t=0$  h for  $f_c=0$ ), a linear approach is proposed here to describe time offset  $\Delta t$  as function of vegetation fraction ( $f_c$ ). NDVI data from OCM, MSG-SEVRI or MODIS will be used to compute  $f_c$

$$\Delta t = 1.5 \cdot f_c \quad (10)$$

Once the soil heat flux is obtained then  $\phi$  is solved if all clear-sky instances prevail throughout the day.

#### 7.4.3 Cloudy sky Latent heat flux ( $\lambda E_{cld}$ )

The latent heat flux under cloudy sky conditions can be estimated using equation (2). Under cloudy sky conditions LST is not available, so the challenge is to retrieve LST under cloudy-sky conditions through inverse modelling.

### 4.5. LST retrieval under cloudy-sky

From the proposed net radiation product, the all-sky net radiation data are pre-requisite for LST recovery under cloudy-sky conditions. The net surface longwave radiation will be obtained as a difference from net surface radiation and net surface shortwave radiation under cloudy sky conditions. Net surface shortwave radiation will be obtained from instantaneous surface insolation product and noon-time sliding monthly albedo composite. The incoming longwave radiation will be deducted using WRF forecast data to retain outgoing longwave radiation ( $R_{locl}$ ). By inverting the equation of stefan-boltzmann law we can recover LST.

$$LST_{cloud} = (R_{locl} / (\epsilon_s \sigma))^{1/4} \quad (11)$$

Here under cloudy sky conditions the 30-day composite value of surface emissivity for cloudy pixel from historical MODIS data or sliding monthly NDVI composite will be used.

If the LST is recovered then by using equation 2, we can obtain latent heat flux under cloudy conditions. ( $\lambda E_{cld}$ )

In this case also, like clear sky conditions for solving  $\phi$  ( $R_n - G$ ) as mentioned in equation (2) & (6) we need to obtain soil heat flux. If LST is recovered under cloudy sky conditions the soil heat flux can be obtained by using TI- based model as discussed above. Here, in case of cloudy conditions for vegetation fraction ( $f_c$ ) we will use sliding monthly NDVI composite value cloudy pixel from external sources. By using equations 7-10 soil heat flux ( $G$ ) will be computed.

Once ' $G$ ' is obtained using method mentioned in figure (3) cloudy sky Latent heat flux ( $\lambda E_{cld}$ )

#### 4.5.1. Daily Evapotranspiration (ET)

The hourly latent heat flux ( $W m^{-2}$ ) will be converted in hourly ET (mm) using expression :

$$\lambda E \text{ (mm depth of water per hour)} = (\lambda E \text{ (Wm}^{-2}\text{)} * 0.0015) \quad (12)$$

This hourly ET will be summed to obtained daily and day time evapotranspiration in mm depth of water loss per day.

#### 4.5.2. AET anomaly

The Agro-Met Field Units (AMFUs) also require anomaly of AET products from mean for Friday-Monday and Tuesday –Thursday of each week. Once the algorithm is tested, validated and

integrated into MMDRPS and declared operational, the algorithm will be for processing of past years INSAT 3D and ancillary data to generate long term daily, time-binned AET, mean and percent anomaly from mean.

#### **4.5.3. Steps for operational implementation**

The following steps need to be followed for operational implementation of evapotranspiration over land (AET) product generation:

- i) Three-hourly temperature data at 2-meter surface height from hourly forecast from WRF (ASCII format) at  $0.03^{\circ} \times 0.03^{\circ}$  /  $0.05^{\circ} \times 0.05^{\circ}$  spatial grid.
- ii) Conversion of all ASCII outputs of (i) and (ii) to raster of dimension approx.  $0.04^{\circ} \times 0.04^{\circ}$  grid resolution as per the INSAT 3DR net radiation product
- iii) The sub setting of LST, current-day noon-time albedo, sliding monthly albedo and NDVI composites, net radiation products as per the bounds of Asia sector products.
- iv) Integration of INSAT derived clear sky net radiation, LST with 2-D surface of WRF variables in to physical model to generate clear sky latent heat flux. ( $\lambda E_{clr}$ )
- v) Integration of INSAT derived cloud mask and cloudy-sky net radiation and recovered LST along with 2-D surface WRF variables into physical model to generate cloudy-sky latent heat flux ( $\lambda E_{cld}$ )
- vi) Computation of daily evapotranspiration in  $\text{mm day}^{-1}$  from hourly latent heat flux and time-binned AET product for four days (Friday – Monday) and three days (Tuesday – Thursday).
- vii) Generation of long-term daily, time-binned, mean AET in mm depth of water to be updated every year), percent anomaly from mean

## 4.6. Outputs

Parameter	Unit	Min	Max	Accuracy	Resolution
Daily ET product over land					
(i) ET (ii) Latitude (iii) Longitude	mm day <sup>-1</sup>	0.01 7°N 67°E	12 37°N 98°E	70-75%	~ 4 km
Time binning product of ET sum over four days (Friday – Monday) and three days (Tuesday – Thursday)	mm	1	50	75-80%	~ 4 km
(i) ET (ii) Percent anomaly (iii) Latitude (iv) Longitude	%	-100	100	Better than 90%	~ 4 km

### ***Product latency of time-binned product for dissemination to agro-met advisory network***

Daily integrated AET will be obtained at the end of current day. For bi-weekly agro-advisories time-binned AET product of four-day (Friday-Monday) and three-day (Tuesday – Thursday)-d sum and percent anomaly from long-term mean corresponding to respective binning period will be disseminated on Tuesday and Friday morning before 11 AM.

## 4.7. Validation

### 4.7.1. Data required

Sensors	Parameters	Time scale	Source
INSAT 3D/3DR Imager	Evapotranspiration ( $ET$ ) and Latent heat flux ( $\lambda E$ )	Three hourly , Daily-day time, weekly, decadal, fortnightly and monthly scale	PR chain of MMDRPS test bed
In situ Eddy Co-variance (EC) Station	Evapotranspiration ( $ET$ ) & Latent heat flux ( $\lambda E$ )	Three hourly , Daily-day time, weekly, decadal, fortnightly and monthly scale	MOSDAC and INCOMPASS Project, IMD
Lysimeter (Data from few active stations will be used)	ET	Daily	IMD
Other satellites such as MSG IOC	Evapotranspiration ( $ET$ ) & Latent heat flux ( $\lambda E$ )	Three hourly , Daily-day time, weekly, decadal, fortnightly and monthly scale	EUMETSAT / EUMETCAST
Reanalysis	Evapotranspiration ( $ET$ ) & Latent heat flux ( $\lambda E$ )	Monthly scale	GIOVANNI site

## 4.8. Sensitivity analysis of STIC model simulated latent heat flux on LST and Albedo

The accuracy of STIC model heavily depends on the quality of land surface temperature data due to its role in retrieving  $T_{SD}$  and  $M$ . One-dimensional sensitivity analysis was carried out to quantify the impacts of uncertainty in  $T_s$  and albedo on  $\lambda E$ . Sensitivity analyses were conducted by increasing and decreasing LST systematically from its original value while keeping the other variables and parameters constant. This procedure was selected because the fluxes and other intermediate outputs of STIC model reflect an integrated effect of change in LST. Firstly, surface fluxes ( $\lambda E$ ) were computed using the original LST data obtained from EC tower observations. Then LST was increased and decreased at constant interval and a new set of fluxes were computed. It was found that  $\lambda E$  was sensitive to the LST uncertainties with a magnitude of error ranging 2-12 % for LST error in the range of 0.5 - 3K.

**Table 4 : Sensitivity analysis of  $\lambda E$  on LST**

Stations	Geographic locations	Deviation (%) in $\lambda E$ from reference					
		(LST ±0.5K)	(LST ±1K)	(LST ±1.5K)	(LST ±2K)	(LST ±2.5K)	(LST ±3K)
		± %	± %	± %	± %	± %	± %
Nawagam-Gujarat, semi arid cropland	22.80°N, 72.57°E	1.1	2.7	5.7	6.4	8.9	10.2
Jaisalmer-Rajasthan, arid grassland	26.99°N, 71.34°E	0.9	1.7	3.6	5.8	7.4	9.6
Samastipur-Bihar, Sub-humid cropland	26.00°N, 85.67°E	1.6	2.1	4.2	7.2	9.1	11.6

**Table 5. Sensitivity analysis of  $\lambda E$  on albedo**

Stations	Geographic locations	Deviation in $\lambda E$ from reference		
		(Albedo±2%)	(Albedo±5%)	(Albedo±10%)
Nawagam-Gujarat, semi arid, cropland	22.80°N,72.57°E	3.2	4.6	8.4
Jaisalmer-Rajasthan, arid grassland	26.99°N,71.34°E	2.6	4.1	7.9
Samastipur-Bihar, Sub-humid cropland	26.00°N,85.67°E	3.4	5.2	9.6

The deviation in  $\lambda E$  from reference was found to be from 3-10 % albedo change in the range of of 2-10 % from its reference value.

### Acknowledgements

We would like to thank Shri Tapan Misra, Director, Space Applications Centre for their encouragement towards the value-addition of operational weather forecast with Indian

geostationary satellite data to develop agro-climatic products. The authors are thankful to Dr. Raj Kumar, Dy. Director, EPSA and Dr. Prakash Chauhan, GD, BPSG for their support and guidance at different stages of this study.

## References

- Abteew,W.,Melesse,A.(2013). Evaporation and Evapotranspiration Measurement, Evaporation and Evapotranspiration Measurements and Estimations (1<sup>st</sup> Ed.). Dordrecht: Springer Netherlands
- Allen, R.G., Pereira, L.S., Raes, D., Smith, M., 1998. Crop Evapotranspiration Guidelines for Computing Crop Water Requirements-FAO Irrigation and Drainage Paper 56, 300. FAO, Rome, pp. 6541.
- Anderson, M. C., Norman, J. M., Mecikalski, J. R., Otkin, J. A., & Kustas, W. P. (2007). A climatological study of evapotranspiration and moisture stress across the continental United States based on thermal remote sensing: 1. Model formulation. *Journal of Geophysical Research-Atmospheres*, 112.
- Bastiaanssen, W.G.M., Menenti, M., Feddes, R.A., Holstag, A.A.M., 1998. A remote sensing surface energy balance algorithm for land (SEBAL): 1. Formulation. *Journal of Hydrology*, 198–212.
- Betts, A., Ball, J., Beljaars, A., Miller, M., Viterbo, P.A., 1996. The land surface atmosphere interaction: a review based on observational and global modeling perspectives. *J. Geophys. Res.* 101, 7209–7226.
- Bhattacharya, B. K. and Kumar, P. (2012a). AMS data Utilization for preliminary evaluation of operational forecast from WRF model. *SAC project report*.
- Bhattacharya, B. K., Padmanabhan, N., Ramakrishnan, R., Panigrahy, S. and Parihar, J.S. (2012b). Algorithm Theretical Basis Document (ATBD) for surface insolation using Kalpana-1 VHRR observations. SAC/EPSA/ISRO-GBP/SR/ATBD/02/2012.
- Bhattacharya, B.K., Dutt, C.B.S. and Parihar, J.S. (2010). INSAT uplinked Agromet Station – A scientific tool with a network of automated micrometeorological measurements for soil-canopy-atmosphere feedback studies. *ISPRS Archives XXXVIII-8/W3 Workshop Proceedings: Impact of Climate Change on Agriculture*. Paper no. TS9.13
- Bimal K. Bhattacharya, Rahul Nigam, M. K. Nanda, N. Singh, P. Raja and G.D. Bairagi (2014), Regional Evapotranspiration and Gross Primary Productivity from Indian Geostationary Satellite. *SAC project report*
- Bisht, G., Bras, R.L., 2011. Estimation of net radiation from the moderate resolution imaging spectroradiometer over the Continental United States. *IEEE Trans. Geosci. Remote Sens.* 49 (6), 2448–2462.

Brutsaert, W., Parlange, M.B., 1998. Hydrologic cycle explains the evaporation paradox. *Nature* 396 (6706), 30

Hu, G., Jia, L. and Menenti, M. (2015). Comparison of MOD16 and LSA-SAF MSG evapotranspiration products over Europe for 2011. *Remote Sensing of Environment*, 56, 510 – 526.

Jiménez, C., Prigent, C., Mueller, B., Seneviratne, S.I., McCabe, M.F., Wood, E.F., Rossow, W.B., Balsamo, G., Betts, A.K., Dirmeyer, P.A., Fisher, J.B., Jung, M., Kanamitsu, M., Reichle, R.H., Reichstein, M., Rodell, M., Sheffield, J., Tu, K., Wang, K., 2011. Global intercomparison of 12 land surface heat flux estimates. *J. Geophys. Res.* 116, D02102. <http://dx.doi.org/10.1029/2010JD014545>.

Jung, K., Reichstein, M., Ciais, P., Seneviratne, S.I., Sheffield, J., Goulden, M.L., Zhang, K. (2010). Recent decline in the global land evapotranspiration trend due to limited moisture supply. *Nature*, 467(7318), 951-954.

Kalma, J.D.; McVicar, T.R.; McCabe, M.F. 2008, Estimating land surface evaporation: A review of methods using remotely sensed surface temperature data. *Surv. Geophys.* ,29, 421–469.

Kumar, P., Singh, R., Joshi, P.C., Pal, P.K., 2011. Impact of Additional Surface Observation Network on Short Range Weather Forecast during Summer Monsoon 2008 over Indian Subcontinent. *Journal of Earth System Sciences*, 120, 2011, 1-12.

Kustas, W. P., and J. M. Norman (1997), A two-source approach for estimating turbulent fluxes using multiple angle thermal infrared observations, *Water Resour. Res.*, 33, 1495– 1508

Li, Z.L.; Tang, R.; Wan, Z.; Bi, Y.; Zhou, C.; Tang, B.; Yan, G.; Zhang, X. 2009 A review of current methodologies for regional evapotranspiration estimation from remotely sensed data. *Sensors* , 9, 3801–3853.

Malamos, N. Barouchas, P.E., Tsirogiannis, I.L., Liopa-Tsakalidi, A., & Koromilas, T. (2015) Estimation of Monthly FAO Penman-Monteith Evapotranspiration in GIS Environment, through a Geometry Independent Algorithm. *Agriculture and Agricultural Science Procedia*, 4, 290-299

Mallick, K., et al. (2014), A surface temperature initiated closure (STIC) for surface energy balance fluxes, *Remote Sens. Environ.*, 141, 243–261.

Mauser, W.; Stephan, S. 1998 Modelling the spatial distribution of evapotranspiration on different scales using remote sensing data. *J. Hydrol.*, 212–213, 250–267.

Miralles, D.G., Holmes, T.R.H., De Jeu, R.A.M., Gash, J.H., Meesters, A.G.C.A., Dolman, A.J., 2011b. Global land-surface evaporation estimated from satellite-based observations. *Hydrol. Earth Syst. Sci.* 15, 453–469

Monteith, J.L., 1965. Evaporation and environment. *Symp. Soc. Exp. Biol.* 19, 205–224.

Norman, J.m., & Becker, F. (1995). Terminology in thermal infrared remote sensing of natural surface, *Agricultural and Forest Meteorology*, 77(3-4), 153-166.

- O. Johansen, "Thermal conductivity of soils," DTIC Document (1977)
- Ohmura, A., Wild, M., 2002. Is the hydrological cycle accelerating Science 298, 1345–1356.
- Penman 1948, H.L. Natural evaporation from open water, bare soil and grass. Proc. R. Soc. Lond. A , 194, 120–145.
- Rodell, M., Famiglietti, J.S., 2002. The potential for satellite-based monitoring of groundwater storage changes using GRACE: the High Plains aquifer, central U S. J. Hydrol. 263, 245–256.
- Singh, R., Kumar, P. and Pal, P. K. (2011). Assimilation of Oceansat-2 Scatterometer Derived Surface Winds in the Weather Research and Forecasting Model. (IEEE Transactions on Geoscience & Remote Sensing .
- Skamarock W. C., Klemp J. B., Dudhia J., Gill D.O., Barker D.M., Duda M.G., Huang X.Y., Wang Wand Powers J. G. (2008). A description of the Advanced Research WRF Version 3. NCAR/TN-475 STR; NCAR Technical Note, Mesoscale and Microscale Meteorology Division, National Center of Atmospheric Research, June 2008, 113
- Su,Z. (2002).The surface Energy Balance System (SEBS) for estimation of turbulent heat fluxes. Hydrology and Earth System Sciences, 6(1),85-100.
- T. Murray and A. Verhoef, "Moving towards a more mechanistic approach in the determination of soil heat flux from remote measurements: I. A universal approach to calculate thermal inertia," Agric. For. Meteorol. 147(1–2), 80–87 (2007).
- Tang, X.G., Li, H.P., Desai, A.R., Nagy, Z., Luo, J.H., Kolb, T.E., Olioso, A., Xu, X.B., Yao, L., Kutsch, W., Pilegaard, K., Köstner, B., Ammann, C., 2014. How is water-use efficiency of terrestrial ecosystems distributed and changing on Earth Scientific Report 4, 7483.
- Verhoef et al., "Spatio-temporal surface soil heat flux estimates from satellite data; results for the AMMA experiment at the Fakara (Niger) supersite," Agric. For. Meteorol. 154–155, 55–66 (2012).
- Wang, K.C., Dickinson, R.E., 2012. A review of global terrestrial evapotranspiration observation, modeling, climatology, and climatic variability. Rev. Geophys. 50 RG2005.
- Xu, C.Y., Singh, V.P., 2005. Evaluation of three complementary relationship evapotranspiration model by water balance approach to estimate actual regional evapotranspiration in different climatic regions. J. Hydrol. 308 (1–4), 105–121.
- Xue, B.L., Wang, L., Li, X.P., Yang, K., Chen, D.L., Sun, L.T., 2013. Evaluation of evapotranspiration estimates for two river basins on the Tibetan Plateau by a water balance method. J. Hydrol. 492, 290–297.
- Yang, Y.T., Long, D., Shang, S.H., 2013. Remote estimation of terrestrial evapotranspiration without using meteorological data. Geophys. Res. Lett. 40, 3026–3030.

Zhang, K., Kimball, J.S., Mu, Q., Jones, L.A., Goetz, S.J., Running, S.W., 2009. Satellite based analysis of northern ET trends and associated changes in the regional water balance from 1983 to 2005. *J. Hydrol.* 379, 92–110.

Zhang, K., Kimball, J.S., Nemani, R.R., Running, S.W., 2010. A continuous satellite- derived global record of land surface evapotranspiration from 1983 to 2006. *Water Resour. Res.* 46 (9), W09522.

Zhang, K., Kimball, J.S., Nemani, R.R., Running, S.W., Hong, Y., Gourley, J.J., Yu, Z.B., 2015. Vegetation greening and climate change promote multidecadal rises of global land evapotranspiration. *Scientific Report* 5, 15956.

Zhang, L.; Lemeur, R. 1995, Evaluation of daily evapotranspiration estimates from instantaneous measurements. *Agric. For. Meteorol.*, 74, 139–154.

Zhang, Y., Leuning, R., Chiew, F.H.S., Wang, E., Zhang, L., Liu, C.M., Sun, F.B., Peel, M. C., Shen, Y.J., Jung, M., 2012. Decadal trends in evaporation from global energy and water balances. *J. Hydrometeorol.* 13, 379–391

## **5. Net Surface Radiation ( $R_n$ ) from INSAT series of data**

S. No.	Product Name	Spatial Resolution	Temporal Resolution
1	Net Surface Radiation ( $R_n$ ) from INSAT series of data	4 km x 4 km	30 minutes (7AM – 5 PM IST)

## 5.1. Algorithm Configuration Information

### 5.1.1. Algorithm name

Net Surface Radiation ( $R_n$ ) from INSAT series of data

### 5.1.2. Algorithm identifier

ISRO\_INSAT\_NET\_RAD

### 5.1.3. Algorithm specification

Version	Date	Prepared by	Description
1.0	15 March 2018	Rahul Nigam, and Bimal K. Bhattacharya	Net Surface Radiation baseline document

## 5.2. Introduction

Monitoring of the earth's radiation budget is essential for improving our understanding of the earth's climate and its changes since the radiative energy exchanges at the top of the atmosphere (TOA) and at the earth's surface regulate the redistribution of energy and determine the energy balance of the earth-atmosphere system. Rather than examining radiation budget as a whole, it is very important to quantify its components, namely incoming and outgoing shortwave and longwave radiation, within the atmosphere, and at the surface. Radiation budget and its different components also listed in essential climatic variables of the emerging Global Framework for Climate Services (BojinSki et al., 2014). Net surface radiation ( $R_n$ ) is a key parameter for energy and mass exchange between land and atmosphere and also play a vital role in many biological processes (Anderson et al. 2007). Radiative energy is the driving force for land surface meteorological and micrometeorological processes, such as sensible and latent heat (evapotranspiration) transfer. The surface radiation balance is one of the major factors that determine the surface temperature of the vegetation canopy and the underlying soil substrate. Thus, accurate estimates of  $R_n$  are essential for understanding the land surface energy distribution, the formation and transformation of air masses, snow melting calculations (Male and Granger, 1981), modeling crop transpiration and evapotranspiration, and addressing water resource management (Bisht and Bras, 2011).  $R_n$  (coupled with other energy balance component such as ground heat flux) serves as a key driving force for the evapotranspiration (ET). Estimation of  $R_n$  is necessary because it is a key input for land surface process and hydrological models, and are also used routinely to calculate evapotranspiration (Monteith, 1965; Kustas & Norman, 1997), which is a critical component of agricultural, hydrological, and ecological research. Over the years, various ET and land surface models have been developed that use remote sensing and ancillary surface and ground-based observations (Bastiaanssen et al., 1998). All ET models require estimates of  $R_n$  at spatial scale. Mallick et al (2009) and Westerhoff (2015) were observed sensitivity of  $R_n$  from 10 to 40% for ET over different agro-ecosystems.

### 5.2.1. Overview and background

$R_n$  is the difference between the incoming and outgoing shortwave and longwave radiation fluxes at the surface. Mathematically described as:

$$R_n = R_{ns} + R_{nl} \quad (a)$$

$$R_{ns} = R_{si} - R_{so} = (1 - \alpha)R_{si} \quad (b)$$

$$R_{nl} = R_{li} + R_{lo} \quad (c)$$

where  $R_{si}$  is the incoming shortwave radiation ( $\text{Wm}^{-2}$ ),  $R_{so}$  is the reflected outgoing shortwave radiation ( $\text{Wm}^{-2}$ ), which is calculated by  $R_{so} = \alpha \times R_{si}$ ,  $\alpha$  is the shortwave broadband albedo (dimensionless), thus  $R_{ns}$  is the net shortwave radiation,  $R_{li}$  is the incoming longwave radiation ( $\text{Wm}^{-2}$ ),  $R_{lo}$  is the outgoing longwave radiation ( $\text{Wm}^{-2}$ ), and  $R_{nl}$  is the net longwave radiation ( $\text{Wm}^{-2}$ ).  $R_n$  is normally positive during the daytime because net shortwave radiation dominates, but negative during the nighttime because net longwave radiation dominates (Allen et al., 1998). If all four components of Eq. (a) are known, the calculation of  $R_n$  is straightforward. Indeed, many radiation measurement towers measure these four components of radiation, thereby allowing us to determine  $R_n$  a given instance and location. Various satellite observations have been used to generate radiation products at regional and global scales (Liang et al., 2010, 2013b; Zhang et al., 2014). MeteoSat Second Generation Spinning Enhanced Visible and Infrared Imager (MSG SEVIRI) Satellite observations from the visible to near-infrared spectrum have been used for estimating incident solar radiation and surface albedo, and thermal-infrared data for estimating longwave radiation. To map the  $R_n$ , it is necessary to combine remote sensing observations with surface and atmospheric data, where the spatial variability is mainly modeled by means of albedo, emissivity, and land surface temperature maps obtained from satellite data. There are roughly two types of algorithms for estimating  $R_n$  (Liang et al., 2010), one calculates radiative quantities from the derived satellite products of all relevant atmospheric and surface variables (e.g., cloud, atmospheric temperature, LST, air and surface emissivity), and another estimates radiation directly from satellite observed radiance using a regression equation established from extensive radiative transfer simulations or using ground measurements.

### 5.2.2. Objectives

The objectives of this document are:

- (iv) To outline the algorithm for the estimation of hourly ( $R_n$ ) and daily net surface radiation ( $R_{ndly}$ ) over land in clear and cloudy sky
- (v) To implement the algorithm in IMDPS GPR (Geophysical Parameter Retrieval) chain for automation of  $R_n$  and  $R_{ndly}$  product generation
- (vi) To describe validation strategy against available *in-situ* measurements and other concurrent satellite products.

### **5.2.3. Instrument and characteristics of input products**

#### **5.2.3.1 Indian geostationary satellite INSAT 3DR**

The Indian National Satellite (INSAT) system is a joint venture of the Department of Space (DOS), Department of Telecommunications (DOT), and India Meteorological Department (IMD). INSAT-3DR carries a multi-spectral Imager (optical radiometer) capable of generating the images of the earth in six wavelength bands significant for meteorological observations, namely, visible (0.55-0.75  $\mu\text{m}$ ), shortwave infrared (1.55-1.68  $\mu\text{m}$ ), middle infrared (3.8-4.1  $\mu\text{m}$ ), water vapor (6.5-7.1  $\mu\text{m}$ ) and two bands in thermal infrared (10.3-11.3  $\mu\text{m}$  & 11.5-12.5  $\mu\text{m}$ ) regions. It also has 19 channel sounder, which is the first such payload to be flown on an ISRO satellite mission. The spatial resolution of VIS band is 1 km x 1 km and 4 km x 4 km for WV and thermal IR bands. The introduction of INSAT Meteorological Data Processing System (IMDPS) provides ([Bhattacharya et al. 2013](#)) both ‘full-globe’ and ‘sector’ data products in all the six bands of imager at half-an-hour interval at 4 km spatial resolution in an automated mode. So, there are maximum 48 acquisitions on a given day. Raw data after reception at each acquisition were corrected for servo, line loss, radiometry, stagger and oversampling removal using the INSAT 3DR data products scheduler. This results into automated generation of co-registered data in each band at Transverse Mercator (TM) projection. The dimension of each band at each acquisition is 1617 rows x 1615 columns for Asia Mercator sector product.

#### **5.2.3.2 Operational surface insolation product**

A spectrally integrated clear-sky and three-layer cloudy-sky models were developed to determine integrated atmospheric transmittances and instantaneous insolation. Half-an-hourly observations from an Indian geostationary satellite sensor, INSAT 3DR will be used to provide minimum ground brightness (surrogate of surface albedo) from previous 30 days, cloud top albedo, brightness temperatures, atmospheric water vapour as inputs to these models in addition to global eight-day aerosol optical depth at 550 nm and columnar ozone. A trapezoidal scheme will be implemented to obtain daily insolation (in  $\text{MJm}^{-2}$ ) from half-an-hour instantaneous insolation ( $\text{Wm}^{-2}$ ) throughout the day for all-sky conditions (clear + cloudy). The whole algorithm has been operationalized ([Bhattacharya et al. 2010 & 2012b](#)) and daily insolation product is available at 4 km from INSAT 3D and at 8 km from Kalpana-1 spatial resolution respectively with Transverse Mercator projection routinely from MOSDAC site (<http://www.mosdac.gov.in>).

#### **5.2.3.3 Operational proposed land surface albedo product**

The proposed algorithm for  $R_n$  will use the other proposed INSAT land surface albedo three hourly or daily composite product in the IMDPS operational chain.

### **5.3. Inputs**

#### **5.3.1. Image and pre-processing data (Dynamic)**

Table 1

Parameter	Resolution	Accuracy	Source
Instantaneous insolation product of Asia Mercator sector	Pixel (4 km x 4 km)	12-18%	PR chain of IMDPS
Instantaneous land surface temperature (LST) product	Pixel (4 km x 4 km)	10-15%	
Instantaneous cloud mask	Pixel (4 km x 4 km)		
Instantaneous Out going longwave radiation (OLR)	Pixel (4 km x 4 km)	1-2%	
30-day dynamic composite of proposed land surface albedo product of Asia Mercator sector	Pixel (4 km x 4 km)		
Geolocation file containing latitude and longitude corresponding to co-registered Imager data	Pixel wise	Less than one pixel	DP h5 product

### 5.3.2. Other auxiliary data and model inputs

Daily land surface emissivity will be generated from ten-year historical data of MODIS or through modelling of land emissivity as a function of 10-day (pre and post monsoon season) or 30-day (monsoon season) NDVI composite as mentioned in table 2.

Table 2

Parameters	Source
Daily emissivity from 10-year historical data from MODIS (2008-2018)	<a href="http://modis-atmod.gsfc.nasa.gov">http://modis-atmod.gsfc.nasa.gov</a>
OCM -2 and AWIFS mosaic NDVI	<a href="http://vedas.sac.gov.in">http://vedas.sac.gov.in</a>

### 5.3.3. Operational product of WRF short-range forecast

Weather Research and Forecasting (WRF; [Skamarock et al., 2008](#)) Model version 3.1 is used for All India Short range weather forecast. WRF is a limited area, non-hydrostatic, primitive equation model with multiple options for various physical parameterization schemes.

The WRF Model is integrated in a triple domain configuration with a horizontal resolution of 45 km, 15 km and 5 km for the All India, with grid points 260×235, 352×373 and 676×721 in x and y directions for the domains 1, 2 and 3, respectively. The model has 36 vertical levels with the top of the model atmosphere located at 10 hPa. The WRF 3D-Var is used for the assimilation of all available conventional including ISRO-AWS data and satellite observations to improve the model

initial conditions. The operational WRF short-range forecasts (Kumar et al., 2011), available at MOSDAC site used climatological land surface and atmospheric parameters from global database and assimilated all available conventional including ISRO-AWS and satellite observations (Kumar et al., 2011; Singh et al., 2011) from India such as Oceansat-2 scatterometer wind data and other International agencies (e.g. EUMETCast). The operational forecast is available at finer spatial resolution ( $\sim 5\text{km}$ ) at hourly interval upto 72 hours. In this algorithm only temperature at 2-meter height from surface will be used for estimation of  $R_n$ .

Parameters	Source
Operational hourly forecast output from WRF at $0.05^\circ \times 0.05^\circ$ spatial resolution for the following parameters in ASCII format (latitude, longitude, parameter) a) Air temperature (K) at 2 m height	MOSDAC

## 5.4. Algorithm functional specifications

### 5.4.1. Clear sky net surface radiation ( $R_{nclr}$ )

Three hourly clear sky day time net radiation over land will estimated using land surface temperature, albedo and surface insolation.  $R_{nclr}$  will estimated as function of net shortwave ( $R_{nsclr}$ ) and net longwave ( $R_{nlclr}$ ) :

$$R_{nclr} = R_{nsclr} + R_{nlclr} \quad (1)$$

$R_{nsclr}$  will be function of instantaneous incoming shortwave ( $R_{siclr}$ ) and albedo ( $\alpha$ ) and in this algorithm the incoming shortwave radiation will be taken from already developed and operationalized INSAT-3D product. Whereas, albedo will be taken from the proposed land albedo product from INSAT data.  $R_{nsclr}$  will be computed only for day-time.

$$R_{nsclr} = (1 - \alpha)R_{siclr} \quad (2)$$

Now net longwave radiation ( $R_{nlclr}$ ) will be function of incoming ( $R_{liclr}$ ) and outgoing ( $R_{loclr}$ ) longwave radiation

$$R_{nlclr} = R_{liclr} + R_{loclr} \quad (3)$$

$R_{liclr}$  is a defined as

$$R_{liclr} = \varepsilon_a \sigma T_i^4 \quad (4)$$

Where,

$\varepsilon_a$  = Air emissivity,  $\sigma$  = Stefan Blotzmann constant &  $T_i$  = Air temperature

$\varepsilon_a$  will be estimated using air emissivity (Bastiaanssen et al, 1998) and defined as

$$\varepsilon_a = 0.85 - \ln T_{sw}^{0.09} \quad (5)$$

Where,  $T_{sw}$  = Atmospheric Transmissivity

$T_{sw}$  will be derived from the ratio of incoming shortwave radiation ( $R_{si}$ ) to extra-terrestrial radiation ( $R_{ext}$ ). The extra-terrestrial radiation will be computed using astronomical units for INSAT pixel for each instantaneous acquisition. The air temperature ( $T_i$ ) will be integrated from hourly daily weather forecast from WRF as mentioned in section 2.3.3.

$R_{loclr}$  again is function of surface emissivity and land surface temperature as defined in equation

$$R_{loclr} = \varepsilon_s \sigma T_s^4 \quad (6)$$

Where,  $\varepsilon_s$  = Air emissivity,  $\sigma$  = Stefan Boltzmann constant &  $T_s$  = Land Surface Temperature (LST)

The daily surface emissivity will be generated from 10-years MODIS emissivity product or from NDVI products from OCM-2, AWIFS India mosaic products as per the availability and quality of data. The land surface temperature will be taken from already operationalized INSAT product. Hence by doing computation of equations 1 to 6  $R_{nclr}$  will be estimated for day time. In night time only net longwave radiation will exist hence only equation (3) will be taken in consideration for computation of clear sky  $R_{nclr}$ .

#### 5.4.2. Cloudy sky net surface radiation ( $R_{ncld}$ )

For cloudy pixel the empirical model will be developed among INSAT derived outgoing longwave radiation (OLR), insolation product and measured net radiation from AMS and eddy tower data over different agro-climatic conditions of India for day and night time separately.

Net shortwave radiation in cloudy pixel ( $R_{nscl}$ )

$$R_{nscl\_day} = (1-\alpha) R_{sicl} \quad (7)$$

$\alpha$ - Albedo will be computed from moving last 20-day composite.

Incoming longwave radiation in cloudy pixel ( $R_{lincl}$ ) during daytime

$$R_{lincl\_day} = f(Ta, RH, CI) \quad (8)$$

Where  $Ta$  = Air temperature,  $RH$  = Relative humidity,  $CI$  = Clearness Index

Incoming longwave radiation in cloudy pixel ( $R_{lincl}$ ) during night time

$$R_{lincl\_night} = f(Ta, RH) \quad (9)$$

Where,  $Ta$  = Air temperature,  $RH$  = Relative humidity

Outgoing longwave radiation in cloudy pixel ( $R_{locld}$ ) during day and night time

$$R_{locld} = f(OLR, LULC) \quad (10)$$

Where, OLR= Out Going Long Wave Radiation, LULC = Land Use Land Cover ( From AWIFS, provided by NRSC)

To estimate  $R_{ncl}$  in cloudy sky first the cloudy pixel will be identified by using INSAT generated cloud mask for each dataset. Then these empirical model will be applied at spatial scale from cloudy-sky acquisition for cloudy pixels. The overall flow of algorithm is shown in Figure 1.

For each hourly acquisition, clear sky and cloudy sky models simultaneously applied and will generate  $R_n$  over Indian land mass. To generate daily average net radiation ( $R_{ndly}$ ) at least one acquisition is required in each two hours to compute  $R_{ndly}$ . If there is two consecutive hourly data gap exists within 24-hours' timeframe, then daily net radiation will not be computed. For each hourly acquisition, clear sky and cloudy sky models simultaneously applied and will generate  $R_n$  over Indian land mass.

#### 5.4.3. Sensitivity Analysis

The 1-dimensional sensitivity analysis of whole algorithm will be done for net shortwave and net longwave in clear sky and cloudy sky. For net shortwave in clear and cloudy sky albedo and for net longwave clear sky LST sensitivity will be evaluated. For cloudy sky, weather forecast based air temperature and humidity along with INSAT derived OLR sensitivity will be done in future. The high resolution (3 Km) and high temporal (1-hour) weather forecast from IMD for evaluation of the surface temperature, relative humidity will also be used simultaneously with MOSDAC weather forecast to develop algorithm followed by sensitivity analysis.

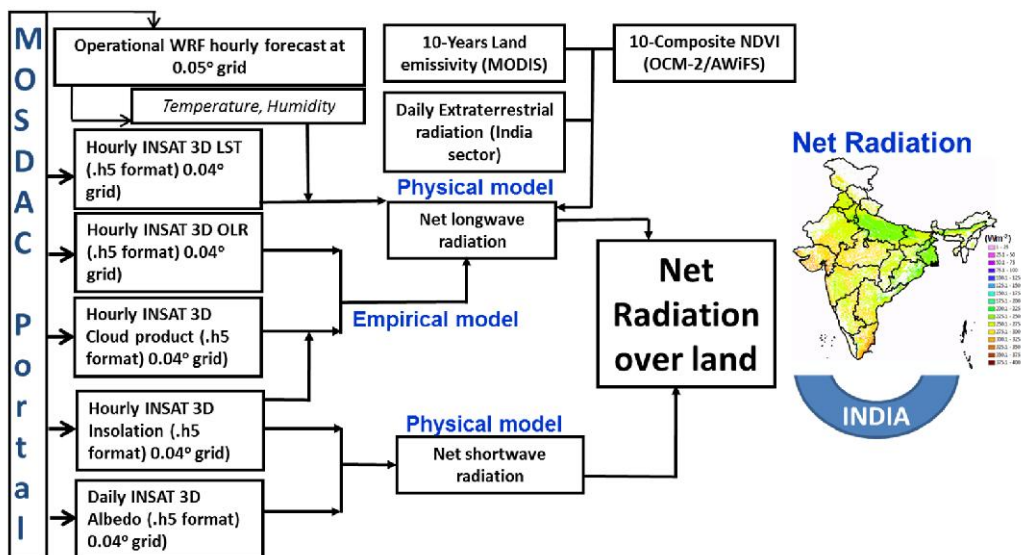


Figure 1 . Flow chart of algorithm for estimation of net radiation ( $R_n$ ) over land

#### **5.4.4. Steps for operational implementation**

The following steps need to be followed for operational implementation of net radiation over land ( $R_n$ ) product generation:

- viii) The hourly temperature and humidity data at 2-meter surface height from forecast from WRF (ASCII format) at  $0.05^\circ \times 0.05^\circ$  spatial grid.
- ix) Conversion of all ASCII outputs of (i) and (ii) to raster of dimension approx.  $0.04^\circ \times 0.04^\circ$  grid resolution as per the INSAT 3D insolation product
- x) The sub setting of LST, albedo and insolation products as per the bounds of Asia sector products.
- xi) Integration of INSAT derived insolation, albedo, LST with 2-D surface of WRF variables in to physical model to generate clear sky net radiation ( $R_n$ ).
- xii) Integration of INSAT derived cloud mask and insolation in to empirical model to generate cloudy sky net radiation ( $R_n$ ).
- xiii) The clear and cloudy sky net radiation at each hour will be used to generate hourly net radiation ( $R_n$ ) over Indian land mass.
- xiv) The average of 24-hours net radiation will be used for generation of daily net radiation ( $R_{ndly}$ ). The pre-condition for generation of  $R_{ndly}$  is that there will no consecutive two-hour data loss within 24-hours of a day.

### **5.5. Outputs**

#### **5.5.1. Format of the output and the domain**

Parameter	Unit	Min	Max	Accuracy	Resolution
Three hourly Net radiation over land consists					
(iv) $R_n$	$\text{W m}^{-2}$	-100	650	70-75%	$\sim 4 \text{ km}$
(v) Latitude		$7^\circ\text{N}$	$37^\circ\text{N}$		
(vi) Longitude		$67^\circ\text{E}$	$98^\circ\text{E}$		

Parameter	Data format	Upper left and lower right corner coordinates	Scan lines and columns	Gains and offsets for converting actual values
Three hourly Net radiation over land consists  (i) $R_n$ (ii) Latitude (iii) Longitude	HDF5	Upper left: 67°37'E, 36°53'N  Lower right: 97°42'E, 7°34'N	Indian domain	Gain for $R_n$ data 0.1, offset zero

## 5.6. Validation

### 5.6.1. Data required

To validate the INSAT derived instantaneous hourly and daily net radiation in situ measured and globally products from other satellite as well as model will be used. The detailed requirement of satellite and in situ data is given in table 5. For validation one-year data covering all season will be used.

*Table 5*

Sensors	Parameters	Time scale	Source
INSAT 3DR Imager	Net radiation ( $R_n$ )	Hourly and Daily	PR chain of IMDPS test bed
AMS and Eddy Co-variance Station	Four component radiation measurements	Hourly data	MOSDAC and other projects
NASA earth observations	Net radiation	Daily ( $0.25^0 \times 0.25^0$ )	<a href="http://www.neo.sci.gsfc.nasa.gov">www.neo.sci.gsfc.nasa.gov</a>
MSG SEVIRI	Net radiation	Daily	<a href="http://www.eumetsat.int">www.eumetsat.int</a>

### Acknowledgements

We would like to thank Shri Tapan Misra, Director, Space Applications Centre for their encouragement towards the value-addition of operational weather forecast with Indian geostationary satellite data to develop agro-climatic products. The authors are thankful to Dr. Raj Kumar, Dy. Director, EPSA and Dr. Prakash Chauhan, GD, BPSG for their support and guidance at different stages of this study.

### References

- Allen, R., et al., 2011. Satellite-based ET estimation in agriculture using SEBAL and METRIC. *Hydrol. Process.* 25 (26), 4011–4027.
- Allen, R.G., Pereira, L.S., Raes, D., Smith, M., 1998. Crop Evapotranspiration-Guidelines for Computing Crop Water Requirements-FAO Irrigation and Drainage Paper 56, 300. FAO, Rome, pp. 6541.
- Anderson, M. C., Norman, J. M., Mecikalski, J. R., Otkin, J. A., & Kustas, W. P. (2007). A climatological study of evapotranspiration and moisture stress across the continental United States based on thermal remote sensing: 1. Model formulation. *Journal of Geophysical Research-Atmospheres*, 112.
- Bastiaanssen, W.G.M., Menenti, M., Feddes, R.A., Holstag, A.A.M., 1998. A remote sensing surface energy balance algorithm for land (SEBAL): 1. Formulation. *Journal of Hydrology*, 198–212.
- Bhattacharya, B. K., N. Padmanabhan, S. Mahammed, R. Ramakrishnan, and J. S. Parihar. 2013. Assessing Solar Energy Potential Using Diurnal Remote-Sensing Observations from Kalpana-1

VHRR and Validation over the Indian Landmass. International Journal of remote Sensing 34: 7069–7090. doi:10.1080/01431161.2013.811311.

Bhattacharya, B. K. and Kumar, P. (2012a). AMS data Utilization for preliminary evaluation of operational forecast from WRF model. *SAC project report*.

Bhattacharya, B. K., Padmanabhan, N., Ramakrishnan, R., Panigrahy, S. and Parihar, J.S. (2012b). Algorithm Theretical Basis Document (ATBD) for surface insolation using Kalpana-1 VHRR observations. SAC/EPSA/ISRO-GBP/SR/ATBD/02/2012.

Bhattacharya, B.K., Dutt, C.B.S. and Parihar, J.S. (2010). INSAT uplinked Agromet Station – A scientific tool with a network of automated micrometeorological measurements for soil-canopy-atmosphere feedback studies. *ISPRS Archives XXXVIII-8/W3 Workshop Proceedings: Impact of Climate Change on Agriculture*. Paper no. TS9.13

Bisht, G., Bras, R.L., 2011. Estimation of net radiation from the moderate resolution imaging spectroradiometer over the Continental United States. *IEEE Trans. Geosci. Remote Sens.* 49 (6), 2448–2462.

Bojinski, S., VerStraete, M., PeterSon, T.C., Richter, C., Simmons, A. and Zemp, M. (2014). The concept of essential climate variables in support of climate research, applications, and policy. *Bull. Amer. Meteor. Soc.* DOI:10.1175/BAMS-D-13-00047.1.

Kumar, P., Singh, R., Joshi, P.C., Pal, P.K., 2011. Impact of Additional Surface Observation Network on Short Range Weather Forecast during Summer Monsoon 2008 over Indian Subcontinent. *Journal of Earth System Sciences*, 120, 2011, 1-12.

Kustas, W. P., and J. M. Norman (1997), A two-source approach for estimating turbulent fluxes using multiple angle thermal infrared observations, *Water Resour. Res.*, 33, 1495– 1508.

Liang, S.L., Wang, K.C., Zhang, X.T., Wild, M., 2010. Review on estimation of land surface radiation and energy budgets from ground measurement, remote sensing and model simulations. Selected topics in applied earth observations and remote sensing. *IEEE J. 3 (3)*, 225–240.

Liang, S.L., Zhang, X.T., He, T., Cheng, J., Wang, D.D., 2013b. Remote sensing of earth surface radiation budget. In: Petropoulos, G.P. (Ed.), *Remote Sensing of Land Surface Turbulent Fluxes and Soil Surface moisture Content: State of the Art*. CRC Press, pp. 125–165.

Male, D., Granger, R., 1981. Snow surface energy exchange. *Water Resources Res.* 17 (3), 609– 627.

Mallick, K., Bhattacharya, B.K., Rao, V.U.M., Reddy, D.R., Banerjee, S., Venkatesh, H., Pandey, V., Kar, G., Mukherjee, J., Vyas, S.P., Gadgil, A.S., Patel, N.K. (2009) Latent heat flux estimation in clear sky days over Indian agroecosystems using noontime satellite remote sensing data. *Agricultural and Forest Meteorology* 149, 1646–1665.

Monteith, J.L., 1965. Evaporation and environment. *Symp. Soc. Exp. Biol.* 19, 205–224.

Singh, R., Kumar, P. and Pal, P. K. (2011). Assimilation of Oceansat-2 Scatterometer Derived Surface Winds in the Weather Research and Forecasting Model. (IEEE Transactions on Geoscience & Remote Sensing <http://dx.doi.org/10.1109/TGRS.2011.2164410>

Skamarock W. C., Klemp J. B., Dudhia J., Gill D.O., Barker D.M., Duda M.G., Huang X.Y., Wang Wand Powers J. G. (2008). A description of the Advanced Research WRF Version 3. NCAR/TN-475 STR; NCAR Technical Note, Mesoscale and Microscale Meteorology Division, National Center of Atmospheric Research, June 2008, 113 pp.

Westerhoff, R.S. (2015). Using uncertainty of Penman and Penman–Monteith methods in combined satellite and ground-based evapotranspiration estimates. *Remote Sensing of Environment* 169, 102–112.

Zhang, X., Liang, S., Zhou, G.S., Wu, H., Zhao, X., 2014. Generating Global and Surface Satellite incident shortwave radiation and photosynthetically active radiation products from multiple satellite data. *Remote Sens. Environ.* 152, 318–332

## **6. Daily Surface Net Shortwave Radiation over Indian Ocean using half-hourly Outgoing Longwave Radiation Data from Indian Geostationary Satellites**

S. No.	Product Name	Spatial Resolution	Temporal Resolution
1	IMG_NSRO	4 km x 4 km	Daily average

## **6.1. Algorithm configuration information**

### **6.1.1 Algorithm name:**

Daily Surface Net Shortwave Radiation over Indian Ocean using half-hourly Outgoing Longwave Radiation Data from Indian Geostationary Satellites (NSRO)

### **6.1.2. Algorithm Identifier:**

INSAT\_IMG\_NSRO

### **6.1.3. Algorithm Specification**

<b>Version</b>	<b>Date</b>	<b>Prepared by</b>	<b>Description</b>
1.0	16.11.2016		
1.1	08.08.2018	Rashmi Sharma and Pradeep Thapliyal	Net surface shortwave radiation over Ocean valid in the warm pool region using high spatio-temporal resolution OLR observations from geostationary satellite

## **6.2. Introduction**

The shortwave radiative flux absorbed by the ocean surface plays an important role in the atmospheric and oceanic circulation through air-sea interaction particularly over the warm pool region of the Indian Ocean [Lukas, 1989]. The accurate information of surface Short Wave Radiation (SWR) would also result in significantly improved representation of the intra-annual oceanic surface processes and long term surface variability. The diurnal variations in the Sea Surface Temperature (SST) are driven by the surface solar radiation that is modulated primarily by the presence of cloudiness. The SWR data available through buoys have sparse coverage due to the large cost and maintenance involved. In the recent years there have been efforts to establish an accurate estimate of the surface shortwave radiation budget (SRB) over Tropical Ocean and to assess its impact on the climate change.

The tropical oceans with SST usually greater than 28 °C, forms a major part of the largest warm pool on the earth. The variations of surface insolation over these warm pool regions are primarily due to the variations in cloudiness which are manifestation of deep convection [Shinoda et al., 1998; Sengupta et al., 2001]. The long-term surface measurements of radiative fluxes are limited primarily to the continental regions [Ohmura and Gilgen, 1991]. The satellite estimates of cloudiness and top of the atmosphere fluxes have been used in conjunction with radiative transfer models to produce global estimates of SRB over land and ocean [Li, 1995; Rossow and Zhang, 1995; Whitlock et al., 1995; Gupta et al., 1997]. The most popular algorithms used in computing

SRB estimates from satellite data are described by Pinker and Laszlo [1992] and Darnell et al. [1992].

The global Analysis, such as the National Center for Environmental Prediction (NCEP) [Kalnay et al., 1996], National Aeronautics and Space Administration/Data Assimilation Office (NASA/DAO) [Schubert et al., 1993], and the European Centre for Medium-Range Weather Forecasts Reanalysis [ERA, 1999] projects have provided climate researchers with alternative estimates of the earth's SRB. Bony et al. [1997] used data from the NASA/DAO and NCEP reanalysis for the period 1987–88 to compare SWR at the surface to satellite estimates in the Tropics ( $30^{\circ}\text{S}$ – $30^{\circ}\text{N}$ ). They found the annual mean bias in NCEP SWR over the tropical ocean ranging from  $-10$  to  $-30 \text{ W m}^{-2}$ , while NASA/DAO SWR biases ranged from  $-50 \text{ W m}^{-2}$  in subsidence regions of the subtropics to  $-25 \text{ W m}^{-2}$  in convective regions near the equator.

Table-1 provides a summary of presently available SWR products from different source alongwith their merits and demerits.

**Table-1 SOURCES OF SWR**

Source	Spatial/ Temporal Res.	Advantage	Disadvantage
Buoy Observations	hourly	Accurate	Sparse observations
Atmospheric models (Reanalysis products)	$1\text{-}2^{\circ}$ / 6-hourly	Global Products	Inaccurate
ISCCP (Satellite data + RT models)	$280 \text{ km}/$ 3-hourly	Global Product	Computationally expensive (Non-availability in real time)
GEWEX (Satellite data + RT models)	$1^{\circ}/$ 3-hourly	Global Product	Computationally expensive (Non-availability in real time)
LY products (Large and Yeager, 2001) Satellite – Model merged	$1^{\circ}/$ Daily	Global Products	Computationally expensive (Non-availability in real time)
Empirical relations (Shinoda et al, 1998)	$\sim 10 \text{ km}/$ Daily	Fast and Simple	Regional products

Note: LY products largely known as Large and Yeager product follows the earlier approach of *Large and Nurser* [2001], in which the NCEP surface radiation and precipitation are replaced by satellite-based estimates.

The present Algorithm Theoretical Basis Document describes a methodology to estimate SWR from half-hourly estimates of Outgoing Longwave Radiation (OLR) obtained from Kalpana observations. Although we have shown the results with Kalpana derived OLR, but the same algorithm has been tested with the data from other Indian GEO satellites.

### **6.3. Physical basis of the SWR Algorithm**

The OLR-based SWR estimates have better accuracy for convective regions because the variations of surface insolation over the warm pool ocean region are primarily due to the variations in cloudiness. Variations in cloudiness are manifestation of deep convection; therefore, OLR is a good proxy for convection. *Shinoda et al* [1998] showed in their study that the coefficient of correlations between SWR and OLR were maximum ( $\sim 0.8$ ) at the equator that decreases as one goes away from the equator and reduces to less than 0.5 beyond  $10^{\circ}\text{N/S}$  latitudes.

*Shinoda et al.* [1998] proposed a simple empirical relationship (referred hereafter as SH98), valid over warm pool oceanic regions, to estimate the daily averaged SWR from the daily averaged OLR products obtained from the NOAA polar orbiting satellite. Shahi et al. [2010], proposed the use of a high temporal resolution data of OLR to improve the diurnal sampling in order to match that of the buoy SWR in computing daily averaged estimates. They demonstrated a significant improvement in the SH98 by using daytime average of OLR obtained from half-hourly geostationary satellite observations. The rationale behind using the daytime OLR as against daily (24-hr average OLR) is that the daily averaged SWR is affected solely by the presence of day-time clouds, and therefore the algorithm performs better than that used in SH98. The empirical relationship developed by Shahi et al [2010], however, was developed for a single buoy location, and is not valid over other locations, particularly over different latitude regions. Shahi et al. [2011] further improved the algorithm to make it valid over a wide Indian Ocean region by including the solar zenith angle in the empirical formulations. The detailed formulation is given in the following section.

### **6.4. Formulation of the SWR Algorithm**

The improved algorithm developed at Space Applications Centre (SAC) to compute the SWR from OLR observations from geostationary satellites is described in detail by Shahi et al. [2011]. The methodology was developed using a large collocated dataset of the spatially well distributed (in latitude) buoy measured SWR and the half-hourly estimates of OLR from geostationary satellite observations over Indian Ocean region. The generalization of the empirical relationship has been achieved by normalizing the SWR values to nadir locations by making use of the solar zenith angle information.

The in-situ SWR is the down-welling shortwave radiation measured by the Research Moored Array for African-Asian-Australian Monsoon Analysis and Prediction (RAMA) buoy. Daily average shortwave radiation is computed as a 24 hour average. Fig.1 shows the locations of the 13 RAMA buoys in the warm pool region of Indian Ocean used for the algorithm development for the period of 2002-2009. The OLR products have been obtained from EUMETSAT for the Indian Ocean coverage of the Meteosat-5 (sub-satellite point at  $57^{\circ}\text{E}$ ) upto December 2006 and Meteosat-7 (sub-satellite point at  $63^{\circ}\text{E}$ ) beyond January 2007. Meteosat derived OLR was estimated from the half-hourly observations in the thermal infrared (TIR,  $10.5\text{-}12.5\mu\text{m}$ ) and water vapor absorption (WV,  $5.7\text{-}7.1\mu\text{m}$ ) channels at spatial resolution of 5 km, using the algorithm developed by Schmetz and Liu [1988]. The accuracy of geostationary satellite derived OLR is shown to be  $\sim 3 \text{ W m}^{-2}$  [Schmetz

and Liu, 1988; Singh et al., 2007] using radiative transfer model based simulation studies. The validation of geostationary satellite derived OLR with the broadband OLR observations from the Clouds and Earth's Radiant Energy System (CERES) onboard polar orbiting satellites TRMM and EOS-Terra reveal the accuracy to be  $\sim 7 \text{ W m}^{-2}$  at a daily time-scale [Ba et al., 2003].

A collocated dataset of daily averaged SWR (24-hr average) using buoy data and daytime averaged OLR (duration of sunshine) was generated for each of the buoy locations. The daytime averaged OLR is obtained using average of the half-hourly observations between sunrise to sunset (computed

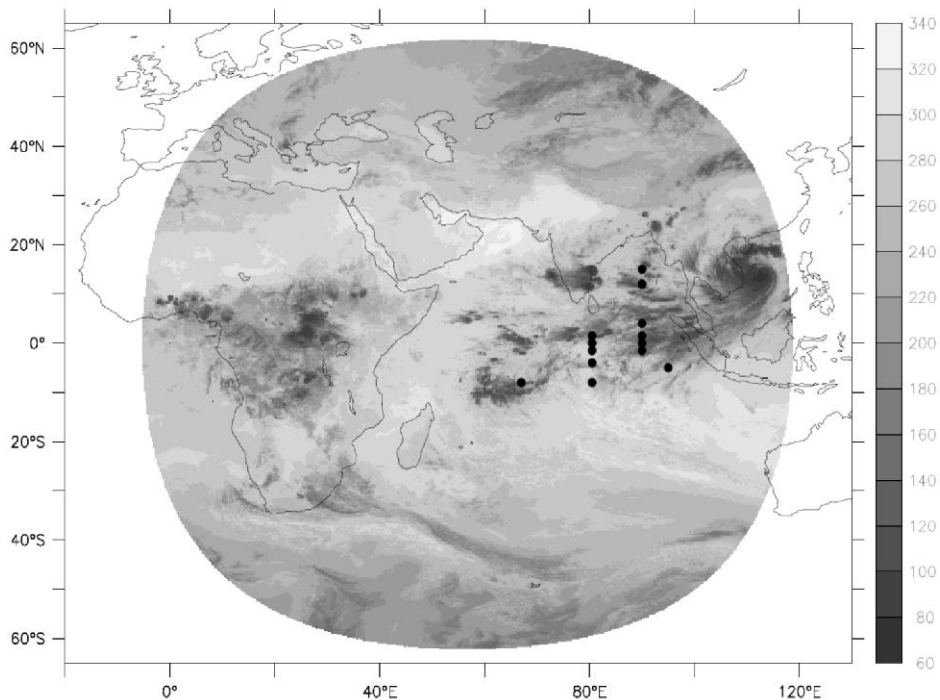


*Figure 1: Locations of RAMA buoys in Indian Ocean overlaid on a sample Meteosat OLR coverage*

using solar zenith angle less than  $80^\circ$ ). A training dataset, using collocated observations from each of the buoys that represent complete annual cycle, was created for the algorithm development and the remaining data treated as the independent testing dataset.

SAC-Algorithm [Shahi et al., 2011] used the normalized SWR w.r.t. the nadir viewing angle, i.e. SWR  $\sec^2(\beta)$ , in the empirical formulation, where  $\beta$  is solar zenith angle at local noon. The polynomial least square equation between normalized SWR and OLR was found to be:

$$(\text{SWR}) \sec^2(\beta) = -0.002434 (\text{OLR})^2 + 2.5401 (\text{OLR}) - 220.75$$

which provides the final expression for computing the SWR as:

$$\text{SWR} = \cos^2(\beta) [-0.002434 (\text{OLR})^2 + 2.5401 (\text{OLR}) - 220.75]$$

The improved algorithm is referred as SAC-SWR Algorithm. The root-mean-squared-error (RMSE) computed for SAC-SWR estimates from the buoy observations was found to be  $\sim 28 \text{ W m}^{-2}$  in the testing dataset in contrast to the  $\sim 39 \text{ W m}^{-2}$  obtained using SH98.

The SAC-SWR algorithm was also compared with other datasets for the year 2007 available from: (i) Global Energy and Water-Cycle Experiment Surface Radiation Budget (GEWEX-SRB) project of NASA World Climate Research Programme (WCRP), (ii) International Satellite Cloud Climatology Project Surface Radiative Flux Dataset (ISCCP-FD), and (iii) National Center for Environmental Prediction (NCEP) analysis. The Spatial resolution of GEWEX-SRB, ISCCP-FD and NCEP SWR products are  $1^\circ$ ,  $2.8^\circ$  and  $1.875^\circ$ , respectively. The RMSE computed for different SWR products from buoy SWR shows that RMSE for SAC-SWR is lowest for the entire range of SWR values, indicating that the accuracy of the SAC-SWR is best under all sky conditions followed closely by GEWEX-SWR.

**For combined dataset RMSE for SAC-SWR is  $27.3 \text{ W m}^{-2}$ , which is the smallest, followed by  $32.7$ ,  $37.5$  and  $59.6 \text{ W m}^{-2}$ , respectively, for GEWEX, ISCCP and NCEP SWR products. The estimate of the standard error on weekly time scales is much smaller than that on daily time scales, with values of  $11.8$ ,  $13.4$ ,  $15.3$ , and  $32.8 \text{ W m}^{-2}$  for SAC, GEWEX, ISCCP, and NCEP products, respectively.**

## 6.5. Algorithm Flow Diagram

We show below a schematic diagram of the SWR algorithm training and retrievals.

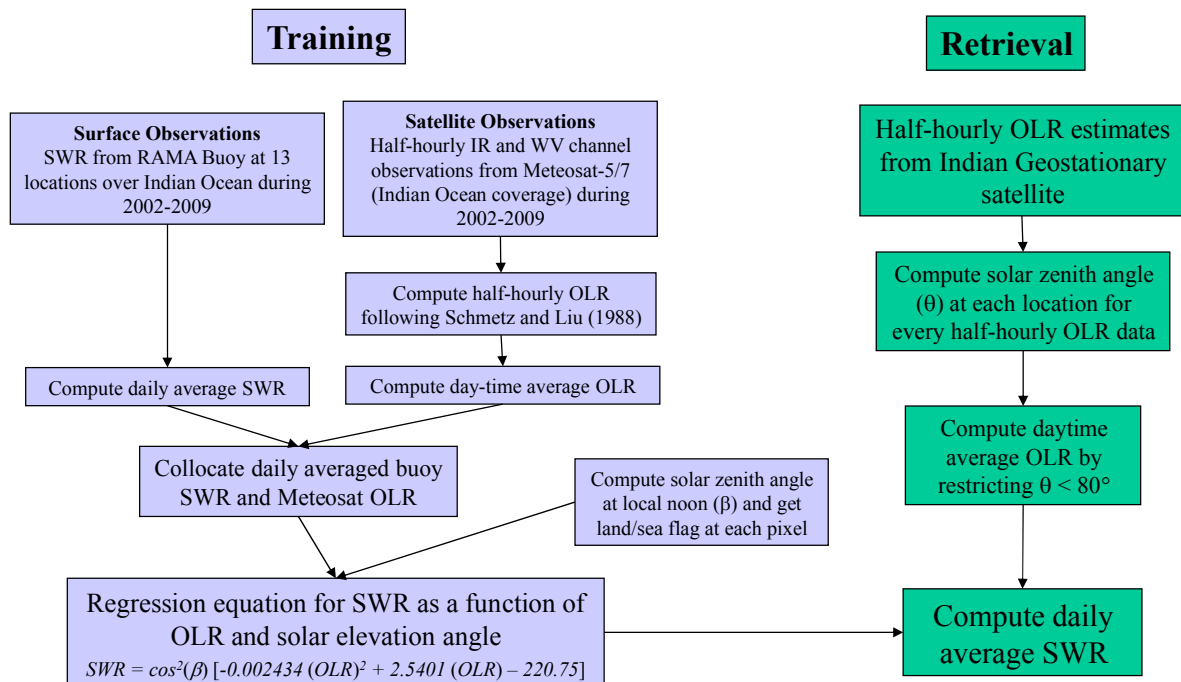


**Fig.2 Schematic diagram of the SWR algorithm training and retrievals**

## 6.6. Operational Implementation

Following steps are used to compute daily average SWR:

- Half-hourly OLR data from Indian GEO Satellites is acquired for a given day.
- For each observation, solar zenith is computed to ascertain the solar illumination conditions i.e. to get information about local time.
- From half-hourly OLR data, the daytime averaged OLR ( $OLR_{dayavg}$ ) is computed at every pixel by restricting the solar zenith angle ( $\theta$ ) to less than  $80^\circ$  at each pixel during averaging.
- Solar zenith angle at local noon ( $\beta$ ) is computed at each pixel location corresponding to the given day of observation. (In bullet 2, also solar zenith is computed)
- Using land/sea flag information, the daily averaged Surface Shortwave Radiation ( $SWR_{dayavg}$ ) is computed over Indian ocean region from the empirical relationship developed at SAC:

$$SWR_{dayavg} = \cos^2(\beta) [-0.002434 (OLR_{dayavg})^2 + 2.5401 (OLR_{dayavg}) - 220.75]$$

## References

- Ba, M. B., R.G. Ellingson, and A. Gruber (2003), Validation of a technique for estimating OLR with the GOES Sounder, *J. Atmos. Ocean. Tech.*, 20, 79-89.
- Bony, S., Y. Sud, K. M. Lau, J. Susskind, and S. Saha (1997), Comparison and satellite assessment of NASA/DAO and NCEP reanalysis over tropical ocean: Atmospheric hydrology and radiation, *J. Climate*, 10, 1441–1462.
- Darnell, W. L., W. F. Staylor, S. K. Gupta, N. A. Ritchey, and A. C. Wilber (1992), Seasonal variation of surface radiation budget derived from ISCCP-C1 data, *J. Geophys. Res.*, 97, 15 741–15 760.
- ERA, (1999), The ECMWF Re-Analysis (ERA) Project. [Available online at <http://www.ecmwf.int/data/reanalysis.html>]
- Gupta, S. K., C. H. Whitlock, N. A. Ritchey, A. C. Wilber, W. L. Darnell, and W. F. Staylor (1997), A climatology of surface radiation budget derived from satellite data, *Current Problems in Atmospheric Radiation*, W. L. Smith and K. Stamnes, Eds., A. Deepak, 1067 pp.
- Kalnay, E., and Coauthors (1996), The NCEP/NCAR 40-Year Reanalysis Project, *Bull. Amer. Meteor. Soc.*, 77, 437–471.
- Large, W. G., and A. J. G. Nurser, (2001), Ocean surface water mass transformation, in: *Ocean Circulation and Climate*, edited by G. Siedler, J. Church, and J. Gould, pp317-336, Academic, San Diego, Calif.
- Li, Z. (1995), Intercomparison between two satellite-based products of net surface shortwave radiation, *J. Geophys. Res.*, 100, 3221–3232.
- Lukas, R., (1989), Observations of air-sea interaction in the western Pacific warm pool during WEPOCS, paper presented at the Western Pacific International Meeting and Workshop for TOGA COARE, Inst.fr. de Rech. Sci. pour le Dev. En Coop. (ORSTOM), Noumea, New Caledonia.
- Ohmura, A., and H. Gilgen (1991), Global energy balance archive GEBA. Rep. 2: The GEBA database: Interactive applications retrieving data (Heft 44), Geographisches Institut, ETH Zurich, 66 pp. [Available from Prof. A. Ohmura, Geographisches Institut, ETH, Winterthurerstr. 190, CH-8057, Zurich, Switzerland.]
- Pinker, R. T., and I. Laszlo (1992), Modeling surface solar irradiance for satellite applications on a global scale, *J. Appl. Meteor.*, 31, 194-211.
- Rossow, W. B., and Y.-C. Zhang (1995), Calculation of surface and top of atmosphere radiative fluxes from physical quantities based on ISCCP datasets. Part II: Validation and first results, *J. Geophys. Res.*, 100 (D1), 1167–1197.

- Schmetz, J., and Q. Liu (1988), Outgoing longwave radiation and its diurnal variation at regional scales derived from Meteosat, *J. Geophys. Res.*, 93, pp. 11, 192-204.
- Schubert, S. D., J. Pfaendtner, and R. Rood (1993), An assimilated dataset for earth science applications, *Bull. Amer. Meteor. Soc.*, 74, 2331–2342.
- Sengupta, D., B. N. Goswami and Retish Senan (2001), Coherent Intraseasonal Oscillations of Ocean and Atmosphere during the Asian Summer Monsoon, *Geophys. Res. Lett.*, 28, 4127-4130.
- Shahi, N. R., N. Agarwal, R. Sharma, P. K. Thapliyal, P. C. Joshi and A. Sarkar (2010), Improved Estimation of Shortwave Radiation over equatorial Indian Ocean using Geostationary Satellite Data, *IEEE GeoSci. Remote Sens. Letts.*, 7, 563-566.
- Shahi, N. R., P. K. Thapliyal, R. Sharma, P. K. Pal, and A. Sarkar (2011), Estimation of net surface shortwave radiation over the tropical Indian Ocean using geostationary satellite observations: Algorithm and validation, *J. Geophys. Res.*, 116, C09031, doi:10.1029/2011JC007105.
- Shinoda, T., H. H. Hendon, and J. Glick (1998), Intraseasonal variability of surface fluxes and sea surface temperature in the tropical western Pacific and Indian Oceans, *J. Climate*, 11, 1685-1702.
- Singh, R., P. K. Thapliyal, C. M. Kishtawal, P. K. Pal, and P. C. Joshi (2007), A new technique for estimating outgoing longwave radiation using infrared window and water vapor radiances from Kalpana very high resolution radiometer, *Geophys. Res. Lett.*, 34, L23815, doi:10.1029/2007GL031715.
- Whitlock, C. H., and Coauthors (1995), First global WCRP shortwave surface radiation budget dataset, *Bull. Amer. Meteor. Soc.*, 76, 905–922.

## **7. Clear Sky Brightness Temperature from INSAT-3D/3DR IMAGER**

S. No.	Product Name	Spatial Resolution	Temporal Resolution
1	IMG_CSBT	0.5° x 0.5° Grids	30 minutes

## 7.1. Algorithm Configuration Information

### 7.1.1. Algorithm Name

Clear Sky Brightness Temperature from INSAT-3D/3DR Imager

### 7.1.2. Algorithm Identifier

ISRO\_INSAT\_IMG\_CSBT

### 7.1.3. Algorithm Specification

Version	Date	Prepared by	Description
1.0	01.03.2018	M. V. Shukla, P. K. Thapliyal, and C. M. Kishtawal	CSBT product is useful for radiance assimilation in NWP model

## 7.2. Background

Numerical Weather Prediction (NWP) models have become an indispensable tool for providing weather forecast. These models are immensely benefited from various in-situ and satellite observations. These observations are used for correcting model forecast trajectories, model output validation and model parameter tuning. Ingestion of various observations has now become a state-of-art and also rapidly growing to meet the challenges posed by huge amount of available observations. With the advancement and maturing of data assimilation (DA) techniques direct satellite observed radiance (or brightness temperatures) are operationally assimilated by various operational agencies. Assimilation of satellite observed radiances can be primarily subdivided into two classes: assimilation of clear sky brightness temperature and assimilation of all sky (clear and cloudy both) observation. Though, cloudy regions probably have a large impact on the accuracy of the NWP model predictions ([McNally 2002](#); [Kumar et al. 2014](#)), but the direct assimilation of cloudy radiances is still beyond the scope of existing global NWP systems ([Pavelin et al. 2008](#)). This is due to the fact, that assimilation of cloudy radiances requires an observation operator having realistic representation of cloud effects, and a NWP model capable of accurately representing cloud at same scales ([Chevallier et al. 2004](#)). Such kind of capabilities of existing NWP model is in development phase and fast radiative transfer (RT) model have large uncertainties over cloudy regions, and have complex nonlinearity in assimilation when clouds exist ([Bauer et al. 2011](#)). Therefore, cloudy infrared (IR) radiance is still part of ongoing research and development activities and is not the part of operational assimilation system. Nevertheless, the method of assimilation of clear sky brightness temperature (satellite observation which are not affected by the presence of clouds) has already reached to matured stage, therefore, used operationally in providing weather forecast. Thus clear sky brightness temperature (CSBT) is a very important parameter from the NWP data assimilation applications. clear sky radiance assimilation has become the indispensable part of assimilation system. For clear sky radiance assimilation, it is essential to eliminate the cloudy pixels in order to retain only clear-sky radiances only. Usually a binary mask (clear/cloudy)

is prepared from satellite data ([Zupanski et al. 2007](#); [Razagui et al. 2011](#)). [Pangaud et al. \(2009\)](#) and [Eresmaa \(2014\)](#) found that if cloudy radiances are assimilated as clear radiances, the quality of the NWP analysis/prediction impacted negatively.

### 7.3. Objective

The main objective of this document is to provide the theoretical basis for calculating clear sky brightness temperature (CSBT) for INSAT-3D/3DR TIR-1 and water vapor channels. The proposed algorithm will be applied to estimate CSBT over  $0.5^{\circ}\times 0.5^{\circ}$  field of regard (FOR) along with statistical parameters and a confidence flag that will help in using CSBT value in DA process. CSBT product is calculated for only clear pixels identified by INSAT-3D/3DR imager cloud mask (CMK) product. The algorithm has no limitation based on geographical location, therefore, can be applied to generate products over full disk or sector products. Nevertheless, the CSBT product is generated from only full disk product.

### 7.4. Inputs

#### 7.4.1. Image and preprocessing data (dynamic)

Parameter	Resolution	Quantization	Accuracy	Source
Radiometric and geometric corrected gray count values of split window IR channel (10.5-11.5 $\mu\text{m}$ and 11.5-12.5 $\mu\text{m}$ ) and WV channel (6.7 $\mu\text{m}$ ) All the data is required in fixed lat-lon grid.	pixel	10 bit	--	Derived from raw data by DP (data processing)
Gray value to brightness temperature conversion table	-	-	0.3 K	Derived by DP
Cloud Mask	pixel			Operational L2 product
Geo-location file	Pixel	-	4 Km	Derived by DP

### 7.5. Algorithm Functional Specifications

#### 7.5.1. Overview

The clear sky brightness temperature (CSBT) from INSAT-3D/3DR imager is intended to be generated at  $0.5^{\circ}\times 0.5^{\circ}$  field of regard (FOR). CSBT product is generated at much coarser resolution than the actual resolution of INSAT-3D/3DR imager observations which are available at nominal resolution of  $\sim 4$  km at nadir for TIR-1, TIR-2, MIR and  $\sim 8$  km for water vapor. The gridding (averaging) over all pixels within  $0.5^{\circ}\times 0.5^{\circ}$  FOR. This averaging is done to enhance the signal to

noise ratio and to make observation less correlated. Data assimilation warrants very accurate, and uncorrelated observations. CSBT product is aimed towards providing observations.

### **7.5.2. Generation of CSBT**

As it is evident from the name of parameter, CSBT is generated for clear sky pixels. Since this product is mainly used in NWP data assimilation, it is re-gridded at coarser resolution of  $0.5^{\circ}\times 0.5^{\circ}$  grid. This helps in reducing noise in value in BT as well as creating uncorrelated observations. Generation of CSBT involves following steps:

### **7.5.3. Preparation of latitude-longitude grid**

INSAT-3D and INSAT-3DR are orbiting in geostationary orbit and are located at  $83.0^{\circ}\text{E}$  and  $74^{\circ}\text{E}$ , respectively. Therefore, the geographical extent of observed area by both the satellites is different particularly in east-west direction. As both the satellites are in geostationary orbit, thus in principle, the viewing location of each pixel does not vary for different acquisitions. Based on the fixed grid of INSAT-3D and INSAT-3DR, a latitude-longitude equal grid is selected and all further processing is done the same grid.

For INSAT-3D grid information is as follows:

Min Latitude = -81.0;    grid size= $0.5^{\circ}$  ;    grid points in north-south direction=325  
Min Longitude = 1.0;    grid size= $0.5^{\circ}$  ;    grid points in east-west direction=325

For INSAT-3D grid information is as follows:

Min Latitude = -81.0;    grid size= $0.5^{\circ}$  ;    grid points in north-south direction=325  
Min Longitude = -3.0;    grid size= $0.5^{\circ}$  ;    grid points in east-west direction=325

### **7.5.4. Averaging of parameters**

A simple box average method is adopted to generate parameters. CSBT, satellite zenith angle and solar zenith angle and land fraction (for a given grid) are generated. In data assimilation, satellite and solar zenith angles and land fraction are required along with CSBT. As already stated that CSBT is calculated for clear pixels only, therefore, for averaging operational cloud mask product is also used. INSAT-3D/3DR operational cloud mask product provides a flag which has one of the four values 0,1,2 and 3. 0 indicates clear pixel, 1 indicates cloudy pixel, 3 is representative of probably clear pixel and 2 indicates probably cloudy pixel. While calculating average of aforementioned parameters, the total of pixels (N), clear pixels (N1) and probably clear pixels (N2) within a given grid are also counted. These counts (N, N1 and N2) determine whether CSBT product will be computed for a given grid or not. A dynamic threshold which is 10% of total count value N is taken. If total number of clear and probable clear pixels (N1+N2) is less than the threshold value and CSBT and other products are not generated, but if this is greater than the threshold value then it is checked if N1 is also greater than threshold or not. However, in both the cases CSBT and other parameters are computed but if N1 is less than the threshold then quality flag of CSBT is termed as not very good quality.

In addition to the average of parameters, standard deviation of BT for a given box is also computed. This standard deviation is also provided along with CSBT values to help in deciding the spread of BT value for a given box. More standard deviation may help in flagging out some of the CSBT value as it may have some contamination of cloud (or cloud edges)

### **7.5.5. Quality indicators**

As it is already discussed in previous section that a flag and standard deviation values are generated along with CSBT product to provide user an indication of quality of CSBT value. The major confidence in quality is determined by the number of clear pixels with a grid box, if more than 50% of grid is covered by clear pixels then that box is given the highest confidence flag 0, but if this number is between 25 to 50% the flag=1 and if it between 10 to 25% then flag=2.

These various flags are given to user to give them a flexibility in optimizing the number of data points in assimilation and the quality of data set.

## **7.6 Outputs**

### **7.6.1 Format of the output and the domain**

Parameter	Unit	Min	Max	Accuracy	Resolution	Format
Clear Sky brightness temperature	K	180.0	340.0	1-2K	0.5° x 0.5°	HDF5

## **7.7. Validation**

### **7.7.1. Data required**

Clear-sky brightness temperature (CSBT) from INSAT-3D/3DR imager will be carried out by using various analysis such as NCMRWF analysis, GFS analysis and various reanalysis such as ERA interim reanalysis. These various analysis and reanalysis will be used to generate brightness temperatures using RTTOV or CRTM radiative transfer models. The validation cannot be carried out for each half-hourly product but validation will be carried out for only synoptic hours.

For validation at specific time period special launch campaign is needed wherein various radiosondes are launched and these soundings could be used in conjunction with radiative transfer model for CSBT validation.

*Table 5*

Sensors	Parameters	Time scale	Data set taken	Source
INSAT-3D/3DR Imager	CSBT	On synoptic hours	Various analysis and reanalysis products	Data is freely available from various websites
INSAT-3D/3DR Imager	CSBT	Depends on RAOB launch	Soundings from specifically launched RAOBs	Special field campaign is needed

## References

- Bauer P, Auligne T, Bell W, Geer A, Guidard V, Heilliette S, Kazumori M, Kim MJ, Liu EHC, McNally AP, Macpherson B, Okamoto K, Renshaw R, Riishøjgaard LP. 2011. Satellite cloud and precipitation assimilation at operational NWP centres. *Q. J. R. Meteorol. Soc.* **137**: 1934–1951.
- Eresmaa R. 2014. Imager-assisted cloud detection for assimilation of Infrared Atmospheric Sounding Interferometer radiances. *Q. J. R. Meteorol. Soc.* **140**: 2342–2352.
- Chevallier F, Lopez P, Tompkins AM, Janiskova M, Moreau E. 2004. The capability of 4D-var systems to assimilate cloud affected satellite infrared radiances. *Q. J. R. Meteorol. Soc.* **130**: 917–931.
- Kumar P, Kishtawal CM, Pal PK. 2014. Impact of satellite rainfall assimilation on Weather Research and Forecasting model predictions over the Indian region. *J. Geophys. Res. Atmos.* **119**(5): 2017-2031.
- Mcnally AP. 2002. A note on the occurrence of cloud in meteorologically sensitive areas and the implications for advanced infrared sounders. *Q. J. R. Meteorol. Soc.* **128**: 2551–2556.
- Pavelin EG, English SJ, Eyre JR. 2008. The assimilation of cloud-affected infrared satellite radiances for numerical weather prediction. *Q. J. R. Meteorol. Soc.* **134**(632): 737-749.
- Pangaud T, Fourrie N, Guidard V. et al. 2009. Assimilation of AIRS radiances affected by mid- to low-level clouds. *Mon. Wea. Rev.* **137**: 4276–4292.
- Razagui A, Bouchouicha K, Bachari NEI. 2011. Cloud type identification algorithm to simulate MSG infrared radiance using the Radiative Transfer Model RTTOV and ALADIN forecasting output. *Revue des Energies Renouvelables* **14**(4): 601-612.
- Zupanski D, Hou AY, Zhang SQ, Zupanski M, Kummerow CD, Cheung SH. 2007. Application of Information Theory in Ensemble Data Assimilation. *Q. J. R. Meteorol. Soc.* **133**: 1533 - 1545.

## **8. Clear-Sky Brightness Temperature Products from INSAT-3D/3DR Sounder**

S. No.	Product Name	Spatial Resolution	Temporal Resolution
1	SND_CSBT	3 x 3 Sounder Pixels (~30 km x 30 km)	1 hour

## **8.1. Algorithm configuration information**

### **8.1.1 Algorithm name**

Clear-Sky Brightness Temperature from INSAT-3D/3DR Sounder

### **8.1.2. Algorithm Identifier**

INSAT\_SND\_CSBT

### **8.1.3. Algorithm Specification**

<b>Version</b>	<b>Date</b>	<b>Prepared by</b>	<b>Description</b>
1.0	08.08.2018	M. V. Shukla, P. K. Thapliyal, and C. M. Kishtawal	Clear sky brightness temperature products from INSAT-3D/3DR Sounder for use in radiance assimilation in NWP model

## **8.2. Introduction**

The aim of Clear-sky brightness temperature (CSBT) product is provide area average brightness temperatures (Tb) for representing cloud free pixels. These products have been recently developed by Space Applications Centre under INSAT Meteorological Data Processing System (IMDPS) project to be used in radiance assimilation in the numerical weather prediction (NWP) models. The high-temporal resolution data of INSAT-3D Sounder (hourly observations) would be extremely useful for monitoring and predicting of the fast developing weather systems through 4D-VAR radiance assimilation in NP models.

## **8.3. Algorithm Description**

The following sections provide details of the procedure for generating CSBT products:

### **8.3.1. Cloud detection**

The first step in CSBT product generation is to filter out cloud contaminated pixels from the Sounder observations and generate a cloud-flag for each of the pixels. This section provides the physical basis for detection of the cloudy pixels from INSAT-3D Sounder observations. The output of cloud mask algorithm gives the degree of presence of a cloud in it. This information enables the subsequent steps to use this information for further processing.

The cloud detection algorithm is carried out in three steps. The flow chart is shown in fig.1.

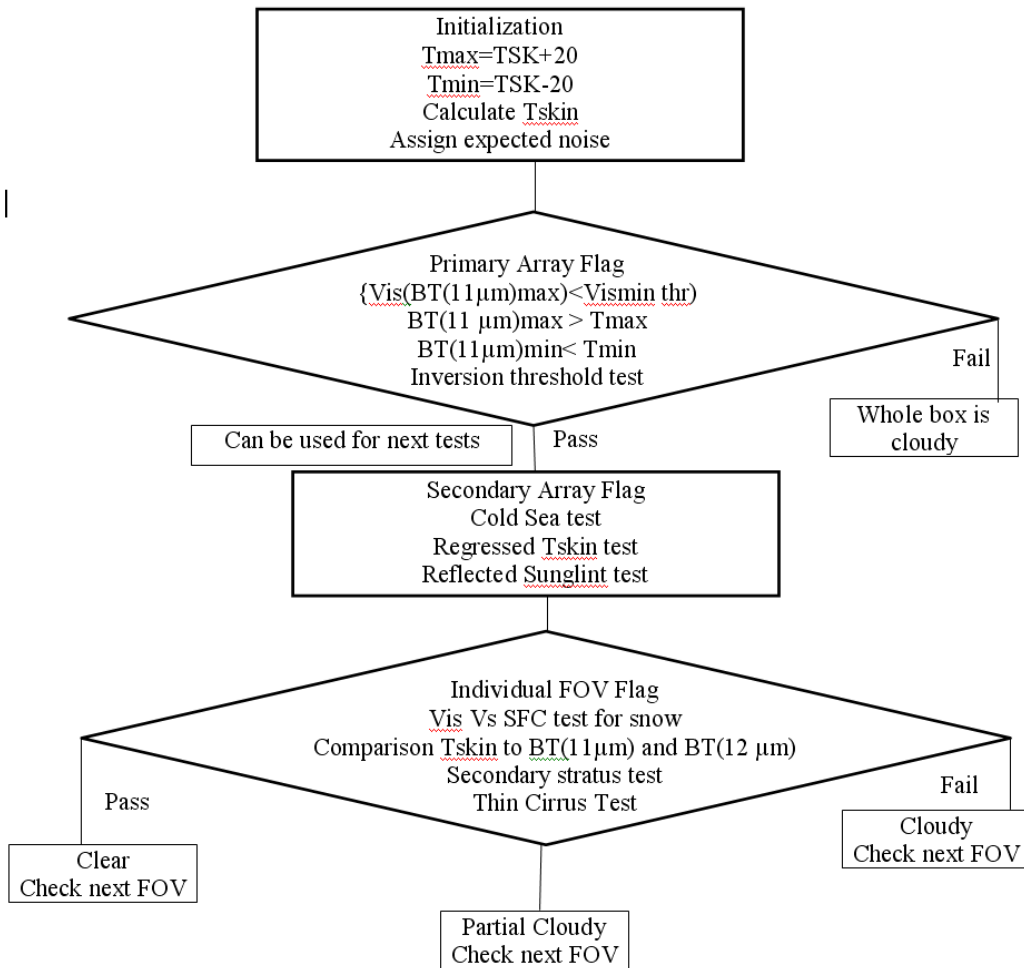


Fig.1: Flow chart of the Sounder cloud detection algorithm

The cloud detection methodology for INSAT-3D sounder follows operational GOES sounder cloud detection procedure developed by Schreiner et al. (2001). This cloud detection algorithm uses 4 infrared channels and a visible channel during daytime for cloud detection and 5 infrared channels for the detection of nighttime clouds. One additional infrared channel is used to detect clouds appearing at dawn time. The various channels used in cloud detection are summarized below:

Ch#3 - 13.3  $\mu\text{m}$  (“CO<sub>2</sub> absorption”, used for detection of thin cirrus)

Ch#6 - 12.6  $\mu\text{m}$  (“Moderate WV-absorption”, used in detecting some low level inversions)

Ch#7 - 12.0  $\mu\text{m}$  (“Weak WV-absorption”, used in detecting low clouds and fog)

Ch#8 - 11.0  $\mu\text{m}$  (“Longwave Window”, used in detecting various level of clouds)

Ch#17 - 4.0  $\mu\text{m}$  (“Shortwave Window”, used to detect low clouds and fog at night)

Ch#18 - 3.8  $\mu\text{m}$  (“Shortwave Window”, used to detect low clouds after sunrise)

Ch#19 - 0.6  $\mu\text{m}$  (“Visible” band used in detecting various level of clouds during daylight)

A series of tests are applied using these channels to detect stratus, cirrus (thin and opaque), fog, snow and inversion. Here for cloud detection algorithm a 3x3 pixel field-of-regard (FOR) is used. The FOR is moved by 1 pixel sequentially in E-W and N-S (along and across the scan-line) to maximize the clear FOR detection. Two types of cloud flags are generated one each for the FOV (single pixel) and FOR (3 x 3 pixel box). In present algorithm the output contains three types of cloud-flags that are given by:

- 0: Clear
- 1: Cloudy
- 2: Partially cloudy

The cloud detection procedure is carried out in three steps to filters out cloudy pixels very accurately and efficiently:

**(a). The first step** is a very gross check and is applied on a FOR of 3x3 pixel box. If it fails in the first check then the whole FOR is declared as cloudy and it moves to the next FOR. In case of passing the first step a series of tests are applied on the FOR in second step. In third and final step, a series of tests are applied on each FOV and the results of these tests decide the final outcome.

**(b). Primary Array Flag (PAF):** This is first step of cloud detection to generate the primary array flag. Four tests are applied on a FOR to generate PAF. Generation of PAF requires computation of two thresholds  $T_{max}$  and  $T_{min}$  from ancillary information.  $T_{max}$  and  $T_{min}$  are computed using surface skin temperature information which is available either through AWS or from model forecast. Here model forecast is used for surface skin temperature.

$$T_{max} = T_S + 20, \text{ and } T_{min} = T_S - 20$$

Where,  $T_S$  is the surface skin temperature. After this calculation the following checks are applied:

- 1) Visible reflectance of the warmest pixel in FOR computed from Ch#8 (11 $\mu\text{m}$ ) must be less than a certain threshold value. The value of threshold for visible channel over land is 25% and over water is 7%. The value of threshold may vary for low surface temperature and low sun angles. If the surface skin temperature is less than 273K the threshold value over land is increased by a factor of 1.5. Similarly, to take care of low sun angles the land limit is multiplied by solar zenith angle. This test is possible only for day time.
- 2) The Ch#8  $T_b$  (11 $\mu\text{m}$ ) of warmest pixel must be less than  $T_{max}$  and must be greater than  $T_{min}$ .
- 3) Inversion test is applied on the difference of maximum Ch#8  $T_b$  (11 $\mu\text{m}$ ) and maximum Ch#18  $T_b$  (3.8  $\mu\text{m}$ ) within FOR. This test is applicable only during night time. For this test a threshold ( $Th_I$ ) is calculated using an empirical relation using the NEAT value of Ch#8 and Ch#18. Difference between the warmest pixel of Ch#18 and the warmest pixel of Ch#8 must be greater than the  $Th_I$  for a pixel to be clear.

If any of these tests fail, then the whole box is assumed to be cloudy and not processed further, otherwise it will proceed for secondary array flag (SAF) procedure.

**(c). Secondary Array Flag (SAF):** The first step of SAF is to compute skin temperature empirically using three channels, Ch#8 ( $T_{b8}$ ), Ch#7 ( $T_{b7}$ ) and Ch#18 ( $T_{b18}$ ) and two channels Ch#8 (11 $\mu$ m) and Ch#7 (12 $\mu$ m). These empirical relations for skin temperature are as follows:

$$T_{S3} = a0 + a1 * T_{b8} + a2 * T_{b7} + a3 * T_{b18} \quad (\text{using 3 channels})$$

$$T_{S2} = b0 + b1 * T_{b8} + a2 * T_{b7} \quad (\text{using 2 channels})$$

These coefficients are pre-determined from a large simulated matchup dataset. The standard tests for SAF are following:

- The difference between  $T_{S3}$  and  $T_{S2}$  must not be greater than 2K.
- The “cold sea test” only over ocean and this test fail if the highest  $T_{b8}$  in FOR FOV is less than 270K.
- The “reflected sunglint test” checks the difference between brightness temperatures for the highest  $T_{b8}$  and  $T_{b18}$ . The difference must be less than 10K.

If any of these SAF test is fail then the whole FOR is assigned as cloudy. Otherwise clear flag is assigned to whole FOR. SAF is followed by final and Individual FOV Flag (IFF). In IFF series of tests are applied to individual FOV of a given box.

#### **(d). Individual FOV Flag (IFF):**

**Snow test:** This test is daytime test and discriminates between snow and cloud. If visible reflectance of FOV is greater than the minimum reflectance (already defined in PAF) and skin temperature is greater than a threshold (275K) then FOV is cloudy otherwise clear. Threshold in this case can be adjusted to any value in the range of 273 to 285 K.

**Secondary stratus test:** In this test difference of moisture corrected  $T_{b7}$  and  $T_{b8}$  is compared with a threshold. The threshold depends on  $T_{b7}$  and difference of skin temperature ( $T_s$ ) and surface air temperature ( $T_a$ ), both from forecast.

$Th_2 = \max[\Delta T(Ch7), 0.25 * (T_a - T_s)]$ , here  $T_s$  is calculated using 2 or 3 channels depending on daytime and nighttime situation.

$$\Delta TPW = \max(T_{b8}) - \max(T_{b7}), \quad \text{in } 3 \times 3 \text{ pixel FOR}$$

$$T_{b7}(\text{corrected}) = T_{b7} + \Delta TPW$$

**Cirrus test:** If the  $T_{b5}$  of FOV under consideration is less than the value of noise corrected  $T_{b5}$  value corresponding to FOV having maximum  $T_{b8}$  in the given FOR, then the test is said to be failed.

$$T_{b5}(\text{Noise corrected}) = \{T_{b5} \text{ corresponding to } \max(T_{b8})\} - 7.0 * \Delta T(Ch5)$$

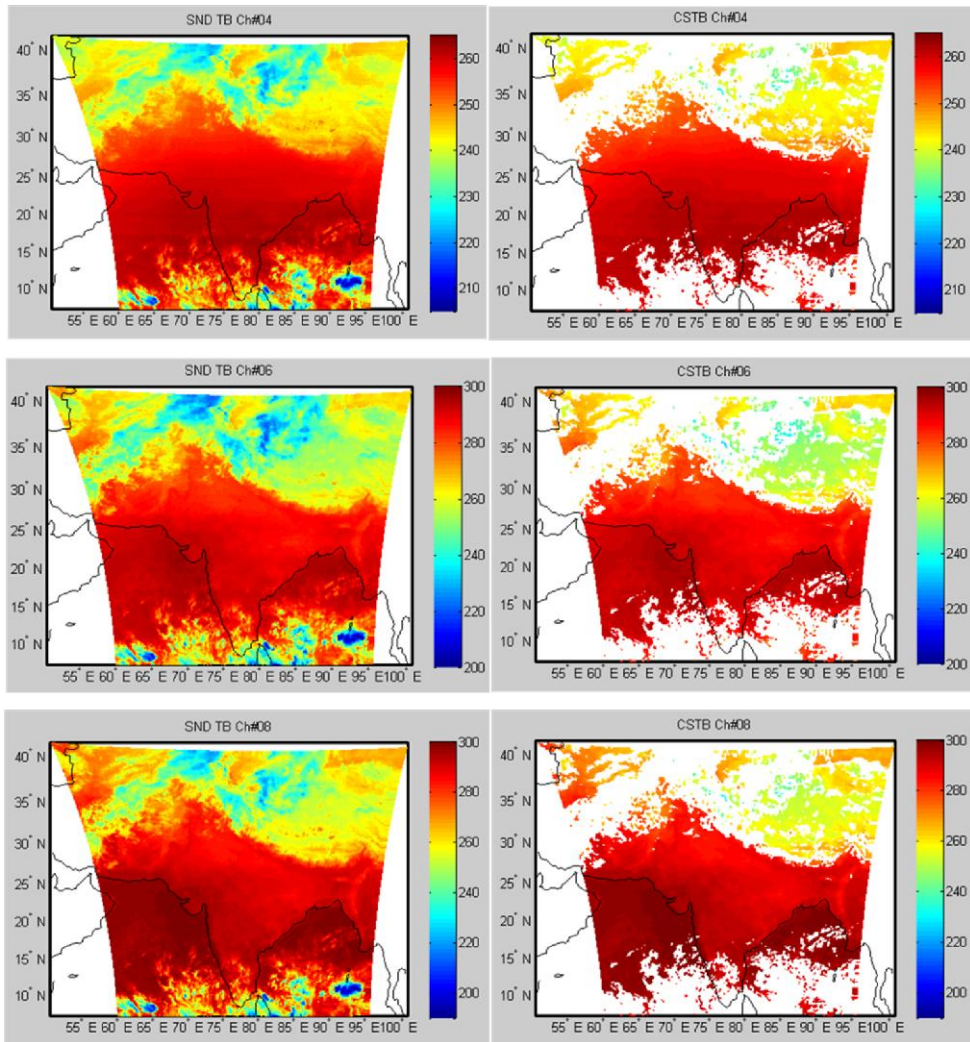
#### **Final skin temperature test:**

$$[T_{b8} + \{T_{b8} - T_{b7}\}_{\max(T_{b7})}] < T_s, \text{ then test is assumed to be fail.}$$

If one FOV passes all the tests then that FOV is upgraded to clear. If FOV fails any of the tests then it is flagged as cloudy or partially cloudy depending on the SAF flag.

### 8.3.2. Clear-Sky Brightness Temperature computation

The CSBT product at for pixel is computed as average of the clear-sky pixel brightness temperatures in the 3x3 FOR centered at the pixel location, if at least 3 clear pixels are found in the FOR. The averaging reduces the impact due to the uncertainty in cloud-detection algorithm as well as reduces the random noise of measurements ( $\Delta T$ ) over individual pixels. The land/sea flag as well as the clear fraction in the FOR is also computed. Fig.1 shows a sample of the INSAT-3D sounder brightness temperatures and corresponding CSBT of each of the channels for 24 November 2014 14:00 GMT.



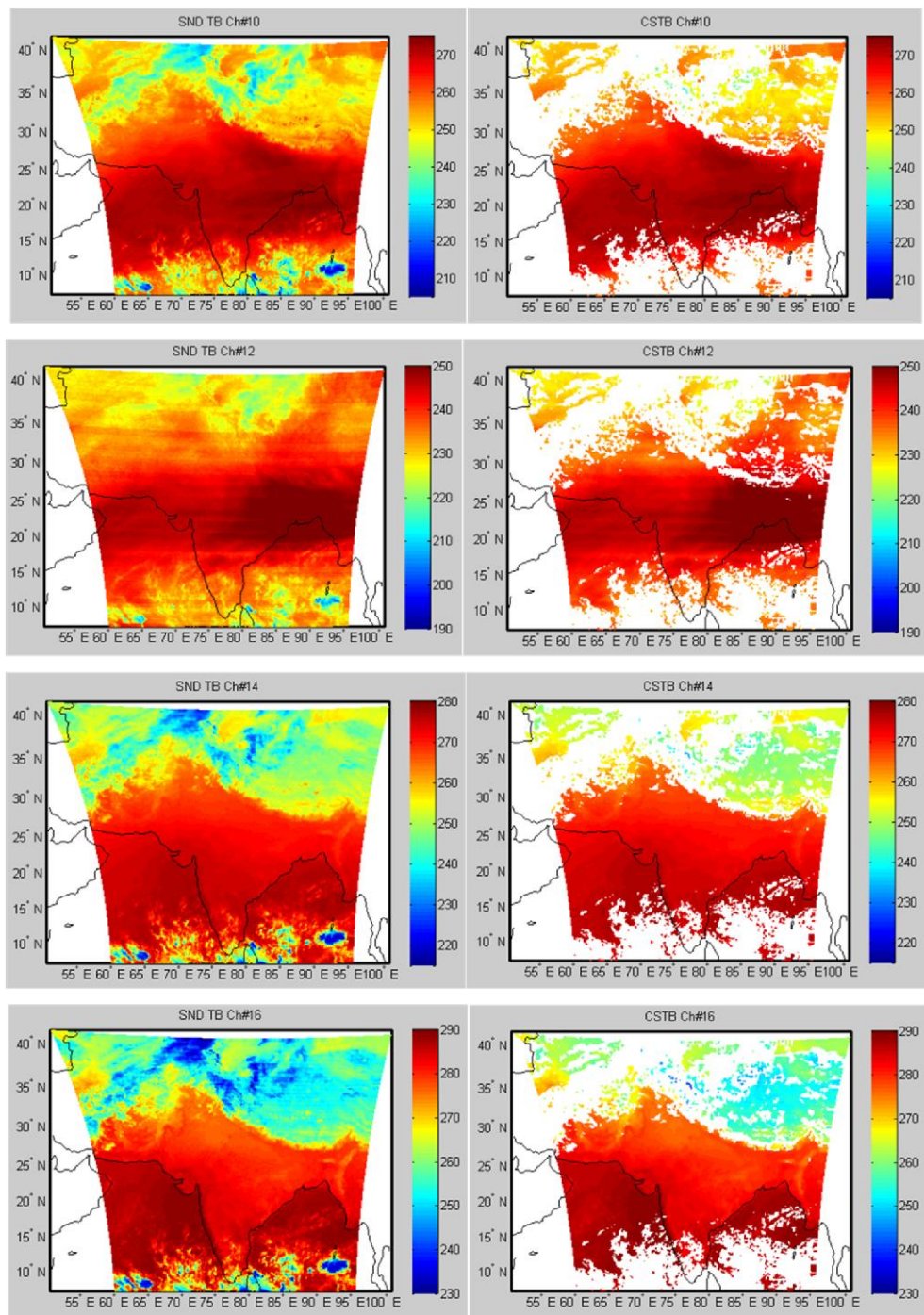


*Fig.1: INSAT-3D Sounder brightness temperatures (left panel) and corresponding Clear-Sky brightness temperatures (right panel) for Ch#4, 6, 8, 10, 12, 14, 16 (24-NOV-2014 14:00Z)*

## 8.4. Outputs

Parameter	Range	Accuracy	Resolution	Format
-----------	-------	----------	------------	--------

Clear-Sky Brightness Temperature	180-340 K	1-2K	<b>Spatial:</b> 3 x 3 sounder pixel (0.3° x 0.3°) <b>Temporal:</b> Hourly products	HDF5
----------------------------------	-----------	------	--	------

## 8.5. Validation

Clear-sky brightness temperature (CSBT) from INSAT-3D/3DR Sounder will be carried out using various analyses, such as NCMRWF, GFS, ECMWF analysis etc. These analyses will be used to generate brightness temperatures using PFAAST/RTTOV/CRTM radiative transfer models. The validation cannot be carried out for each half-hourly product but validation will be carried out for only synoptic hours.

For validation at specific time-period special launch campaign will be carried out where high quality radiosondes are launched and these soundings would be used with radiative transfer model for CSBT validation.

Apart from this inter-satellite comparison will be carried out using CSBT products from hyperspectral sounder observation collocated with INSAT-3D/3DR Sounder and convolving with the SRFs.

## References:

Schreiner et al., (2001): J. Geophy. Res., vol 16 (D17), pp 20249-20363.

## **9. Cloud Top Pressure/Cloud Top Temperature and effective cloud amount from INSAT-3D/3DR IMAGER**

S. No.	Product Name	Spatial Resolution	Temporal Resolution
1	IMG_CTP	9 x 9 TIR pixels (~36 km x 36 km)	30 minutes

## **9.1. Algorithm Configuration Information**

### **9.1.1. Algorithm Name**

Cloud Top Pressure/Cloud Top Temperature and effective cloud amount from INSAT-3D/3DR IMAGER

### **9.1.2. Algorithm Identifier**

ISRO\_INSAT\_IMG\_CTP

### **9.1.3. Algorithm Specification**

Version	Date	Prepared by	Description
1.0	01.01.2015	M. V. Shukla, and P. K. Thapliyal	Cloud properties are useful for weather prediction applications

## **9.2. Background**

The purpose of this document is to present an algorithm for retrieving Cloud properties such as cloud top temperature, cloud top pressure and effective cloud amount from two INSAT-3D thermal infrared window channels ( $10.5\text{-}11.5\text{ }\mu\text{m}$ , and  $11.5\text{-}12.5\text{ }\mu\text{m}$ ) and water vapor ( $6.7\text{ }\mu\text{m}$ ) channels. This document also describes the validation procedure. In this document some background and the methodology employed to derive the cloud top temperature/pressure and effective cloud amount is discussed. It mainly discusses the theoretical basis and practical aspects of the retrieval algorithm for cloud parameters from INSAT-3D imager channels and outlines the intended validation approach with validation results.

The cloud properties such as cloud cover, cloud height etc. are very important for various climate and weather applications. The clouds at different heights affects weather and climate phenomenon in different ways. It is very difficult to imagine variety of weather phenomenon without clouds. Clouds do not only add beauty and variability in atmosphere but also cause the wide variety of atmospheric activities. Clouds vary in its appearance, extent, composition and physical properties, therefore, different clouds affect weather and climate differently. For example, rapidly growing cumulus clouds are precursor to sever thunderstorm, low water clouds with strong temperature inversion results in fog. Thin cirrus clouds do not play a critical role in short to medium range weather activities, but they play a very crucial role in earth's heat budget and also helps in tracking upper level winds. Thin cirrus clouds are thin enough to allow incoming solar radiation to pass through it but doesn't allow outgoing infrared radiation, thus increases the radiative energy and eventually leads to the warming of earth-atmosphere system.

Cirrus clouds are crucially important to global radiative processes and the heat balance of the Earth; they allow solar heating while reducing infrared radiation to space. Models of climate changes will

have to correctly simulate these clouds to have the proper radiative terms for the Earth's heat budget. Past estimates of the variation of cloud cover and the Earth's outgoing longwave radiation have been derived primarily from the longwave infrared window (10-12  $\mu\text{m}$ ) radiances observed from polar orbiting and geostationary satellites (Rossow and Lacis, 1990; Gruber and Chen, 1988). The occurrence of semi-transparent clouds is often underestimated in these single channel approaches. Recently, multispectral techniques have been used to better detect cirrus in global (Wylie et al., 2005; Wu and Susskind, 1990) and North American (Wylie and Menzel, 1989) cloud studies.

Additionally, clouds are very important to study weather phenomena at various spatial and temporal scales including its diurnal cycle. Diurnal cycle of various physical processes such as radiative exchange, precipitation, small and large-scale dynamics are of great importance and are greatly linked with clouds, therefore, underlines the study of diurnal cycles of clouds too. Ackerman and Cox (1981) had reported the diurnal oscillation of cloudiness in some tropical areas. These diurnal oscillations are part of dynamic-radiative feedback mechanism that operates on various spatial scales. (Foltz and Gray, 1979)

### 9.3. Objective

The main objective of this document is to provide the theoretical basis for deriving cloud top pressure/ cloud top temperature and effective cloud amount from INSAT-3D/3DR imager channels. The proposed algorithm will be applied to retrieve cloud properties from imager channels over each pixel defined as confidently cloudy from CMK product. The algorithm has no limitation based on geographical location, therefore, can be applied to generate products over full disk or sector products.

### 9.4. Inputs

#### 9.4.1. Static Data

Parameter	Resolution	Accuracy	Source
Land/sea flag	~2 km x 2 km	--	Global topographic datasets (Available)
Surface Elevation	Each Pixel 10 km x 10 km	--	Global topographic datasets (Available)
Monthly mean spectral surface Emissivity	Each Pixel 10 km x 10 km	--	Univ. of Wisconsin (Available)
<b><i>Global training dataset for ozone profile (Ozonesonde)</i></b>	<b><i>Surface to 0.01 hPa levels</i></b>	--	<b><i>Univ. of Wisconsin/ IMD (Available)</i></b>

#### 9.4.2. Image and pre-processing data (dynamic)

Parameter	Resolution	Quantization	Accuracy	Source
Radiometric and geometric corrected gray count values of split window IR channel (10.5-11.5 $\mu\text{m}$ and 11.5-12.5 $\mu\text{m}$ ) and WV channel (6.7 $\mu\text{m}$ )  All the data is required in fixed lat-lon grid.	pixel	10 bit	--	Derived from raw data by DP (data processing)
Gray value to brightness temperature conversion table	-	-	0.3 K	Derived by DP
Cloud Mask	pixel			Operational L2 product
Geo-location file	Pixel	-	4 Km	Derived by DP

#### 9.4.3. Other Auxiliary data and Model Inputs

Parameter	Resolution	Accuracy	Source
Numerical model forecast of humidity for all levels	0.5 degree	<30%	NCEP GFS
All levels model forecast Temperature		1° K	

### 9.5. Algorithm Functional Specifications

#### 9.5.1. Overview

The cloud top pressure/temperature and cloud effective emissivity from INSAT-3D/3DR imager is intended to be retrieved at ~50 km nominal resolution. The cloud products are retrieved at coarser resolution than to resolution of actual INSAT-3D/3DR imager observations which are available at nominal resolution of ~4 km at nadir. The averaging over a Field of Regard (FOR) of 9x9 pixels is used to enhance the signal to noise ratio over cloudy pixels. In general, noise over cloudy pixels is higher in comparison to clear pixels, therefore, it becomes essential to take average of observed radiances/brightness temperatures to reduce the noise for accurate estimation of cloud properties.

For each 9x9 pixel box cloud top pressure, cloud top temperature and effective cloud amount is retrieved using Infrared window channel method or water vapor - window intercept method.

Generally, window method does not give accurate retrievals over semi-transparent thin high clouds, therefore, water vapor - window intercept method is used over those FOR.

### 9.5.2. Infrared Window Channel (WIN) method

In this method the height assignment using a single satellite channel is made by comparing either infrared window or water vapor brightness temperature (BT) values with NWP model forecast temperature profiles. However, for INSAT-3D/3DR Imager at present only Infrared window observations are used in this method. Cloud heights are determined by interpolating the cloud temperature, which is an average of coldest 20% of pixels, to the interpolated model guess field at the target location. A 6-h NWP model forecast from National Center for Environmental Prediction (NCEP) Global Forecast System (GFS) is the source of temperature profile. This method works well with opaque clouds.

### 9.5.3. Water Vapor–Infrared Window Intercept Method ( $H_2O$ )

Cloud top pressure derived with this method are based on the fact that radiances from two different spectral bands are linearly related for different cloud amounts within the field of regard at a specified height. Observed radiance measurements are a function of clear sky and opaque cloud radiances.

$$R(N) = (1 - nE)R_{cl}(N) + nER_{bcd}(N, P_c) \quad (1)$$

Opaque cloud radiance can be calculated from:

$$R_{bcd}(N, P_c) = R_{cl}(N) - \int_{P_c}^{P_s} t(N, p) \frac{db[N, T(p)]}{dp} dp \quad (2)$$

Where,  $R_{bcd}$  is the opaque ("black") cloud radiance,  $R_{cl}$  is the clear sky radiance,  $t(N, p)$  is the fractional transmittance for radiation in spectral band  $N$  emitted from the atmospheric layer at pressure  $p$  arriving at the top of the atmosphere ( $p=0$ ),  $n$  is the fraction of FOR covered with cloud,  $P_s$  is the surface pressure,  $P_c$  is the cloud top pressure, and  $b[N, T(p)]$  is the Planck radiance of the spectral band  $N$  for a temperature  $T(p)$ . The second part of the above equation represents the radiance decrease from clear sky conditions introduced by an opaque cloud at a pressure level  $p$ . This calculation is dependent upon an "accurate" estimation of the current atmospheric temperature and moisture structure, which are provided by a NWP model forecast profile. By comparing the observed radiances with the calculated radiances (for an observed atmosphere defined by the model guess profiles), an estimation of the cloud height can be derived for a completely opaque cloud. In the **Fig. 1**, observed WV and IR radiances at each Field of Regard (FOR) are plotted with the calculated radiances at different heights for opaque clouds in the atmosphere (curved line). The straight line connects the center points of the warmest and coldest clusters, which approximates the observed surface and cloud conditions.

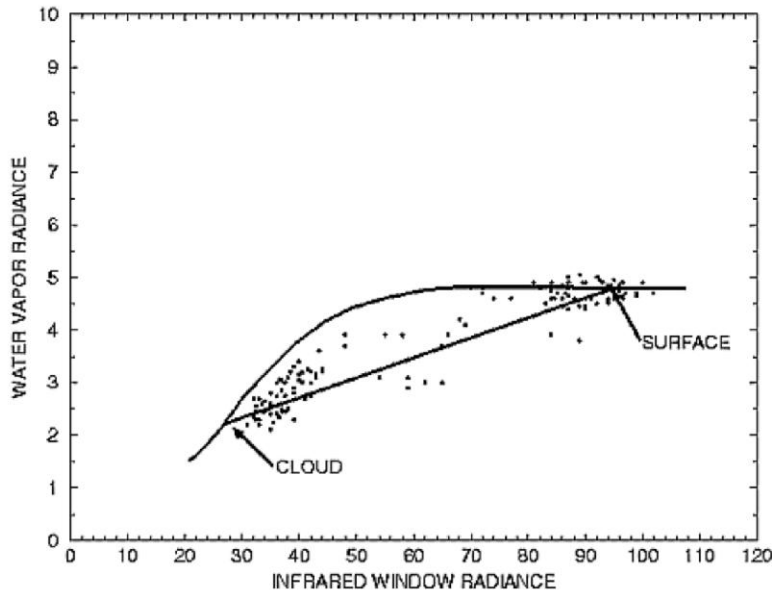


**Fig 1:** Measured radiances ( $\text{mW m}^{-2} \text{ sr}^{-1} \text{ cm}$ ) for fields of view partially filled with clouds (Nieman et al., 1993)

By extrapolating this line to intersect the calculated radiance curve, where the cloud amount is one (representing an opaque cloud), the cloud top temperature/pressure can be determined. The cluster determination algorithm used is a modified version of the bivariate asymmetric Gaussian histogram analysis (Rossow et al., 1985; Tomassini, 1981), and it involves ten steps. These steps are outlined in detail in Nieman et al. (1993) and Nieman et al. (1997). Calculated water vapor radiances can be in error due to incorrect NWP model forecast profiles. This error would lead to calculated radiances being systematically higher or lower than observed radiances. When the calculated radiances are systematically lower, an adjustment is applied to the radiances obtained using the above equation (2). When the calculated radiances are greater than observed radiances, no adjustment is applied since it is assumed that the lower measured radiance is due to cloud contamination. The accuracy of this method can be affected by the amount of water vapor in the atmosphere. Dry atmospheric conditions lead to a steeper slope between the IR and WV radiances, leading to an overestimate in the target height (lower pressure value). The NCEP GFS model forecast are used here as the guess fields.

After retrieving the value of cloud top pressure effective cloud amount or effective emissivity is computed using eq (3)

$$a_{eff} = \frac{R(v) - R_{cl}(v)}{B[v, T(P_c)] - R_{cl}(v)} \quad (3)$$

where  $N$  is the fractional cloud cover within the FOV,  $N\varepsilon$  the effective cloud amount,  $v$  is the window channel wavenumber, and  $B[v, T(P_c)]$ , is the opaque cloud radiance corresponding to window channel frequency and  $R_{cl}(v)$  is the clear sky radiance corresponding to window channel.

#### 9.5.4. Cloud top height and cloud top temperature from cloud top pressure

The value of cloud top height, cloud top temperature for INSAT-3D/3DR Imager is derived corresponding to the retrieved cloud top pressure from INSAT-3D/3DR Imager. These values are again derived using the aforementioned NCEP forecast profiles. NCEP forecast fields contains the temperature and moisture profiles with pressure levels as its vertical coordinates. Geopotential height formulae is used to compute cloud height for given temperature profile. Geopotential height (GPH) is then given by

$$GPH = \frac{R_o Z}{R_o + Z}$$

Where  $R_o = 6356.766$  km, the average radius of the earth. For given pressure, temperature and humidity profile from surface to 0.1 hPa, height of any pressure level or thickness of atmospheric layer from surface to a particular pressure level can be computed using the formula

$$Z = \frac{R_d \bar{T}_v}{g} \ln\left(\frac{P_s}{P}\right)$$

$P_s$  – Surface Pressure,  $P$  – Given pressure where geopotential height is to be calculated,  
 $\bar{T}_v$  - Layer mean virtual temperature. This can be computed at all the retrieved pressure levels.

Virtual temperature  $T_v$  is given by  $T_v = (1 + 0.61q)T$  where  $q$  is specific humidity expressed in Kg/Kg,  $T$  is temperature in K.

#### 9.5.5. Effective cloud amount

Effective cloud amount  $N^*$  for a given FOR is computed by using the eq (3)

$$N^* = N_{cld} a_{eff} / N_{tot}$$

Where  $N^*$  is the effective cloud amount for a given FOR,  $N_{cld}$  is the total number of cloudy pixels within a given FOR,  $N_{tot}$  is the total number of pixels in a FOR and  $a_{eff}$  is the effective cloud amount retrieved. For window channel method  $a_{eff} = 1$

#### 9.5.6. Radiance bias adjustment

It is evident from the previous sections that cloud top properties retrieval algorithm is heavily dependent on quality of NCEP forecast fields and the fast forward RT model. If forward simulations are not in consonance with observations, then there will be error in the retrieved products. To make observations and forward model simulations consistent, a radiance bias adjustment is necessary step.

Radiance bias adjustment is carried out by using previous eight days of good quality matchup data of INSAT-3D/3DR Imager clear-sky observations and spatially and temporally collocated simulated INSAT-3D/3DR Imager radiances. The simulation is carried out by using NCEP GFS analysis and RTTOV radiative transfer model. In this matchup data set INSAT-3D/3DR clear sky observations are average over 9x9 FOR and only those FOR are selected in which more than 90% pixels are clear. The radiance bias adjustment is done for land and ocean pixels separately. In addition to it, only those points are taken up for matchup data wherein satellite zenith angle is less than 30°. An outlier rejection method is also applied before computing radiance bias adjustment factor in terms of slope and offset.

## References

- Ackerman, S. A., and S. K. Cox, 1981: GATE Phase III mean synoptic-scale radiative convergence profiles. *Mon. Wea. Rev.*, 109, 371-383.
- Foltz, G. S., and W. M. Gray (1979): Diurnal variation in the troposphere's energy balance. *J. Atmos. Sci.*, 36, 1450-1466
- Gruber, A., and T. S. Chen, 1988: Diurnal variation of outgoing longwave radiation. *J. Clim. Appl. Meteor.*, 8, 1-16
- Nieman SJ, Schmetz J, Menzel WP (1993) A comparison of several techniques to assign heights to cloud tracers. *Journal of Applied Meteorology* 32:1559–1568.
- Nieman S, Menzel WP, Hayden CM, Gray D, Wanlong S, Velden C, Daniels J (1997) Fully automated cloud-driftwinds in NESDIS operations. *Bulletin of American Meteorological Society* 78: 1121–1133.
- Le Marshall, J., 1994: An operational system for generating cloud drift winds in the Australian region and their impact on numerical weather prediction. *Wea. Forecasting*, 9, 361-370.
- Rossow, W. B. and A. A. Lacis, 1990: Global and seasonal cloud variations from satellite radiance measurements. Part-II Cloud properties and radiative effects. *J. Clim.*, 3,11, 1204-1253.
- Rossow WB, Mosher F, Kinsella E, Arking A, Debois M, Harrison E, Minnis P, Ruprecht E, Seze G, Simmer C, Smith E (1985) ISCCP clouds algorithm inter-comparison. *Journal of Climate and Applied Meteorology* 24: 877-903.
- Schmetz J, Holmlund K, Hoffman J, Strauss B, Mason B, Gaertner V, Koch A, van de Berg L (1993) Operational cloud-motion winds from Meteosat infrared images. *Journal of Applied Meteorology* 32: 1206–1225.
- Tomassini C (1981) Objective analysis of cloud fields. *Proc. Satellite Meteorology of the Mediterranean* ESA, SP-159: pp.73-78.
- Wylie, D. P., D. L. Jackson, W. P. Menzel, and J.I. Bates, 2005: Global cloud cover trends inferred from two decades of HIRS observations. *J. Clim.*, 18,15,3021-3031

Wu, M. L. and J. Susskind, 1990: Outgoing longwave radiation computed from HIRS2/MSU soundings. *J. Geophys. Res.*, 95D, 7579-7602.

Wylie, D. P. and W. P. Menzel, 1989: Two years of cloud cover statistics using VAS. *J. Clim.*, 2, 380-392.

## **10. Cloud Top Pressure/Cloud Top Temperature from INSAT-3D/3DR SOUNDER**

S. No.	Product Name	Spatial Resolution	Temporal Resolution
1	SND_CLDP	5 x 5 Sounder Pixels (~50 km x 50 km)	1 hour

## **10.1. Algorithm Configuration Information**

### **10.1.1. Algorithm Name**

Cloud Top Pressure/Cloud Top Temperature from INSAT-3D/3DR Sounder

### **10.1.2. Algorithm Identifier**

ISRO\_INSAT\_SND\_CLDP

### **10.1.3. Algorithm Specification**

Version	Date	Prepared by	Description
1.0	01.01.2015	M. V. Shukla, and P. K. Thapliyal	Cloud properties are useful for weather prediction applications.

## **10.2. Introduction**

The purpose of this document is to present a conceptual framework and algorithm for retrieving cloud properties such as cloud top temperature, cloud top pressure and effective cloud amount from CO<sub>2</sub> absorption and window channels of INSAT-3D/3DR sounder. This document also describes the validation procedure. In this document some background and the methodology employed to derive the cloud top temperature/pressure and effective cloud amount is discussed. It mainly discusses the theoretical basis and practical aspects of the retrieval algorithm for cloud parameters from INSAT-3D/3DR sounder channels and outlines the intended validation approach with validation results.

### **10.2.1. Overview and background**

The cloud properties such as cloud cover, cloud height etc. are very important for various climate and weather applications. The clouds at different heights affects weather and climate phenomenon in different ways.

### **10.2.2. Objective**

The main objective of this document is to provide the theoretical basis for deriving cloud top pressure/ cloud top temperature and effective cloud amount from INSAT-3D/3DR sounder channels. The proposed algorithm will be applied to retrieve cloud properties from sounder channels over a Field of Regard (FOR) of 5x5 sounder pixels defined as confidently cloudy from sounder cloud mask output. The algorithm has no limitation based on geographical location, therefore, can be applied to generate products at any geographical location.

## 10.3. Inputs

### 10.3.1. Static Data

Parameter	Resolution	Accuracy	Source
Land/sea flag	~2 km x 2 km	--	Global topographic data
Surface Elevation	10 km x 10 km	--	Global topographic data
Monthly mean spectral surface Emissivity	10 km x 10 km	--	Univ. of Wisconsin

### 10.3.2. Sounder data (dynamic)

Parameter	Resolution	Accuracy	Source
Radiometric and Geometric corrected gray count values of sounder channels #1-19	Each Pixel	--	Derived from raw data by DP
Geolocation information	each pixel	1 pixel	Derived by DP
Calibration Coefficients to convert gray values to radiances/Tb	-	-	Derived by DP
Brightness temperature quality flag for sounder channels	each pixel	-	Derived by DP

### 10.3.3. Other Auxiliary data and Model Inputs

In addition to Sounder data, numerical model forecast and surface observations of temperature and humidity are required to improve the retrieval accuracy.

Parameter	Resolution	Accuracy	Source
Forecast temperature and humidity profiles valid at observation time	0.5° x 0.5° at model pressure levels	--	NCEP and/or IMD/NCMRWF
Forecast surface pressure and surface skin temperature valid at observation time	0.5° x 0.5°	--	NCEP and/or IMD/NCMRWF
Observed surface pressure, surface air temperature and humidity	AWS locations	--	IMDs Automatic Weather Station (AWS)

## **10.4. Algorithm Functional Specifications**

It is very difficult to imagine variety of weather phenomenon without clouds. Clouds do not only add beauty and variability in atmosphere but also cause the wide variety of atmospheric activities. Clouds vary in its appearance, extent, composition and physical properties, therefore, different clouds affect weather and climate differently. For example, rapidly growing cumulus clouds are precursor to severe thunderstorm, low water clouds with strong temperature inversion results in fog. Thin cirrus clouds are not very exciting clouds from short to medium range weather activities but play a very crucial role in earth's heat budget and also helps in tracking upper level winds. Thin cirrus clouds are thin enough to allow incoming solar radiation to pass through it but doesn't allow outgoing infrared radiation thus increase the radiative energy and eventually leads to the warming of earth-atmosphere system.

Cirrus clouds are crucially important to global radiative processes and the heat balance of the Earth; they allow solar heating while reducing infrared radiation to space. Models of climate changes will have to correctly simulate these clouds to have the proper radiative terms for the Earth's heat budget. Past estimates of the variation of cloud cover and the Earth's outgoing longwave radiation have been derived primarily from the longwave infrared window (10-12  $\mu\text{m}$ ) radiances observed from polar orbiting and geostationary satellites (Rossow and Lacis, 1990; Gruber and Chen, 1988). The occurrence of semi-transparent clouds is often underestimated in these single channel approaches. Recently, multispectral techniques have been used to better detect cirrus in global (Wylie et al., 2005; Wu and Susskind, 1990) and North American (Wylie and Menzel, 1989) cloud studies.

Clouds are very important to study at various spatial and temporal scale including its diurnal cycle. Diurnal cycle of various physical processes such as radiative exchange, precipitation, small and large-scale dynamics are of great importance and are greatly linked with clouds, therefore, underlines the study of diurnal cycles of clouds too. Ackerman and Cox (1981) had reported the diurnal oscillation of cloudiness in some tropical areas. These diurnal oscillations are part of dynamic-radiative feedback mechanism that operates on various spatial scales (Foltz and Gray, 1979).

The cloud top pressure/temperature and cloud effective emissivity from INSAT-3D/3DR sounder is intended to be retrieved at ~50 km nominal resolution. The cloud products are retrieved at coarser resolution than to resolution of actual INSAT-3D/3DR sounder observations which are available at nominal resolution of ~10 km at nadir. The averaging of 5x5 pixels will enhance the signal to noise ratio over cloudy pixels. In general, noise over cloudy pixels is higher in comparison to clear pixels, therefore, it becomes essential to take average of observed radiances/brightness temperatures to reduce the noise for accurate estimation of cloud properties.

Cloud properties from INSAT-3D/3DR sounder observations are very important parameters to study diurnal, seasonal or annual variations in cloud cover as these parameters are available at high temporal resolution at the same geographical location. These parameters could also help in

segregating semi-transparent transmissive clouds (partially transparent to terrestrial radiation) opaque clouds in the analysis of cloud cover (Wylie and Menzel, 1989). Similar kind of studies are already carried out by Wylie et al. (1994) using NOAA-HIRS observations.

## 10.5. Algorithm Theoretical Description

This section presents the theoretical basis of the algorithm and practical considerations. Retrieval of cloud products (CTP, CTT and effective cloud amount) is a combination of two methods: Window channel method and CO<sub>2</sub> slicing method. Both of these methods require forecast fields of temperature and moisture. The CO<sub>2</sub> slicing method requires the use of radiative transfer model.

In this section physics of deriving cloud height and effective cloud amount from INSAT-3D/3DR sounder observations is discussed. This sections presents the conceptual framework of retrieval algorithm.

## 10.6. Physical Basis of the Cloud Top Pressure/Temperature/Height Algorithm

### 10.6.1. CO<sub>2</sub> Slicing: Mid- to High-Level Clouds

The assumptions made for the application of the CO<sub>2</sub> -slicing algorithm are (Menzel et al., 1992):

- (i) the emissivity of the cloud is the same in all channels used,
- (ii) clouds occur as a single cloud layer,
- (iii) lower cloud layers are ignored, and
- (iv) the surface temperature and the temperature structure of the atmosphere and its transmittance at the used wavelengths are known.

Retrieval of cloud top pressure and effective cloud amount (i.e., cloud fraction multiplied by cloud emittance) are performed using radiances measured in those spectral bands that are located within the broad 15  $\mu\text{m}$  CO<sub>2</sub> absorption region. The CO<sub>2</sub> slicing technique makes use of combination of 15  $\mu\text{m}$  CO<sub>2</sub> absorption channels that have different opacity, therefore, sensing different layer of atmosphere. This helps in assigning height of clouds. The channels of INSAT-3D/3DR used in the cloud top pressure and amount algorithm are described in Table 1.

*Table 1: Channel characteristics of INSAT-3D used in cloud top properties retrieval*

INSAT-3D Channel number	INSAT-3D Channel characteristics		Principal Absorbing gas	Approximate peak in weighting function
	Central wavelength (wavenumber)	Bandwidth $\mu\text{m}$ ( $\text{cm}^{-1}$ )		
8	10.99 (910)	0.611 (51)	Window	Surface
7	11.98 (834)	0.768 (53)	Water Vapor	Surface
5	13.33 (750)	0.352 (20)	$\text{CO}_2$	Low level atmosphere
4	13.64 (733)	0.351 (19)	$\text{CO}_2$	Mid-level atmosphere
3	14.03 (713)	0.321 (16)	$\text{CO}_2$	Upper level atmosphere
2	14.31 (699)	0.305 (15)	$\text{CO}_2$	Tropopause level

The  $\text{CO}_2$  slicing method is a well-established method and is extensively used for deriving cloud properties from a wide range of GEO and LEO satellite observations. Keeping this fact in mind the latest series of GOES-12/13/14 had a  $\text{CO}_2$  channel instead of the split window thermal IR channel. This method is used for deriving cloud top pressure and temperatures from VISSR Atmospheric Sounder (VAS) (Menzel and Strabala 1989; Menzel et al 1992) observations, High resolution Infrared Radiometer Sounder (HIRS) (Wylie and Menzel 1999) observations, MODerate resolution Imaging Spectroradiometer (MODIS) (Plantick et al. 2003; Menzel et al. 2008) radiances and the Geostationary Operational Environmental Satellite (GOES) sounder (Menzel et al. 1992; Menzel and Purdom 1994) observations. Several sensitivity studies such as Menzel et al. (1992) and Baum and Wielicki (1994) have already been carried out to quantify errors arising from different sources.

The  $\text{CO}_2$  slicing technique can be understood by calculating the radiances using radiative transfer models in an atmosphere with a single cloud layer. For a given cloud element in a field of view (FOV), i.e. a single sounder pixel, the radiance observed,  $R(\nu)$ , in spectral band  $\nu$ , can be written as:

$$R(\nu) = NR_{cld} + (1 - N)R_{clr} \quad \dots \quad (1)$$

Where  $R(\nu)$  is observed radiance in band  $\nu$ ,  $N$  is the fractional cloud coverage,  $R_{clr}$  is radiance from clear portion and  $R_{cld}$  is radiance from the cloud covered portion.

Cloud covered radiance can be written as:

$$R_{cld} = \varepsilon R_{op} + (1 - \varepsilon)R_{clr} \quad \dots \quad (2)$$

Where  $\varepsilon$  is the emissivity of cloud and  $R_{op}$  is radiance from the opaque cloud.

By combining Eq (1) and Eq (2) we get:

$$R(v) = (1 - N\varepsilon)R_{clr}(v) + N\varepsilon R_{op}(v) \quad \text{----- (3)}$$

Now from radiative transfer equation  $R_{cld}$  and  $R_{clr}$  are given as:

$$R_{cld} = B(P_t)\tau(P_t) - \int_0^{P_t} \tau(v, p) \frac{dB[v, T(p)]}{dp} dp \quad \text{----- (4)}$$

$$R_{clr} = B(P_t)\tau(P_t) - \int_0^{P_s} \tau(v, p) \frac{dB[v, T(p)]}{dp} dp \quad \text{----- (5)}$$

Where  $P_s$  is the surface pressure,  $P_t$  is pressure corresponding to the top of single level cloud,  $\tau(v, p)$  is the top of the atmosphere ( $p = 0$ ) transmittance of radiation of spectral band  $v$  emitted from the atmospheric level at pressure  $p$ , and  $B[v, T(p)]$  is the Planck radiance for spectral band  $v$  for temperature  $T$  at pressure level  $p$ . Thus first terms of Eq (4) and (5) represents the contribution to radiance from the surface term (which is cloud top in Eq (4) and surface in Eq(5)), whereas, the second term represents the absorption of radiation by atmosphere above the surface or cloud top. These equations neglect the scattering by clouds or atmosphere which is very valid assumptions for clear atmosphere and opaque clouds at the desired sounder spectral bands.

Now expanding above equations by integrating by parts and solving we get:

$$R_{op}(v, P_c) = R_{clr}(v) - \int_{P_t}^{P_s} \tau(v, p) \frac{dB[v, T(p)]}{dp} dp \quad \text{----- (6)}$$

Now by substituting Eq (6) in Eq (3) we get:

$$R(v) - R_{clr}(v) = N\varepsilon \int_{P_S}^{P_t} \tau(v, p) \frac{dB[v, T(p)]}{dp} dp \quad \text{----- (7)}$$

This is the basic equation used in CO<sub>2</sub> slicing method. It is evident from the Eq (7) that with the help of a-priori information of  $R_{clr}(v)$  and  $\tau(v, p)$ , value of  $P_t$  that is cloud top pressure could be inferred. However, even with this a-priori information, there are two unknowns ( $N\varepsilon$  and  $P_t$ ) in Eq (7). To solve this problem, the ratio of Eq (7) for two observations made in nearby spectral bands is taken. Thus radiance ratios between two spectral bands in similar frequencies (Chahine, 1974; Smith and Platt, 1978) gives the information of cloud top pressure.

The ratio of the deviations in observed radiances,  $R(v)$  to their corresponding clear-sky radiances,  $R_{clr}(v)$  for two spectral bands of frequency  $v_1$  and  $v_2$  viewing the same FOV is written as

$$\frac{R(v_1) - R_{clr}(v_1)}{R(v_2) - R_{clr}(v_2)} = \frac{N\varepsilon_1 \int_{P_S}^{P_T} \tau(v_1, p) \frac{dB[v_1, T(p)]}{dp} dp}{N\varepsilon_2 \int_{P_S}^{P_T} \tau(v_2, p) \frac{dB[v_2, T(p)]}{dp} dp} \quad \text{----- (8)}$$

As it is already stated that channels with wavenumber (or wavelength) that are very similar in wavenumber (wavelength) are taken to satisfy the assumption that cloud emissivities in both channels are same that is  $\varepsilon_1$  is approximately equal to  $\varepsilon_2$ . With this assumption we are left with only one unknown in Eq (8) and that can be easily estimated.

After retrieving the value of cloud top pressure using a-priori information of  $R_{clr}(v)$  and  $\tau(v, p)$  in eq (8), effective cloud amount or effective emissivity is computed using eq (9)

$$N\varepsilon = \frac{R(\nu) - R_{clr}(\nu)}{B[\nu, T(P_c)] - R_{clr}(\nu)} \quad (9)$$

where N is the fractional cloud cover within the FOV,  $N\varepsilon$  the effective cloud amount,  $\nu$  is the window channel wavenumber, and  $B[\nu, T(P_c)]$ , is the opaque cloud radiance corresponding to window channel frequency and  $R_{clr}(\nu)$  is the clear sky radiance corresponding to window channel.

It is evident from the equation (9) that effective cloud amount or effective cloud emissivity is multiplication of N (fractional cloud cover within the FOV) and  $\varepsilon$  (Cloud emissivity), therefore, effective cloud amount can be less than 1 because of:

- broken cloud ( $N < 1, \varepsilon = 1$ ) has filled the FOV
- overcast transmissive cloud ( $N = 1, \varepsilon < 1$ )
- broken transmissive cloud ( $N < 1, \varepsilon < 1$ )

Therefore, it is difficult to quantify exactly the emissivity of clouds using the effective cloud amounts from approximately 50 km x 50 km INSAT-3D/3DR sounder products.

The cloud top products from CO<sub>2</sub> slicing technique are matched with other methods to filter out any other clouds that are not upper level clouds. Upper level clouds are flagged by using the combination of highly absorbing channels (such as water vapor absorption channel in 6.7 μm or CO<sub>2</sub> absorption channel in 15 μm band) and channels with less absorption. In general, the brightness temperatures in strong absorption channels are much cooler than the brightness temperatures (BT) in weak absorption channels for clear atmospheric condition or low level clouds. Contrary to this, for high level clouds BT in strong absorption channel is warmer than the weak absorption channels (Soden and Bretherton, 1993; Schmetz et al., 1997). Appropriate thresholds were taken to identify the high level clouds in INSAT-3D/3DR cloud top retrieval algorithm. In present algorithm 14.03 μm (channel 3) and 13.33 μm (channel 5) of INSAT-3D/3DR sounder are used for this purpose. If BT of ch#3 is greater than the BT of ch#5 by a given threshold, then the cloud is assumed to be high cloud and cloud top pressure from CO<sub>2</sub> slicing method is retained.

Equation (8) is used to retrieve cloud top pressure for a 5 x 5 FOR. The left side of Equation (8) contains the terms for observed radiances as well as clear radiances. The value of observed radiances is calculated by taking the average of cloudy pixels within 5x5 FOR. Cloud top computation is carried out only if 16 or more cloudy pixels are found within 5x5 box. Computation of clear sky radiances and transmittances is carried out using a fast forward radiative transfer model called RTTOV (Eyre 1991; Saunders et al. 1999; Matricardi et al 2001) developed at European Center for Medium Range Weather Forecasting (ECMWF). RTTOV uses the Pressure Layer Optical Depth algorithm (Hannon et al 1996). This model is very flexible and can take any number of pressure levels for forward model computation, however, internally it interpolates atmospheric profiles to fixed 43 pressure levels ranging from 1013 to 0.1 hPa. This interpolation is done because fast forward coefficients for INSAT-3D/3DR sounder SRFs are derived on given 43 pressure

levels. The forward calculations from RTTOV takes satellite zenith angle, absorption by well-mixed gases (including nitrogen, oxygen, and carbon dioxide), water vapor (including the water vapor continuum), and ozone into account. The forecast field from NCEP containing temperature, moisture profiles, surface air temperature, skin temperature etc. are used to simulate clear sky transmittances and radiances.

The right hand side of Equation (8) uses aforementioned transmittance profiles. Integration is carried out by using trapzoidal method wherein integration limit is bounded by surface pressure and tropopause pressure level.

For the retrieval of cloud top pressure from INSAT-3D/3DR sounder a “top-down” approach, similar to MODIS cloud top pressure retrieval method is followed. In this approach pair of two channels are selected based on their decreasing opacity. If retrieval of cloud top pressure is successful for a given pair, then there will no need for applying eq (8) for other pair of channels which are relatively less opaque. For INSAT-3D/3DR sounder first pair of ch#2 and ch#3 are taken which are considered to be the most opaque channels for CO<sub>2</sub> slicing method. If eq (8) appropriately converges for this pair, then retrieval is considered to be successful, otherwise the same procedure is repeated with pairs of (ch#3, ch#4) or (ch#4, ch#5). If none of these pairs are able to give value of cloud top pressure, then window channel method is used for retrieval of cloud top pressure.

#### **10.6.2. Window Channel method for cloud top pressure for low to mid clouds**

In this method the cloud top pressure is carried out by comparing infrared window channel brightness temperature (BT) values with NWP model forecast temperature profiles. A 6-h NWP model forecast from National Center for Environmental Prediction (NCEP) Global Forecast System (GFS) is the source of temperature profile (GFS; Derber et al. 1991). This method assumes that clouds are overcast and non-transmissive ( $\varepsilon=1$ ). Generally, cloud top temperatures/pressure of low level overcast clouds are determined by using window channel method. In addition to it, wherein, cloud top pressure is not determined by CO<sub>2</sub> slicing method, window channel method is used to retrieve cloud top properties for those pixels too. In this method cloud top pressure is determined by interpolating the cloud temperature, which is an average of BT cloudy pixels in 5x5 FOR, to the interpolated model guess field at the target location. The cloud emissivity is assumed to be unity and  $N\varepsilon=N/25$ .

Finally, all cloudy FORs are assigned a cloud top pressure either by CO<sub>2</sub> slicing or infrared window technique.

### **10.7. Cloud top height and cloud top temperature from cloud top pressure**

The value of cloud top height and cloud top temperature for INSAT-3D/3DR sounder are derived corresponding to the retrieved cloud top pressure from INSAT-3D/3DR sounder. These values are again derived using the aforementioned NCEP forecast profiles. NCEP forecast fields contains the temperature and moisture profiles with pressure levels as its vertical coordinates. Geopotential

height formulae is used to compute cloud height for given temperature profile. Geopotential height (GPH) is then given by

$$GPH = \frac{R_o Z}{R_o + Z} \quad \text{----- (10)}$$

Where  $R_o = 6356.766$  km, the average radius of the earth. For given pressure, temperature and humidity profile from surface to 0.1 hPa, height of any pressure level or thickness of atmospheric layer from surface to a particular pressure level can be computed using the formula

$$Z = \frac{R_d \bar{T}_v}{g} \ln\left(\frac{P_s}{P}\right) \quad \text{----- (11)}$$

$P_s$  – Surface Pressure,  $P$  – Given pressure where geopotential height is to be calculated,  $\bar{T}_v$  - Layer mean virtual temperature. This can be computed at all the retrieved pressure levels.

Virtual temperature  $T_v$  is given by  $T_v = (1 + 0.61q)T$  where  $q$  is specific humidity expressed in Kg/Kg,  $T$  is temperature in K.

## 10.8. Radiance bias adjustment

It is evident from the previous sections that cloud top properties retrieval algorithm is heavily dependent on quality of NCEP forecast fields and fast forward RT model. If forward simulations are not in consonance with observations, then there will be error in retrieved products. To make observations and forward model simulations consistent, radiance bias adjustment is a necessary step.

Radiance bias adjustment is carried out by previous eight days of good quality matchup data of INSAT-3D/3DR sounder clear-sky sounder observations and spatially and temporally collocated simulated INSAT-3D/3DR sounder radiances. The simulation is carried out by using NCEP GFS analysis and RTTOV radiative transfer model. In this matchup data set INSAT-3D/3DR clear sky observations are average over 5x5 FOR and only those FOR are selected in which more than 90% pixels are clear. The radiance bias adjustment is done for land and ocean pixels separately. In addition to it, only those points are taken up for matchup data wherein satellite zenith angle is less than  $30^{\circ}$ . An outlier rejection method is also applied before computing radiance bias adjustment factor in terms of slope and offset.

## References

- Ackerman, S. A., and S. K. Cox, 1981: GATE Phase III mean synoptic-scale radiative convergence profiles. Mon. Wea. Rev., 109, 371-383.
- Baum, B. A. and. B. A. Wielicki, 1994: Cirrus cloud retrieval using infrared soundin data.: Multilevel cloud errors. J. Appl. Meteor., 33, 1, 107-117.

- Chahine, M. T., 1974: Remote sounding of cloudy atmospheres. Part-I. The single cloud layer. *J. Atmos. Sci.*, 31, 233-243.
- Derber J. C., D. F. Parrish and S. J. Lord, 1991: A new global operational analysis system at National Meteorological Center. *Wea. Forecasting*, 6, 538-547.
- Eyre, J. R.(1991): A fast radiative transfer model for satellite sounding system. European Center for Medium Range Weather Forecast., U. K. Tech. Memo., 176, 1991
- Foltz, G. S., and W. M. Gray (1979): Diurnal variation in the troposphere's energy balance. *J. Atmos. Sci.*, 36, 1450-1466
- Gruber, A., and T. S. Chen, 1988: Diurnal variation of outgoing longwave radiation. *J. Clim. Appl. Meteor.*, 8, 1-16
- Hannon S., L. L. Strow and W. W. McMillan (1996). Atmospheric infrared fast transmittance models: A comparison of two approaches. *Proc. SPIE Conf. Opt. Spectroscopic Tech. Instrum. Atmos. Space Res. II*, vol. 2830, 94-105
- Matricardi, M., F. Chevallier, and S. Tjemkes (2001): An improved general fast radiative transfer model for assimilation of radiance observations, ECMWF, ECMWF Res. Dept., Tech. Memo, 345
- Menzel, W. P. and K. I. Strabal, 1989: Preliminary report on the demonstration of the VAS CO<sub>2</sub> cloud parameters (cover,height, and amount) in support of the automated surface observing systems (ASOS). NOAA Tech Memo NESDIS 29.
- Menzel, W. P., D.P. Wylie, and K. I. Strabala, 1992: Seasonal and diurnal changes in cirrus clouds as seen in four years of observations with VAS. *J. Appl. Meteor.*, 31, 370-385.
- Menzel, W. P., R. A. Frey, H. Zhang, D. P. Wylie, C. C. Moeller, R. A. Holz, B. Maddux, B. A. Baum, K. I. Strabal, and L. E. Gumley, 2008: MODIS global cloud-top pressure and amount estimation: algorithm description and results. *J. Appl. Meteor. Clim.*, 47, 1175-1198.
- Minnis P. and E. F. Harrison (1984): Diiurnal variability of regional cloud and clear-sky radiative parameters derived from GOES data. Part I: Analysis method, *J. Clim. Appl. Meteor.*, 23,7, 993-1011
- Minnis P. and E. F. Harrison (1984): Diiurnal variability of regional cloud and clear-sky radiative parameters derived from GOES data. Part II: November 1978 cloud distributions, *J. Clim. Appl. Meteor.*, 23, 1012-1031
- Plantick. S., M. D. King, S. A. Ackerman, W. P. Menzel, B. A. Baum, and R. A. Frey, 2003: The MODIS cloud products: Algorithms and examples from Terra. *IEEE Trans. Geosci, Remote Sens.* 41, 459-473.
- Rossow, W. B. and A. A. Lacis, 1990: Global and seasonal cloud variations from satellite radiance measurements. Part-II Cloud properties and radiative effects. *J. Clim.*, 3,11, 1204-1253. ;

- Saunders, R. W., M. Matricardi and P. Brunel (1999): An improved fast radiative transfer model for assimilation of satellite radiance observations, *Q. J. R. M. S.*, vol. 125, 556, 1407-1425.
- Schmetz, J., S. A. Tjemkes, M. Gube, and L. van de Berg, 1997: Monitoring deep convection and convective overshooting with Meteosat, *J. Adv. Space Res.*, 10, 433-441
- Smith, W. L., and C. M. R. Platt, 1978: Intercomparison of radiosonde, ground based laser, and satellite deduced cloud heights. *J. Appl. Meteor.*, 17, 1796-1802.
- Soden, B. J., and F. B. Bretherton, 1993: Upper tropospheric relative humidity from the GOES 6.7  $\mu\text{m}$  channel: Method and climatology for July 1987. *J. Geophysical Research*, 98, 16669-166688
- Wu, M. L. and J. Susskind, 1990: Outgoing longwave radiation computed from HIRS2/MSU soundings. *J. Geophys. Res.*, 95D, 7579-7602.
- Wylie, D. P. and W. P. Menzel, 1989: Two years of cloud cover statistics using VAS. *J. Clim.*, 2, 380-392.
- Wylie, D. P., and W. P. Menzel, 1999: Eight years of global high cloud statistics using HIRS. *J. Clim.*, 12, 170-184
- Wylie, D. P., D. L. Jackson, W. P. Menzel, and J.I. Bates, 2005: Global cloud cover trends inferred from two decades of HIRS observations. *J. Clim.*, 18, 15, 3021-3031
- Wylie, D. P., W. P. Menzel, H. M. Woolf, and K. I. Strabala, 1994: Four years of global cirrus cloud statistics using HIRS. *J. Clim.*, 7, 1972-1986

## **11. INSAT-3D Cloud Micophysical Product**

S. No.	Product Name	Spatial Resolution	Temporal Resolution
1	IMG_CMP	4 km x 4 km	30 minutes

## **11.1. Algorithm configuration information**

### **11.1.1. Algorithm name:**

INSAT-3D/3DR Cloud Microphysical Product (CMP)

### **11.1.2. Algorithm Identifier:**

INSAT\_3D\_CMP

### **11.1.3. Algorithm Specification**

<b>Version</b>	<b>Date</b>	<b>Prepared by</b>	<b>Description</b>
1.0	14.12.2015		
1.1	27.11.2016	Bipasha Paul Shukla,	Cloud Microphysical
1.2	01-08-2018	Jinya John	parameter retrieval Baseline
1.3	29-08-2018		Document
1.31	14-09-2019		

## **11.2. Introduction**

In this document, we offer some background to the cloud microphysics retrieval over oceans using INSAT-3D imager data, describe the theoretical basis of the cloud microphysics retrieval algorithm, discuss inputs required, output deliverables and the practical aspects of the algorithm implementation, the technical issues and the future scope.

## **11.3. Overview and Background**

Clouds are suspension of tiny water droplets or ice crystals. They are of varying sizes and shapes. They can be of water, ice or mixed phase. The size of cloud droplets is of the order of  $10 \mu\text{m}$ . Clouds strongly modulate the Earth's energy balance and its atmosphere through their interaction with the solar and terrestrial radiation (Roebeling et al., 2005). Their impact on the radiation budget can result in a heating or cooling of the planet, depending on the radiative properties of the cloud and their altitude (Stephens et al., 1981). The radiative properties of the clouds depend upon the various cloud microphysical parameters which includes optical depth, effective particle radius, thermodynamic phase etc. Clouds interact with radiation in many ways like scattering, emission, absorption and this interaction is sensitive towards each of the microphysical parameters. The temporal monitoring of cloud-top microphysics is of extreme importance in the precipitation development processes. The retrieval of cloud microphysical properties like effective radius, optical depth, thermodynamic phase etc. from INSAT 3D has been made possible due to the inclusion of  $1.6\text{ }\square\text{m}$  channel in INSAT 3D imager. This is a major enhancement as compared to the derivation of only the cloud top temperature from Kalpana VHRR. Earlier studies show that

the simulation of convective systems is very sensitive to the parameterization of cloud microphysics. Thus retrieval of the microphysical parameters from INSAT 3D aids in monitoring and accurate prediction of convective weather events. The cloud-microphysical parameters at high temporal resolution will be very helpful in tracking the evolution of local as well as mesoscale systems.

The sensitivity of different microphysical parameters to different regions of electromagnetic spectrum can be studied with the help of a radiative transfer (RT) model. A Radiative transfer model (RTM) computes the radiative transfer of the electromagnetic radiation through the atmosphere. The retrieval of cloud microphysical properties is done with the help of an RT model using the imager channels of INSAT-3D. The INSAT-3D channels which may be used for cloud properties retrieval includes Visible ( $0.65\mu\text{m}$ ) and Shortwave Infrared (SWIR- $1.66\mu\text{m}$ ). The importance of retrieving the optical thickness and effective radius derives not only from the fact that such a retrieval is possible, but from the fact that shortwave cloud radiative properties depend almost exclusively on these two parameters.

## **11.4. Objective**

The main objective of this document is to provide step wise algorithm, inputs and outputs as expected from the INSAT-3D cloud microphysical product. This document will form the basis of operational implementation of the algorithm.

## **11.5. Inputs**

Inputs to the algorithm will include geo-referenced, corrected Albedo, Digital counts for Visible channel and SWIR along with satellite viewing geometry (solar zenith angle, satellite zenith angle, azimuth angle).

### **11.5.1. Static data**

This will consist of the Look-up Table (LUT) which is generated using a RT model and stored. A random dataset of cloud microphysical parameters with solar geometry is also stored as static file. These files will be required by the inversion model.

### **11.5.2. Dynamic data**

The following table gives a list of inputs required for algorithm input and calibration:

Table 3: IMAGE AND CALIBRATION INPUTS

Parameter	Resolution	Quantization
Radiometric and geometric corrected gray count values of VIS channel (0.65)	4 Km (at present) 1 Km (Testing TBD)	10 bit
Radiometric and geometric corrected gray count values of SWIR channel (1.66)	4 Km (at present) 1 Km (Testing TBD)	10 bit
Gray value to albedo (VIS and SWIR) conversion table	-	-
Geolocation file	4 Km (at present) 1 Km (Testing TBD)	-

#### 11.5.3. Other Auxillary data and Model Inputs

Table 4: AUXILARY DATA

Parameter	Resolution
Solar Zenith Angle	4 Km (at present) 1 Km (Testing TBD)
Satellite Zenith Angle	4 Km (at present) 1 Km (Testing TBD)
Satellite Azimuth angle	pixel

### 11.6. Algorithm Functional Specifications

In this section we describe the theoretical basis and algorithm overview for deriving cloud microphysical parameters using INSAT-3D channels.

#### 11.6.1. Overview

The underlying principle on which the retrieval of these microphysical parameters is based is the fact that the reflection function of clouds in the visible band is primarily a function of the cloud optical thickness, whereas the reflection function at a water (or ice) absorbing band in the shortwave infrared (SWIR) is primarily a function of cloud particle size.

#### 11.6.2. Theoretical Background

The visible ( $0.7\mu\text{m}$ ) channel is a non-absorbing channel; the reflectance depends only upon the cloud optical depth. Hence, there is a very significant difference between the radiances of very thick clouds and thin clouds in the visible spectrum. The radiance values are higher for very thick clouds as compared to thin clouds. This kind of behaviour indicates a pronounced effect of optical depth on the visible portion of the spectrum. For the SWIR bands, the droplet absorption increases

approximately linearly with effective radius, and hence the asymptotic reflectance of a cloud decreases with increasing particle size. Thus the visible band contains information primarily regarding cloud optical thickness, whereas the absorbing bands eventually reach an optical thickness where they are primarily dependent on particle size alone. A combination of visible and shortwave-infrared absorbing bands therefore provides information on both optical thickness and effective radius.

### 11.6.3. Algorithm Overview

To retrieve the cloud optical thickness ( $\tau_c$ ) and effective particle radius ( $r_e$ ), a radiative transfer model was first used to compute the reflected intensity field. The values of the reflection function were stored for different combinations of cloud optical thickness and particle size at three geometrical angles in the form of a look-up-table. The determination of optical thickness and cloud effective radius from spectral reflectance measurements constitutes the inverse problem. This has been solved by comparing the measured reflectances of INSAT-3D visible and SWIR channels with entries in the lookup table (LUT) and searching for the combination of  $\tau_c$  and  $r_e$  that gives the best fit.

In the present case, we have used SBDART (Santa Barbara DISORT Atmospheric Radiative transfer) radiative transfer model for computing the LUT. SBADART computes plane parallel radiative transfer in clear and homogeneous cloudy conditions within the Earth's atmosphere for the region from 0-50,000  $cm^{-1}$  (Ricchiazzi et al., 1998). SBDART can compute the radiative effects of several lower and upper atmosphere aerosol types. The radiative transfer equation is numerically integrated with DISORT. This module was designed to treat the plane parallel radiative transfer. The discrete ordinate method provides a stable algorithm to calculate the plane parallel radiative transfer equation in vertically inhomogeneous atmosphere. SBDART contains pre-computed scattering parameters for the effective radii in the 2-128 $\mu m$  range. In order to compute the radiative transfer through the cirrus clouds, it also includes scattering parameters of spherical ice grains for single size distribution. SBDART computes intensity of scattered and thermally emitted radiation at different heights. It allows up to 50 atmospheric layers and 20 radiation streams.

The determination of cloud optical depth and cloud effective radius from spectral reflectance measurements constitutes the inverse problem and is typically solved by comparing the measured reflectances with entries in a lookup table and searching for the combination of  $\tau_c$  and  $r_e$  that gives the best fit (Twomey and Cocks 1982, 1989).

#### 11.6.4. Flow Chart

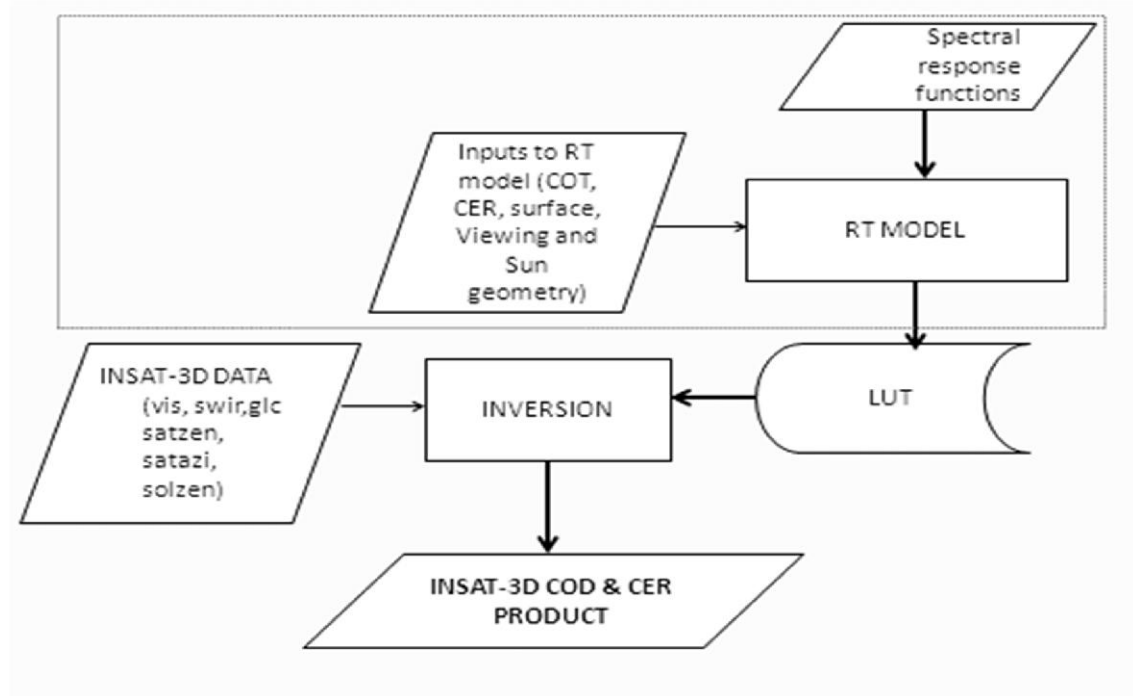


Figure 1: Flow diagram for cloud microphysical parameter retrieval

#### 11.7. Operational retrieval implementation

The operational implementation of the retrieval process can be enumerated as follows:

- Generation of random values within range of solar zenith angle (SZA), cloud optical depth, cloud effective radius
- Running of RT model for the random vectors and range of satellite zenith (satzen) and azimuth angles (satazi) to generate LUT for visible and swir channel
- The input random vectors and corresponding LUT is stored.
- Steps (1-3) are offline processes.
- In online algo, pixel wise value of swir radiance, vis radiance, SZA, satzen, satazi are taken as input. Using land-sea mask, only oceanic geo-type pixels are chosen.
- A triple vector search is performed in input fields of LUT to find closest sun –satellite geometry.
- The corresponding simulated radiances in visible and swir channels is compared with observed radiance from INSAT-3D for cloudy pixels to get the best match, and corresponding values of COD and CER are assigned to that pixel.

## 11.8. Output (over Ocean)

Parameter	Unit	Accuracy	Resolution
Cloud Optical Depth	None	TBD	Pixel
Cloud Effective Radius	$\mu\text{m}$	TBD	pixel

## 11.9. Initial Validation

The initial validation by comparing with MODIS is given in the table below

Month	No. of collocated points	Correlation coefficient		RMSD	
		COD	CER	COD	CER ( $\mu\text{m}$ )
January 2016	10945	0.60	0.40	12.4	6.5
July 2016	45250	0.69	0.47	13.3	5.7

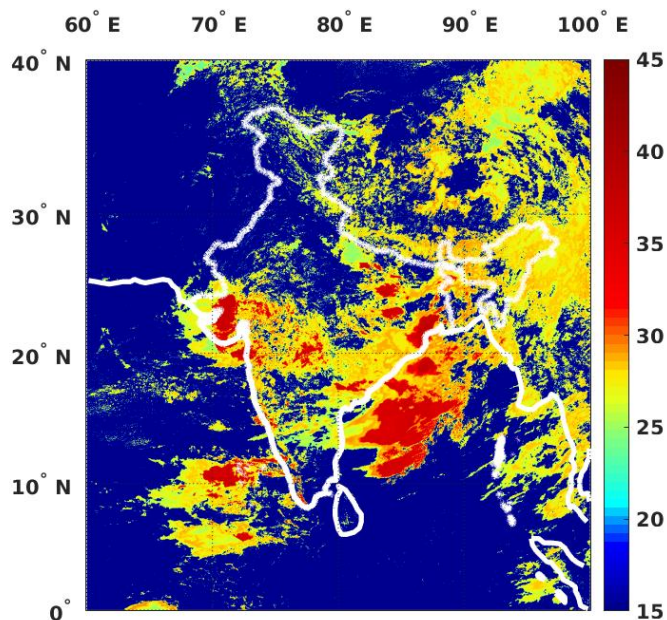


Figure 2(a) INSAT-3D Cloud Effective Radius

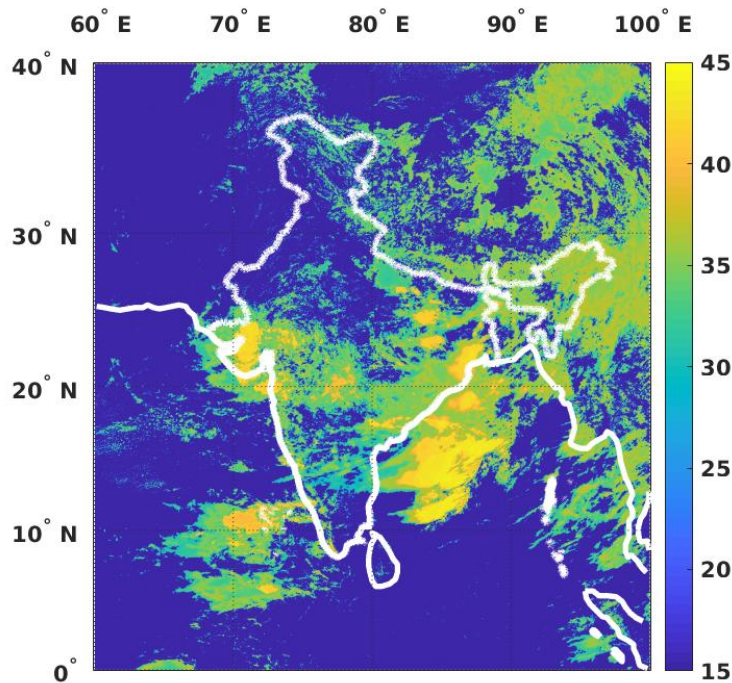


Figure 2(b) INSAT-3D Cloud Optical Thickness

### 11.10. Limitations

- Only daytime detection is possible.
- Multi-level clouds can be a major source of error.
- In case of thin clouds or highly inhomogeneous clouds , there may be inaccuracy.
- Other sources of errors will include cloud water vapour absorption, inaccuracy in cloud top height assumptions, drizzle in cloud.

### 11.11. Future work

- To test the current algorithm for 1-km resolution sector VIS-SWIR radiance product (currently not operational).
- With support from IMD, NCMRWF, validation will also be carried from in-situ, aircraft campaigns and earlier campaign data from IITM. However, issues arising out of the dynamic nature of clouds and their sampling from different platforms can result in non-converging results.

## References

- Stephens, G. L., and P. J. Webster, 1981: Clouds and climate: Sensitivity of simple systems. *J. Atmos. Sci.*, 38, 235–247.
- Roebeling, R. A., A. Berk, A.J. Feijt, W. Frerichs, D. Jolivet, A. Macke and P. Stammes, 2005: Sensitivity of cloud property retrievals to differences in radiative transfer simulations.
- Twomey, S., and T. Cocks, 1982: Spectral reflectance of clouds in the near infrared: Comparison of measurements and calculations. *J. Meteor. Soc. Japan*, 60, 583–592.
- Twomey, S., and T. Cocks, 1989: Remote sensing of cloud parameters from spectral reflectance in the near-infrared. *Beitr. Phys. Atmos.*, 62, 172–179.
- Ricchiazzi, P., Shiren Yang, Catherine Gautier, and David Sowle, 1998: SBDART: A Research and Teaching Software Tool for Plane Parallel Radiative Transfer in the Earth's Atmosphere, *Bull. Amer. Meteor. Soc.*, 79, 2101-2114.

## **12. 5-Day Composite Atmospheric Motion Vectors (AMV)**

S. No.	Product Name	Spatial Resolution	Temporal Resolution
1	IMG_AMV5	Tracer size : $1^{\circ} \times 1^{\circ}$	5-day

## **12.1. Algorithm Configuration Information**

### **12.1.1. Algorithm Name**

5-Day Composite Atmospheric Motion Vectors (AMV)

### **12.1.2. Algorithm Identifier**

ISRO\_INSAT\_PRO\_AMV\_COM\_A001

### **12.1.3. Algorithm Specification**

Version	Date	Prepared by	Description
1.0	26.06.2018	S. K. Deb, and C.M. Kishtawal	5-DAY AMV composite Maps 5-DAY AMV Composite Maps At following layers: 1. High-Level (100-400 hPa) 2. Mid-Level (401-700 hPa) 3. Low-Level (701-950 hPa)

## **12.2. Introduction**

The purpose of this document is to present the methodology for deriving 5-day composite maps using Atmospheric Motion Vectors (AMVs) from INSAT-3D/3DR at different broad atmospheric levels. The out of six imager channels in INSAT-3D/3DR, AMVs are derived using four channels and they are: i) Visible (VIS) covering [0.55 – 0.75  $\mu\text{m}$ ], ii) Mid-wave Infrared (MIR) covering [3.8 – 4.0  $\mu\text{m}$ ], iii) Water Vapor (WV) covering [6.5 – 7.1  $\mu\text{m}$ ] and iv) Thermal Infrared (TIR1) covering [10.2 – 11.3  $\mu\text{m}$ ] ranges of spectrum respectively. In this document some background and general characteristic of different AMV-derived products; the methodology employed to derive the 5-day composite maps are presented.

## **12.3. Overview and background**

The Atmospheric Motion Vectors (AMVs) derived by considering the movement of cloud and water vapour tracers in successive images of geostationary satellites (Nieman et al., 1997; Velden et al., 1997; Schmetz et al., 1993; Kishtawal et al. 2009) are considered as one of the most reliable source of wind information with higher spatial-temporal coverage over the ocean as well as land regions. The AMVs is one of the important inputs to the global and regional assimilation systems for the improvement of Numerical Weather Prediction (NWP). The role of AMVs is particularly significant over the oceans and high latitudes where in-situ observations are scarce. The vertical coverage of AMVs spreads through high to low-levels as per the channel used during retrieval viz. AMV retrieved using: i) infrared channel data covers entire ranges of atmosphere i.e. from 100-950 hPa, ii) water vapour channel data covers only high-level i.e. from 100-500 hPa, while iii) visible and mid-infrared channel data covers low-levels i.e. from 600-950 hPa respectively. 5-Day

composite winds maps derived using the retrieved AMVs in three broad atmospheric levels are very useful for monitoring of monsoon flows over Indian region. The following Fig-1 shows an example of weekly low-level monsoon flow for the weeks viz. 01-07 July 2017 and 08-14 July 2017 respectively.

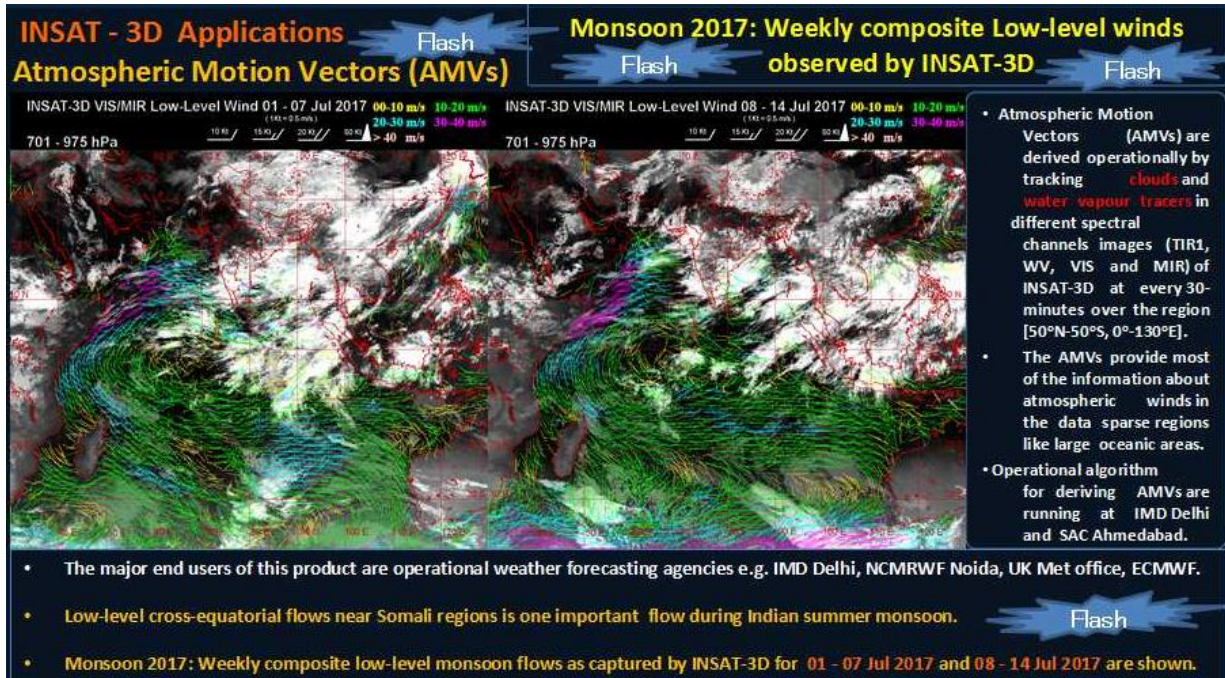


*Figure-1: Low-level (701 - 950 hPa) weekly monsoon flow derived using visible AMVs for the weeks 01-07 July 2017 and 08-14 July 2017 respectively.*

This type of 5-day composite wind map derived from AMVs can be used to monitor the progress of monsoon on operational basis.

## 12.4. Objective

The main objective of this study is to discuss the procedure for deriving the 5-day composite wind maps derived using atmospheric motion vectors (AMVs) retrieved from INSAT-3D/3DR over land and sea at every half-hour interval. The region over which these products will be retrieved is same as the domain where AMVs are retrieved i.e. in the region 30-130E, 50S-50N.

## 12.5. Inputs

### 12.5.1. Retrieved AMVs (Dynamic)

Parameter	Resolution	Accuracy
AMV retrieved from TIR1 channel of INSAT-3D/3DR	Spatial: 120km x 120km Temporal: 30 Minutes	5 to 6 m/s (high/mid levels) 1 to 4 m/s (low-levels)
AMV retrieved from WV channel of INSAT-3D/3DR	Spatial: 120km x 120km Temporal: 30 Minutes	6 to 5 m/s (in high level)
AMV retrieved from VIS channel of INSAT-3D/3DR	Spatial: 120km x 120km Temporal: 30 Minutes	2.5 to 3 m/s (in low-levels)
AMV retrieved from MIR channel of INSAT-3D/3DR	Spatial: 120km x 120km Temporal: 30 Minutes	3 to 4 m/s (in low-levels)

## 12.6. Algorithm Functional Specifications

### 12.6.1. Methodology

To compute 5-day composite of AMV maps for three broad atmospheric levels (high, mid and low-levels), retrieved scattered AMVs, available at 30-minutes interval, are gridded into 0.5 degree x 0.5 degree horizontal resolution covering the areas 0E-130E, 50S-50N and by taking 50 hPa vertical difference. The vertical pressure levels considered in this case are: 100, 150, 200, 250, 300, 350, 400, 450, 500, 550, 600, 650, 700, 750, 800, 850, 900, 950 hPa respectively. Where-ever AMV is not available an undefined value of -999 are assigned to the grid point. Once gridded AMV at every 30-minute interval is generated, 5-day composite maps are generated by taking average of all available AMVs for a particular grid point.

- i) High-level Map: Gridded AMVs available in the levels 100 hPa to 400 hPa are averaged for 5-Day to generate 5-Day composite High-level Map.
- ii) Mid-level Map: Gridded AMVs available in the levels 401 hPa to 700 hPa are averaged for 5-Day to generate 5-Day composite mid-level Map.
- iii) Low-level Map: Gridded AMVs available in the levels 701 hPa to 950 hPa are averaged for 5-Day to generated 5-Day composite low-level Map

### 12.6.2. Operational Implementation

**Step 1:** Extracting 30-minute AMVs from HDF5 file for current acquisition time.

**Step 2:** 30-minutes AMV are gridded into 05 x 05 degree horizontal resolution and 18 vertical levels.

**Step 3:** 5-day average is done to generate 5-Day composite AMV map for High, Mid and Low-levels.

## 12.7. Outputs

Parameters	Unit	Minimum	Maximum	Accuracy	Resolution
5-Day AMV composite Maps (running averaged) for High (100-400 hPa), Mid (401-700 hPa) and Low (701-950 hPa) (i.e. GIF/TIF images) at every 30-minute interval	Not Applicable  High-Level : TIR1 and WV AMVs available in 100-400 hPa  Mid-Level : TIR1, WV and VIS/MIR AMVs available in 401-700 hPa  Low-Level: TIR1 and VIS/MIR AMVs available in 701-950 hPa				
	Domain: 0-130°E, 50°S-50°N				

### **13. High Resolution Visible Winds (HRVIS)**

S.No.	Product Name	Spatial Resolution	Temporal Resolution
1	3RIMG_L2P_HVW	Point (Tracer location)	30 minutes

## **13.1. Algorithm Configuration Information**

### **13.1.1. Algorithm Name**

High Resolution Visible Winds (HRVIS)

(Ref : IMD RFP Section 11.14 )

### **13.1.2. Algorithm Identifier**

3RIMG\_L2P\_HVW

### **13.1.3. Algorithm Specification**

<b>Version</b>	<b>Date</b>	<b>Prepared by</b>	<b>Description</b>
1.0	04.08.2018	S.K. Deb, C.M. Kishtawal, Dineshkumar K. Sankhala	Visible winds Baseline Document

## **13.2. Introduction**

The purpose of this document is to present an algorithm for retrieving High Resolution Visible Winds (HRVIS) from INSAT-3DR imager channel and its validation procedure. The INSAT-3DR will have one visible channel (0.55 – 0.75 (m). In this document some background and general characteristic of satellite-derived winds from visible channels and INSAT-3DR visible channel characteristics; the methodology employed to derive the vector fields, theoretical basis and practical aspects of this algorithm and outlined the planned validation approach.

### **13.2.1. Overview and background**

Spatio-temporal analysis of meteorological events is an important part of routine numerical weather analysis. In that context, a cloud tracking method is presented here for a sequence of geostationary satellite images. Given a pair of remotely sensed images, captured at a fixed time interval (typically, 30 min), the objective is to derive motion vectors associated with the cloud mass. This correspondence process is a useful precursor to cloud motion vector studies and spatio-temporal analysis of cloud life cycles. The spatio-temporal life cycle includes the generation, dissipation and assimilation of clouds that can be observed in a sequence of geostationary satellite images. During the 1970's and early 1980's, cloud motion winds were produced in major operational centers like NESDIS (National Environmental Satellite Data and Information Service) using a combination of automated and manual techniques. Early automated techniques supplied quality low-level vectors from visible channels but often yielded in consistent quality for mid- and high-level motions. Height assignment for the visible winds is done with collocated infrared images using infrared window technique. In the subsequent years, due to the developments in image-processing and pattern recognition techniques (Merill et al., 1991), it was possible to design fully automatic techniques for wind retrieval, and NESDIS began its application in 1992. In later

time, several new developments were made to make accurate retrievals of winds from satellite images.

### **13.2.2. Objective**

The main objective of this study is to derive the High Resolution Visible Winds (HRVIS) over sea using multiple successive half hourly High resolution visible images. The region over which the winds are derived should be in the range of 500 from sub-satellite point.

## **13.3. Inputs**

### **13.3.1 Static Data**

Parameter	Resolution	Source
Continental boundary data	1 km	DP (IMD data)

### **13.3.2. Image and preprocessing data (Dynamic)**

Parameter	Resolution	Quantization	Accuracy
Radiometric and geometric corrected gray count values of split window IR channel (10.5-11.5 $\mu\text{m}$ and 11.5-12.5 $\mu\text{m}$ ) and VIS channel (0.65 $\mu\text{m}$ )  (All the data is required in fixed lat-lon grid for continuous 4-images separated by 30 minutes time interval)  L1C-sector generated product at 1 Km resolution	pixel	10 bit	--
Gray value to brightness temperature conversion table	-	-	0.3 K
Geo-location file	Pixel	-	1 km

### 13.3.3. Other Auxiliary data and Model Inputs

Parameter	Resolution	Accuracy	Source
Numerical model forecast of wind for all levels	0.5 degree	2 m/s (speed) 20° (direction)	NCEP
All levels model forecast Temperature		1° K	

## 13.4. Algorithm Functional Specifications

### 13.4.1. Tracer selection:

At the National Environmental Satellite, Data, and Information Service (NESDIS), the initial cloud features are selected by locating the highest pixel brightness values for each target domain and computing the local gradients around those locations ([Nieman et al., 1997](#)). Any gradients greater than 15° K are assigned as target locations, and prospective targets also undergo a spatial coherence analysis ([Coakley and Bretherton, 1982](#)) to filter out unwanted targets. Water vapor tracers are generally identified using the local bi-directional gradients in a template of specified size and compared with empirically determined thresholds to identify the features with sufficient variability ([Velden et al., 1997](#)) and those that pass the threshold value are identified as tracers for cloud-free environments. The pixel with maximum bi-directional gradient is the location of the tracer. At the European Organization for the Exploitation of Meteorological Satellites (EUMETSAT), the tracers in the Meteosat (first-generation satellites) images are selected using multispectral histogram analysis ([Tomassini, 1981](#)), which extracts the dominating scenes in an image segment. Later the selected templates undergo a spatial coherence analysis ([Coakley and Bretherton, 1982](#)) to filter the image, to enhance the upper-level cloud. In the present study the features are selected by computing local image anomaly in a 24 x 24 template window (in pixel), both in cloudy regions of the visible images. The local image anomaly is calculated using the following formula:

$$a = \sum_i \sum_j |I(i, j) - \bar{I}| \quad (1)$$

Where  $I(i, j)$  represent the grey value for  $(i, j)$  pixel of a template window and bar represents the mean of grey values within that template. The anomaly-based tracers are generally produced by a smooth feature field in comparison to the gradient-based features. This difference can help in reducing the tracking errors ([Deb et al., 2008](#)).

### **13.4.2. Height assignment**

The height assignments of the selected tracers selected based on the above criterion are derived using the collocated infrared images with the following widely used methods viz. such as the infrared window (WIN) technique and the cloud base method ([LeMarshall, 1993](#)). Once final height is selected a few gross error checks are also applied. A brief description of each method is following:

#### **(a) Infrared Window Channel (WIN):**

In this method the height assignment using a single satellite channel is made by comparing either infrared window brightness temperature (BT) values with NWP model forecast temperature profiles. Cloud heights are determined by interpolating the cloud temperature, which is an average of coldest 20% of pixels, to the interpolated model guess field at the target location. A 6-h NWP model forecast from National Center for Environmental Prediction (NCEP) Global Forecast System (GFS) is the source of temperature profile. This method works well with opaque clouds. However, movement of opaque clouds usually does not accurately represent atmospheric motion at the assigned level ([Nieman et al., 1993](#)), resulting in a lower derived wind speed than observed.

#### **(b) Cloud Base Method (BASE):**

Wind speeds for low-level cumulus clouds (cloud top pressures greater than 600 hPa or altitudes lower than 600 hPa) have been found to be best represented by the movement at the cloud base level instead of the mid or upper levels of the cloud ([Hasler et al., 1979](#)). A method was developed at the Australian Bureau of Meteorology ([LeMarshall, 1993](#)) to estimate this height using the Infrared Window channel. This method first constructs a histogram of the BT values over a selected region surrounding the cloud target being examined. This histogram is then smoothed and Hermite polynomials are fitted to the histogram to separate the distribution into two components; a cloudy and clear sky region. Assuming the distributions are normal, the cloud base height can be estimated. The mid cloud temperature is determined by examining the second derivative histogram of the cloudy distribution, while the cloud top temperature is estimated to be located at the coldest 5% of the cloudy distribution. The cloud base temperature is estimated to be located the same distance from the mid cloud temperature as the cloud top temperature. The calculated cloud base temperature is converted to a pressure using model field interpolated to the target location. As mentioned previously, this height assignment method is only applied to those targets which are calculated to have a cloud top pressure of greater than 600 hPa (i.e. altitude lower than 600 hPa). This "initial" target cloud top height is provided by one of the previous Infrared Window height assignment methods. The BASE method is used to adjust only these winds, and is not utilized for water vapor winds or winds with pressures less than 600 hPa (i.e. altitudes higher than 600 hPa).

Once the visible tracers heights using the above two algorithms have been calculated, the best height among the available heights is determined. The lowest pressure (highest altitude) value of all the calculated height values is used as the final pressure height. However, if for a specific visible

tracer final height is WIN and a valid BASE height is available, then the BASE height is used as the final height. Once the final height using the above height assignment method is established, the pressure height is optimized using minimized differences with first guess winds up to 75 hPa in upwards and downwards directions.

### 13.4.3. Tracking

If a traceable feature is found in the first image and corresponding height of the selected tracers are estimated, the match of this template is searched in the second image within a bigger “search window”, centered at the same point as the template window. To optimize the search window size, the first guess model wind direction at the tracer location is also considered. The search area is optimized within  $\pm 30$  degree from the model wind direction at that level of atmosphere. The 24 X 24 template (in pixel) in the second image that lies within the search window should have the same class as the template in the first image; otherwise the template in the second window is rejected. The cross-correlation technique is used operationally for tracking the tracer between two images in most operational centers. However, in this study the degrees of matching between two successive images are calculated by the Nash-Sutcliffe model efficiency ([Nash and Sutcliffe, 1970](#)) coefficient ( $E$ ). It is defined as

$$E = 1 - \frac{\sum_{i=1}^n (I_t - I_s)^2}{\sum_{i=1}^n (I_t - \bar{I}_t)^2} \quad (2)$$

Where  $I_t$  and  $I_s$  are the variance of the grey values for template window and search window and  $\bar{I}_t$  is the average of variance of template window. Here  $n$  is 24 x 24 (in pixel) and this is the size of template window and corresponding template of same size in the searching area. The size of the searching area in the subsequent image is taken as 64 x 64 (in pixel). The coefficient  $E$  is normalized to values between  $-\infty$  and +1. An efficiency  $E = 1$  corresponds to a perfect match,  $E = 0$  means that search window is as accurate as mean of the template window and  $E < 0$  implies the lack of matching between template and search window. The closer the model efficiency to 1, the more accurate the matching between the windows. A cut-off value of  $E=0.8$  is defined, below which a matching of target is not considered. The Nash-Sutcliffe model efficiency coefficient ( $E$ ) is normalized and its value lies between  $-\infty$  and 1, towards the higher end (e.g. as  $E \rightarrow 1.0$ ), the value of  $E$  approaches  $r^2$ , where  $r$  is the correlation coefficient. Thus a value of  $E=1$  is exactly equivalent to a correlation of 1.0 between two objects. The maximum value of  $E$  is chosen as the best fit for tracking. One of the main advantages of this matching technique is that it reduces the possibility of multiple maxima, because the parameter  $E$  has a higher sensitivity to differences between two features compared to maximum cross correlation coefficient (MCC). Thus, when the degree of mismatch between two objects increases, the value of  $E$  falls more sharply compared to that of MCC, making  $E$  a better index for matching two objects. The application of this tracking

method in estimation of water vapor winds has shown some improvement over Indian Ocean region ([Deb et al., 2008](#)).

#### 13.4.4. Wind buffer generation and Quality control

Quality indicator of a derived wind vectors is traditionally represented as the degree of the coherence of a given vector with its surrounding. In most of the operational centers the AMVs are derived from three successive satellite images and the quality control of the retrieved winds are done either through Quality Indicator (QI) ([Holmlund, 1998](#)) followed at EUMETSAT or through 3-dimensional recursive filter function followed at NESDIS ([Nieman et al., 1997](#)) or both the algorithms together. In the present study a new technique of wind buffer generation and subsequently QI procedure followed at EUMETSAT is proposed. In this technique, a wind buffer is created using previous three images between a pair of images (viz. between 1-2 and 2-3) and stored in a file (**Fig. 1**). The previous three images were considered to maintain the minimum 4-hour decorrelation timescale during retrieval. In quality control procedure consists of a coherence analysis which forms the basis for acceptance/rejection of a vector and degree of coherence computed is used to assign quality flags to the derived vector. The value of quality flag falls sharply by an exponential function, as the disagreement of a given vector with its surroundings increases. Here each vector wind is represented by a complex number  $V_{i,j}^c = u_{i,j} + i v_{i,j}$ . For every new vector under consideration, (from current image-pair), its vector difference from the buffer is computed at the same as well as 3 X 3 neighborhood (**Fig. 1**), provided, the vectors to be compared show similar brightness characteristics (to maintain the similar height).

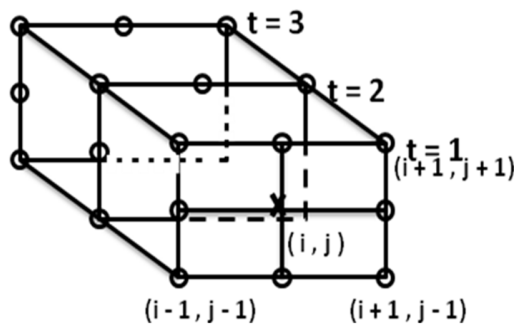


**Fig 1:** A schematic diagram of quality control process.

Here X (cross sign) at the centre of first box represents the current vector under consideration and O (circle sign) represents spatial and temporal neighborhood vectors. The vector differences (magnitude of complex numbers) are calculated as  $\{V_{dif}\}_{i,j,t} = V^c - \{V\}_{i,j,t}$ . Here  $V^c$  represents the current vector at  $(i, j)$  point and  $\{V\}_{i,j,t}$  neighborhood vectors with  $-1 \leq i \leq 1, -1 \leq j \leq 1$  and temporal scale  $t$  varies from 1 to 3. If all spatial and temporal neighborhood vectors are present, then the difference set will contain 27 vectors (9 spatial neighborhoods with 3 temporal scales). However, all vectors may not be there all the times. The quality control process begins if at least 10 vector differences  $V_{dif}$ , excluding the difference corresponding to current  $(i, j)$ , are present in

the set. In the next step, set of vector differences  $\{V_{dif}\}$  is arranged in ascending order. The quality control process begins is the average of 10  $V_{dif}$  is greater than 2.5 m/s. In the next step, the QI value for each vector is determined by using EUMETSAT procedure where four different tests are performed, which is normalized by a tanh-function that returns the value between 0 and 1. A weighted average of these individual quality indicators is then used for screening of poor quality vectors from final output. If any vector is not present in the immediate two pairs, then instead of rejecting, search process goes to the previous time steps of the wind buffer and if still it is not present it goes to next previous times steps and so on.

If  $S$  is the mean “speed” of a vector computed from two pair of images, then different quality functions are computed as below:

**Direction Consistency Function:**

$$DCF = 1.0 - \left[ \tanh\left(\frac{\Delta\theta}{A_1 \exp(-S/B_1) + C_1}\right)\right]^{D_1}$$

**Speed Consistency Function:**

$$SCF = 1.0 - \left[ \tanh\left(\frac{\Delta S}{MAX(A_2 S, B_2) + C_2}\right)\right]^{D_2}$$

**Vector Consistency Function:**

$$VCF = 1.0 - \left[ \tanh\left(\frac{\Delta V}{MAX(A_3 S, B_3) + C_3}\right)\right]^{D_3}$$

**Spacial Consistency Function:**

$$PCF = 1.0 - \left[ \tanh\left(\frac{\Delta V_m}{MAX(A_4 S, B_4) + C_2}\right)\right]^{D_4}$$

In the above formulation,  $\Delta\theta, \Delta S, \Delta V$  represent the difference of direction (degrees), difference of speed, and the length of the difference vector between first and second satellite wind component.  $\Delta V_m$  is the length of difference vector between satellite wind component and its best neighbor. The best neighbor is determined by the smallest vector difference. Quantities  $A_N, B_N, C_N$ , and  $D_N$  are constants. The final quality indicator of a wind vector is given as

$$QI = \frac{DCF + SCF + VCF + PCF}{4.0}$$

All the vectors with  $QI < 0.6$  are rejected.

The constant quantities  $A_N, B_N, C_N$ , and  $D_N$  are chosen as:

Direction consistency	A1	50	Vector consistency	A3	0.8
	B1	15		B3	0.01
	C1	15		C3	1.0
	D1	8		D3	5.0
Speed consistency	A2	0.5	Spatial consistency	A4	0.2
	B2	0.01		B4	0.01
	C2	2.0		C4	1.5
	D2	0.7		D4	0.75

In the conventional triplet based methodology requires that a vector is available in both sets (i.e. in 1-2 and 2-3), if not so, such vectors are rejected, because they don't get "support". Hundreds of "isolated" vectors thus get eliminated, even though they represent the real situation. In the current method, the vector under consideration receives support from the past eight images. This method produces higher number of valid retrieval in the low-level and captures upper-level meridional flow very prominently. To explain this more explicitly, if we take three satellite images each with 30-minute interval starting at 02:30 UTC to 03:30 UTC, then winds retrieved using each-image pair are stored as buffer in a file and represented as wind buffer generated at 03:30 UTC. The buffer generated at 03:30 UTC is used for quality control for wind retrieved using 03:30 UTC and 04:00 UTC images and the second image time is given as actual observation time of retrieved wind. For example, winds retrieved using 03:30 UTC wind buffer and 03:30 UTC and 04:00 UTC images is given as 04:00 UTC observation time. As a whole to complete the process once it requires four images. Similarly, the buffer is updated at every 30-minute with the latest available image and process is repeated for next cycle of wind retrieval. This method produces higher number of valid retrieval in all levels and captures upper-level meridional flow very prominently.

### 13.5. Operational Implementation

#### Step 1: Tracer selection from image

- Cloud tracer selection will be done by evaluating the local image anomaly surrounding each pixel in the target array and selecting the maximum brightness temperature of the window.

## **Step 2: Height assignment**

- Assign height of the selected tracer using IR window technique. In this case the brightness temperature in the target window will be averaged and matched with collocated numerical model temperature profile. The level of optimum fit will be assigned as initial height.
- Re-assign the height using cloud-base height assignment technique.
- Assign correct height after implementing all the height assignment technique mentioned above.

## **Step 3: Tracking**

- The tracking employs a simple search for the mean absolute difference of the radiance difference between the target and search arrays in subsequent half hourly images. This search will be done in the direction of  $\pm 30^\circ$  of model wind.

## **Step 4: Wind buffer generation & quality control**

- The wind buffer is created using previous three images between pairs of images (viz. the winds retrieved between 1-2 and 2-3) and stored in a file. The selection of three images is consistent with decorrelation timescales of winds over tropical region.
- Use quality control criteria for selecting wind using the wind buffer.
- Calculate wind speed and direction.

## **13.6. Outputs**

Parameter	Unit	Min	Max	Accuracy	Resolution
U and V component of HRVIS	m/sec	0	90	2-3 m/sec (lower level)	--
Domain of output : $30^\circ\text{E} - 130^\circ\text{E} :: 50^\circ\text{S} - 50^\circ\text{N}$					

### **13.6.1. Format of the output and the domain**

As output of HRVIS wind the following parameters will be provided to IMD:

- Zonal and meridional components of the wind vectors.
- Latitudinal and longitudinal position.
- Height of wind

The format of the final product:

Parameter	Lat	Lon.	Level	U-component	V-component	Quality Flag	Wind Speed (m/s)	Wind direction (clockwise from North)	Wind zenith angle
Unit	°N	°E	hPa	m/s	m/s	0.0 to 0.9	m/s	Deg	Deg

## 13.7. Validation

### 13.7.1. Data required

Parameter	Type	Source
Wind	Collocated Radiosonde Profiles	IMD

### 13.7.2. Methods of validation

The evaluation of HRVIS winds should be taken into both qualitative and quantitative measures. Quantitative assessment of the HRVIS winds product is possible from statistical analyses and impact on NWP. The traditional method of validation is matching observations with collocated radiosondes. The statistical validation will be done according to the CGMS winds evaluation reporting guidelines. These statistics can provide a fixed measure of product quality over time and can be employed in determining observation weight in objective data assimilation. At the CGMS XXIII the Working Group on Satellite Tracked Winds recommended that evaluation of operational wind production quality should be accomplished with a new standardized reporting method. The recommended three parts to the report.

- i) Monthly means of speed bias and rms vector difference between radiosondes and satellite winds for low (>700 hPa), medium (700-400 hPa), and high (< 400 hPa) levels together with the radiosonde mean wind speed. This should be done for three latitude bands: north of 20 N, the tropical belt (20 N to 20 S), and south of 20 S.
- ii) Trends of the evaluation statistics for the monthly cloud motion vectors and water vapor motion vectors through the last 12 months.
- iii) Information on recent significant changes in the wind retrieval algorithm.

The vector Difference (VD) between an individual wind report (i) and the collocated radiosonde report used for verification is given by

$$(VD) = [(U_i - U_r)^2 + (V_i - V_r)^2]^{\frac{1}{2}}$$

The speed bias is given by

$$(BIAS)_i = \frac{1}{N} \sum_{i=1}^N [(U_i^2 + V_i^2)^{\frac{1}{2}} - (U_r^2 + V_r^2)^{\frac{1}{2}}]$$

The mean vector difference (MVD) traditionally reported is

$$(MVD) = \frac{1}{N} \sum_{i=1}^N (VD)_i$$

And the standard deviation (SD) about the mean vector difference traditionally reported is

$$(SD) = [\frac{1}{N} \sum_{i=1}^N ((VD)_i - (MVD))^2]^{\frac{1}{2}}$$

The root-mean-square error (RMSE) traditionally reported is the square root of the sum of the squares of the mean vector difference and the standard deviation about the mean vector difference,

$$(RMSE) = [(MVD)^2 + (SD)^2]^{\frac{1}{2}}$$

It must be noted that this definition of the mean vector difference is not the same as the mean component difference. The mean difference is calculated from the sum of the squares of the deviations of each component (u and v) of the wind vector.

$$\begin{aligned} (\Delta U^2) &= \sum_{i=1}^N (U_i - U_r)^2 \\ (\Delta V^2) &= \sum_{i=1}^N (V_i - V_r)^2 \end{aligned}$$

To avoid confusion, a common terminology will be accepted. It is suggested to report mean vector difference (MVD) and standard deviation (SD). The standard accuracy according to CGMS guideline for CMV is that the root mean square error (RMSE) for WV winds should be 7m/s respectively with respect to radiosonde observations. The mean bias for both sets of winds should be about zero.

### 13.8. Technical Issues (Limitations etc.)

Accuracy of the product depends on the accuracy of the registration of the images. If the registration has an error of 1 pixel, then error of the final product will be increased. However, the following limitations of the present study have to be kept in mind. However, the retrieved vectors in regions are lacking in defining moisture structure, though they have the ability to obtain trackable information in extremely dry air masses and regions of strong subsidence is limited. The

individual vectors represent single level reports; however, upper level vertical winds profiles are possible by using multi-spectral observations.

**a) Sensitivity of error in height assignment to the error in wind speed retrieval**

This sensitivity will depend upon the structure of wind circulation over different vertical levels as well as different geographical regions. For example, in the vicinity of atmospheric jets, the retrieved wind vectors will be highly sensitive to the errors in the assigned pressure levels. Based on some standard analysis (e.g. NCEP reanalysis of 6-hourly sampling), we will provide a quantitative assessment of the vertical and spatial structure of this sensitivity.

**b) Numerical model to be used for AMV height assignment**

We plan to use IMD's operational regional model output during height assignment procedure. However, if the domain of this regional model is smaller than the area of AMV retrieval, either IMD may be requested to increase the domain of its operational model, or a lower-quality solution based on the output of coarser-resolution GCM will be generated over the regions not covered by IMD's regional model.

**c) Whether RT model to be used in real-time for height assignment**

To use RT model in real-time height-assignment application is generally required to find the optimum solution. However, it is computationally expensive and may increase the AMV turn-around time very significantly. Efforts are currently underway to develop an empirical version of RT model that can be used for simulation of IR and water-vapor channel radiances for a variety of cloud heights. The inverse of this empirical model will then be used in real-time applications.

**d) Comparison of maximum-correlation and minimum-difference methods for tracking of cloud-tracers.**

The comparison has been made for a large number of image samples and it was found that the efficiencies of minimum-difference method (MDM) and maximum cross correlation (MCC) methods are comparable, while the MDM method is significantly faster than MCC.

## References

- Bedka KM, Mecikalski JR (2005) Application of satellite-derived atmospheric motion vectors for estimating meso-scale flows. *Journal of Applied Meteorology* 44: 1761-1772.
- Deb SK, Kishtawal CM, Pal PK (2010). Impact of *Kalpana-1* derived water vapor winds on Indian Ocean Tropical cyclones forecast. *Monthly Weather Review* 138 (3): 987-1003.

Deb SK, Kishtawal CM, Pal PK, Joshi PC (2008) A modified tracer selection and tracking procedure to derive winds using Water vapor imagers. *Journal of Applied Meteorology and Climatology* 47: 3252-3263.

Deb SK, Kishtawal CM, Kaur Inderpreet, Pal PK, Kiran Kumar AS (2012a). Multiplet based Technique to derive Atmospheric winds from Kalpana-1, *The Proceedings 11<sup>th</sup> International Wind Workshop*, 20-24 February, 2012, Auckland, New Zealand.

Deb SK, Kaur Inderpreet, Kishtawal CM, Pal PK (2012b). Atmospheric Motion Vectors from Kalpana-1: An ISRO Status, *The Proceedings 11<sup>th</sup> International Wind Workshop*, 20-24 February, 2012, Auckland, New Zealand.

Deb SK, Kishtawal CM, Prashant Kumar, Kiran Kumar AS, Pal PK, Nitesh Kaushik, SangarGhansham (2016). Atmospheric Motion Vectors from INSAT-3D: Initial quality assessment and its impact on track forecast of cyclonic storm NANAUK. *Atmospheric Research* 169: 1-16.

García Pereda J, Borde R, Randriamampianina R (2012). LATEST DEVELOPMENTS IN NWC SAF HIGH RESOLUTION WINDS PRODUCT. *Proceedings Eleventh International Winds Workshop*, Auckland, New Zealand.

Hasler AF, Skillman WC, Shenk WE, Steranka J (1979) In situ aircraft verification of the quality of satellite cloud winds over oceanic regions. *Journal of Applied Meteorology* 18: 1481–1489.

Holmlund K (1998) The utilization of statistical properties of satellite-derived Atmospheric Motion Vectors to derive quality indicators. *Weather Forecasting* 13:1093-1104.

Kelly G (2004) Observing system experiments of all main data types in the ECMWF operational system. 3<sup>rd</sup> WMO Numerical Weather Prediction OSE Workshop, Alpbach, Austria, WMO, Tech Rep. 1228: pp 32-36.

Kishtawal CM, Deb SK, Pal PK, Joshi PC (2009). Estimation of Atmospheric Motion Vectors from Kalpana-1 imagers. *Journal of Applied Meteorology and Climatology* 48: 2410-2421.

LeMarshall J, Pescod N, Khaw A, Allen G (1993). The real-time generation and application of cloud-drift winds in the Australian region. *Australian Meteorological Magazine* 42: 89–103.

Merrill, R. T., Menzel W. P, Baker W, Lynch J. and Legg E, (1991): A report on the recent demonstration of NOAA's upgraded capability to derive cloud motion satellite winds. *Bull. Amer. Meteor. Soc.*, 72, 372-376.

Nieman SJ, Schmetz J, Menzel WP (1993) A comparison of several techniques to assign heights to cloud tracers. *Journal of Applied Meteorology* 32:1559–1568.

Nieman S, Menzel WP, Hayden CM, Gray D, Wanlong S, Velden C, Daniels J (1997) Fully automated cloud-driftwinds in NESDIS operations. *Bulletin of American Meteorological Society* 78: 1121–1133.

Rossow WB, Mosher F, Kinsella E, Arking A, Debois M, Harrison E, Minnis P, Ruprecht E, Seze G, Simmer C, Smith E (1985) ISCCP clouds algorithm inter-comparison. *Journal of Climate and Applied Meteorology* 24: 877–903.

Schmetz J, Holmlund K, Hoffman J, Strauss B, Mason B, Gaertner V, Koch A, van de Berg L (1993) Operational cloud-motion winds from Meteosat infrared images. *Journal of Applied Meteorology* 32: 1206–1225.

Tokuno M (1996) Operational system for extracting cloud motion and water vapor motion winds from GMS-5 image data. Proc. Third Int. Winds Workshop, EUM P18, Ascona, Switzerland, EUMETSAT, 21–30.

Tokuno M (1998) Collocation area for comparison of satellite winds and radiosondes. Proc. Fourth Int. Winds Workshop, EUM P24, Saanenmoser, Switzerland, EUMETSAT 21–28.

Tomassini C (1981) Objective analysis of cloud fields. Proc. Satellite Meteorology of the Mediterranean ESA, SP-159: pp.73–78.

Velden CS, Hayden CM, Nieman SJ, Menzel WP, Wanzong S, Goerss JS (1997) Upper-tropospheric winds derived from geostationary satellite water vapor observations. *Bulletin of American Meteorological Society* 78:173–195.

## **14. Atmospheric Motion Vectors: Staggering**

## **14.1. Algorithm Configuration Information**

### **14.1.1. Algorithm Name**

Staggered Atmospheric Motion Vectors Winds (TIR1 and WV)

(Ref : IMD RFP Section 11.14 )

### **14.1.2. Algorithm Identifier**

3DIMG\_L2P\_IRW\_MERGED; 3RIMG\_L2P\_IRW\_MERGED

3DIMG\_L2P\_WV\_MERGED; 3RIMG\_L2P\_WV\_MERGED

### **14.1.3. Algorithm Specification**

<b>Version</b>	<b>Date</b>	<b>Prepared by</b>	<b>Description</b>		
1.0	19.11.2018	S.K. Deb C.M. Kishtawal	Staggered Document	AMV	Baseline

## **14.2. Introduction**

The geostationary satellite derived winds, also known as Atmospheric Motion Vectors (AMVs) are considered as one of the most reliable source of wind information over oceanic region where normal ground based observations are very rare. Presently in India operationally AMVs are available from two advanced meteorological satellites *INSAT-3D* (Deb et al., 2016, Kishtawal et al., 2009) and *INSAT-3DR* using consecutive 30-minutes images ([www.mosdac.gov.in](http://www.mosdac.gov.in)). It is also well established that assimilation of AMVs in the numerical weather prediction (NWP) model leads to significant improvement in the weather forecast (Deb et al., 2010; Kaur et al., 2015; Kumar et al. 2016) over the Indian Ocean region. The purpose of this document is to present an algorithm for retrieving Atmospheric Motion Vectors (AMVs) from INSAT-3D and INSAT-3DR in staggering mode and its validation procedure. The INSAT-3D/3DR have two IR window channels (10.5-11.5 $\mu$  and 11.5-12.5  $\mu$ ). In this document some background and general characteristic of satellite-derived AMV and INSAT-3D/3DR IR channel characteristics; the methodology employed to derive the vector fields, theoretical basis and practical aspects of this algorithm and outlined the planned validation approach.

### **14.2.1. Overview and background**

The availability of data from both *INSAT-3D* and *INSAT-3DR* with similar spectral characteristic and region of interest, at every 15-minutes has motivated us to re-look further for the improvement in retrieval algorithm to get better quality AMVs over the Indian Ocean region. The specific reason for this motivation is that instead of using 30-minute images for winds retrieval, the accuracy of winds will improve if shorter spatio-temporal images are used during the retrieval. For example,

if *INSAT-3D* captured image at 0000 UTC, then *INSAT-3DR* does at 0015 UTC and similar nomenclature follows for other time of the day. The operational meteorological parameters derived using *INSAT-3DR* are same as that of *INSAT-3D*, with 15 minute time gap. In both the satellites, spectrum of the atmosphere is covered by six imager channels i.e. the Visible (VIS), Short-wave infrared (SWIR), Mid-wave infrared (MIR), Water vapor (WV) and two split window thermal infrared (TIR1 and TIR2) channels. The image registration accuracy significantly improved because of star sensors are present on both the satellites. The individual *INSAT-3D* and *INSAT-3DR* AMVs are derived every 30-minute intervals. As an example, the *INSAT-3D* AMVs are retrieved at 0000, 0030, 0100 UTC, while *INSAT-3DR* AMVs are derived at 0015, 0045, 0115 UTC respectively. The AMV derived from these satellites are widely accepted by different national and international operational agencies. In the present study, the algorithm for deriving AMVs using infrared and water vapor images from *INSAT-3D* and *INSAT-3DR* data in staggering mode is demonstrated. Subsequently, this new AMVs generated using staggering mode will be inter-compared with individually retrieved *INSAT-3D* and *INSAT-3DR* AMVs.

#### **14.2.2. Objective**

The availability of data from both *INSAT-3D* and *INSAT-3DR* with similar spectral characteristic and region of interest, at every 15-minutes has motivated to re-look further for the improvement in retrieval algorithm to get better quality AMVs over the Indian Ocean region. The specific reason for this motivation is that instead of using 30-minute images for winds retrieval, the accuracy of winds will improve if shorter spatio-temporal images are used during the retrieval. The main objective of this study is to derive the algorithm for retrieving AMVs using infrared and water vapor images from *INSAT-3D* and *INSAT-3DR* data in staggering mode.

### **14.3. Inputs**

#### **14.3.1. Static Data**

<b>Parameter</b>	<b>Resolution</b>	<b>Source</b>
Continental boundary data	4 km	DP (IMD data)

### 14.3.2. Image and pre-processing data (Dynamic)

Parameter	Res.	Accuracy	Source
Registered radiometric and geometric corrected gray count values of split window TIR1 channel (10.5-11.5 $\mu\text{m}$ ) and WV channel (6.7 $\mu\text{m}$ )  (All the data is required in fixed lat-lon grid for continuous 8-images separated by 30 minutes time interval for each satellite)  L1C- Sector generated images over common area.  <b>It is assumed here that all input images (both INSAT-3D and INSAT-3DR) are well registered.</b>	pixel	--	Derived from raw data by DP (data processing)
Gray value to brightness temperature conversion table	-	0.3 K	Derived by DP
Geo-location file	Pixel	4 km	Derived by DP

### 14.3.3. Other Auxiliary data and Model Inputs

Parameter	Resolution	Accuracy	Source
Numerical model forecast of wind for all levels	0.5 degree	2 m/s (speed) 20° (direction)	NCEP
All levels model forecast Temperature		1° K	

## 14.4. Algorithm Functional Specifications

### 14.4.1. Methodology

The operationally four different spectral channels of *INSAT-3D* and *INSAT-3DR* are used to derive AMVs over the Indian Ocean region and operational retrieval algorithm is described in [Deb et al. 2016](#). In the present document, a new staggering algorithm is discussed where data from infrared (i.e. TIR1) and water vapor (i.e. WV) channels of both the satellites are used simultaneously for higher temporal scale retrieval. Although the major steps of retrieval algorithm (i.e. Tracer

selection, height assignment, tracking and quality control etc) staggering algorithm is same as present operational algorithm, however a few changes incorporated in the new algorithm to minimize the inaccuracies due to two separate satellite platform is shown in the following Figure -1.

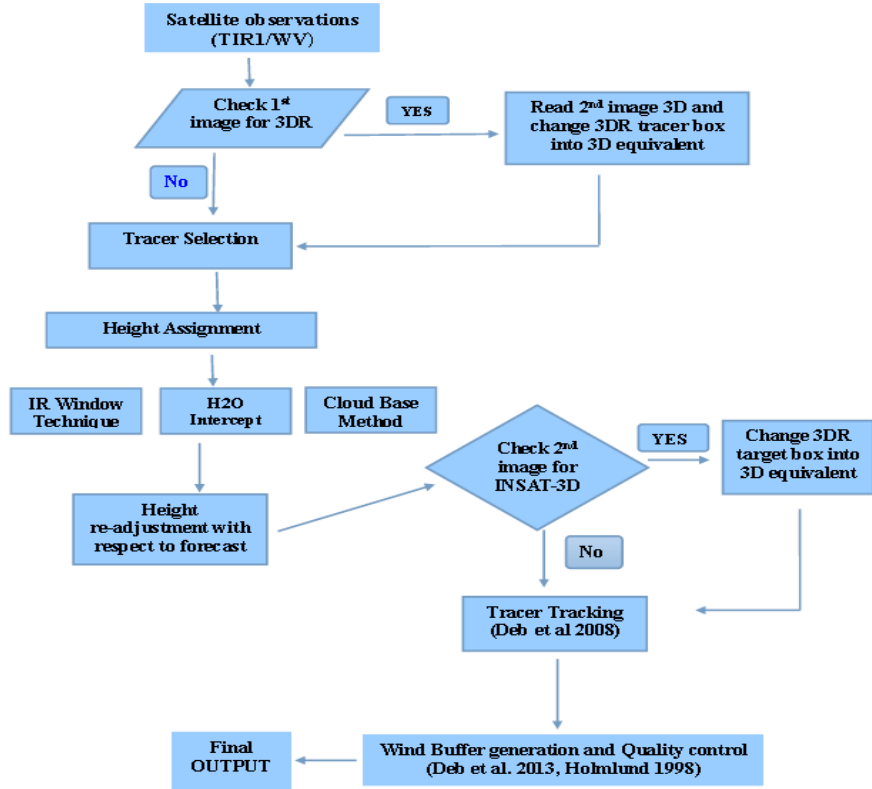


Figure 1: The flowcharts of staggering AMVs retrieval algorithm using INSAT-3D/3DR data

At first, the satellite ID from which first input image is coming is checked, if it is from *INSAT-3DR*, then second image from *INSAT-3D* is read. In the first image possible cloud tracers are identified and each selected tracer is represented by a box of 32 x 32 pixel. The tracer box in the first image (i.e. *INSAT-3DR*) is calibrated with respect to the collocated box in second image (i.e. *INSAT-3D*) using the following formula:

$$I_1 = \left( I_1 - \bar{I}_1 \right) \frac{\text{var}(I_2)}{\text{var}(I_1)} + \bar{I}_2$$

Here,  $I_1$  and  $I_2$  represent the 32 x 32 (in pixel) tracer boxes from first and second image respectively.  $\text{Var}(I_1)$  and  $\text{Var}(I_2)$  represent the variance of the tracer boxes. This is performed to reduce the uncertainty in inter-calibration of two different satellites, all-though their sensor specifications are exactly same. Then cloud tracers are selected by local image anomaly technique in a particular image and subsequently height of the selected tracers is calculated. The height assignment component of operational AMV retrieval algorithm uses widely used traditional

methods viz. the infrared window (WIN) technique, the H<sub>2</sub>O intercept method ([Nieman et al., 1993](#)) and the cloud base method ([LeMarshall et. al., 1993](#)). Then selected tracers are tracked in larger window in the subsequent image by using the Nash-Sutcliffe model efficiency [[Nash and Sutcliffe, 1970](#)] coefficient. The detailed description of each step is already discussed in the Algorithm Theoretical Basis Document (ATBD) of infrared and water vapor winds from INSAT-3D or INSAT-3DR ([Deb et al. 2008](#))

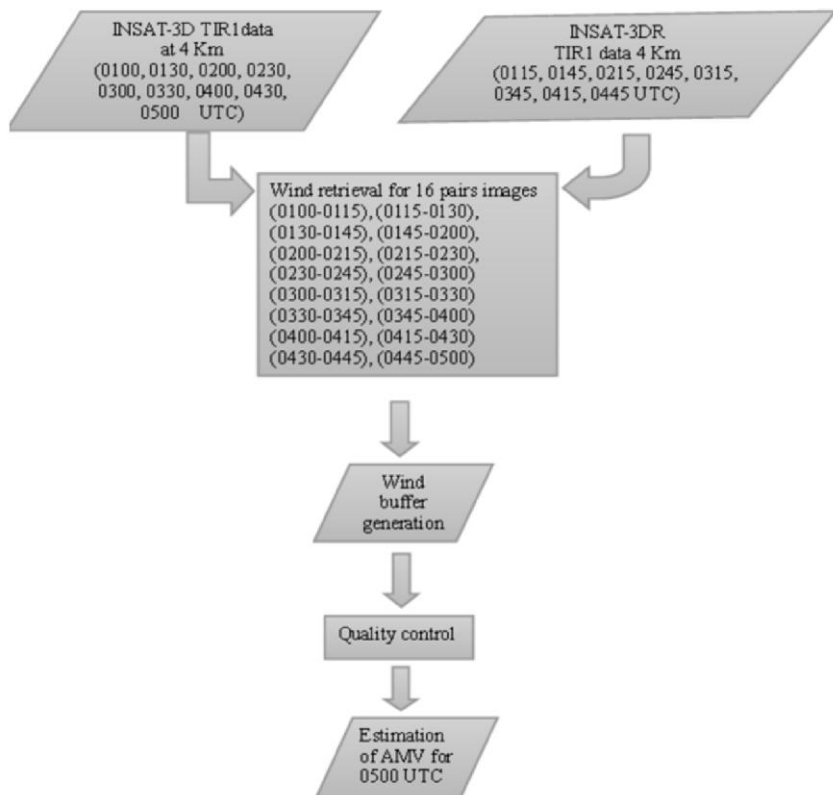


*Figure 2: A sample flow-diagram of methodology for the retrieval of AMVs in staggering mode for a particular time 0500 UTC.*

If the selected first image is from *INSAT-3D*, the tracers are selected and height assignment is done, then before tracking the selected tracers in the second *INSAT-3DR* image, collocated tracer box in *INSAT-3DR* is calibrated to *INSAT-3D* equivalent. The process of tracer selection, height assignment and tracking is repeated for sixteen pair of images to generate sixteen pairs of raw winds which is called as wind buffer. Later, this wind buffer is used for quality control of AMVs. During the quality control, temporal, spatial consistency checks are performed with neighboring vectors extracted from the wind buffer. A sample flow-diagram of methodology for the retrieval of staggering AMVs at 0500 UTC is shown in [Figure-2](#). To derive winds valid at 0500 UTC requires total seventeen images of 15-minute interval viz. nine images from *INSAT-3D* starting from 0100 UTC and eight images from *INSAT-3DR* starting from 0115 UTC. In the next steps

wind buffer is calculated using sixteen wind pairs. In the following step quality control technique is applied to wind buffer to estimate the final output valid at 0500 UTC.

#### **14.4.2. Operational Implementation**

##### **Step 1 : Conversion from gray count to BT**

- Since accuracy of the wind is dependent on image registration and it is assumed here that all input images are well registered. The details algorithm for registration is defined in the data product document as provided by DP team. In this step a radiation model will be used to convert the instrument measured radiance into brightness temperature. This requires an accurate definition of the spectral response of the satellite.

##### **Step 2: Tracer selection from image**

- Read first two registered images from INSAT-3D and INSAT-3DR.
- Choose the tracer box in the first image (i.e. 3D) and calibrate the similar tracer box from 3DR from second image into 3D equivalent.
- Cloud tracer selection will be done by evaluating the maximum local gradients surrounding each pixel in the target array and selecting the maximum brightness temperature of the window.

##### **Step 3: Height assignment**

- For height assignment use brightness temperature from single satellite (i.e either 3D or 3DR) to avoid height inaccuracies due to inter-calibration of two satellites.
- Assign height of the tracer using IR window technique. In this case the brightness temperature in the target window will be averaged and matched with collocated numerical model temperature profile. The level of optimum fit will be assigned as initial height.
- Re-assign the height using H<sub>2</sub>O intercept technique for semi-transparent tracers.
- Re-assign the height using cloud-base height assignment technique.
- Assign correct height after implementing all the height assignment technique mentioned above.
- Height optimization using minimized differences with first guess.

##### **Step 4: Tracking**

- Before tracking the tracer selected from first image in the second image, bigger tracking area in the second image is calibrated with respect to the first image.
- The tracking employs a simple search for the mean absolute difference of the radiance difference between the target and search arrays in subsequent half hourly images. This search will be done in the direction of 30° of model wind.

### Step 5: Wind buffer generation & quality control

- The wind buffer is created using previous eight images between pairs of images (viz. the winds retrieved between 1-2, 2-3, 3-4, 4-5, 5-6, 6-7 and 7-8) and stored in a file. The selection of eight images is consistent with decorrelation timescales of winds over tropical region.
- Use quality control criteria for selecting wind using the wind buffer.
- Use EUMETSAT automatic quality control method to get the QI
- Calculate wind speed and direction.

### 14.5. Outputs

Parameter	Unit	Min	Max	Accuracy	Resolution
U and V component of staggered AMV	m/sec	0	90	4-6 m/sec (upper level) 3-4 m/sec (lower level)	--
Domain of output : 30°E – 130°E :: 50°S – 50°N					

#### Format of the output and the domain

As output of AMV the following parameters will be provided to IMD:

- Zonal and meridional components of the wind vectors.
- Latitudinal and longitudinal position.
- Height of AMV

The format of the final product will be like this:

Parameter	Lat	Lon	Level	U-component	V-component	Quality Flag	Wind Speed (m/s)	Wind direction (clockwise from North)	Wind zenith angle
Unit	Deg N	Deg E	hPa	m/s	m/s	0.0 to 0.9	m/s	Deg	Deg

## 14.6 Validation

### 14.6.1. Data required

Parameter	Type	Source
Wind	Collocated Radiosonde Profiles	IMD

### 14.6.2. Methods of validation

The evaluation of CMV should be taken into both qualitative and quantitative measures. Quantitative assessment of the CMV product is possible from statistical analyses and impact on NWP. The traditional method of validation is matching observations with collocated radiosondes. The statistical validation will be done according to the CGMS winds evaluation reporting guidelines. These statistics can provide a fixed measure of product quality over time and can be employed in determining observation weight in objective data assimilation. At the CGMS XXIII the Working Group on Satellite Tracked Winds recommended that evaluation of operational wind production quality should be accomplished with a new standardized reporting method. The recommended three parts to the report.

- a. Monthly means of speed bias and rms vector difference between radiosondes and satellite winds for low ( $>700$  hPa), medium (700-400 hPa), and high ( $<400$  hPa) levels together with the radiosonde mean wind speed. This should be done for three latitude bands: north of 20 N, the tropical belt (20 N to 20 S), and south of 20 S.
- b. Trends of the evaluation statistics for the monthly cloud motion vectors and water vapor motion vectors through the last 12 months.
- c. Information on recent significant changes in the wind retrieval algorithm.

The vector Difference (VD) between an individual wind report (i) and the collocated radiosonde report used for verification is given by

$$(VD) = [ (U_i - U_r)^2 + (V_i - V_r)^2 ]^{1/2}$$

The speed bias is given by

$$(BIAS)_i = 1/N \sum_{i=1}^N [(U_i^2 + V_i^2)^{1/2} - (U_r^2 + V_r^2)^{1/2}]$$

The mean vector difference (MVD) traditionally reported is

$$(MVD) = 1/N \sum_{i=1}^N (VD)_i$$

And the standard deviation (SD) about the mean vector difference traditionally reported is

$$(SD) = \left[ \frac{1}{N} \sum_{i=1}^N (VDi - MVD)^2 \right]^{1/2}$$

The root-mean-square error (RMSE) traditionally reported is the square root of the sum of the squares of the mean vector difference and the standard deviation about the mean vector difference,

$$(RMSE) = [(MVD)^2 + (SD)^2]^{1/2}$$

$$(\Delta U^2) = \left[ \frac{1}{N} \sum_{i=1}^N (Ui - Ur)^2 \right]$$

$$(\Delta V^2) = \left[ \frac{1}{N} \sum_{i=1}^N (Vi - Vr)^2 \right]$$

$$(MCD) = [(\Delta U^2) + (\Delta V^2)]^{1/2} \neq (MVD)$$

It must be noted that this definition of the mean vector difference is not the same as the mean component difference. The mean difference is calculated from the sum of the squares of the deviations of each component (u and v) of the wind vector.

To avoid confusion, a common terminology will be accepted. It is suggested to report mean vector difference (MVD) and standard deviation (SD). The standard accuracy according to CGMS guideline for CMV is that the root mean square error (RMSE) for WV winds should be 7m/s respectively with respect to radiosonde observations. The mean bias for both sets of winds should be about zero.

#### **14.7. Technical Issues (Limitations etc)**

Accuracy of the product depends on the accuracy of the registration of the images. If the registration has an error of 1 pixel, then error of the final product will be increased. However the following limitations of the present study have to be kept in mind. The spatially coherent, high resolution coverage of upper tropospheric winds are possible from geostationary satellite remote sensing of water vapor. CMV are comparable in quality to operational upper-level cloud-motion vectors. However, the retrieved vectors in regions are lacking in defining moisture structure, though they have the ability to obtain track-able information in extremely dry air masses and regions of strong subsidence is limited. The individual vectors represent single level reports; however, upper level vertical winds profiles are possible by using multi-spectral observations.

##### **a. Sensitivity of error in height assignment to the error in wind speed retrieval**

This sensitivity will depend upon the structure of wind circulation over different vertical levels as well as different geographical regions. For example, in the vicinity of atmospheric jets, the retrieved wind vectors will be highly sensitive to the errors in the assigned pressure levels. Based on some standard analysis ( e.g. NCEP reanalysis of 6-hourly sampling), we will provide a quantitative assessment of the vertical and spatial structure of this sensitivity.

**b. Numerical model to be used for AMV height assignment**

We plan to use IMD's operational regional model output during height assignment procedure. However, if the domain of this regional model is smaller than the area of AMV retrieval, either IMD may be requested to increase the domain of its operational model, or a lower-quality solution based on the output of coarser-resolution GCM will be generated over the regions not covered by IMD's regional model.

**c. Whether RT model to be used in real-time for height assignment**

To use RT model in real-time height-assignment application is generally required to find the optimum solution. However, it is computationally expensive and may increase the AMV turn-around time very significantly. Efforts are currently underway to develop an empirical version of RT model that can be used for simulation of IR and water-vapor channel radiances for a variety of cloud heights. The inverse of this empirical model will then be used in real-time applications.

**d. Comparison of maximum-correlation and minimum-difference methods for tracking of cloud-tracers.**

The comparison have been made for a large number of image samples and it was found that the efficiencies of minimum-difference method (MDM) and maximum cross correlation (MCC) methods are comparable, while the MDM method is significantly faster than MCC.

## References

- Deb, S.K., C.M. Kishtawal, and P.K. Pal, 2010. Impact of Kalpana-1 derived water vapourwinds on Indian Ocean Tropical cyclones forecast. Mon. Weather Rev. 138 (3), 987–1003. <http://dx.doi.org/10.1175/2009MWR3041.1>.
- Deb, S. K., C.M.Kishtawal, Prashant Kumar, A.S. Kiran Kumar, P. K. Pal, Nitesh Kaushik, and Ghansham Sangar, 2016. Atmospheric Motion Vectors from INSAT-3D: Initial quality assessment and its impact on track forecast of cyclonic storm NANAUK. Atmos. Res. 169, 1-16
- Horvath, A., and R. Davies, 2001. Feasibility and error analysis of cloud motion wind extraction from near-simultaneous multi-angle MISR measurement. J Atmos Ocean Technol. 18(4):591–608.
- Kaur, Inderpreet, Prashant Kumar, S.K.Deb, C.M. Kishtawal, P.K.Pal, and Raj Kumar, 2015. Impact of Kalpana-1 retrieved Atmospheric Motion Vectors on meso-scale model forecast during

summer monsoon 2011. Theor. Appl. Climatol. 120 (3-4), 587–599.  
<http://dx.doi.org/10.1007/s00704-014-1197-9>.

Kishtawal, C.M., S. K. Deb, P.K.Pal, and P.C.Joshi, 2009. Estimation of atmospheric motion vectors from Kalpana-1. J. Appl. Meteorol. Climatol. 48, 2410–2421.  
<http://dx.doi.org/10.1175/2009JAMC2159.1>.

Kumar, Prashat, S.K. Deb, C.M. Kishtawal, and P.K.Pal, 2016. Impact of assimilation of INSAT-3D retrieved atmospheric motion vectors on short-range forecast of summer monsoon 2014 over the South Asian region. Published online 13 January 2016. Theor Appl Climatol, DOI 10.1007/s00704-015-1722-5.

LeMarshall, J.F., N. Pescod, A. Khaw, and G. Allen, 1993. The real-time generation and application of cloud-drift winds in the Australian region. Aust. Meteorol. Mag. 42, 89–103.

Lonitz, K., and A. Horváth, 2011. Comparison of MISR and Meteosat-9 cloud motion vectors. J Geophys Res 116:D24202. doi:10.1029/2011JD016047.

Nash, J.E., and J. V. Sutcliffe, 1970. River flow forecasting through conceptual models part I: a discussion of principles. J. Hydrol. 10 (3), 282–290. [http://dx.doi.org/10.1016/0022-1694\(70\)90255-6](http://dx.doi.org/10.1016/0022-1694(70)90255-6).

Nieman, S.J., J. Schmetz, and W.P. Menzel, 1993. A comparison of several techniques to assign heights to cloud tracers. J. Appl. Meteorol. 32, 1559–1568. [http://dx.doi.org/10.1175/1520-0450\(1993\)032b1559:ACOSTTN2.0.CO;2](http://dx.doi.org/10.1175/1520-0450(1993)032b1559:ACOSTTN2.0.CO;2).

Nieman, S., W.P. Menzel, C.M. Hayden, D.D.Gray, S. Wanzong, C.S. Velden, and J. Daniels, 1997. Fully automated cloud-driftwinds in NESDIS operations. Bull. Am. Meteorol. Soc. 78, 1121–1133. [http://dx.doi.org/10.1175/1520-0477\(1997\)078b1121:FACDWIN2.0.CO;2](http://dx.doi.org/10.1175/1520-0477(1997)078b1121:FACDWIN2.0.CO;2).

Tokuno, M., 1998. Collocation area for comparison of satellite winds and radiosondes. Proceedings of the 4th International Winds Workshop, Saanenmöser, Switzerland, 20–23 October 1998. vol. EUM P24, pp. 21–28 ([http://cimss.ssec.wisc.edu/iwwg/iww4/p21-28\\_Tokuno-Colocation.pdf](http://cimss.ssec.wisc.edu/iwwg/iww4/p21-28_Tokuno-Colocation.pdf)).

Velden, C.S., C. M. Hayden, S.J.Nieman, W.P. Menzel, S. Wanzong, and J.S Goerss, 1997. Upper-tropospheric winds derived from geostationary satellite water vapour observations. Bull. Am. Meteorol. Soc. 78 (2), 173–195. [http://dx.doi.org/10.1175/1520-0477\(1997\)078b0173:UTWDFGN2.0.CO;2](http://dx.doi.org/10.1175/1520-0477(1997)078b0173:UTWDFGN2.0.CO;2).

Velden, C. S, and K Holmlund, 1998. Report from the working group on verification and quality indices (WG III), Fourth International Winds Workshop, EUMETSAT, Saanenmoser, Switzerland. [http://cimss.ssec.wisc.edu/iwwg/iww4/p19-20\\_WGReport3.pdf](http://cimss.ssec.wisc.edu/iwwg/iww4/p19-20_WGReport3.pdf).

## **15. Modified GPI and IMSRA method**

S.No.	Product Name	Spatial Resolution	Temporal Resolution
1	IMG_IMSRA	4 km x 4 km	30 minutes

## **15.1. Algorithm Configuration Information**

### **15.1.1. Algorithm Name**

Modified Quantitative Precipitation Estimation (QPE) from GPI and IMSRA Techniques

### **15.1.2 Algorithm Identifier**

3DIMG\_L2G\_IMR

3DIMG\_L3G\_IMR\_DLY

### **15.1.3. Algorithm Specification**

<b>Version</b>	<b>Date</b>	<b>Prepared by</b>	<b>Description</b>
1.0	15.08.2012	R M Gairola A.K. Varma	QPE Baseline Document
2.0	01.05.2016	R M Gairola C. Mahesh MT Bushair	QPE Baseline Document
3.0	01.08.2018	R M Gairola C. Mahesh Ipshita Dey	QPE Baseline Document

## **15.2. INTRODUCTION**

Weather and climate affects many sectors of the human activity as well as many aspects of the world's natural ecosystems. The hydrological cycle is one of the important components of Weather and climate system. The hydrological cycle describes the exchange of water substance between sea, air, soil, rock, plants and animals. The precipitation and evaporation processes significantly affect the global hydrological cycle. The quantitative assessment of precipitation is needed to improve understanding of the behavior of global energy and circulation patterns as well as the nature of climate variability. The choice of measured parameter has been influenced by the cost of installation, operation, longevity and temporal as well as spatial coverage of the instruments. The land based techniques of rainfall estimation are not sufficient for global rainfall assessment as about 70% of the Earth is covered with water. The space borne measurement and monitoring of rainfall is, therefore, a topic of major interest since they provide global coverage both on land and ocean for an extended period of time. A longstanding promise of meteorological satellites is the improved identification and quantification of precipitation at time scales consistent with the nature and development of precipitation processes. Meteorological satellites expand the coverage and time span of conventional ground-based rainfall data for a number of applications. The primary

scope of satellite rainfall monitoring is to provide information on rainfall occurrence, amount and distribution over the regional to continental scales. The uneven distribution of rain gauges and weather radars and the relative lack of rainfall measurements over the oceans have significantly limited the use of global as well local data. Precipitation is one of the most variable quantities in space and time. Precipitation also has a direct impact on human life that other atmospheric phenomena seldom have: an example is represented by heavy rain events and flash floods (Barrett and Michell, 1991). Geostationary weather satellite visible (VIS) and infrared (IR) imagers provide the rapid temporal update cycle needed to capture the growth and decay of precipitating clouds. Microwaves provide the interaction of radiation with hydrometeors but with coarser resolution and limited swath widths of satellites with in tropical orbit such as the Tropical Rainfall Measuring Mission (TRMM) (Kummerow et al., 1998) and of sensors in polar orbits like the Special Sensor Microwave Imager (SSM/I) series.

### 15.2.1 Overview

Operational applications, require quantitative rainfall determination from a variety of precipitating systems, which differ both dynamically and microphysically. This fact prompts for non-unique solutions based on the physics of precipitation formation processes. Barrett and Martin (1981) and Kidder and Vonder Haar (1995) give excellent reviews of the available methods. Petty (1995) has examined the status of satellite rainfall estimation over land. Recent reviews Levizzani et al. (2001) has covered results and future perspectives from the geostationary orbit. The perspective varies widely from the relatively simple methods used for climatic-scale analyses (e.g. Arkin and Ardanuy, 1989; Arkin and Janowiak, 1991) to the more elaborate instantaneous rainrate estimations for research and nowcasting (Ba and Gruber, 2001; Turk et al., 2000; Vicente et al., 1998).

Recent technological developments of MW instruments on board polar orbiters have been dramatic but the use of VIS, IR and water vapor (WV) channels of geostationary satellites is still indispensable. In particular, the launch of the newest generation of geostationary satellites, the Geostationary Operational Environmental Satellite GOES-I-M series (Menzel and Purdom, 1994) and the upcoming METEOSAT Second Generation (MSG) (Schmetz et al., 2002) with its Spinning Enhanced Visible and Infrared Imager (SEVIRI), adds new channels to the traditional VIS/IR/WV triplet. Some of the new channels have been tested for decades as part of the Advanced Very High Resolution Radiometer (AVHRR) series on board the National Oceanic and Atmospheric Administration (NOAA) polar orbiters or have other heritages.

Multispectral data have long since been available both from polar orbiting and geostationary satellite sensors and used for retrieving cloud properties. The relevant channels for cloud characterization were part of the payload of the polar satellites, while the sensors at geosynchronous altitude were almost exclusively devoted to VIS-IR operational monitoring of precipitation system displacements. This has considerably changed in the past few years since

more and more sophisticated sensors have been conceived for the GEO orbits that will allow for global real-time cloud characterization.

Cloud radiative properties at VIS, near IR (NIR) and IR wavelengths have long since been studied and documented (among others Arking and Childs, 1985; Cheng et al., 1993, Saunders and Kriebel, 1988; Slingo and Schrecker, 1982). In the thermal IR the radiative properties are sensitive to the size distribution of the hydrometeors. In particular, an increase in the particle size increases the transmissivity, decreasing the reflectivity and increasing the emissivity of the cloud layer. This latter dominates at these wavelengths. In the NIR (e.g. the 3.9 mm MSG channel) the emissivity of a cloud layer is lower than in the thermal IR window: there is a large contribution of reflected radiation at the cloud top. Clouds with small hydrometeors scatter and reflect much of the 3.9 mm radiance. An increase in cloud particle size or the presence of large drops or ice crystals near the cloud top reduces the 3.9 mm reflectance from the cloud. containing more ice reflect less solar radiation in the 3.7 - 3.9 mm range as ice strongly absorbs at these wavelengths and ice crystals are generally larger than cloud droplets at cloud top. NIR reflectance mostly refers to cloud particles effective radius ( $re$ ). VIS reflectance is primarily due to cloud optical depth.

Several methods have been proposed for the retrieval of cloud parameters from various cloud types. Pioneering studies were conducted by Arking and Childs (1985) and Nakajima and King (1990). Water Vapor images show the presence of water in the gas form between 22,000 and 35,000 feet above the earth's surface. The brighter white color indicates areas of moisture. Black depicts neutral. Lensky and Rosenfeld (1997) have conceived a multispectral rainfall estimation technique based on the method of Rosenfeld and Gutman (1994). They concentrated on areas of around 2000 km<sup>2</sup> that Rosenfeld and Gagin (1989) showed to be the critical limit beyond which a further increase in cloud cluster area does not result in higher rain rates.

IR and NIR channels other than the thermal IR window show some potential for application to rainfall estimations. Techniques for the instantaneous delineation of convective rainfall areas using split window data were initially conceived for the NOAA AVHRR (Inoue, 1987a,b, 1997) and are instrumental for the detection of semi-transparent cirrus clouds (Inoue, 1985). These techniques rely upon the detection of non-precipitating cirrus and low-level cumulus clouds using the two window channels at 10.5 - 11.5 and 11.5 - 12.5  $\mu\text{m}$  (the so-called *split window*). The information content of the split window channels partially corrects erroneous rainfall area delineation (and consequent frequent rainfall overestimate) of simple IR techniques producing better false alarm ratios (FAR). The NIR 3.9  $\mu\text{m}$  channel of GOES-8/9 satellites includes spectral features suitable for applications to rainfall detection and estimation. This channel was included for a long time in NOAA/AVHRR instruments (centered at 3.7  $\mu\text{m}$ ) for a variety of purposes including ice discrimination and sun-glint detection. Vicente (1996) developed a simple and fast algorithm for rainfall retrieval using the 11 and 3.9  $\mu\text{m}$  channels with the obvious advantage of nighttime use and sensitivity to the presence of ice and water vapor.

In the present ATBD document the description of the scientific algorithms which will be developed and used to estimate rainfall from two of the standard operational algorithms of NOAA from the data acquired by the Very High Resolution Radiometer (VHRR) onboard INSAT-3D satellite. VHRR produces images in six spectral channels, in the Visible (VIS), Near Infra-red (NIR), Mid Wave Infra-Red (MWIR), and Infra-Red (IR) part of the spectrum covering the following channels: VIS  $0.6\mu\text{m}$ , NIR  $1.6\mu\text{m}$ , MWIR  $3.9\mu\text{m}$ , WV  $6.7\mu\text{m}$ , IR  $10.8\mu\text{m}$ , IR  $12.0\mu\text{m}$ . Each channel of the Imager has different resolution as mentioned in the Table-1 in sections ahead.

### **15.2.2. Objectives**

There are two main objectives under the rainfall retrieval algorithms from INSAT-3D.. These techniques are now known as GOES Precipitation Index (GPI) and INSAT Multispectral Rainfall Algorithm Technique (IMSRA). Both the algorithms are state of art and aimed at estimation of rainfall with different applications at different spatial and temporal requirements respectively. First GPI related objectives are the implementation of the algorithm following Arkin (1979), while the second one is related to the development of the algorithm named GMSRA following Ba and Gruber (2001). Originally the GPI technique has been in operation for a large scale rainfall estimation by National community for more than two decades. The IMSRA on the other hand is a new one and is developed

The inherent limitations of optical channels remains persistent for rainfall retrieval as the rainfall in the ground is inferred by cloud top signatures only. There is no direct physical connection between the rain/cloud and ice hydrometeors within the clouds with radiance emanating from cloud tops to the sensor. The accuracy of rainfall estimate is improves only marginally even with significant new efforts. However, the high spatial and temporal coverage of Geostationary optical measurements is the very strong point along with the resolution capabilities of the sensors. At the same time microwaves have a direct physical connections with vertical structure of rainfall and thus with the cloud, rain and ice hydrometeors. But the non-portability of microwave sensors to the geostationary platforms till date due to technological constraints is a limitation and thus only low earth orbiting satellites can provide the rainfall information of land, ocean and atmosphere as on now. With the advent of active and passive radar and radiometric sensors onboard a single satellite (e.g. Tropical Rainfall Measuring Mission-TRMM) we envisaged that a technique like GMSRA can be further improved for Indian tropical regions and more reliable rainfall information can be retrieved. We henceforth call this technique as INSAT Multispectral Rainfall Algorithm (IMSRA), as a specific technique for Indian Tropical regions. Our objectives for both the techniques (GPI and IMSRA) here are based on these premises and are outlined below (mainly in cases of IMSRA).

#### **A1. INSAT-3D Rainfall using GPI Method:**

1. To generate a total day rainfall maps using 3 hourly brightness temperatures of IR ( $11\mu\text{m}$ ) images for  $1.0 \times 1.0$  deg latitude /longitude boxes in an area  $-50^{\circ}$  to  $+50^{\circ}$  lat and  $30^{\circ}\text{E}$  to  $130^{\circ}\text{E}$  using Arkin's GPI method.

2. To generate mean spatial variance and histogram of 24 classes of temperatures at 1.0 x 1.0 deg latitude/longitude.
3. To derive QPE based on daily basis following the 3 hourly data of IR observations (8 images a day).
4. Validation of rainfall products using rain gauges and Doppler Weather Radar data.
- 5 . Inter-satellite comparison using other contemporary satellites like Meteosat, NOAA etc.
6. Estimation of rainfall on pentad, monthly mean, seasonal mean and annual mean scales after due calibration/validation from radar and inter-satellite comparisons as above, rainfall.

**A2. To Develop Precipitation Estimates Using the Multispectral Rainfall Algorithm (IMSRA) Technique:**

The relation between precipitation amount and cloud fraction as seen from satellite passive radiometers in case of GPI technique above, though simple and straightforward it might seem, has not yet reached completely satisfactory accuracy, effectiveness, and time/space coverage. There are numerous applications in meteorology and hydrology where accurate information at scales smaller than the existing  $1.0^{\circ}$  products (e.g. daily or sub daily estimates at resolutions of  $1^{\circ}$  and down to the  $0.10^{\circ}$  and pixel scales) would be invaluable. There is also increasing demand from the meteorology and climate community for such products over extended periods. High-resolution rainfall information is available for limited areas using combinations of ground-based radar and dense networks of rain gauges. In India in particular, where the need of high spatial and temporal rainfall is essential, for large and varied areas of India (Western Ghats, plateaus, Himalayan Regions, North-Eastern Regions, Arid and Semi-Arid Zones) however, the *in-situ* infrastructure necessary for this form of precipitation monitoring network is not in place. Recent developments mostly refer to microwave (MW) sensors on board polar orbiters, but the use of visible (VIS) and infrared (IR) sensors of geostationary satellites for a variety of applications is by no means over. Thus a suit of both supplementing each others would be the ideal situation, particularly when the highly advanced microwave sensors data from various international satellites are available on near real time basis.

The main objectives here in IMSRA algorithm are to estimate rainfall by developing a Multispectral Rainfall Algorithm which is an optimal combination of GMSRA and some of the innovative proposed approaches that utilizes microwave remote sensing measurements from polar orbiting satellites. Here, the rainfall algorithm is with more advantageous that combines satellite passive microwave and infrared (IR) data to account for limitations in both data types. Rainfall estimates are produced at the high spatial resolution and temporal frequency of the IR data using rainfall information from the PMW data. Over the last few years, a number of groups world wide have embarked on development of such techniques wherein the advantages of geosynchronous viz. vast coverage and near sufficient space-time sampling, and polar passive microwave radiometers viz. more physically based retrievals, are synergistically used to

generate tropical rainfall on various scales (e.g. Adler et al. 1994, Todd et al. 2001, Gairola and Krishnamurti 1992). With above background the objectives for Multi Spectral Rainfall Algorithm (IMSRA) are as follows.

The technique has the following components:

1. Identify areas for very deep convective cores from IR and WV channels ( $11\mu\text{m}$ - $6.7\mu\text{m}$ ), which corresponds well with rainfall.
2. To screen mid-to upper level clouds with or without thin cirrus above the rain and non-rain baring clouds.
3. Cloud growth classification based on temporal gradients of TIR – TB's.
4. Filtering of low and non raining clouds along with the warm and semi-transparent clouds based on IR and WV when rainfall is estimated for clouds having brightness temperatures colder than 240K.
5. Spatial and temporal co-location of INSAT-TIR brightness temperature, and TRMM / SSM/I rainfall for creation of matched database.
6. To compute instantaneous rain rate using pre-calibrated rain rate for cloud top brightness temperature ( $11\mu\text{m}$ ) for each pixel classified as containing raining clouds along with Satellite Microwave Radiometric measurements (e.g TRMM Microwave Imager-TMI).
7. The global bias correction based on a polynomial model of the suitable form designed on the basis of comparison with TRMM-3B42 daily average rain (June and July).
8. The orographic correction is based on the climatological ratio bias between IMSRA and TRMM-3B42 for the orographic regions (Mahesh et al., 2014).
9. Cloud growth/decay correction based on the study of Mahesh et al., 2014 and Woodley , Sancho and Vicente (1972)
10. Validation of rainfall with Doppler Weather Radar data and fine tuning of algorithm.
11. Finally to estimate rainfall would be estimated in different spatial and temporal grid scales based on all the above components of the IMSRA algorithm.
12. Estimation of daily merged rainfall products from both satellite based IMSRA and IMD's national Rain Gauge data.

### **15.3. Inputs**

#### **15.3.1. Image and preprocessing data (Dynamic)**

The details for the required satellite data for both GPI and IMSRA are provided in following table:

<b>Parameter</b>	<b>Accuracy</b>	<b>Source</b>
Radiometric and geometric corrected gray count values of TIR-1 channel (10.5)	--	Derived from raw data by DP (data processing)
Radiometric and geometric corrected gray count values of TIR-2 channel (11.5)	-	Derived from raw data by DP
Radiometric and geometric corrected gray count values of VIS channel	-	Derived from raw data by DP
Radiometric and geometric corrected gray count values of WV channel (6.7)	-	Derived from raw data by DP
Radiometric and geometric corrected gray count values of 3.9 mm	-	Derived from raw data by DP
Gray value to brightness temperature conversion table	0.3 K	Derived by DP
Geolocation file	1 IR pixel	Derived by DP using Calibration Table

### 15.3.2. Other Auxiliary data and Model Inputs

In addition to satellite data from INSAT-3D, radar and rain gauge data, and atmospheric moisture products (integrated precipitable water and relative humidity from 500-mb surface) obtained from the IMD/Eta Model analysis are essential on required grid spacing in different temporal scales. The gridded rainfall data from Doppler Weather Radars are needed from IMD at every half hourly time interval on its original resolution grids that will be regridded as is required by the proposed grid resolution for GPI and IMSRA techniques. The rainfall from those DWRs, which will be well calibrated using an appropriate site specific  $Z-R$  relationship over Indian regional sites of the respective radar locations will be used for validation. In some cases one hourly rainfall from fast response rain gauges would be highly desirable particularly the areas where the DWR coverage is not at all there. Thus 1 to 3 hourly gauge-adjusted DWR rain rates, and hourly and daily gauge rainfall obtained from the IMD stations are important.

<b>Parameter</b>	<b>Resolution</b>	<b>Accuracy</b>	<b>Source</b>
Doppler Weather Radar - Surface Rain  Surface Rain Gauge on hourly basis (from Fast Response Rain Gauges, AWS ) and Total Day basis	Original DWR grid resolutions	70% as compared with ground based data	DWR observations at IMD Sites (Every 1/2 Hour, ----- At IMD Sites --- ---
TRMM / GPM Rainfall	1. Scan-mode Orbital data 2. Grid mode $0.1^{\circ} \times 0.1^{\circ}$ data		From Internet Sites

## 15.4. Algorithm Functional Specifications

### 15.4.1. Overview:

NOAA/NESDIS emphasizes use of meteorological satellites for the study of flash floods. Heavy precipitation and flash floods are often a multi scale and concatenating event from the global scale to the synoptic scale, to the mesoscale and finally to the storm scale. Satellite-derived algorithms, conceptual models, and interpretation techniques are used to provide information on these various scales to monitor, assess, and predict heavy precipitation and flash floods. In the satellite data, global scale connections between the tropics and middle latitudes are observed. These connections are movements, surges, or plumes of water vapor that are often associated with unstable air and prepare the environment for heavy precipitation and flash floods. On the synoptic scale, the  $6.7 \mu\text{m}$  water vapor is especially useful for detecting jet streaks, vorticity centers and other features that are associated with upward vertical motion and lift the moist, unstable air resulting in the production of clouds and precipitation. Whether or not heavy precipitation and flash floods will occur are generally determined on the mesoscale to storm scale. On the mesoscale, infrared ( $10.7 \mu\text{m}$  and  $3.9 \mu\text{m}$ ), visible, and water vapor ( $6.7 \mu\text{m}$ ) are used to locate boundaries (both frontal and thunderstorm-produced) and short waves that may initiate, focus, and maintain the heavy precipitation. Terrain features such as orographic uplift have the same effect of anchoring, intensifying, and prolonging the precipitation. On the storm scale, the intensity, movement, and propagation of the precipitation system (e.g., thunderstorms) is used to determine how much, when, and where the heavy precipitation is going to move during the next zero to three

hours (called Nowcasting). High resolution infrared ( $10.7\text{ }\mu\text{m}$ ) and visible are the principal data sets used in this diagnosis.

Large scale precipitation values are of importance in many fields and anomalies in large scale precipitation are also known to have a close relationship with global circulation anomalies. Satellite based rain estimation techniques can be classified into two broad categories, viz, (1) estimation of precipitation on near real time, e.g. Scofield and Oliver (1977), etc. and (2) estimation of average precipitation over a large area for a period of time ranging from a day to a month e.g., Richards and Arkin (1981) etc. In any of these two the estimation criteria is based on some statistical relationship.

In case of GOES, data from five channels are used: the visible channel ( $0.65\text{ mm}$ ), used when available to select optically thick clouds; channel 2 ( $3.9\text{ mm}$ ), used to retrieve reff of hydrometeors during daytime; the water vapor channel ( $6.7\text{ mm}$ ); and thermal channels 4 ( $11\text{ mm}$ ) and 5 ( $12\text{ mm}$ ). The  $11\text{ mm}$  channel is used to determine cloud-top brightness temperature, and the  $12\text{-mm}$  channel is used in conjunction with the  $11\text{-mm}$  channel to estimate cloud-top temperature. The estimated cloudtop temperature is utilized to compute the thermal emission at  $3.9\text{ mm}$ , which is then subtracted from measurements of that channel to yield the reflected solar radiation in the  $3.9\text{-mm}$  spectral band.

In the statistical relationship between IR cloud pixel brightness temperature from satellite sensor and surface rainfall measurements the mean rainfall rate  $R$  varies as a function of brightness temperature (BT). But the uncertainty in rainfall rate is quite large and also varies with BT. The GPI method uses a simple two-piece threshold function approximation of this relationship. Although crude, the GPI method works quite well for the estimation of monthly rainfall over large areas, partly because the over- and underestimation of spatial and temporal errors cancel each other in the aggregation procedure.

Complete software package for derivation of QPE using Kalpana-1, INSAT-3D,3DR VHRR data from two important algorithms like GPI, and IMSRA has been attempted. Both of them are the operational at NOAA/NESDIS and has been developed after years of research and development efforts by various investigators. The theoretical background for GPI and GMSRA respectively are given below:

#### **15.4.1.1. Theoretical Background for GPI Algorithm:**

##### **15.4.1.1.1 Physical explanation of rainfall with infrared (IR) images**

The satellite IR images are composed of measured radiant energy originating in the atmosphere or from the land and water surface below. The intensity of this energy integrated over all wavelength, by Stefan-Boltzmann law, is proportional to fourth power of temperature. The Stefan-Boltzmann law is valid for a perfect black body. If the medium emits spectral radiant energy according to some temperature less than its thermal temperature, than a second factor called emissivity is introduced. The emissivity of a body determine its emission efficiency. Thus, we can define

brightness temperature of a body  $T_b$ , which is related to its physical temperature  $T$  by following equation:

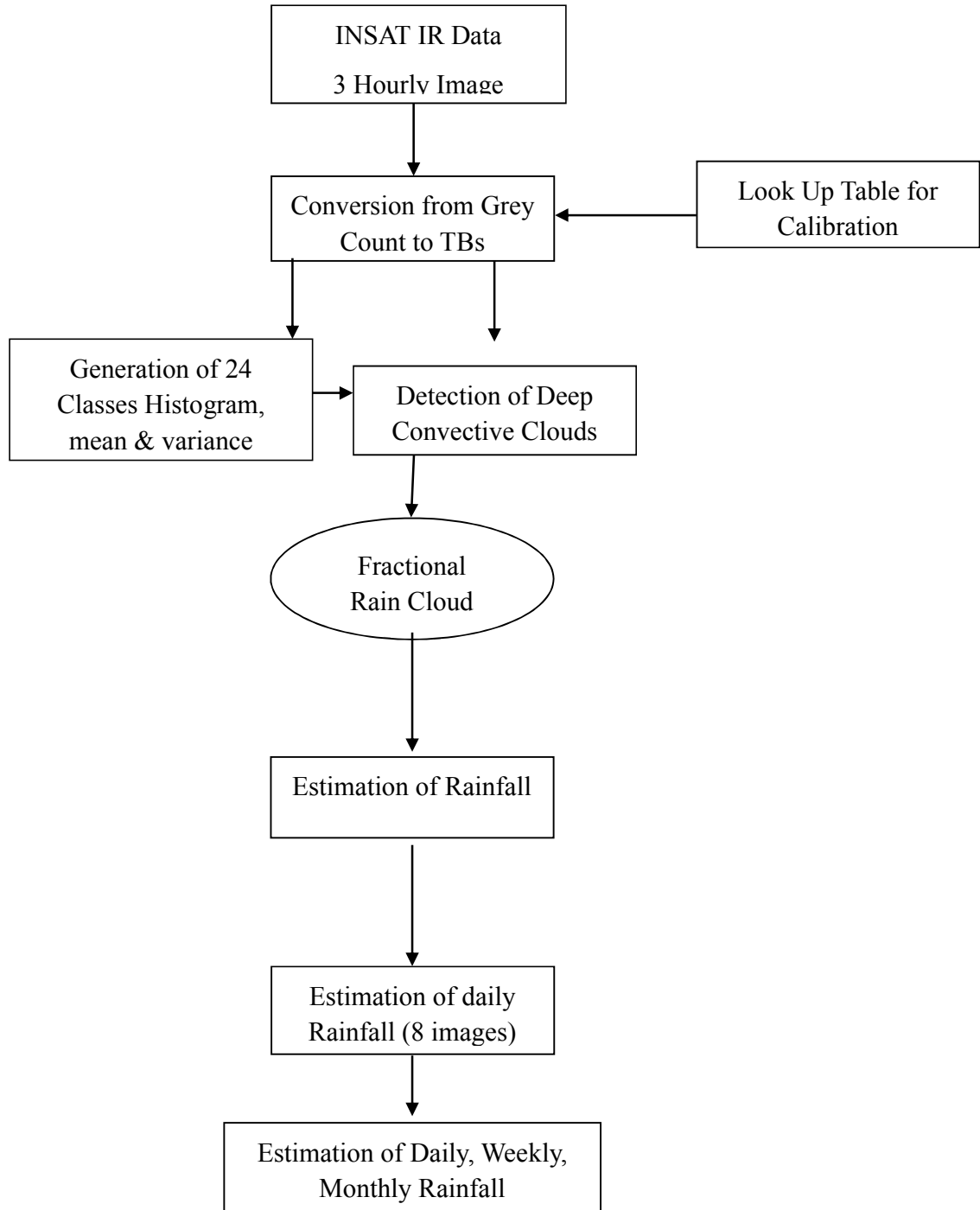
$$T_b = \varepsilon T$$

where,  $\varepsilon$  is emissivity of the object. If  $\varepsilon = 1$ ,  $T_b = T$ , its a black body; if  $\varepsilon = 0$ ,  $T_b = 0$ , its a white body; if  $0 < \varepsilon < 1$ ,  $T_b < T$ , and its a gray body.

The IR, for rainfall estimation, refers to thermal IR band that is 10.0 - 12.5  $\mu\text{m}$ . This is a atmospheric window, and all earthly objects radiate maximum spectral power in this band. In this band the absorption is strong for clouds and land/water surfaces and slight for gaseous constituents of the atmosphere. For surfaces, which are opaque and do not transmit radiation, measured intensity is closely approximated by the fourth power of the temperature. For those surfaces, which are not opaque - such as some clouds - measured intensity is approximated by effective emissivity times fourth power of the temperature. This effective emissivity will be referred more often as cloud emissivity here after. The cloud emissivity cannot be measured from observations at a single wavelength interval. Often it is simply assumed to be unity. Then the temperature calculated from observed intensity of radiation is called 'brightness temperature'. Only when  $\varepsilon = 1$ , brightness temperature equals to black body temperature.

The value of IR measurements to rainfall estimate lies in the nearly universal condition of lapse of temperature with height through the troposphere. If the temperature is known with height, either from actual sounding or from climatology, the height of the cloud can be infrared from the satellite IR observations. Ordinarily, gray clouds are not useful in this context, because  $\varepsilon < 1$  implies clouds which are thin (and therefore without precipitation). The more serious problem is distinguishing between cold clouds that are radiometerelly thick but are confined to the upper and middle troposphere, and cold clouds which extend into lower troposphere.

#### 15.4.1.1.2 Flow Chart for QPE from GPI:



### **15.4.1.1.3. Operational Implementation**

#### **Step 1 : Conversion from gray count to BT**

The INSAT-3D infrared thermal images of 0000, 03000, 0600, ...., 2100 UTC, i.e., every three hours, are to be used. Infrared pixel has dimensions of 4x4 km in case of INSAT-3D, 3DR, so that several pixels fall within  $1.0^{\circ} \times 1.0^{\circ}$  box. The grey shade value (0-1023) of each pixel in a given image is read and the corresponding brightness temperature is to be calculated from a look-up table. Pixel lying outside the chosen area of analysis are to be ignored while within it are assigned to appropriate box.

#### **Step 2: Histogram Generation:**

After the temperatures of all the pixels in a box are known they are to be distributed to generate 3 hourly 24 class histogram of brightness temperatures of IR (11 um) images for  $1.0 \times 1.0$  deg latitude /longitude boxes in an area -50 to + 50 deg. lat and 30 to 130 deg longitude from the sub-satellite point.

#### **Step 3: Grid-wise Statistics**

Generate 3 hourly mean and spatial variance of temperatures at  $1.0 \times 1.0$  deg latitude/longitude within the area 40 deg lat/long from the sub-satellite point.

#### **Step 4: Grid-wise Rain Clod Detection:**

The fractional cloud coverage within a grid box is the ratio of the pixels of cooler than specified threshold temperature to the total number of pixels. This gives the measure of the fractional area of the box covered by clouds with tops colder than threshold. Finally the estimates of precipitation using the GPI technique in the grid spacing of  $1.0^{\circ} \times 1.0^{\circ}$  lat/lon will be carried out. This work indicated a high correlation between the fractional coverage of "cold" clouds and observed rainfall. It was determined that the highest correlation between the parameters was produced using a 1.0 degree latitude/longitude spatial scale. An estimation method using linear regression was developed. The regression procedure yielded the simple estimation equation:

$$R = [3 \text{ mm h}^{-1}] \times [\text{frac}] \times [\text{hours}]$$

where R is the rainfall estimate in millimeters; frac is the fractional coverage of cloud-top temperature  $< 235\text{K}$  for the desired 1.0 degree latitude/longitude region; and hours indicate the number of hours in the observation period.

#### **Step: 5 Validations:**

Regarding the validation of the derived QPE the DWR and Surface Rain Gauges (SFRG) Data at different spatial and temporal scales will be highly desirable in and around the maximum validation sites in temporal window of every hour.

#### **Remarks:**

During the days when all the 8 images per day are not available, rain rate will be provided with a flag. Provisions of average rainfall estimation will be made for all the cases when more than 50% of data is available. Similar approach will be followed with the Pentad or Monthly scale average rainfall estimates.

### **15.4.1.2. IMSRA Technique:**

#### **15.4.1.2.1. Theoretical Background:**

The developmental work related to the INSAT Multi-Spectral Rainfall Algorithm (IMSRA) proposed here as an inhouse R & D effort, originally follows the GMSRA approach along with innovative alternative features (i.e. the satellite microwave radiometric measurements) for the estimation of precipitation. The theoretical basis is that

1. Bright clouds in the VIS and clouds with cold tops in the IR imagery that are expanding (in early and mature stages of development) produce more rainfall.
2. Clouds with cold tops that are becoming warmer produce little or no rainfall.
3. Merging of cumulonimbus (Cb) clouds increases the rainfall rate of the merging clouds.
4. Most of the significant rainfall occurs in the upwind (at anvil level) portion of a convective system.
5. Cloud micro-physics plays an important role in understanding the precipitation and thus effective radius of cloud top temperatures are to be known (say 3.9 mm during day time).
6. For each pixel classified as containing raining clouds based on above criterions, the associated instantaneous rain rate will be computed using pre-calibrated mean rain rate and cloud top brightness temperature relationship based on the equation developed using a large data base of IR-TBs and TRMM-Precipitation Radar data (Gairola et al. 2010b) The retrieved rainfall from earlier step and Doppler Weather Radar data on available locations in India would be used for offline validation of the algorithm. This will be based on the large collocated data base of DWR and IMSRA rainfall within 0.1x0.1 deg resolution.
7. Production of rainfall maps on every half hourly and daily basis on pixel scale with option for higher grid spacing.

Several such features are integrated in finalizing the estimation of rainfall using measurements from mult-spectral channels (Vis, IR, WV and microwave etc.). Physical explanation of rainfall with infrared (IR) images have been discussed previously which is common for GPI algorithm. In addition the Physical explanation of rainfall with visible (vis) images is being presented here in brief. Various researches so far have pointed that that with thicker clouds the probability of rainfall and rain intensity is increased. This relationship is strongest for clouds warmer than -15° C. It is also noted that marine clouds produce heavier rainfall. The possible explanation for this lies in the process of cloud growth and droplet growth rates. In clouds warmer than -15° C, precipitation results from coalescence. The large cloud thickness allows more time for growth before droplets fall out of the cloud. However, the other factors like droplet concentration, evaporation and cloud temperature are also important. Differences in precipitation probability between marine and

continental clouds were attributed to difference in concentration of condensation nuclei and of droplets, and difference in evaporation below the cloud base.

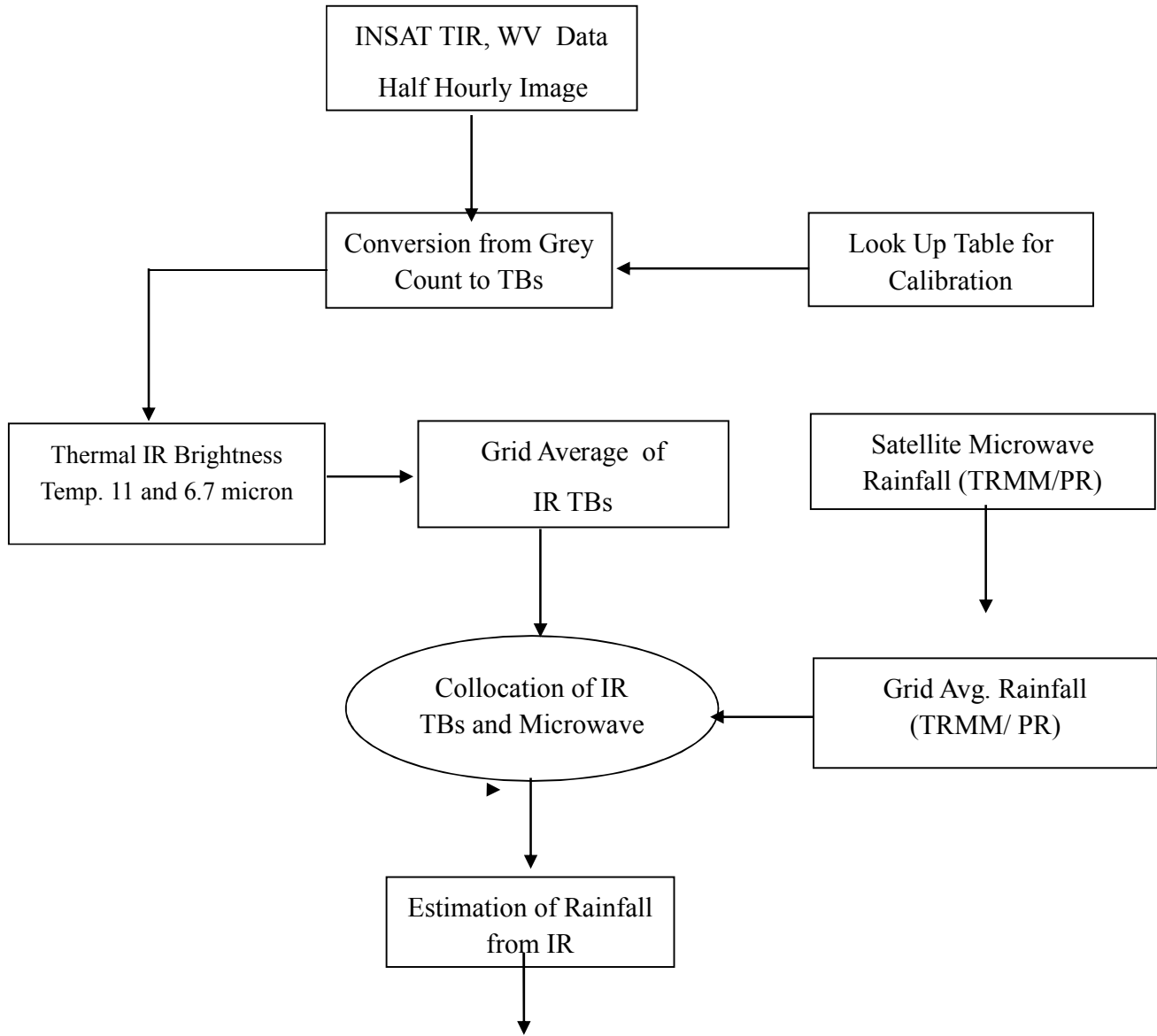
Satellite passive microwave and more recently, active microwave rain radar are able to provide accurate estimation of rain rates. However they are known to have but poor temporal sampling. Again the estimates from polar orbiting satellites are subject to the bias in regions where diurnal cycle of rainfall is pronounced. Still the instantaneous measurements of rainfall from microwave sensors are more accurate and thus are useful in calibrating other sensors like visible and IR. At present, the algorithms for the quantitative estimation of rainfall from microwave observations are quite successful but suffer from a scarcity of sufficient verification data over the oceans. Theoretical and empirical studies addressing the problem of rain retrieval and their critical assessment continues to appear. A definitive algorithm is continuously in developing stage because of the complex and variable microphysical and mesoscale structure of precipitation vis-à-vis coarser resolution of microwave sensors. As a source of microwave measurements, we use the rainfall data from the SSM/I Defense Meteorological Satellite Program (DMSP). Several algorithms have been developed for various SSM/I sensors of the DMSP series. The SSM/I rainfall used here is based on Ferraro and Marks (1995). The SSM/I had a conical scan with a swath width of about 1400 km and TRMM has swath width of about 800 km and the rainfall is retrieved by NASA-GPROF (Goddard Profiling) algorithm. Use of microwave data with those of VI/IR is most plausible choice to mitigate the problem of resolution in microwaves and augmentation of rain estimates from IR measurements.

Following the main features of Ba and Gruber (2001), from GMSRA, IMSRA is thus proposed in combination with additional satellite microwave measurements. Thus the principal innovations of IMSRA relative to previous infrared/visible algorithms alone is that it combines several cloud properties used in a variety of techniques in a single and comprehensive rainfall algorithm.

However our recent sensitivity study has suggested that the environmental correction factor (PWRH) is more suitable for larger scale rainfall (such as in GPI within  $1^{\circ} \times 1^{\circ}$ ) than for (IMSRA within or less than  $0.1^{\circ} \times 0.1^{\circ}$ ). This factor now has not been invoked on IMSRA algorithm any more.

#### 15.4.1.2.2 IMSRA Algorithm

**Fig. 2 Flow Chart for IMSRA Algorithm**



#### 15.4.1.3 Modified INSAT-3D Rainfall IMSRA scheme:

So far the IMSRA, that has been working as an operational algorithm at IMD combines multispectral optical measurements of the satellites to estimate rainfall along with the additional satellite microwave measurements. Thus the principal innovations of IMSRA relative to previous infrared/visible algorithms alone is that it combines several cloud properties used in a variety of techniques in a single and comprehensive rainfall algorithm. For example, the technique uses

cloud-top temperatures as a basis of rain estimation (e.g., Arkin and Meisner 1987; Ba et al. 1995; Vicente et al. 1998), and it utilizes the effective radii of cloud particles (e.g., Rosenfeld and Gutman 1994) and spatial and temporal temperature gradients (e.g., Adler and Negri 1988; Vicente et al. 1998) to screen out nonraining clouds. The algorithm have the number of steps which are already incorporated and described in Gairola et al. (2007).

Based on a number of case studies and research works carried out during last few years, some more innovative elements are recognized for further refinements of the algorithm. In this regard, a three –tier correction scheme is designed for IMSRA algorithm based on the intercomparison with TRMM-3B42 rainfall estimates. The Procedure adopts an overall correction of rain followed by corrections for orography and cloud growth/decay correction based on the study of Woodley , Sancho and Vicente (1972). Finally to further refine the IMSRA rainfall estimates the synergistic use of INSAT-3D derived IMSRA rainfall and rain gauge data from IMD is proposed based on the objective criteria.

Here the the original IMSRA algorithm has been retained as it is, except the environmental correction factor module has been dropped as it is adding more errors due to different decorrelation lengths of rainfall and relative humidity & precipitable water. The flowchart of the modified algorithm is given in Figure 3 where recent developments have been added to the original scheme in above flowchart Figure 2, tested and implemented in many case studies by Mahesh et al. (2015).

The global bias correction based on a priory data base is followed from a polynomial model of the form  $y=\sum a_i x^i$ ,  $i=0..2$  and the orographic correction is based on the climatology and using an elliptical weighting function (Mahesh et al., 2014). The global bias correction is designed on the basis of comparison with TRMM-3B42 daily average rain (June and July). The average bias between the rain estimates of TRMM-3B42 and IMSRA rain is absorbed into a polynomial model. Orographic correction is computed on the basis of a climatological ratio bias between IMSRA and TRMM-3B42 for the orographic regions. It is applied as a symmetrically reducing elliptical weighting function of the form

$$W = (A^2 - S^2) / (A^2 + S^2 - 2LF^2)$$

$A = d_1 + d_2$  where  $d_1$  and  $d_2$  are the distances from the end points of a line with two foci as the ends and  $A$  is the length of semi major axis.  $LF$  is the distance between two foci.  $S$  is the sum of Euclidean distance calculated for every point from the two foci. The graphical representation of the function is given in figure 4.

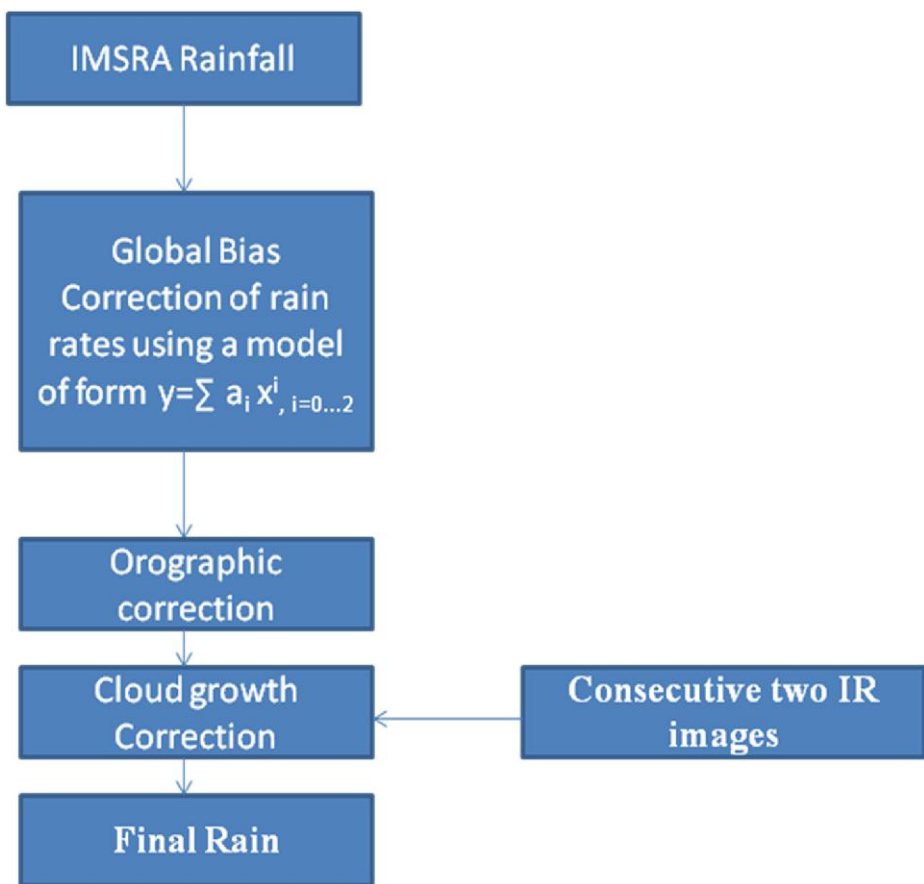


**Figure 3 : Flowchart of the proposed Modified IMSRA scheme**

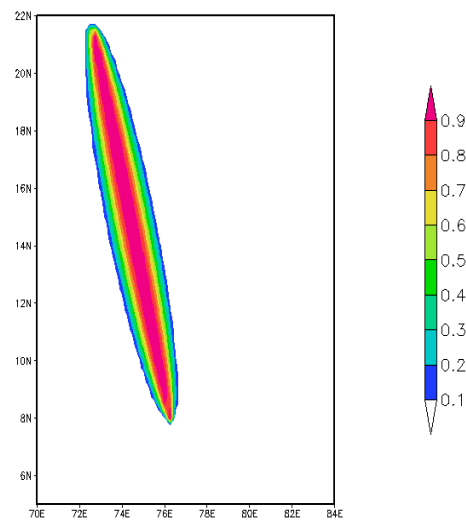


**Figure 4: contour plot of elliptical weighting function**

The cloud growth correction takes two consecutive IR images and makes rain/no rain distinction based on the studies of Woodley and sancho (1971), Vicente et al. (1998) and Mahesh et al. (2014). It was observed that expanding clouds or clouds with cold tops that are becoming colder increases the rainfall rates and decaying clouds or clouds with cold tops that are becoming warmer produce little or no rainfall. Under this assumption, cloud growth correction factor is applied to discriminate rain/no-rain situation. The correction factor is 0 when the cloud is becoming warmer and as 1 when the cloud is becoming colder.

#### 15.4.1.4 Case Study

Figure 5 shows the spatial comparison of rainfall estimates based on present IMSRA and after correction with TRMM-3B42 on 15 July 2014. The comparison suggests that the over estimation tendencies of IMSRA algorithm has reduced considerably by the correction scheme: central Indian region and the Bay of Bengal region shows the improvement in the improved version. Orographic regions also show significant improvement by the application of IMSRA correction scheme and the inherent under estimation tendencies have reduced in corrected version of IMSRA.

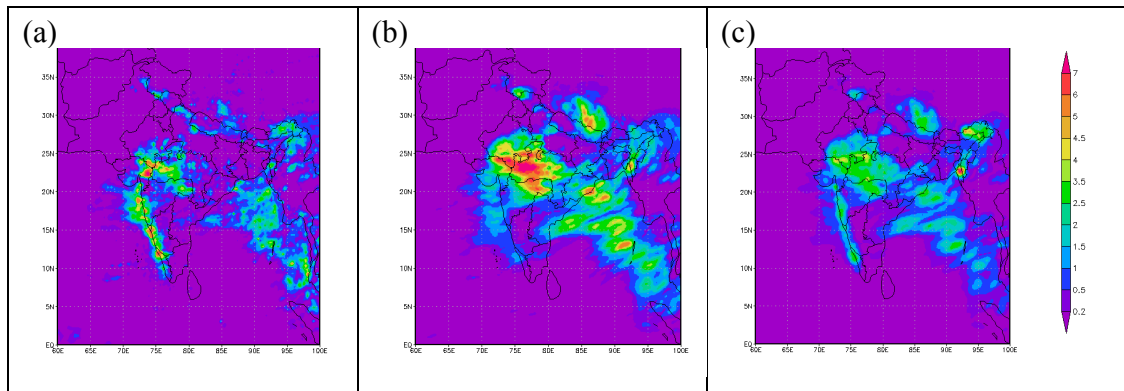


*Figure 5: Intercomparison of average daily rainfall estimates ( $\text{mm h}^{-1}$ ) on 15 July 2014 from (a) TRMM-3B42 (b) Operational IMSRA (c) IMSRA after correction scheme*

#### 15.4.1.5 Preliminary Statistical Comparison with TRMM-3B42

Preliminary validation of IMSRA rain estimates before and after correction is carried out from june to august 2014. The results are presented in figure 6. The density plots suggest that operational IMSRA has in general over estimation tendency with respect to TRMM-3B42, which is improved by the correction. The statistics of the same is given in table -1. Comparison suggest that correlation has improved from 0.64 to 0.67 and rmse has reduced from  $0.46 \text{ mm h}^{-1}$  to  $0.36 \text{ mm h}^{-1}$ . The statistical comparison over the orographic region is shown in table-2 the correlation has improved from 0.53 to 0.68 and rmse has reduced from  $1.01 \text{ mm h}^{-1}$  to  $0.87 \text{ mm h}^{-1}$ .

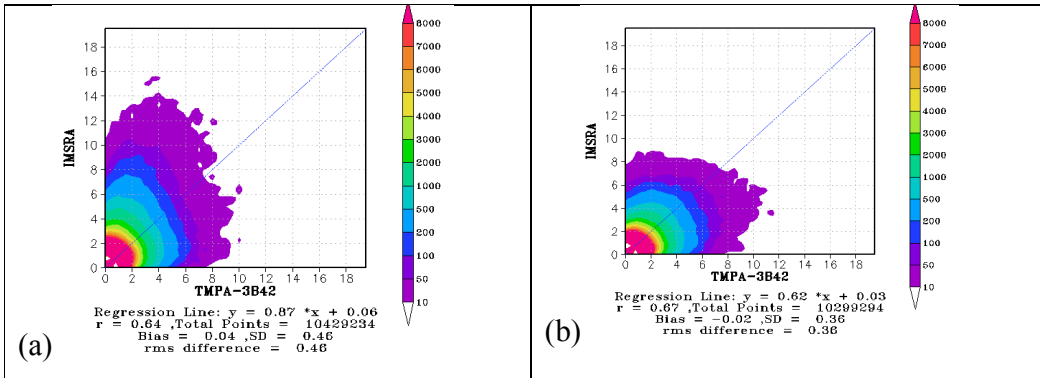


*Figure 6: Density plots of average daily rainfall estimates ( $\text{mm h}^{-1}$ ) for June-august 2014 for (a) IMSRA (b) IMSRA after applying correction scheme*

**Table1:** Statistical comparison of average daily rainfall estimates  $\text{mm h}^{-1}$  (June-Aug,2014)

	Existing	Improved
Correlation	0.64	0.67
RMSE	0.46	0.36
Bias	0.04	-0.01
No of Points	10299330	10299330

**Table2:** Statistical comparison of average daily rainfall estimates over orographic region

	Existing	Improved
Correlation	0.53	0.68
RMSE	1.01	0.87
Bias	-0.42	-0.25
No of Points	28999	28999

#### 15.4.1.6 Operational Implementation Steps for QPE from IMSRA

Step 1 : Conversion from gray count to BT: With the calibration and geolocation information the raw counts are to be converted into the brightness temperatures at different pixel locations respectively.

Step 2: Cloud Classification (Deep Convective (DC), DC with/without thin Cirrus (DCC), Mid to upper level clouds with/without thin Cirrus using an IR and WV channels. This threshold

based cloud classification is provided in detail by Inoue (1987) and Roca and Ramanathan (2000).

Step 3: Grid Average of IR TBs ( $0.1^{\circ} \times 0.1^{\circ}$ ) to match with microwave rainfall from TRMM (i.e. collocation of KALPANA-IR-TBs and TRMM rainfall applied to the INSAT-3D-IR-TBs based on histogram matching technique).

Step 4: Calibration of IR brightness temperatures with the contemporary microwave radiometric measurements of rainfall (e.g. TRMM Rainfall from NASA's GPROF algorithm).

Step 5: The global bias correction based on a polynomial model of the suitable form designed on the basis of comparison with TRMM-3B42 daily average rain (June and July).

Step 6: the orographic correction is based on the climatological ratio bias between IMSRA and TRMM-3B42 for the orographic regions (Mahesh et al., 2014).

Step 7: Cloud growth/decay correction based on the study of Mahesh et al., 2014 and Woodley , Sancho and Vicente (1972)

Step 8. Validation and fine tuning of the algorithm based on IMD's DWR and AWS and fast response rain gauges on hourly basis.

Step 9. Processing of the data for the different temporal scales (Half hourly, daily, weekly, monthly and seasonal etc.) based on the above steps of the development and validation of the algorithm.

## 15.5 Outputs

<b>Parameter</b>	<b>Unit</b>	<b>Min</b>	<b>Max</b>	<b>Accuracy</b>	<b>Resolution</b>
QPE (GPI)	mm	0	72 mm/ day	TBD	$1^{\circ} \times 1^{\circ}$
Histogram of BT's	K	< 180 K	> 280 K	24 Class	$1^{\circ} \times 1^{\circ}$
Daily, Weekly, Monthly & seasonal rainfall	mm	0	72 mm/day	TBD	$1^{\circ} \times 1^{\circ}$
QPE (IMSRA)	mm	0	TBD	TBD	4 km x 4 km (TIR Resol.)
½ Hourly, 3 Hourly, Daily, Weekly, Monthly & Seasonal rainfall	mm	0	TBD	TBD	-- do --

### **Format of the output**

Basic format would be to obtain QPE on a give domain with geolocation, and rainfall values. However, the QPE would be represented in various shades, contours and with desired color coding thereof. The 24 class histogram also will be generated.

**Domain :** For both GPI and IMSRA the domain for rainfall estimation mainly would be  $40^{\circ}$  S to  $40^{\circ}$  N,  $30^{\circ}$  E to  $130^{\circ}$  E.

### **15.6. Validation**

Rainfall products from the operational algorithms are to be obtained from two different methods mentioned above. These are required to be used for many diverse meteorological, climate, hydrological, agricultural, and other applications. It is therefore important to have an idea of their accuracy and expected error characteristics. This is done by validating the satellite precipitation estimates against "ground truth" from rain gauge and radar observations. A thorough verification of satellite-based precipitation products should quantify their accuracy in a wide range of weather and climate regimes, give users information on the expected errors in the estimates, help algorithm developers understand the strengths and weaknesses of the satellite rainfall algorithms. To get good estimates of absolute accuracy satellite products are verified against very high quality radar and gauge data. However, these sites are only few in number. To get estimates of regional and spatial accuracy it is necessary to use a much larger quantity of data, for example, from national rain gauge networks. While these verification data are less reliable than those from high-quality sites, their errors are usually much smaller than those associated with the satellite estimates, at least on short time scales. For validation of QPE with the ground truth on different temporal and spatial scale are required mainly with the data of DWR and Rain Gauges.

Finally the retrieved rainfall from earlier steps and Rain gauges and Doppler Weather Radar data on available locations in India would be used both for calibration and validation of the algorithm. The error analysis will be carried out and accordingly the algorithm will be fine tuned. A complete error statistics (regression, correlation, RMSE, BIAS, Mean, Standard Deviation etc.) will be performed for the desired period (validation period of about 3-4 months).

Rainfall maps on every 1/2 hourly and daily basis on pixel and any desired bigger grid spacing will be produced with all provisions to have maximum possible information (like contours, color shades, statistical information etc.). Based on this algorithm QPE on daily, pentad, monthly mean, seasonal mean and annual mean will be produced. The capability of to derive QPE from IMSRA over meteorological subdivisions will be attempted along with Image Analysis System Group. Accordingly the algorithm will be made operational after due testing and validation.

### 15.6.1. Data Required:

The following data for validation will be needed

Parameter	Resolution	Source
Doppler Weather Radar	$0.10^0 \times 0.10^0$	IMD - at all DWR locations (Every 1/2 Hourly basis $0.1^0 \times 0.1^0$ grids)
Fast Response Rain Gauges (for hourly rainfall) & Other Rain gauge Data Rain/day	Ground Truth (over land and oceans) point observation	IMD - At all Daily observation sites and to plan for oceanic locations
Total Water Vapour	$0.5 \times 0.5$ deg	3-6 hourly Eta /IMD Model Analysis from IMD, (500 mb to surface)
Relative Humidity	$0.5 \times 0.5$ deg	
TRMM Analysed Data GPM-IMERG data	Orbital and $\frac{1}{2}, 3$ hourly $0.1^0 \times 0.1^0$ , - $0.25^0 \times 0.25^0$ and $1^0 \times 1^0$	Data available through internet

### 15.6.2. Method of Validation:

Currently pulsed Doppler technique are applied in weather radars to map severe storm reflectivity and velocity structure with great success in showing in real time the development of cyclones providing quantitative measure of intensity, track and information on winds within and around the storm. By studying the characteristics of radar returns and analyzing the variations in their amplitude (or power received), phase or frequency shift or change in polarization state, DWR quantifies the different characteristics of the precipitating medium within the pulse volume. The amount of received power from the distributed target depends on the number of particles within the pulse volume of the beam, their size, composition, shape, orientation etc.

The DWR's are located at various sites all over the country. All are working operationally. DWR's estimates 3 base products namely Reflectivity (Z), Velocity (V) and Spectrum Width (W) as a function of range. From these base products, advanced data products are required to be generated to meet the validation needs.

Ground-based radar and gauge rainfall observations (from IMD, ISRO's AWS etc), at high resolution (hourly), are thus required to be used for validating rain product. High resolution IMD DWR products (hourly 4 Km x 4 Km) is required for evaluation over several small size study sites with hourly (daily when hourly is not available) rain-gauge density, for instance in  $1^{\circ} \times 1^{\circ}$  degrees. The size of every validation study site varies from  $0.5^{\circ} \times 0.5^{\circ}$  to  $2^{\circ} \times 2^{\circ}$  degrees, depending on the density and distribution of available hourly rain-gauge stations over the study site and horizontal

rain extents. In case of proper validation of GPI rainfall in particular, which is for a grid size of  $1.0^{\circ} \times 1.0^{\circ}$ , there should be minimum 3 rain gauges (IMD or AWS) to average out for comparison within a GPI grid size. For IMSRA, an hourly, and daily DWR and rain gauge information would be required on routine basis, preferably in  $0.25^{\circ} \times 0.25^{\circ}$  or atleast in  $0.5^{\circ} \times 0.5^{\circ}$  grids.

### **Pre-launch Field Experiments**

Pre-launch validation campaign were launched earlier for existing Kalpana, INSAT-3A based rainfall algorithms as a prelude to INSAT-3D, 3DR. A three months period will be selected (mainly rainy season) for collecting data from DWRs, all possible and quality assured rain gauges and the algorithm will be tested.

### **Post-Launch Special Field Experiments**

Many of the present ground-truth observations data networks are being augmented for the measurements of precipitation on ground. This includes the plans of IMD to put more DWR in various Indian regions. However, the existing ground based data sources will be utilized for the INSAT-3D Imager derived rainfall estimates. Some more details of the validation campaigns (timing, location, instrumentation, etc.) will be decided later in mutual consultation with IMD.

### **15.7. Merged Rain Products (IMSRA and Rain Gauges):**

To merge in situ rainfall data from the AWS rain gauges with INSAT-3D derived IMSRA rainfall estimates, one of the simplest and state-of-the-art techniques, called the successive correction method (Cressman, 1959; Thiebaux and Pedder, 1987) has been found suitable enough for objective analysis,. It involves the successive modification of satellite rainfall estimates based on observed rain gauge rainfall data. The objective analysis scheme benefits from the relative advantages of satellite and in situ data. In this method, the background field is corrected by the observed values iteratively during several analysis scans until the correction between the interpolated value and actual observation converges (Gairola et al. 2015). The interpolated weights are computed using the distance-dependent scheme and the correction (C) (Cressmaqn 1959) is done using the following equation:

$$C = (\sum W (P_0 - P_p)) / N \quad (1)$$

where  $P_0$  is rainfall at the observation point,  $P_p$  is the interpolated grid point data at observation point,  $N$  is the number of observations, and the weight ( $W$ ) is given by

$$\begin{aligned} W &= (R^2 - d^2) / (R^2 + d^2) \text{ for } d^2 \leq R^2 \\ &= 0 \text{ for } d^2 > R^2 \end{aligned} \quad (2)$$

where  $R$  is the radius of rainfall influence and  $d$  is the distance of the in situ data point from the grid point. The appropriate radius of rainfall influence is determined by the spatial autocorrelation analysis of daily IMSRA derived rainfall data. In recent study by Gairola et al. 2015), the objective analysis applied for rainfall estimates show noticeable improvement over the satellite-based

rainfall estimates. Comparison with independent rain gauge observations shows a considerable improvement in terms of correlation, bias and root-mean-square error after objective analysis, especially over the regions where density of rain gauge is fairly good. Overall results reveal that the synergistic use of satellite and in situ observations has potential for more accurate rainfall estimations over the Indian monsoon region.

#### Flow Chart for Merged Rain Products (IMSRA and Rain Gauges)

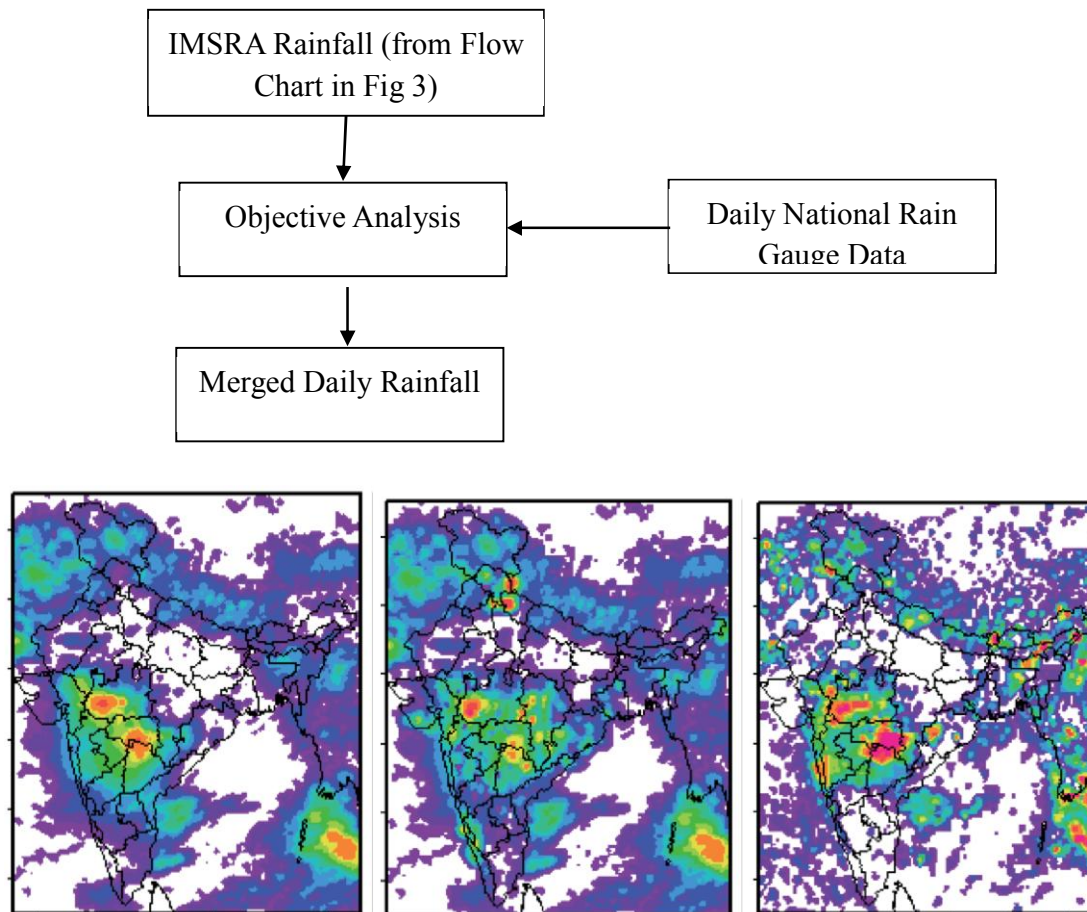


*Fig. 5. An example of Distributions of daily-accumulated rainfall (mm) over the Indian monsoon region derived from IMSRA, merged-IMSRA, and TMPA-V7 for August 6, 2010.*

#### 15.7.1. Major Conclusions

- The overestimation tendencies of IMSRA Rain can be considerably reduced by new scheme (Cloud growth & global bias correction).
- Orographic region shows significant improvement by the climatological orographic bias correction.
- Finally the merged rainfall over India from IMSRA and surface rain gauge data shows the

- improved rain estimates at a  $0.1^\circ$  latitude  $\times 0.1^\circ$  longitude spatial resolution.
- While the modified IMSRA rain products will be available after every half hourly, the merged products will be generated every next day for daily rainfall subject to the availability of rain gauge data from IMD.

## 15.8. Future Scope

Due to the heterogeneity of precipitation over the Earth's surface it is important that corrections be applied time to time to the algorithms depending on region specific processes. Conventional means are restricted primarily to certain land regions, and although satellite measurements are now commonly available, these have limitations too. Frequent observations from visible (VIS) and infrared (IR) sensors are hindered by the fact that estimates of precipitation are indirect and therefore prone to errors caused by cloud-top to surface rainfall variations. More direct measurements of precipitation through the use of passive microwave (PMW) instruments are somewhat restricted due their relative infrequent sampling of precipitation. Thus the algorithms for merging of microwave data with IR images to generate rainfall rates at the spatial and temporal resolutions of the IR sensor is highly desirable. The combined approaches can improve rainfall estimates using the temporal sampling of the VIS/IR data and the more direct nature of the microwave estimates, avoiding the mentioned weaknesses and re-inforce the mutual strengths. At present we have proposed to use Geostationary optical channels and low earth orbiting microwaves for the rainfall estimation by their inter-calibration process and finally validations with the ground truth. In future this approach can be further advanced by optimally integrating optical and microwave measurements by proper data assimilation schemes which will provide better rainfall than any of the sensors (optical, microwave and ground truth) alone.

In future sensitivity studies could be made to estimate rainfall over the Indian monsoon region by the synergistic use of the geostationary INSAT-3D -derived IMSRA rainfall estimates and rain data from GPM Microwave Radiometer (GMI), using a suitable objective analysis method. This will benefit from high spatial and temporal resolutions of the geostationary satellite and infrequent but more accurate microwave based rainfall estimates.

## References

- Adler, R. F., and A. J. Negri, 1988: A satellite infrared technique to estimate tropical convective and stratiform rainfall. *J. Appl. Meteorol.*, **27**, 30-51.
- Adler, R. F., G. J. Huffman, and P. R. Keehn, 1994: Global tropical rain estimates from microwave-adjusted geosynchronous IR data. *Remote Sens. Rev.*, **11**, 125-152.
- Arkin, P. A., 1979: The relationship between fractional coverage of high cloud and rainfall accumulations during GATE over the B-scale array. *Mon. Wea. Rev.*, **106**, 1153-1171.

- Arkin, P. A., and P. Xie, 1994: The Global Precipitation Climatology Project: First algorithm intercomparison project. *Bull. Amer. Meteor. Soc.*, **75**, 401–419.
- Arking, A., and J. D. Childs, 1985: Retrieval of cloud cover parameters from multispectral satellite images. *J. Climate Appl. Meteorol.*, **24**, 322-333.
- Ba, M. B., and A. Gruber, 2001: GOES Multispectral Rainfall Algorithm (GMSRA). *J. Appl. Meteorol.*, **40**, 1500-1514.
- Ba, M. B., D. Rosenfeld, and A. Gruber: 1998: AVHRR multispectral derived cloud parameters: relationship to microwave scattering signature and to cloud-to-ground lightning. *Prepr. 9th Conf. Satellite Meteorology and Oceanography*, AMS, 408-411.
- Barrett, E. C., and D. W. Martin, 1981: *The Use of Satellite Data in Rainfall Monitoring*. Academic Press, 340 pp.
- Bushair M. T., C. Mahesh and R.M.Gairola, Assessment of Kalpana-1 Rainfall product over Indian Meteorological Sub-Divisions during Summer Monsoon Season, Journal of Indian Society of Remote Sensing, 2015.
- Cheng, M., R. Brown, and C. G. Collier, 1993: Delineation of precipitation areas using METEOSAT infrared and visible data in the region of the United Kingdom. *J. Appl. Meteorol.*, **32**, 884-898.
- Cressman G. P., 1959. An operational objective analysis system. *Mon. Weather Rev.* **87**, 367-374.
- Gilberto A. Vicente, Roderic A. Scofield and W. Paul Menzee, 1998. Bulletin of American Meteorological Society.
- Espinoza, R. C., Jr., and Harshvardhan, 1996: Parameterization of solar near-infrared radiative properties of cloudy layers. *J. Atmos. Sci.*, **53**, 1559-1568.
- Ferraro, R. R., and G. F. Marks, 1995: The development of SSM/I rain-rate retrieval algorithms using ground-based radar measurements. *J. Atmos. Oceanic Technol.*, **12**, 755–770.
- Gairola R.M. and T.N. Krishnamurti, Rain rates based on OLR, SSM/I and rain gauge data sets. *Meteorology and Atmospheric Physics*. **50**, 165-174 (1992).
- Gairola R.M., and Varma, A. K., 2007, Algorithm Theoretical Basis Document for Hydroestimator Method, in “INSAT Geophysical Parameter Retrieval System – ATBD Document”, report# SAC/IMDPS/TN-05/Version-1, pp 37-62.
- Gairola1 R. M., Satya Prakash, M. T. Bushair and P. K. Pal, Rainfall estimation from Kalpana-1 satellite data over Indian land and oceanic regions, CURRENT SCIENCE, VOL. 107, NO. 8, 25 OCTOBER 2014.
- Gairola, R. M., A. Mishra, S. Prakash, and C. Mahesh, 2010a: Rainfall estimation from Kalpana-1 IR data using GPI approach and initial validations using AWS observations, *Scientific Report*, SAC/EPSA/AOSG/INSAT/SR-36/2010, pp.37.

- Gairola, R. M., A. Mishra, S. Prakash, and C. Mahesh, 2010b: Development of INSAT Multi-Spectral Rainfall Algorithm (IMSRA) for monitoring rainfall events over India using KALPANA-IR and TRMM-Precipitation Radar observations, *Scientific Report*, SAC/EPSC/AOSG/INSAT/SR-39/2010, pp.22.
- Gairola R. M. and T. N. Krishnamurti, 1992. Rain rates based on SSM/I, OLR and rain gauge data sets. *Meteorol. Atmos. Phys.* 50, 165-174.
- Gairola R. M., S. Prakash and C. Mahesh, 2012. Synergistic use of Kalpana-1 and rain gauge data for rainfall estimation: A case study over Gujarat. Workshop on Meteorological Satellite Kalpana: A decade of Service to the Nation. Ahmedabad, India, October 2012.
- Gairola R. M., S. Prakash and, P. K. Pal, Improved rainfall estimation over the Indian monsoon region by synergistic use of Kalpana-1 and rain gauge data, *Atmósfera* 28(1), 51-61 (2015).
- Gruber, A., X. Su, M. Kanamitsu, and J, Schemm, 2000: The comparison of two merged rain gauge-satellite precipitation datasets. *Bull. Am. Meteorol. Soc.*, **81**, 2631-2644.
- Houze R. A. Jr., 2012 Houze R. A. Jr.: Orographic effects on precipitating clouds, *Reviews of Geophysics*, 50(2012), RG1001, doi:10.1029/2011RG000365.
- Huffman, G. J., R. F. Adler, M. M. Morrissey, D. T. Bolvin, S. Curtis, R. Joyce, B. McGavock, and J. Susskind, 2001: Global precipitation at one-degree daily resolution from multisatellite observations. *J. Hydrometeorol.*, **2**, 36-50.
- Inoue, T., and K. Aonashi, 2000: A comparison of cloud and rainfall information from instantaneous Visible and InfraRed Scanner and Precipitation Radar observations over a frontal zone in East Asia during June 1998. *J. Appl. Meteorol.*, **39**, 2292-2301.
- Iguchi et al., 2000 Iguchi, T., T. Kozu, R. Meneghini, J. Awaka and K. Okamoto: Rain-profiling algorithm for the TRMM Precipitation Radar, *Journal of Applied Meteorology*, 39(2000), pp.147–150
- Inoue, T., 1987a: A cloud type classification with NOAA 7 split-window measurements. *J. Geophys. Res.*, **92 D**, 3991-4000.
- Inoue, T., 1987b: An instantaneous delineation of convective rainfall area using split window data of NOAA-7 AVHRR. *J. Meteorol. Soc. Japan*, **65**, 469-481.
- Janowiak, J. E., R. J. Joyce, and Y. Yarosh, 2001: A real-time global half-hourly pixel-resolution infrared dataset and its applications. *Bull. Am. Meteor. Soc.*, **82**, 205-217.
- Jobard, I., and M. Desbois, 1994: Satellite estimation of the tropical precipitation using the Meteosat and SSM/I data. *Atmos. Res.*, **34**, 285-298.
- Kidd, C., D. Kniveton, and E. C. Barrett, 1998: The advantages and disadvantages of statistically derived-empirically calibrated passive microwave algorithms for rainfall estimation. *J. Atmos. Sci.*, **55**, 1576-1582.

Kidder, S. Q., and T. H. Vonder Haar, 1995: *Satellite Meteorology: An Introduction*. Academic Press, 466 pp.

King, M. D., S.-C. Tsay, S. E. Platnick, M. Wang, and K.-N. Liou, 1997: Cloud retrieval algorithms for MODIS: optical thickness, effective particle radius, and thermodynamic phase. *MODIS Algorithm Theoretical Basis Doc.*, ATBD-MOD-05 and MOD-06.

Kummerow, C. D., W. Barnes, T. Kozu, J. Shiue, and J. Simpson, 1998: The Tropical Rainfall Measuring Mission (TRMM) sensor package. *J. Atmos. Oceanic Technol.*, **15**, 809-817.

Kummerow, C. D., Y. Hong, W. S. Olson, S. Yang, R. F. Adler, J. McCollum, R. Ferraro, G. Petty, D.-B. Shin, and T. T. Wilheit, 2001: The evolution of the Goddard Profiling Algorithm (GPROF) for rainfall estimation from passive microwave sensors. *J. Appl. Meteorol.*, **40**, 1801-1820.

Kuligoski R.J., Davenport J.C. and Scofield R.A., The hydro-estimator technique for high resolution geostationary satellite rainfall estimates, Pre-print, 2006.

Kuligoski R.J., Scofield R.A., and Gruber A., The NESDIS satellite verification program. Priprint, 11<sup>th</sup> Conf. on Satellite Meteorology and Oceanography, Madison, WI, Amer. Meteor. Soc., 383-384.

Lensky, I. M., and D. Rosenfeld, 1997: Estimation of precipitation area and rain intensity based on the microphysical properties retrieved from NOAA AVHRR data. *J. Appl. Meteorol.*, **36**, 234-242.

Levizzani, V., J. Schmetz, H. J. Lutz, J. Kerkmann, P. P. Alberoni, and M. Cervino, 2001: Precipitation estimations from geostationary orbit and prospects for METEOSAT Second Generation. *Meteorol. Appl.*, **8**, 23-41.

Mahesh, C., S. Prakash, V. Sathiyamoorthy, and R. M. Gairola: 2014: An improved approach for rainfall estimation over Indian summer monsoon region using Kalpana-1 data, *Advances in Space Research*, 54(4), 685-693, doi:10.1016/j.asr.2014.04.019.

Mahesh, C., S. Prakash, R. M. Gairola, S. Shah, and P. K. Pal: Meteorological sub-divisional scale rainfall monitoring using Kalpana-1 VHRR measurements, *Geographical Research* (2014), doi:10.1111/1745-5871.12068.

Mahesh C. et al., 2011 C. Mahesh, Satya Prakash, V. Sathiyamoorthy, R.M. Gairola: Artificial neural network based microwave precipitation estimation using scattering index and polarization corrected temperature, *Atmospheric Research*, 102(2011), pp.358–364

Mahesh et al., 2014 C. Mahesh, S. Prakash, V. Sathiyamoorthy, and R. M. Gairola, 2014: An improved approach for rainfall estimation over indian summer monsoon region using kalpana-1 data, *Advances in Space Research*, doi:10.1016/j.asr.2014.04.019.

Mishra Anoop Kumar, R.M. Gairola, A.K. Varma, Vijay K. Agarwal, Improved rainfall estimation over the Indian region using satellite infrared technique, 2011, doi:10.1016/j.asr.2011.02.016.

Nakajima, T., and M. D. King, 1990: Determination of the optical thickness and effective particle radius of clouds from reflected solar radiation measurements. Part I: theory. *J. Atmos. Sci.*, **47**, 1878-1893.

Menzel, W. P., and J. F. W. Purdom, 1994: Introducing GOES-I: the first of new generation of Geostationary Operational Environmental Satellites. *Bull. Am. Meteor. Soc.*, **75**, 757-781.

Miller, S. W., P. A. Arkin, and R. J. Joyce, 2000: A combined microwave/infrared rain rate algorithm. *Int. J. Remote Sens.*, **22**, 3285-3307.

Prakash S., R. M. Gairola & A. K. Mitra: Comparison of large-scale global land precipitation from multisatellite and reanalysis products with gauge-based GPCC data sets. *Theoretical and Applied Climatology*, DOI 10.1007/s00704-014-1245-5

Prakash, S., V. Sathiyamoorthy, C. Mahesh, and R. M. Gairola, 2014: An evaluation of high-resolution multisatellite rainfall products over the Indian monsoon region, *International Journal of Remote Sensing*, 35(9), 3018-3035, doi:10.1080/01431161.2014.894661.

Prakash et al., 2010 Prakash, S., C. Mahesh, R. M. Gairola, P. K. Pal : Estimation of Indian summer monsoon rainfall using Kalpana-1 VHRR data and its validation using rain gauge and GPCP data, *Meteorology and Atmospheric Physics*, 110(1-2)(2010), pp.45-57.

Prakash et al., 2009 Prakash S., C. Mahesh, A. Mishra, R. M. Gairola, A. K. Varma, P. K. Pal: Combined use of microwave and IR data for the study of Indian monsoon rainfall-2009, ISPRS Archives XXXVIII-8/W3 Workshop Proceedings: Impact of Climate Change on Agriculture(2009), pp.227-230, 17-18 Dec., SAC, Ahmedabad, India

Rajeevan et al., 2006 Rajeevan, M., J. Bhate, K. D. Kale, B. Lal: High resolution daily gridded rainfall data for the Indian region: Analysis of break and active monsoon spells, *Current Science*, 91(2006), pp.296-306.

Roe and G.H., 2005 Roe, G. H.: Orographic Precipitation, *Annu. Rev. Earth Planet. Sci.*, 33(2005), pp.645-671

Roca Remi, and V. Ramanthan, Scale dependence of Monsoon convective systems over the Indian Ocean, *J. of Climate* , Vol 13, April, 2000, 1286-1299.

Roca Remi, Voiler, M. Desbois, 2002, A multi satellite analysis of deep convectionand its moist environment over Indian ocean during winter monsoon, *Jour Geophys. Res.*

Rosenfeld, D., and G. Gutman, 1994: Retrieving microphysical properties near the tops of potential rain clouds by multispectral analysis of AVHRR data. *Atmos. Res.*, **34**, 259-283.

Rosenfeld, D., and I. M. Lensky, 1998: Satellite-based insights into precipitation formation processes in continental and maritime convective clouds. *Bull. Am. Meteor. Soc.*, **79**, 2457-2476.

Rosenfeld, D., and A. Gagin, 1989: Factors governing the total rainfall yield of ontinental convective clouds. *J Appl. Meteorol.*, **28**, 1015-1030.

- Rosenfeld, D., and A. Gagin, 1989: Factors governing the total rainfall yield of continental convective clouds. *J Appl. Meteorol.*, **28**, 1015-1030.
- Schmetz, J., P. Pili, S. A. Tjemkes, D. Just, J. Kerkmann, S. Rota, and A. Ratier, 2002: An introduction to Meteosat Second Generation (MSG). *Bull. Amer. Meteor. Soc.*, in press.
- Slingo, A., and H. M. Schrecker, 1982: On the shortwave radiative properties of stratiform water clouds. *Q. J. R. Meteorol. Soc.*, **108**, 407-426.
- Sheu, R.-S., J. A. Curry, and G. Liu, 1995: Satellite retrieval of tropical precipitation using combined International Satellite Cloud Climatology Project DX and SSM/I data. *J. Geophys. Res.*, **101**, 21 291–21 301.
- Saunders, R. W., and K. T. Kriebel, 1988: An improved method for detecting clear sky and cloudy radiances from AVHRR data. *Int. J. Remote Sensing*, **9**, 123-150.
- Scofield and R. A., : The NESDIS operational convective precipitation technique, *Monthly Weather Review*, 115(1987), pp.1773–1792
- Suprit, K. and D. Shankar, 2008 Suprit, K., D. Shankar: Resolving orographic rainfall over the Indian West Coast, *International Journal of Climatology*, 28(5)(2008), pp.643-657
- Tjemkes, S. A., L. van de Berg, and J. Schmetz, J., 1997: Warm water vapour pixels over high clouds as observed by METEOSAT. *Contr. Atmos. Phys.*, **70**, 15-21.
- Todd MC, C. Kidd, D Kniveton, TJ Bellerby, A combined satellite infrared and passive microwave technique for estimation of small scale rainfall.
- Turk, F. J., J. Hawkins, E. A. Smith, F. S. Marzano, A. Mugnai, and V. Levizzani, 2000a: Combining SSM/I, TRMM and infrared geostationary satellite data in a near-realtime fashion for rapid precipitation updates: advantages and limitations. *Proc. The 2000 EUMETSAT Meteorological Satellite Data Users' Conference*, 452-459.
- Vicente, G. A., 1996: Algorithm for rainfall rate estimation using a combination of GOES-8 11.0 and 3.9 micron measurements. *Prepr. 8th Conf. Satellite Meteorology and Oceanography*, AMS, 274-278.
- Vicente, G. A., R. A. Scofield, and W. P. Menzel, 1998: The operational GOES infrared rainfall estimation technique. *Bull. Am. Meteor. Soc.*, **79**, 1883-1898
- Woodley, W. L., B. Sancho: A first step towards rainfall estimation from satellite cloud photographs , *Weather*, 26(7)(1971), pp.279–289
- Xu, L., X. Gao, S. Sorooshian, P. A. Arkin, B. Imam: A microwave infrared threshold technique to improve GOES Precipitation Index, *Journal of Applied Meteorology*, 38(1999), pp.569-579

## **16. MIR Reflectance**

S.No.	Product Name	Spatial Resolution	Temporal Resolution
1	3DRIMG_MIR_REF	4 km x 4 km	30 minutes

## **16.1. Algorithm Configuration Information**

### **16.1.1. Algorithm Name**

MIR Reflectance (MIR\_REF)  
(Ref : IMD RFP )

### **16.1.2. Algorithm Identifier**

3DRIMG\_MIR\_REF

### **16.1.3. Algorithm Specification**

Version	Date	Prepared by	Description
1.0	24.02.2018	Shailendra S. Srivastava and Nitesh Kaushik	MIR Reflectance Baseline Document

## **16.2. Introduction**

This document describes the land surface reflectance retrieval algorithm for the MIR spectral band (3.8-4.0  $\mu\text{m}$ ) of Imager sensor of INSAT-3DR. MIR reflectance consists of both reflective and emissive parts. Previous studies have shown that, full radiance (reflective and emissive) can not be used for the studies involving global studies, where temperature gradients are due to the latitudinal/topographical variations. We remove the emissive component using the brightness temperature computed from the 11  $\mu\text{m}$  channel and making simple assumptions about the emissivities and transmittivities in both the channels, i.e. MIR and 11  $\mu\text{m}$ . These assumptions are found to be conservative in the expected range of temperatures( $T > 290$  K). More appropriate values of emissivities and transmittivities would be adopted in the subsequent version of the algorithm, which would evolve with time and experimentation. This algorithm is analyzed through the comparison with the collocated and synchronous MODIS/METEOSAT surface reflectance products.

### **16.2.1. Overview and background**

Mid-IR channel on Imager can be utilized for the detection of dark dense vegetation, burned areas etc., which can be used for land use/cover dynamics related studies. Red and NIR channels are traditionally used for detecting burned areas. However, these channels are highly affected by the aerosol scattering and absorption caused by the biomass burning (Kaufman and Remer, 1994), and hence affects the values of NDVI (Normalized Difference Vegetation Index). MIR part of the spectrum is also sensitive for the changes in the state of the vegetation (due to active chlorophyll associated with liquid water in the leaves), but it is virtually unaffected by the presence of most of the types of aerosols (except dust). Monitoring the MIR reflectance can help to study the vegetation

cover more reliably. However, MIR reflectance should be used with caution for the studies performed over global scales, only reflected component of the MIR should be utilized (Libonati et al., 2010). The emitted component of the signal may not represent the intrinsic properties of the surface. We remove the emissive component using the brightness temperature computed from the 11  $\mu\text{m}$  channel of INSAT-3DR and making simple assumptions about the emissivities and transmittivity in both the channels, i.e. MIR and 11  $\mu\text{m}$ .

### **16.2.2. Objective**

The main objective of this document is to briefly present the algorithm to generate surface reflectance (only reflective component) for the MIR band of INSAT-3DR Imager.

## **16.3. Inputs**

### **16.3.1. Static data**

Parameter	Resolution	Quantization	Accuracy	Source

### **16.3.2 Image and pre-processing data (Dynamic)**

The following table gives a list of inputs required for algorithm input and calibration:

Parameter	Resolution	Accuracy	Source
Radiometric and geometric corrected gray count values of MIR channel (3.9 $\mu\text{m}$ )	pixel	--	Derived from raw data by DP (data processing)
Radiometric and geometric corrected gray count values of TIR-1 channel (11 $\mu\text{m}$ )	pixel	--	--do--
Solar Zenith Angle	pixel	--	--do--
Solar Azimuth Angle	pixel	--	--do--
Satellite Zenith Angle	pixel	--	--do--
Satellite Azimuth Angle	pixel	--	--do--
WV	0.5° X 0.5°	---	Forecast

## 16.4. Algorithm Functional Specifications

### 16.4.1. Overview

#### 1.4.1.1 Theoretical Background

In the thermal infrared spectral region and in the day time observations, thermal emission and solar reflection are in the same order of magnitude (Petitcolin & Vermote, 2002). Assuming cloud free atmosphere under local thermodynamic equilibrium, the sensor measured MIR radiance  $I_{MIR}$  is given by the following equation (A.-L. Li et al., 2013):

$$I_{MIR}(\theta, \phi) = R(\theta, \phi)\tau(\theta, \phi) + R_{at\uparrow}(\theta, \phi) + R_{sc\uparrow}(\theta, \phi) \quad \dots \quad (1)$$

Where,  $R$  is attenuated (by atmosphere) radiance from the ground (path 1 in the following figure),  $\tau$  is the transmittance of the atmosphere. The second term on the right hand side,  $R_{at\uparrow}$  is the upward atmospheric thermal radiance (path 2 in the figure), and  $R_{sc\uparrow}$  is the upward solar diffusion radiance resulting from atmospheric scattering of the solar radiance (path 3 of the figure).  $R$  can further be decomposed in the following equation (path 4 to 7 in the figure).

$$\begin{aligned} R(\theta, \phi) = & \varepsilon(\theta, \phi)B(T_s) + [1 - \varepsilon(\theta, \phi)]R_{at\downarrow} + [1 - \varepsilon(\theta, \phi)]R_{sc\downarrow} \\ & + \rho_b(\theta, \phi, \theta_s, \phi_s)E \cos(\theta_s)\tau(\theta_s, \phi_s) \quad \dots \quad (2) \end{aligned}$$

$\varepsilon B(T_s)$  represents the radiance emitted by the surface due to its physical temperature ( $T_s$ ), and its emissivity (intrinsic property of the surface, primarily depends on surface composition and is a gauge of the efficiency of a surface in radiating thermal energy in comparison to that of a blackbody at equivalent wavelength). ‘ $\theta$ ’ and ‘ $\phi$ ’ are view zenith and azimuth angles respectively.  $R_{at\downarrow}$  is the downward atmospheric thermal radiance.  $R_{sc\downarrow}$  is the downward solar diffusion radiance.  $(1-\varepsilon)$  represents the reflection. The last term of the above equation  $\rho E \tau$  is the direct solar radiance reflected by the surface.

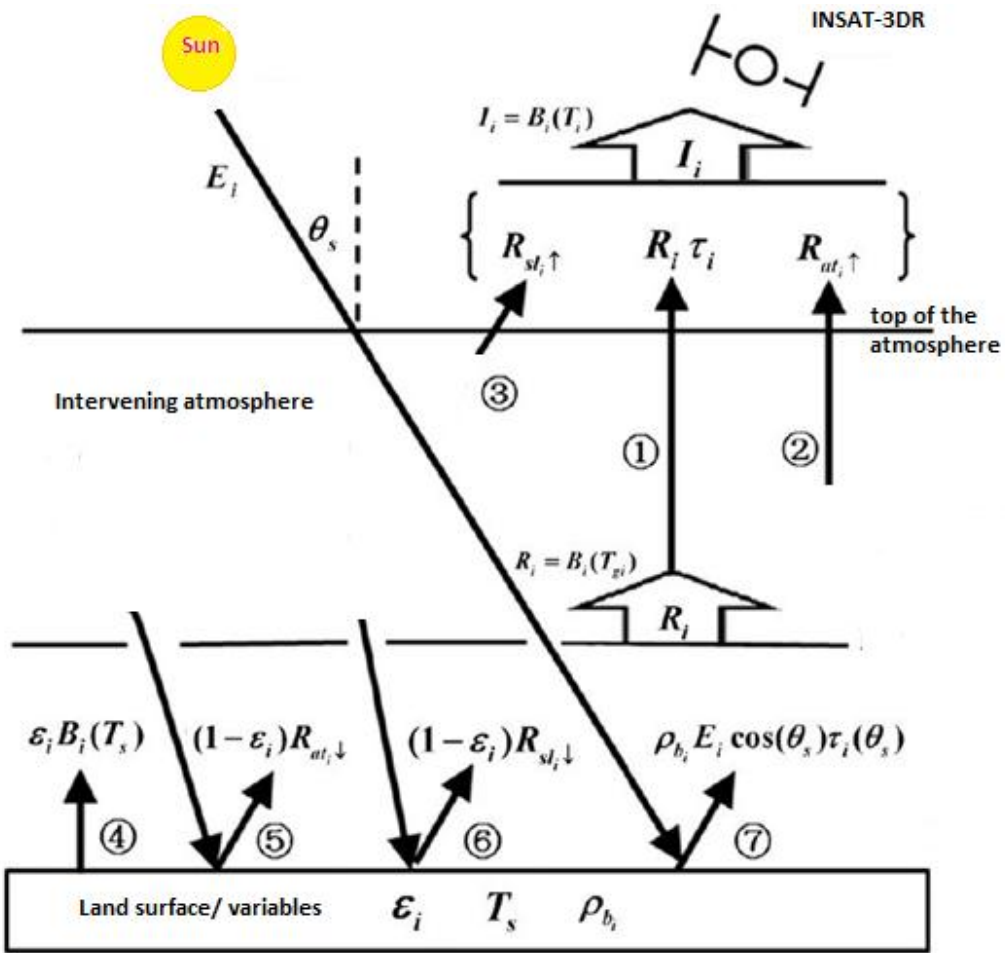


Figure 1: Transfer of radiation from surface to sensor (Taken from Zhao-Liang Li et al., 2013.)

#### 1.4.1.2 Algorithm Overview

The MIR radiance consists of two components, one is reflective and another is emissive.

$$L_{mir} = \tau'_{mir} \rho_{mir} \frac{F_0 \mu_0}{\pi} + \tau_{mir} \varepsilon_{mir} B_{mir}(T) --- (3)$$

Where,  $L_{mir}$  is the radiance in MIR channel,  $\tau'_{mir}$  is two way transmission,  $\tau_{mir}$  is one way transmission  $\rho_{mir}$  is the reflectance in the MIR channel,  $F_0$  is the incident solar flux at the top of the atmosphere,  $\mu_0$  is the cosine of the solar zenith angle,  $\varepsilon_{mir}$  is the emissivity of the surface at MIR band, and  $T$  is the brightness temperature.

$T$  is computed by inverting the Planck function.

$$L_{11,\mu m} = \tau_{11,\mu m} \varepsilon_{11,\mu m} B_{11,\mu m}(T) --- (4)$$

Where,  $L_{11\mu\text{m}}$  is the radiance measured in the 11  $\mu\text{m}$  channel of INSAT-3DR,  $\tau_{11\mu\text{m}}$  is one way transmission,  $B_{11\mu\text{m}}$  is the Planck function, and  $\varepsilon_{11\mu\text{m}}$  is the emissivity of the surface at 11  $\mu\text{m}$ .

As the Earth's surface is not transparent, so we can safely assume  $\rho_{\text{mir}} = 1 - \varepsilon_{\text{mir}}$  and solve the above equations to retrieve MIR reflectance.

$$\rho_{\text{mir}} = \frac{L_{\text{mir}} - \tau_{\text{mir}} B_{\text{mir}}(T)}{\tau_{\text{mir}} \frac{F_0 \mu_0}{\pi} - \tau_{\text{mir}} B_{\text{mir}}(T)} \quad \dots \quad (5)$$

The transmission functions depend on the temperature and water vapor in the atmospheric column.

In the present version of the algorithm, we would assume the emissivities and transmittivities to equal to 1.0. This assumption should cause errors within acceptable limits i.e.,  $\leq 0.02$  in reflectance units in the retrieved MIR reflectance.

We would try and incorporate the more appropriate values of emissivities and transmittivities in the subsequent version of the algorithms.

#### **16.4.2. Operational retrieval Implementation**

The operational implementation of the retrieval process can be enumerated as follows:

*Step 1:* Extraction of the radiance (of MIR and 11 $\mu\text{m}$ ) and WV data.

*Step 2:* Preprocessing of all the ancillary inputs in terms of bringing all the inputs on the same geometrical scale.

*Step 3:* Computation of the MIR reflectance (reflected component) using analytic equations (4 and 5, substituting value of T from 4 into 5).

### **16.5. Outputs**

Generation of surface reflectance for the MIR band of INSAT-3DR/3D Imager.

#### **16.5.1. Format of the output and the domain**

Geo-Tiff Image of Bottom of Atmosphere Surface reflectance and Top of Atmosphere Reflectance.

### **16.6. Validation**

Validation is still pending and to be discussed with calibration/validation team of SAC.

#### **16.6.1. Data required**

Collocated MODIS/METEOSAT data of MIR band would be required for the comparison.

### **16.6.2. Methods of validation**

Collocated data of INSAT-3DR and MODIS/METEOSAT would be compared over various uniform targets of different reflectance, for example over soil, vegetation and over some bright targets.

## **16.7 Technical issues (limitation etc.)**

Accuracy of the product will depend on the accuracy of the inputs. It would also be dependent on the calibration of the product.

In the present version of the algorithm, we would assume the emissivities and transmittivities to be equal to 1.0. This assumption should cause errors within acceptable limits i.e.,  $\leq 0.02$  in reflectance units in the retrieved MIR reflectance. We would try and incorporate more appropriate values of emissivities and transmittivities in the subsequent version of the algorithms. Emissivity/Temperature discrimination is not attempted in the present implementation.

## **16.8 Future Scope**

Correction for the emission component and out of band correction in a more accurate manner would be attempted.

## **References**

Kaufman, Yoram J., and Lorraine A. Remer, "Detection of forests using Mid-IR Reflectance: An application for aerosol studies", *IEEE Transactions on Geoscience and Remote Sensing*, Vol. 32, No. 3, pp. 672-683, May 1994.

Li, Zhao-Liang, Bo-Hui Tang, Hua Wu, Huazhong Ren, Guangjian Yan, Zhengming Wan, Isabel F. Trigo, Jose A. Sobrino, "Satellite-derived land surface temperature: current status and perspectives", *Remote Sensing of Environment*, pp. 14-37, Vol. 131, 2013.

Libonati, Renata, Carlos C. CaCamara, Jose Miguel C. Pereira, Leonardo F. Peres, "Retrieving middle-infrared reflectance for burned area mapping in tropical environments using MODIS", *Remote Sensing of Environment*, Vol. 114, pp. 831-843, 2010.

Petitcolin, Francois, and Eric verMOTE, "Land surface reflectance, emissivity and temperature from MODIS middle and thermal infrared data", *Remote Sensing of Environment*, pp. 112-134, Vol. 83, 2002.

## **17. Potential evapotranspiration (PET) from INSAT 3D insolation product and short-range forecasts**

S. No.	Product Name	Spatial Resolution	Temporal Resolution
1	IMG_PET		

## **17.1. Algorithm Configuration Information**

### **17.1.1. Algorithm name**

Potential evapo-transpiration

### **17.1.2. Algorithm identifier**

INSAT\_IMAGER\_PET

### **17.1.3. Algorithm specification**

<b>Version</b>	<b>Date</b>	<b>Prepared by</b>	<b>Description</b>
1.0		Dr. Rahul Nigam and Dr. Bimal K. Bhattacharya	Potential evapo- transpiration baseline document

## **17.2. Introduction**

The process of evapotranspiration ( $ET$ ) acts as one of the main drivers of the hydrological or water cycle. One of the distinguishing factors of  $ET$  is its role as a key player between the energy and water cycles. The potential ET rate ( $ET_o$ ) is influenced by several factors such as solar radiation, wind speed, air temperature and vapour pressure deficit. Among them, solar radiation is the most sensitive parameter influencing almost 60-70% variability of  $ET_o$ . The potential evapotranspiration (PET), hereafter referred as grass reference evapo-transpiration ( $ET_o$ ), is expressed in terms of amount of water transferred per unit time to atmosphere from water non-limiting surface covered with a uniformly and actively growing short grass such as Alfalfa.  $ET_o$  represents the evaporative demand of the atmosphere for a given climatic region. Deficiency in required supply of moisture leads to water stress. Reference evapo-transpiration is an agrometeorological variable widely used in hydrology and agriculture. Together with precipitation, it is a major input in soil water balance models. Several of these models require daily or hourly evapo-transpiration data to provide acceptable estimate of plants' water requirements. This would provide regional water demand in different agro-climatic settings and agricultural growing season. The combination of spatial rainfall with  $ET_o$  would help in monitoring water deficit and surplus during a growing season for rainfed agriculture.

Some contours of monthly climatic  $ET_o$  have been generated by Department of Agricultural Meteorology, IMD (India Meteorological Department) from measurements of limited surface observatories in India. But interpolation from such contours will propagate large errors. No digital map of  $ET_o$  is available to scientific community, modelers, resource managers and planners in India. Moreover, real-time updated spatial  $ET_o$  product at weekly, ten-day, fortnightly and monthly scales would aid in knowing the intra and inter-seasonal climatic variability of water stress factors and their impact on deviation in biomass and yield. The climatic moisture index (ratio of rainfall

and PET) is essential to know surface wetness and suitability of sowing or transplanting operations. Therefore, it has the relevance for national agro-advisory services to farmers as well as crop forecasting.

### 17.2.1. Overview and background

The latent heat of vaporization, which is the energy required for evaporating water is significant in weather and climate dynamics (Priestley & Taylor, 1972; Monteith, 1973; Rowntree, 1991; Anderson et al., 2007). Although the concept of “evaporation” has been known since approximately 500 B.C. (see Brutsaert, 1982 for a chronological sketch), most of the understanding of the governing factors has been achieved in the last two centuries. Dalton (1802) was the first who proposed relationship of vapor pressure deficit ( $e_{\text{sat}} - e_{\text{act}}$ ) of the near surface air to the evaporation rate. Later, many empirical relationships were developed based on other environmental factors (Blaney and Criddle, 1950; Hargreaves, 1975; Thornthwaite, 1948). Based on available energy considerations and turbulent flux theory, Penman (1948) developed his evaporation equation for natural surfaces for water non-limiting conditions. This is known as potential evapotranspiration (PET). Monteith (1964) developed a modified version of the Penman equation in which biophysics was introduced through a surface or canopy resistance – the now well-known Penman–Monteith (P-M) combination equation – that allowed for vegetation control on transpiration rates.

Choudhury (1997) proposed a method to assess by means of satellite data, such as remotely sensed solar radiation, air temperature (derived from infrared images and weather station measurements) and vapor pressure deficit. This method provides good evapo-transpiration estimates for low-resolution applications such as worldwide scale and monthly time step. The accuracy is limited by the high uncertainties provided by satellite-sensed vapor pressure estimation.

Later, Bois et al. (2008) used remotely sensed solar radiation from METEOSAT observations from Heliosat-2 approach (Rigollier et al. 2004) and air temperature data to estimate  $ET_o$  using Hargreaves approach. The  $ET_o$  can also be available as forecast bi-product from weather forecasting model. However, recent evaluation of predicted radiative fluxes and operational short-range forecasts (24 hrs average) of routine weather elements from model for a limited winter months showed that the incident shortwave radiative flux produced the highest root mean square error to the tune of 110% (Bhattacharya et al, 2012a) amongst others as compared to *in situ* measurements from INSAT-linked micrometeorological stations (popularly known as AMS). However, the errors of short-range forecast of air temperatures, relative humidity, atmospheric pressure, wind speed at 10 m height were 3%, 12%, 21% and 1.4% respectively over plain and plateau regions. The per cent RMSE for last four variables were found to increase in the hilly terrain (Bhattacharya et al, 2012a). Expectedly, the  $ET_o$  would have substantial errors propagated mainly from incident solar radiation flux estimation. on the other hand, the operational product on daily insolation from Kalpana-1 VHRR produced around 25% RMSE (Bhattacharya et al, 2012b) with respect to same ground reference and the per cent RMSE decreased with averaging over

weekly, ten-day, fortnightly and monthly scales up to 15%. After improvement in the cloud flagging and the spatial resolution of operational insolation product from INSAT 3D, it is expected to produce substantially less errors. Therefore, it seems wise to use the combination of daily insolation product from INSAT 3D and operational forecasts of air temperatures, relative humidity, wind speed and atmospheric pressure to generate real-time digital and regional product of potential evapo-transpiration.

### **17.2.2. Objectives**

The objectives of this document are :

- To outline the algorithm for the estimation of potential evapo-transpiration ( $ET_o$ ) based on Penman-Monteith (P-M) approach (FAO-56 model)
- To integrate operational product of daily insolation from INSAT 3D and 24 hrs average operational forecast of routine weather elements at finer spatial resolution to generate product of spatial  $ET_o$  at 5 km spatial resolution
- To implement the algorithm in IMDPS GPR (Geophysical Parameter Retrieval) chain for automation of  $ET_o$  product generation
- To describe validation strategy against *in-situ* measurements with initial results

### **17.2.3. Instrument and characteristics of input products**

#### **17.2.3.1 Indian geostationary satellite (INSAT 3D)**

The Indian National Satellite (INSAT) system is a joint venture of the Department of Space (DOS), Department of Telecommunications (DOT), and India Meteorological Department (IMD). INSAT 3D is an exclusive meteorological satellite in the INSAT system, which was launched at geostationary orbit in 2013. This radiometer consists of four bands : broad VIS (0.52-0.75), SWIR (1.55-1.70), MIR(3.8-4.0), WV(6.5-7.0) and two thermal TIR1(10.2-11.2), TIR2 (11.5-12.5) with nineteen sounder channel. The spatial resolution of VIS and SWIR band is 1 km x 1 km and 4 km x 4 km for MIR, WV and two thermal IR bands. The introduction of INSAT Meteorological Data Processing System (IMDPS) provides both ‘full-globe’ and ‘sector’ data products in all the bands at half-an-hour interval at 4 km spatial resolution in an automated mode. So, there are maximum 48 acquisitions on a given day. Raw data after reception at each acquisition were corrected for servo, line-loss, radiometry, stagger and oversampling removal using the INSAT 3D data products scheduler. This results into automated generation of co-registered data in each band at Transverse Mercator (TM) projection. The dimension of each band at each acquisition is 676 rows x 721 columns for Asia Mercator sector product.

### **17.2.3.2. Operational insolation product**

A spectrally integrated clear-sky and three-layer cloudy-sky models were developed to determine integrated atmospheric transmittances and instantaneous insolation. Half-an-hourly observations from an Indian geostationary satellite sensor, INSAT 3D, were used to provide minimum ground brightness (surrogate of surface albedo) from previous 30 days, cloud top albedo, brightness temperatures, atmospheric water vapour as inputs to these models in addition to global eight-day aerosol optical depth at 550 nm and columnar ozone. A trapezoidal scheme was implemented to obtain daily insolation (in  $\text{MJm}^{-2}$ ) from half-an-hour instantaneous insolation ( $\text{Wm}^{-2}$ ) throughout the day for all-sky conditions (clear + cloudy). The whole algorithm (Bhattacharya et al, 2010 & 2012b) will be operationalized and daily insolation product can available at 4 km spatial resolution with Transverse Mercator projection routinely from MOSDAC site (<http://www.mosdac.gov.in>).

### **17.2.3.3. Operational product of WRF short-range forecast**

Weather Research and Forecasting (WRF; Skamarock et al., 2008) Model version 3.1 is used for All India Short range weather forecast. WRF is a limited area, non-hydrostatic, primitive equation model with multiple options for various physical parameterization schemes. This version employs Arakawa C-grid staggering for the horizontal grid and a fully compressible system of equations. The terrain following hydrostatic pressure co-ordinate with vertical grid stretching is followed in vertical. The time-split integration uses 3<sup>rd</sup> order Runge-Kutta scheme with a smaller time step for acoustic and gravity wave modes. The WRF physical options used in this proposal consists of the WRF Single Moment 6-class simple ice scheme for microphysics (WSM6); the Grell-Devenyi ensemble cumulus convection parameterization scheme; and the Yonsei University (YSU) planetary boundary layer scheme.

The WRF Model is integrated in a triple domain configuration with a horizontal resolution of 45 km, 15 km and 5 km for the All India, with grid points 260×235, 352×373 and 676×721 in x and y directions for the domains 1, 2 and 3, respectively. The model has 36 vertical levels with the top of the model atmosphere located at 10 hPa. The WRF 3D-Var is used for the assimilation of all available conventional including ISRO-AWS data and satellite observations to improve the model initial conditions. The operational WRF short-range forecasts (Kumar et al., 2011), available at MOSDAC site used climatological land surface and atmospheric parameters from global database and assimilated all available conventional including ISRO-AWS and satellite observations (Kumar et al., 2011; Singh et al., 2011) from Indian and other International agencies (e.g. EUMETCast). The operational forecast is available at finer spatial resolution (~5km) at three hourly interval upto 72 hours.

Examples of operational daily insolation product and 24 hrs average WRF forecast product of air temperature, relative humidity, wind speed and atmospheric pressure over Indian region are shown in Figure 1.

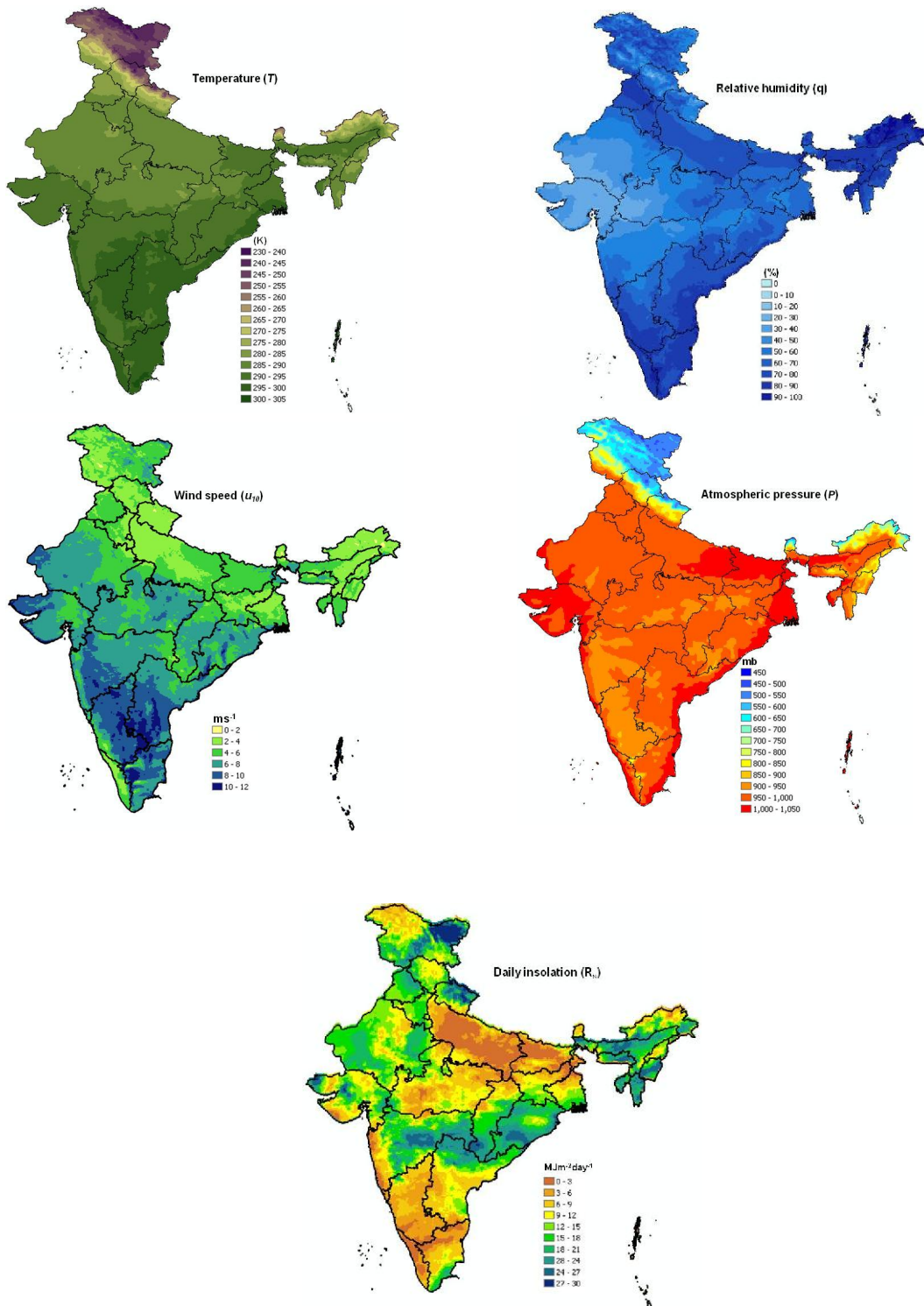


Figure 1. Example set of spatial inputs generated from WRF and K1VHRR for August 2011

### 17.3. Inputs

17.3.1. Static data: NIL

17.3.2. Image and pre-processing data (Dynamic)

**Table 1**

Parameter	Resolution	Quantization	Accepted accuracy	Source
Daily insolation product of Asia Mercator sector (e.g. h5 format)	Pixel (4km x 4km)	10-bit (integer) with scale factor of 0.01	10-15%	PR chain of IMDPS chain at BES
Geolocation file containing latitude and longitude corresponding to coregistered INSAT 3D data	Pixel wise	16-bit (floating point)	Less than one pixel	DP h5 product

17.3.3. Other auxiliary data and model inputs

**Table 2**

Parameters	Source
Operational three-hourly forecast output from WRF at $0.05^\circ \times 0.05^\circ$ spatial resolution for the following parameters in ASCII format (latitude, longitude, parameter) Air temperature (K) at 2 m height Relative humidity (%) at 2 m height Atmospheric pressure (mb) Wind speed ( $\text{ms}^{-1}$ ) at 10 m height	MOSDAC

### 17.4. Algorithm functional specifications

In 1948, Penman combined the energy balance with the mass transfer and derived an equation to compute the evaporation from an open water surface from standard meteorological records of sunshine, temperature, humidity and wind speed. This combination method was further extended to vegetated surface by introducing resistance term. The aerodynamic and surface resistances have been added to the original equation of Penman to estimate Potential evapotranspiration ( $ET_o$ ) from

a surface. This formulation is referred as FAO-56 Penman and Monteith (Allen et al., 1998)  $ET_o$  for a day. This is treated as standardized model worldwide. This is described as follows:

$$ET_o = \frac{0.408\Delta(R_n - G) + \gamma \frac{900}{T+273} u_2(e_s - e_a)}{\Delta + \gamma(1 + 0.34u_2)} \quad (1)$$

$ET_o$  = reference evapotranspiration for a day ( $\text{mm day}^{-1}$ )

$R_n$  = net radiation at the crop surface ( $\text{MJ m}^{-2} \text{day}^{-1}$ )

$G$  = Soil heat flux ( $\text{MJ m}^{-2} \text{day}^{-1}$ )

$T$  = mean daily air temperature at 2 meter height ( $^{\circ}\text{C}$ )

$u_2$  = wind speed at 2 meter height ( $\text{ms}^{-1}$ )

$e_s$  = saturation vapour pressure ( $\text{kPa}$ )

$e_a$  = actual vapour pressure ( $\text{kPa}$ )

$e_s - e_a$  = saturation vapour pressure deficit ( $\text{kPa}$ )

$\Delta$  = slope of vapour pressure curve ( $\text{kPa } ^{\circ}\text{C}^{-1}$ )

$\gamma$  = Psychrometric constant ( $\text{kPa } ^{\circ}\text{C}^{-1}$ )

$T_{hr}$  = mean hourly air temperature ( $^{\circ}\text{C}$ )

The above FAO Penman and Monteith equation is a close representation of the physical and physiological factors governing the evapotranspiration process. To compute  $ET_o$  from FAO-56 Penman-Monteith approach following intermediate inputs are calculated as follows:

#### 17.4.1. Saturation vapour pressure ( $e_s$ )

As saturation vapour pressure (SVP) is related to air temperature, it can be calculated as:

$$e^o(T) = 0.6108 \exp\left[\frac{17.27T}{T+237.3}\right]$$

$e^o(T)$  = Saturation vapour pressure ( $\text{kPa}$ ) at the air temperature  $T$

$T$  = air temperature ( $^{\circ}\text{C}$ )

#### 17.4.2. Slope of saturation vapour pressure curve ( $\Delta$ )

The relationship between saturation vapour pressure (SVP) and temperature  $\Delta$ , is required. The slope of the curve at a given temperature is given by:

$$\Delta = \frac{4098[0.6108 \exp\left(\frac{17.27T}{T+237.3}\right)]}{(T+237.3)^2}$$

$\Delta$  = slope of saturation vapour pressure curve at air temperature  $T [kPa^{\circ}C^{-1}]$

#### 17.4.3. Actual vapour pressure ( $e_a$ )

As the dewpoint temperature is the temperature to which the air needed to be cooled to make the air saturated, the actual vapour pressure (AVP) can be computed as follows:

$$e_a = \left( \frac{RH}{100} \right) e_s$$

$RH$  = Relative humidity ( % )

$e_s$  = Saturation vapour pressure (kPa)

#### 17.4.4. Psychrometric constant ( $\gamma$ )

The psychrometric constant ( $\gamma$ ) is given as:

$$\gamma = \frac{C_p P}{\varepsilon \lambda} = 0.000665 * P$$

$P$  = atmospheric pressure (kPa)

$\lambda$  = latent heat of vaporization (2.45 MJkg<sup>-1</sup>)

$C_p$  = Specific heat at constant pressure (1.013 x 10<sup>-3</sup> MJkg<sup>-1</sup>°C<sup>-1</sup>)

$e$  = ratio of molecular weight of water vapour and dry weight (0.622)

#### 17.4.5. Extraterrestrial radiation ( $R_a$ )

The radiation striking perpendicular at the top of the earth's atmosphere called the solar constant (0.082 MJm<sup>-2</sup>min<sup>-1</sup>). The local intensity of radiation is dependent on angle between the direction of Sun's rays and the normal to atmosphere. This angle will change within a day and with latitude on different days of the year. Solar radiation received at the top of the earth's atmosphere on a horizontal surface is called extraterrestrial (solar) radiation,  $R_a$ . It is computed using astronomical units as listed by Iqbal (1983).

$$R_a = \frac{24(60)}{\pi} G_{SC} d_r [\omega_s \sin(\varphi) \sin(\delta) + \cos(\varphi) \cos(\delta) \sin(\omega_s)]$$

$R_a$  = Extra-terrestrial radiation [MJm<sup>-2</sup>day<sup>-1</sup>]

$G_{SC}$  = Solar constant (0.82 MJm<sup>-2</sup>min<sup>-1</sup>)

$d_r$  = inverse of relative distance between earth and sun

$\omega_s$  = Sunset hour angle (radian)

$\varphi$  = Latitude (radian)

$\delta$  = Solar declination (radian)

#### **17.4.6. Solar or shortwave radiation ( $R_s$ )**

The radiation penetrates the atmosphere, some of the radiation is scattered, reflected or absorbed by the atmospheric gases, cloud and dust. The amount of solar radiation reaching horizontal plane is known as the incident solar radiation at surface  $R_s$ . The  $R_s$  should be in  $\text{MJm}^{-2}\text{day}^{-1}$ .

#### **17.4.7. Net solar or net shortwave radiation ( $R_{ns}$ )**

The net shortwave radiation is net balance between incoming and reflected solar radiation in short wave range and is given by,

$$R_{ns} = (1 - \alpha)R_s$$

$R_{ns}$  = net solar or shortwave radiation ( $\text{MJm}^{-2}\text{day}^{-1}$ )

$\alpha$  = albedo which is 0.23 for reference grass (e.g. Alfalfa)

$R_s$  = incoming solar radiation [ $\text{MJm}^{-2}\text{day}^{-1}$ ] received at ground surface

#### **17.4.8. Net longwave radiation ( $R_{nl}$ )**

The longwave radiation emission is proportional to the absolute temperature of the surface raised to the fourth power as per Stefan-Boltzmann law. The net radiation leaving the earth's surface is however, less than emitted due to the absorption and downward radiation from the sky. The atmospheric constituents like water vapour, clouds, carbon dioxide and dust are absorbers and emitters of longwave radiation. Their concentration should be vital for assessing the net outgoing radiation. The Stefan-Boltzmann law is corrected for water vapour and cloudiness by assuming the concentration of other atmospheric constituents remain constant.

$$R_{nl} = \sigma [T_K^4] \left[ 0.34 - 0.14\sqrt{e_a} \right] \left( 1.35 \frac{R_s}{R_{so}} - 0.35 \right)$$

$R_{nl}$  = net outgoing longwave radiation [ $\text{MJm}^{-2}\text{day}^{-1}$ ]

$\sigma$  = Stefan-Boltzmann constant [ $4.903 \times 10^{-9} \text{ MJK}^{-4}\text{m}^{-2}\text{day}^{-1}$ ]

$T_K$  = Mean absolute temperature (K) during a day

$e_a$  = actual vapour pressure [KPa]

$\frac{R_s}{R_{so}}$  = relative short wave radiation ( $\leq 1$ )

$R_s$  = estimated solar radiation [ $\text{MJm}^{-2}\text{day}^{-1}$ ]

$R_{so}$  = calculated clear sky radiation [ $\text{MJm}^{-2}\text{day}^{-1}$ ]

The term  $(0.34 - 0.14\sqrt{e_a})$  expresses the correction for air humidity and becomes smaller if humidity increases. The cloudiness is expressed as  $\left(1.35 \frac{R_s}{R_{so}} - 0.35\right)$  and it becomes smaller if the cloudiness increases and hence  $R_s$  decreases.

The clear-sky radiation,  $R_{so}$  is required for computing net long wave radiation

$$R_{so} = (0.75 + 2 * 10^{-5} Z) R_a$$

$Z$  = station elevation above sea level (meter)

$R_a$  = Extraterrestrial radiation [MJ m<sup>-2</sup> day<sup>-1</sup>]

The above equation is valid for station elevation less than 6000 m having low air turbidity. The equation was developed by linearizing Beer's radiation extinction law as a function of station elevation and assuming that the average angle of the sun above the horizon is about 50°. For areas of high turbidity caused by pollution or airborne dust or for regions where the sun angle is significantly less than 50° so that the path length of radiation through the atmosphere is increased, an adaption of Beer's law can be employed where  $P$  is used to represent atmospheric mass:

$$R_{so} = R_a \exp\left(\frac{-0.0018 * P}{K_t \sin \varphi}\right)$$

$K_t$  = turbidity coefficient,  $0 < K_t \leq 1.0$  where  $K_t = 0.0$  for clean air and

$K_t = 1.0$  for extremely trubid, dusty or polluted air.

$P$  = atmospheric pressure [kPa]

$\varphi$  = angle of the sun above the horizon [radian]

$R_a$  = extraterrestrial radiation [MJ m<sup>-2</sup> d<sup>-1</sup>]

#### 17.4.9. Net radiation ( $R_n$ )

The net radiation ( $R_n$ ) is difference between the incoming net shortwave radiation ( $R_{ns}$ ) and the outgoing net longwave radiation  $R_{nl}$ .

$$R_n = R_{ns} - R_{nl}$$

#### 17.4.10. Wind speed

For calculation of  $ET_0$ , wind speed measured at 2 meter above the surface is required. To adjust wind speed data obtained from instruments placed at elevations other than the standard heights of 2 meter, a logarithmic wind speed profile may be used for such conversion.

$$u_2 = u_z \frac{4.87}{\ln(67.82z - 5.42)}$$

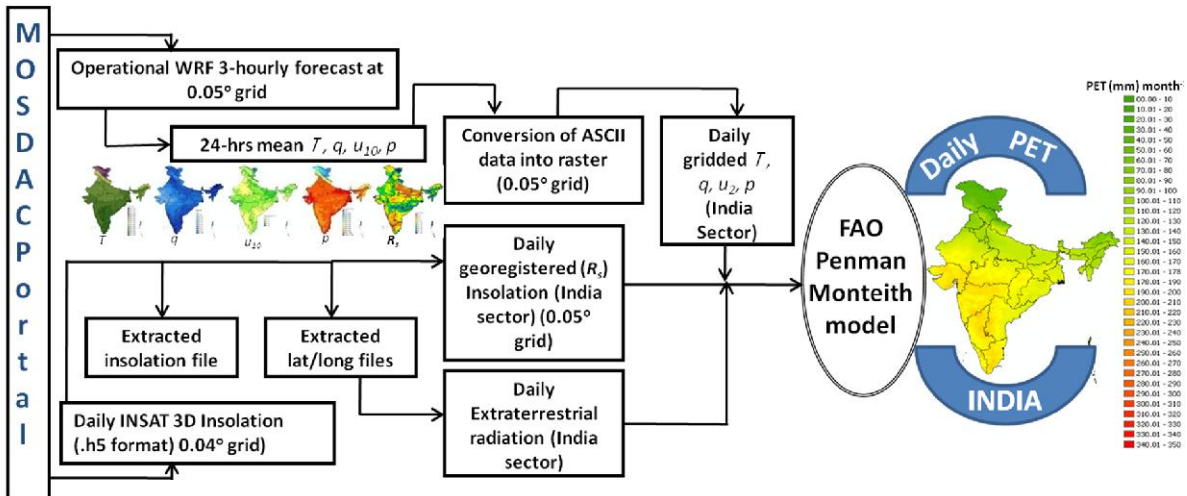
$u_2$  = wind speed at 2 meter above ground surface [m s<sup>-1</sup>]

$u_z$  = measured wind speed at z meter above ground surface [m s<sup>-1</sup>]

$z$  = height of measurement above ground surface [m]

#### 17.4.11. Flow chart

Figure 2



#### 17.4.12. Steps for operational implementation

The following steps need to be followed for operational implementation of Potential evapotranspiration product generation:

- Daily (24 hours) average meteorological data are to be carried out by averaging 3-hourly forecast from WRF (ASCII format) at  $0.05^{\circ} \times 0.05^{\circ}$  spatial grid for all the four variables
- Maximum , minimum air temperatures and relative humidity need to be generated from 3-hourly forecasts in a given day
- Conversion of all ASCII outputs of (i) and (ii) to raster of dimension approx.  $0.05^{\circ} \times 0.05^{\circ}$  grid resolution
- Conversion of all INSAT 3D generated insolation output to raster of dimension approx.  $0.05^{\circ} \times 0.05^{\circ}$  grid resolution
- Reprojection of operational daily insolation product present Transverse Mercator to geographic projection
- Resampling of gridded insolation to WRF grid resolution followed by subsetting for India with same dimensions as that of WRF.
- Integration of reprojected daily insolation and 2-D surface of WRF variables in to FAO P-M model to generate regional spatial output of daily  $ET_o$  is given in flow diagram (Fig.2).

## 17.5. Outputs

Table 3

Parameter	Unit	Min	Max	Accuracy	Temporal resolution	Spatial resolution
Daily Potential Evapo-transpiration output consist of ET <sub>0</sub> Latitude Longitude	mmd <sup>-1</sup>	0.5 5°N 68°E	15 40°N 100°E	80 to 90%	Daily Ten-day	~ 5 km

### 17.5.1. Format of the output and the domain

Table 4

Parameter	Data format	Upper left and lower right corner coordinates	Scan lines and columns	Gains and offsets for converting actual values
Daily Potential Evapo-transpiration output consist of ET <sub>0</sub> Latitude Longitude	In HDF5 format  BYTE  Floating-point	Upper left : 68°E, 40°N  Lower right : 5°N, 100°E	Indian domain (approx. 676 x 721)	Gain for ET data 0.1, offset zero

## **17.6. Validation of INSAT 3D generated daily Potential evapo-transpiration**

### **17.6.1. Data required**

**Table 5**

Sensors	Parameters	Time scale	Source
Agro-Met Station (AMS)	Radiation, routine weather variables	Half-an-hourly basis	MOSDAC & EME-VS project database
MODIS	MOD16 product containing Potential evapotranspiration at 1 km	Eight-day basis	<a href="http://www.ntsg.umt.edu/project">http://www.ntsg.umt.edu/project</a>
Reanalysis field	Pot evap.	Daily, monthly basis	MEERA 2D / NCEP

## **17.7. Study of Potential Evapo-transpiration with K1 VHRR data**

The spatio-temporal pattern of monthly cumulative  $ET_o$  for year 2011 is shown in Figure 3. The gradual increase and decrease was observed throughout the year with the seasonal transition. Monthly  $ET_o$  linearly increased throughout India from January to June and then decreased in monsoon during July and August. After that, gradual rise in September coincident to higher insolation due to withdrawal of monsoon. The  $ET_o$  again decreases in October and November but there is rise in western part of India during December due to increase in day length in last dekad of December.

### **17.7.1. Sensitivity of P-M model to weather variables for error budgeting**

The sensitivity of P-M model  $ET_o$  was carried out by Bois et al (2008) using ‘Sobol’ method. It consists of numerous simulations of the models using two independent samples of ‘N’ repetitions (rows) and ‘k’ input variables (columns), retrieved from existing data or randomly generated data from the probability distribution function (PDF) of each ‘k’ input variable. One or several variables in the first sample are substituted by the same variable (s) taken from the second sample. For each of the  $(2^k - 1)$  possible combinations of variable substitutions between the two samples, ‘N’ runs of the model are computed. The sensitivity of the model to input variables was based on so-called sensitivity or Sobol’ indices, which were calculated on the principle of the decomposition of the total variance (V) of the model output, in response to individual or simultaneous variations of the ‘k’ model inputs.

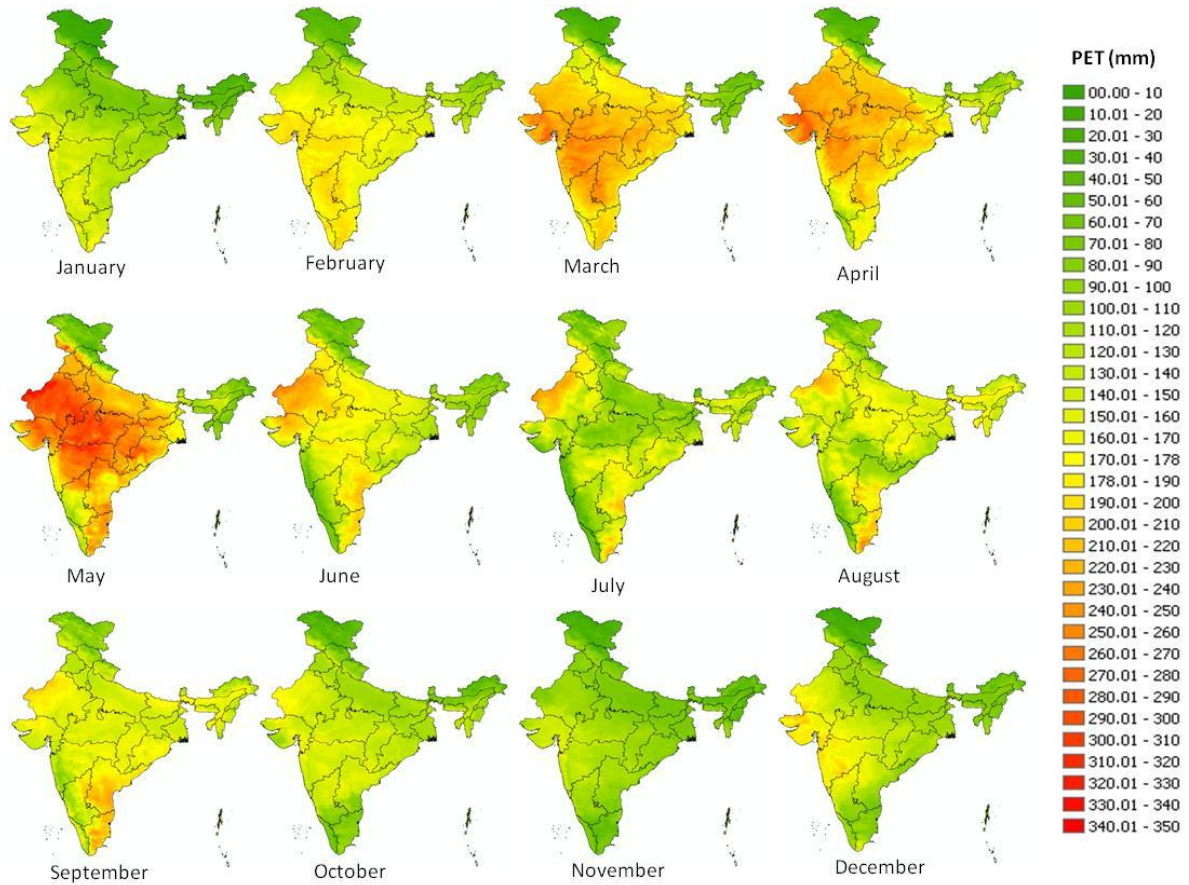


*Figure 3. Example of monthly distribution of  $ET_0$  from VHRR insolation and WRF forecasts over Indian region*

In oceanic climate, the results of monthly sensitivity analyses computed using Southwest area (SW) data show clear seasonal trends (Figure 4). During the winter period (from November to February), wind speed is the main source of variation in  $ET_0$  values calculated using P-M method (e.g. 38% of  $ET_0$  total variance in January). Then come relative humidity and air temperature (32% and 17% of  $ET_0$  total variance in January, respectively). Solar radiation, daily amplitude of air temperature and daily amplitude of relative humidity have little impact on evapo-transpiration process during winter. This trend changes during March and October. From April to September,  $ET_0$  is mostly sensitive to solar radiation (up to 74% of  $ET_0$  total variance in May, and 70% in July). From May to July, P-M formula is not very sensitive to relative humidity, air temperature and their diurnal amplitudes. Mean daily air temperature participate from 11% to 15% of  $ET_0$  variance, from May to September. Total sensitivity indices show that, when added to other variables' variations, air temperature has a greater impact on  $ET_0$  variability during summer, and wind speed has a greater impact during winter (Figure 4B).

In Mediterranean climate, sensitivity of  $ET_0$  computation to climate input variables using P-M method in Southeast area (SE) is very close to the one observed. Wind speed as a major impact on

$ET_0$  calculation during winter and solar radiation is clearly the most influent variable during summer (Figure 4C and D). The present analysis highlights the great sensitivity of this Penman–Monteith formula to solar radiation during summer period, when  $ET_0$  reaches its highest values, and when its calculation is critical for irrigation process and ecological modelling. These results were obtained for Mediterranean and Oceanic climate, at medium latitudes. A recent work published by Gong et al. (2006) on a large range of climatic conditions in Southern China leads to similar results, except for relative humidity which had a greater impact on  $ET_0$  during winter than it has been shown in the present study. Considering the results of Penman–Monteith sensitivity to solar radiation, it seems reasonable to evaluate the benefits of satellite-sensed solar radiation to  $ET_0$  calculation.

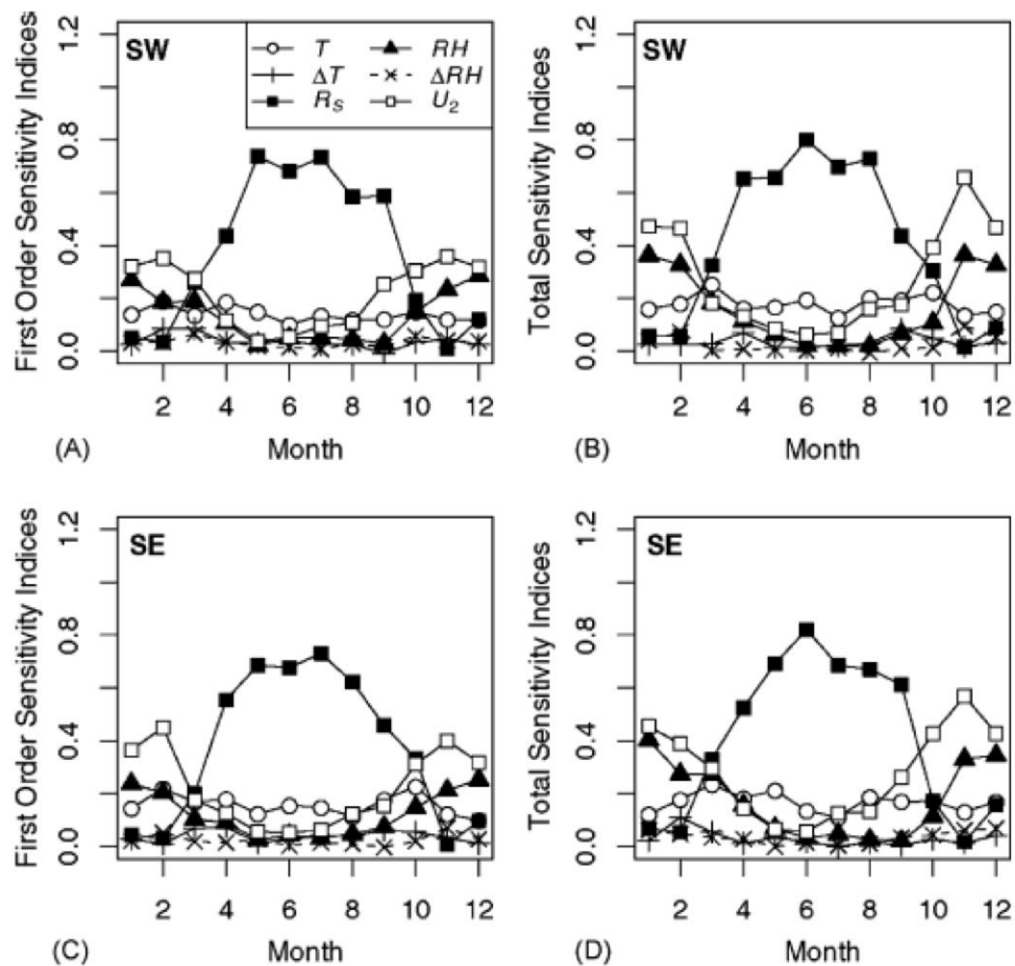


Figure 4. Plots of sensitivity indices (A–C) Southwest area (SW), and (D–F) Southeast area (SE) of  $ET_0$  to different climatic variables

### 17.7.1.1. Preliminary comparison with in-situ measurements

The daily insolation product (Bhattacharya et al., 2012b) from K1VHRR available through MOSDAC (Meteorological and Oceanic Satellite Data Archival Centre) for the period January 1, 2011 to December 31, 2011 to derive radiation parameters and other routine inputs from WRF forecast were ingested into P-M model to generate daily, dekadal (ten-day) and monthly  $ET_0$  estimates at regional scale following the steps mentioned in section 4.12. To validate satellite based regional  $ET_o$  estimates, the measurements from INSAT-linked AMS (Agro-Met-Station) data were used (Bhattacharya et al, 2009). The AMS provides all radiation and meteorological variables at 30 minutes interval and represent a fetch area of 1 km x 1 km. The AMS data from six sites over different agro-climatic zones were used to compute  $ET_o$  on daily basis for different time period as listed in Table 6. The  $ET_o$  was calculated on daily basis using AMS half-an-hour average measurements.

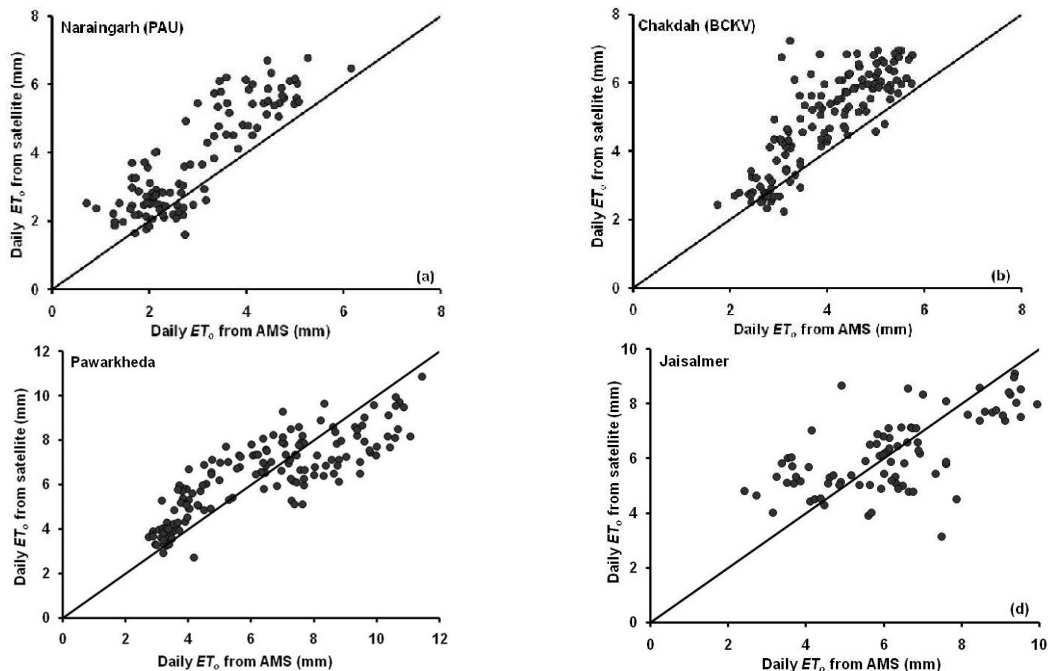
*Table 6. Details of AMS stations and data used*

Station Name	Time period	Agro-climatic region	Latitude	Longitude
Naraingarh PAU (Punjab)	Farm, 1 Jan to 20 April	Trans gangetic plain region	30°36'44.92"N	76°19'17.75"E
BCKV(W. Bengal)	1 Jan to 7 June	Lower gangetic plain region	22°41'53.46"N	77°44'5.06"E
Jaisalmer (Rajasthan)	11 July to 30 Sept	Western dry region	26°50.83"N	71°18.083"E
Pawerkheda (Madhya Pradesh)	1 Jan to 8 June	Central plateau and hill region	22°41'53.46"N	77°44'5.06"E
LPSC Mahendergiri (Tamil Nadu)	1 Jan to 7 Dec	Southern plateau and hill region	8°17'53.89"N	77°33'21.77"E
Diglipur (Andaman & Nicobar)	15 Feb to 8 Dec	Island region	13°01'25"N	93°0'27"E

### 17.7.1.2. Validation results

#### A. Daily scale

Daily  $ET_o$  estimated using P-M approach was compared with daily  $ET_o$  computed from AMS measurements for different agro-climatic regions as listed in Table 6. The 1:1 plot is shown in Figure 5 and temporal comparison is shown in Figure 6. The daily  $ET_o$  computed from AMS varied from 0.7 mm to 12.0 mm while satellite derived  $ET_o$  varied from 1.1 to 11.7 mm over different seasons for selected stations. The error analysis showed the root mean square deviation (RMSD) varied from 1.13 to 3.82  $\text{mm} \text{d}^{-1}$  to the tune of 21 to 38 % of measured mean over six stations (Table 7). The overall pooled data set showed RMSD of 1.34  $\text{mm} \text{d}^{-1}$  with 29% deviation from measured mean. This was due to high fluctuation of  $ET_o$  on daily temporal scale as shown in Figure 5 for all six AMS stations. The estimated daily  $ET_o$  showed underestimation as well as overestimation for all AMS stations but extent of temporal pattern matches quite well in all the stations.



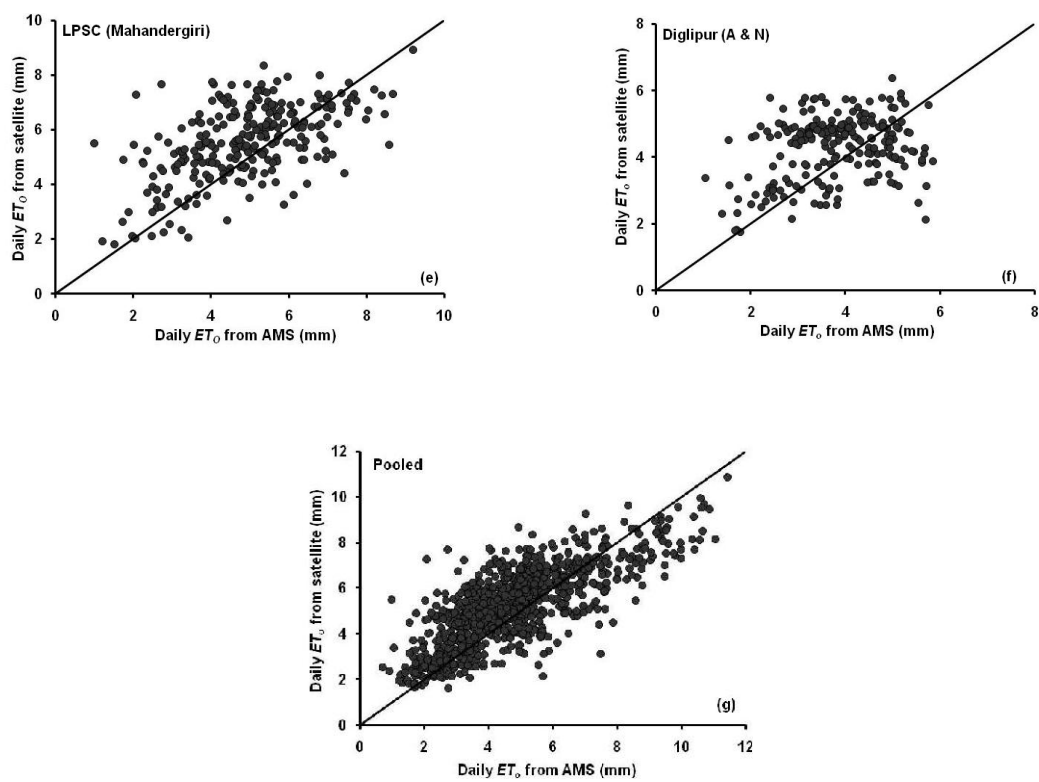


Figure 5. 1:1 scatter plot between daily  $ET_o$  from AMS and estimates from satellite and WRF

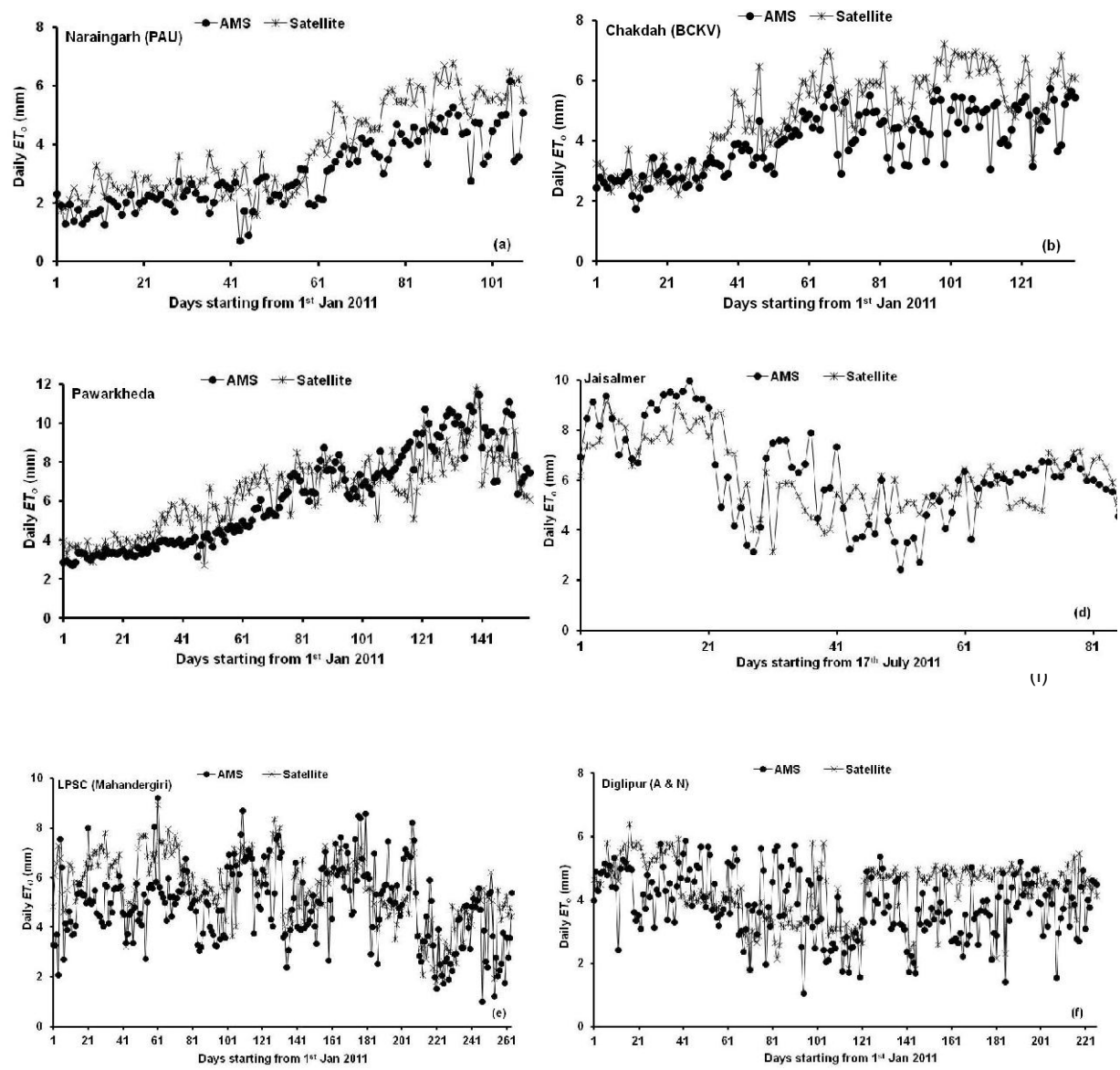


Figure 6. Comparison of temporal profile of daily  $ET_o$  from AMS and spatial estimates

*Table 7. Error statistics for daily  $ET_o$*

Station name	N	RMSD	RMSD(% AMS mean)	of MAB
Naraingarh Farm (PAU)	108	1.1	38.1	0.9
Chakdah (BCKV)	136	1.2	31.1	1.0
Pawarkheda	157	1.3	21.5	1.1
Jaisalmer	85	1.4	22.8	1.1
LPSC	265	1.5	31.1	1.8
Diglipur	226	3.8	33.0	1.0
Overall	977	1.3	29.0	1.0

$$\text{RMSD (Root Mean Square Deviation)} = \sqrt{\frac{\sum_{i=1}^N [(P_i) - (O_i)]^2}{N}}$$

$$\text{MAB (Mean Absolute Bias)} = \frac{\sum_{i=1}^N ABS[(P_i) - (O_i)]}{N}$$

Where  $P_i$  – PET<sub>AMS</sub> at i<sup>th</sup> case

$O_i$  = PET<sub>estimated</sub> at i<sup>th</sup> case

N = number of daily paired datasets

## B. Dekadal scale

The daily  $ET_o$  fluctuation was high and leads to high deviation from measured AMS mean so data were summed for 10-days for further analysis. The 10-days cumulative estimated  $ET_o$  was validated with cumulative  $ET_o$  from AMS data. The temporal 10-day  $ET_o$  over different stations are shown in Figure 7 for six selected stations and error statistics are given in Table 8. The dekadal change in estimated  $ET_o$  matched well with AMS  $ET_o$ . The seasonal change was also well captured in 10-day cumulative  $ET_o$ .

In Naraingarh, Punjab, the comparison was made for the period from January to April. In January and February,  $ET_o$  remained low in the range of 16 mm to 24 mm due to low radiation and temperature. It started rising in March and reached up to 62 mm per dekad. The rise and fall of computed  $ET_o$  was well captured in estimated  $ET_o$  during January to April. The RMSD was 9.3

mm which is 28.9% of AMS mean for the stated period. The 1:1 scatter (Figure 8) showed a 91 % correlation.

*Table 8. Error statistics for dekadal (10-day)  $ET_o$*

Station Name	N	RMSD	RMSD (%of AMS mean)	MAB
Naraingarh, Punjab	14	9.3	28.9	8.2
Chakdah, W.B.	14	10.5	27.4	9.1
Pawarkheda, M.P.	15	10.4	18.6	8.9
Jaisalmer, Rajasthan	8	6.3	10.2	5.8
Mahendragiri, T.N.	30	9.4	21.4	8.2
Diglipur, A.N.	22	9.3	25.0	8.4
Overall	99	9.5	21.6	8.3

*N= number of dekadal paired datasets*

The site in West Bengal represents lower gangetic plain of agro-climatic regions having moderate cold season of January and February to moderate hot season during March and April. During this period *rabi* rice is grown with available irrigation facility. The dekadal temporal profile of estimated  $ET_o$  matched well with AMS  $ET_o$  but showed small amount of deviation during April. This may be due to application of irrigation water in rice crop and was only captured in computed  $ET_o$  from AMS but not reflected in estimated  $ET_o$ . The temporal variation of dekadal  $ET_o$  was 28 to 30 mm in January with gradual rise in February. The maximum  $ET_o$  was observed in April due to rise in temperature and radiation load. This seasonal change of  $ET_o$  was well captured in the estimates. The overall RMSD was found to be 10.5 mm (27.4 % of AMS mean) on January to April with respect to AMS.

The central plateau and hill agro-climatic region is represented here by AMS at Powarkheda site. The area falls under the catchment of Narmada where annual rainfall varies from 800 to 1200 mm. The wheat crop is dominant during *rabi* season. The estimated dekadal  $ET_o$  estimates matched well throughout January to May. The dekadal high and low value matched quite well and estimated  $ET_o$  always remained high as compared to AMS  $ET_o$  up to March during growth of wheat crop. After that, estimated  $ET_o$  underestimated measured  $ET_o$ . In January, both showed low values in the range of 30 to 37 mm and 35 to 46 mm but goes up to 97 to 103 mm (AMS) and 82 to 94 mm (estimated) in May. The temporal profiles matched quite well and showed RMSD of 10.4 mm over ten days (16.6% deviation from AMS mean).

The typical Indian arid region lies in western, dry agro-climatic region and represented here by Jaisalmer. The climate remains hot throughout the year except in January and February. The data over monsoon season (July, August and September) were used for computation of  $ET_o$ . In this part

of India, S-W monsoon starts in July and it was well captured by dekadal  $ET_o$  variation during stated months. During July,  $ET_o$  remained higher but later in the season it reduced in both the cases. The satellite estimated  $ET_o$  showed both underestimation and overestimation for selected season as compared to AMS. The temporal profile of  $ET_o$  of two followed the same pattern. The RMSD of 6.3 mm was found for monsoon season which is 10.2% with respect to AMS  $ET_o$ .

The southern part of India, AMS located in LPSC Mahandragiri represents the natural scrub vegetation. The AMS data for January to May and August to November were used for comparison with AMS  $ET_o$  value. The temporal profile of dekadal  $ET_o$  matched well with AMS  $ET_o$ . The difference between two was maximum during north-east monsoon season (January to February) but later on, the difference was reduced further in May and November. The data showed a RMSD of 9.4 mm (21.4% deviation of measured AMS mean).

The island agroclimatic region of Andaman & Nicobar have different climatic conditions as compared to above stated regions. As this region is surrounded by Bay of Bengal so climatic condition remains humid throughout the year. The data from March to May and August to November were used for comparison. The AMS  $ET_o$  on an average had a range of 23 to 50 mm throughout the selected time domain. Similar order of magnitude was observed for estimated  $ET_o$ . The dekadal behaviour of estimated  $ET_o$  matched well with AMS  $ET_o$  but showed little higher deviation during August and September. It showed RMSD of 9.3 mm (25.0% of AMS mean).

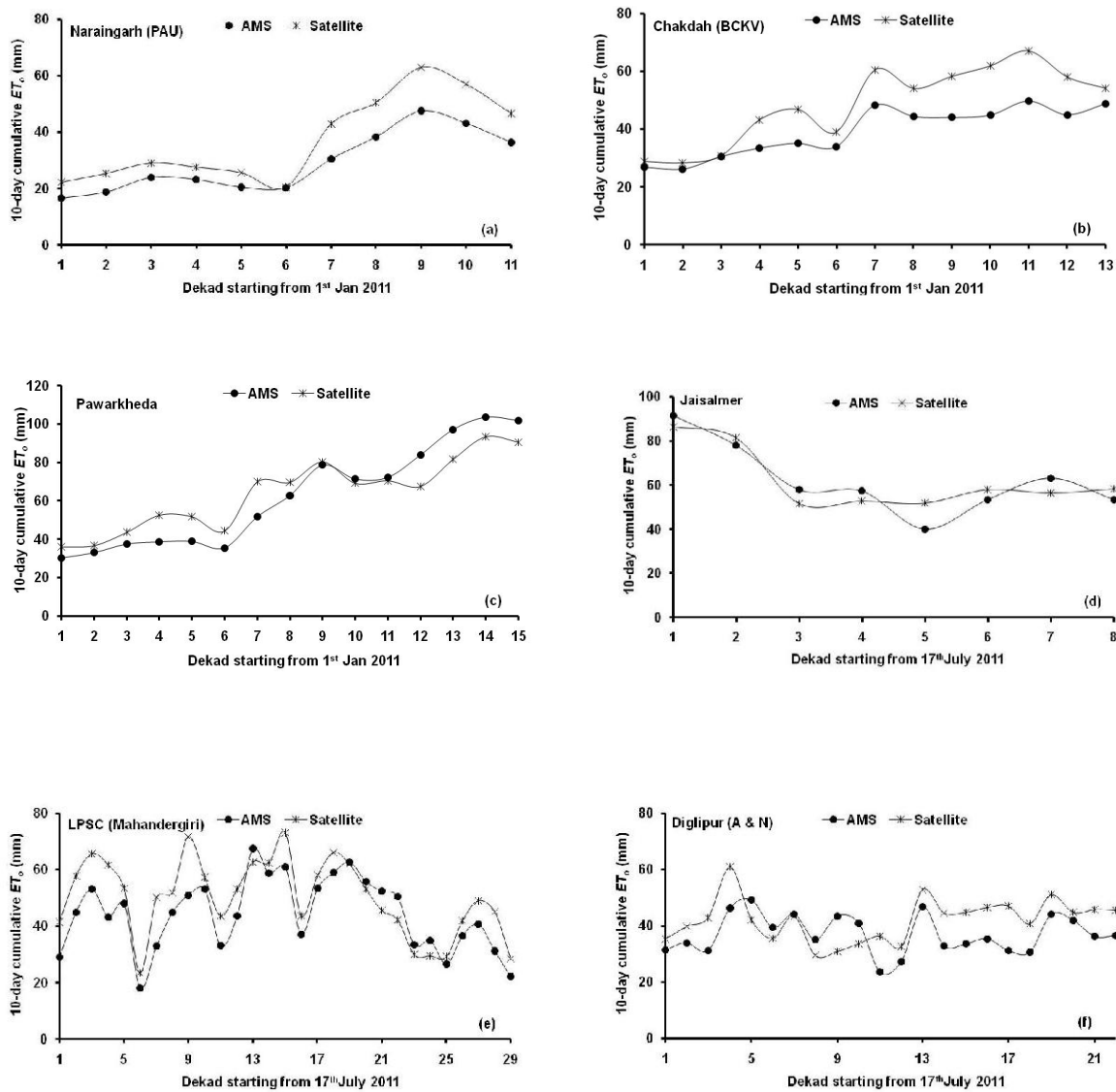


Figure 7. Temporal profiles of dekadal sum of potential evapotranspiration ( $ET_o$ ) computed from AMS and fusion of satellite and WRF data.

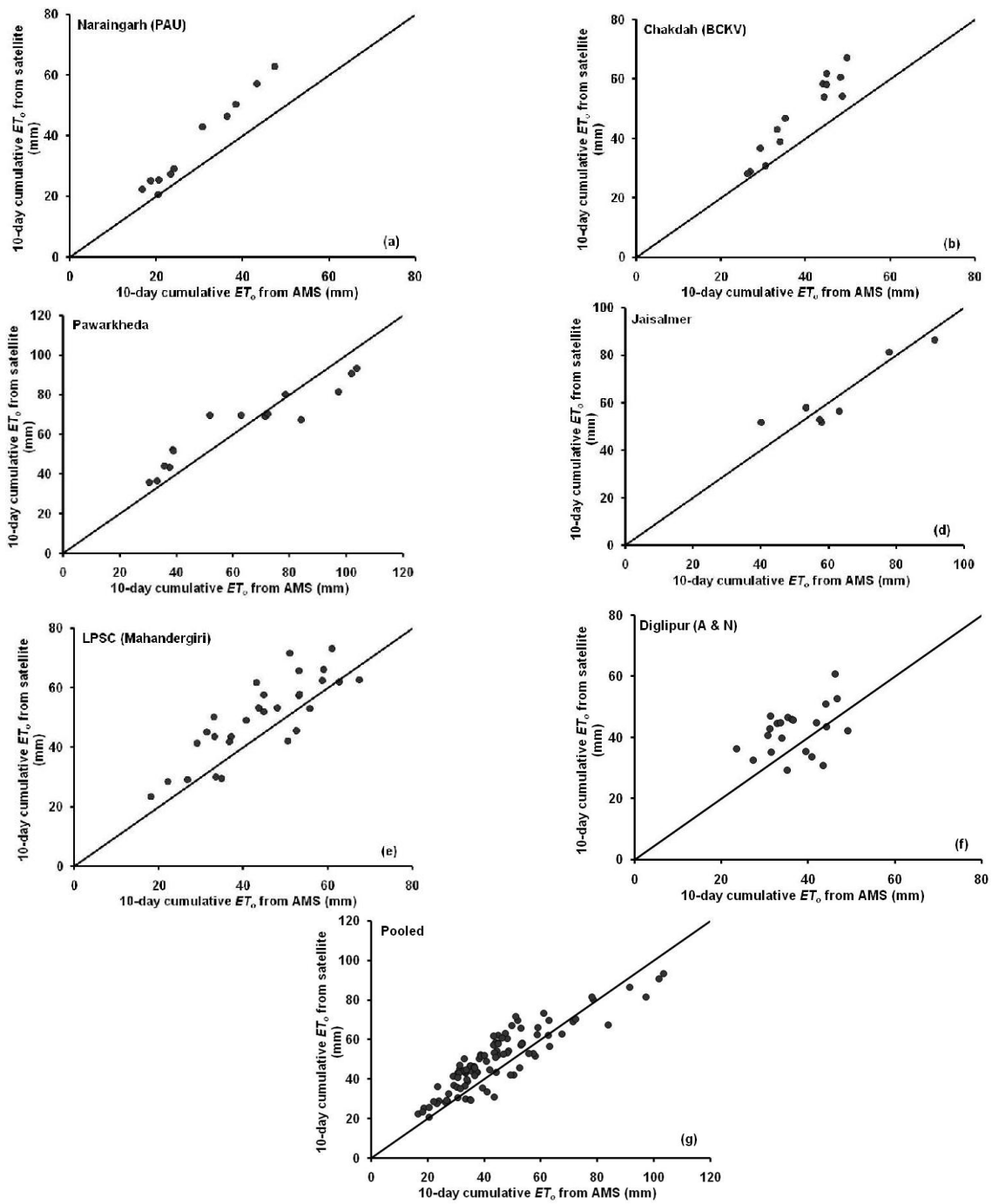


Figure 8. 1:1 Scatter plot between dekadal PET computed from AMS and with spatio-temporal estimates.

### 17.7.1.3. Error analysis of $ET_o$ for variable-time accumulation

The daily estimated and AMS  $ET_o$  was compared for different time windows viz. 3-day, 5-day, 7-day and 10-day. The correlation coefficient between estimated and measured  $ET_o$  gradually increased from daily to 10-day but maximum increase was observed from daily to 7-day i.e from 8% to 23% for six AMS stations. The rise of correlation coefficient from 7-day to 10 days was nominal in Nariangarh (PAU) (0.7%), Chakdah (BCKV) (2%), Pawarkheda (2.3%) and Jaisalmer (6.3%) as compared to LPSC (Mahandergiri) (13.8%) and Diglipur (12.6%) as shown in Figure 8. Similarly per cent deviation from mean of AMS measurements also showed a similar trend as the deviation drastically came down from daily to 7-days and further nominal decrease in 10-day except than in Jaisalmer. For the latter, it decreases from 14.8% to 10.2% for 7 to 10-days as marked in Figure 9. The analysis showed that error was significantly reduced from daily to 7-days and further in 10-days over different agro-climatic zones. This will help us use this  $ET_o$  data in various applications on different time scales with known errors.

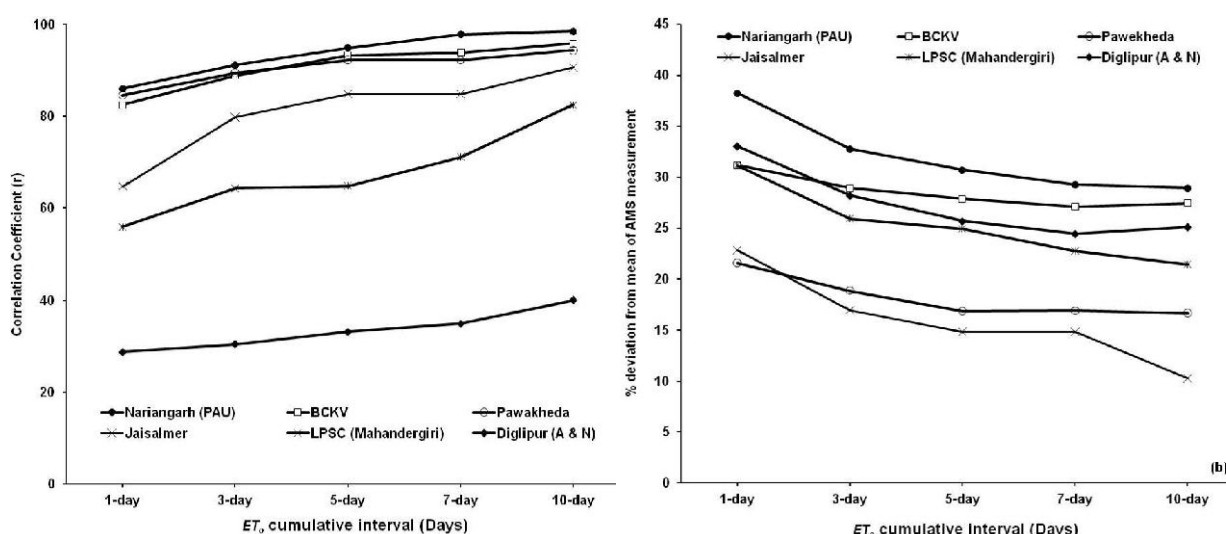


Figure 9. Error analysis of  $ET_o$  for variable-time accumulation

### 17.7.1.4. Comparison of errors from similar studies elsewhere

Considering the results of Penman–Monteith sensitivity to solar radiation, it seems reasonable to evaluate the benefits of satellite-sensed solar radiation to estimate spatial  $ET_o$  as no regular spatial record are available for solar radiation. Choudhury (1997) attempted monthly global  $ET_o$  at  $0.25^\circ \times 0.25^\circ$  from P-M method using solar radiation from International Satellite Cloud Climatology Project (ISCCP). He derived vapour pressure and vapour pressure deficit (VPD) from TIROS operational vertical sounder TOVS data with air temperature based on interactive GCM forecast

retrieval assimilation system applied to the TOVS data. He has compared the estimated  $ET_o$  with lysimeter data and on monthly scale the error was found between 15 to 40% from measured mean.

Bois et al. (2008) used remotely sensed solar radiation and weather data from AWS equipped with humidity, thermal sensors and cup anemometer to estimate  $ET_o$  using FAO-56 P-M method. They used the solar radiation prepared from Meteosat data by following Heliosat-2 method (Rigollier et al. 2004). The study found that most of the errors occurred in partial cloudy days due to uncertainties in retrieving daily solar radiation. On daily scale, the RMSD was between 0.34 to 1.32 mm (11% to 110% from daily mean) but on annual scale the RMSD remained low (11% of  $ET_o$  mean value) at  $0.05^\circ \times 0.05^\circ$  spatial resolution. This error again came down to (9.1% to 5% of  $ET_o$  mean value) during clear days in summer. Our study was unique as we used operational product of K1VHRR insolation WRF 3-hourly forecast for at  $0.05^\circ$  grid for estimation of  $ET_o$  at  $0.08^\circ \times 0.08^\circ$ . On daily scale, RMSD was 1.1 to 3.8 mm (21% to 38% from measured mean) but it came down to 10% to 28% from mean on dekadal time scale and further in monthly scale (21% from monthly mean). The overall error at different temporal domain were found in good harmony with reported errors in other part of world.

## **17.8. Sources of errors / uncertainties in $ET_o$ estimates and validation issues**

The following sources of uncertainties were traced out while evaluating spatial output of  $ET_o$  estimates and its comparison with ground reference

### **(i) Influence of vegetation in AMS**

The FAO 56 P-M method is generally applied for a specific site using meteorological and radiation data from meteorological observatories or AWS weather data including direct measurement of radiation. In India, ISRO-AWS does not provide solar radiation data in terms of standard energy units. IMD AWS provide data with some lag period. The sensitivity analysis of P-M method by Gong et al. (2006) and Bois et al. (2008) highlighted that solar radiation and wind speed were clearly the most influent variables for  $ET_o$  estimation. The pyranometer and routine weather data from AMS are used. But these measurements were recorded over different vegetation cover types. Since vegetation growth influences ambient weather conditions, the  $ET_o$  computed from AMS would definitely have differential vegetation influence when compared to  $ET_o$  estimates from integration of satellite based solar radiation and WRF forecast weather variables.

### **(ii) Scale mismatch**

Spatial  $ET_o$  was generated at approximately 8 km spatial resolution with  $64 \text{ km}^2$  pixel area while the average footprint of AMS varies from 0.25 to 1  $\text{km}^2$ . This scale mismatch puts constrain in validation statistics. But this scale mismatch will reduced with INSAT 3D.

### **(iii) Difference in time sampling**

For spatial  $ET_o$ , daily solar radiation was generated from diurnal observations at instantaneous snapshots with half-an-hour interval from satellite platform. But half-an-hourly averages from AMS measurements were used to generate validation datasets

### **(iv) Accuracy in cloud flagging**

The product version of surface insolation algorithm has cloud detection capability of approximately 80%. It could not detect thinner clouds. Therefore,  $ET_o$  estimates have higher errors during the period more cloudy spells or for AMS sites with higher cloud dynamics such as Diglipur (A & N), LPSC, Mahendragiri etc.

### **(v) Quality of WRF forecast**

An initial evaluation of WRF forecast quality showed an average error to the tune of 1-2°C, RH of 5-10% as compared to large error in wind speed and predicted radiation terms. The inherent errors in first three variables will have implications on the overall error budget.

## **17.9. Future scope of improvement**

Recent improvement has taken place in the cloud detection of INSAT 3D insolation algorithm using additional criteria based on cloudiness index from VIS band observations. Much of the uncertainties in insolation and  $ET_o$  estimates in cloudy-skies will hopefully be improved.

Recent study on impact of updated vegetation fraction from INSAT 3A CCD showed improvement in air temperature, humidity and rainfall forecast from WRF. The use of real-time satellite based other land surface products such as albedo, LAI and soil moisture would definitely help in improving the quality of operational forecasts. Future work should address the retrieval / estimation of those variables from Indian geostationary satellites.

The INSAT 3D will provide relatively finer spatial resolution of observation of insolation. This would reduce the scale mismatch uncertainty for validation.

## **References**

- Allen, R., Pereira, L., Raes, D., Smith, M., 1998. Crop evapotranspiration. Guidelines for Computing Crop Water Requirements. FAO Irrigation and Drainage Series No. 56, 15-28.
- Anderson, M. C., Norman, J. M., Mecikalski, J. R., Otkin, J. A., & Kustas, W. P. (2007). A climatological study of evapotranspiration and moisture stress across the continental United States based on thermal remote sensing: 1. Model formulation. *Journal of Geophysical Research-Atmospheres*, 112.
- Blaney, H. F. and Criddle, W. D. (1950). Determining water requirements in irrigated areas from climatological and irrigation data (pp. 48). : US Department of Agriculture Soil Conservation Service.
- Bhattacharya, B.K., Dutt, C.B.S. and Parihar, J.S. (2009). INSAT uplinked Agromet Station – A scientific tool with a network of automated micrometeorological measurements for soil-canopy-atmosphere feedback studies. *ISPRS Archives XXXVIII-8/W3 Workshop Proceedings: Impact of Climate Change on Agriculture*. Paper no. TS9.13
- Bhattacharya, B. K. and Kumar, P. (2012a). AMS data Utilization for preliminary evaluation of operational forecast from WRF model. *SAC project report (no. awaited)*
- Bhattacharya, B. K., Padmanabhan, N., Ramakrishnan, R., Panigrahy, S. and Parihar, J.S. (2012b). Algorithm Theretical Basis Document (ATBD) for surface insolation using Kalpana-1 VHRR observations. SAC/EPSA/ISRO-GBP/SR/ATBD/02/2012
- Bhattacharya, B. K., Mallick, K., Patel, N.K. and Parihar, J.S. (2010). Regional clear sky evapotranspiration over agricultural land using remote sensing data from Indian geostationary meteorological satellite. *Journal of Hydrology*, 387, 65-80.
- Bois, B., Pieri, P., Van Leeuwen, C., Wald, L., Huard, F., Gaudillere, J. P., Saur, E. (2008). Using remotely sensed solar radiation data for reference evapotranspiration estimation at a daily time step. *Agricultural and Forest Meteorology*. 148, 619-630.
- Brutsaert, W. (1982). *Evaporation into the atmosphere: Theory, History and Applications* (1st ed.). Springer.
- Choudhury, B. J. (1997). Global pattern of potential evaporation calculated from the Penman-Monteith equation using satellite and assimilated data. *Remote Sensing of Environment*. 61, 64-81.
- Dalton, J. (1802). Experimental essays the constitution of mixed gases; on the force of steam of vapor from waters and other liquids in different temperatures, both in a torricellian vacuum and in air; on evaporation; and on the expansion of gases by heat. *Memoirs of the Manchester Lit. & Phil. Soc.*, 535–602.

- Gong, L., Xu, C.-y., Chen, D., Halldin, S., Chen, Y.D. (2006). Sensitivity of the Penman–Monteith reference evapotranspiration to key climatic variables in the Changjiang (Yangtze River) basin. *J. Hydrol.* 329 (3/4), 620–629
- Hargreaves, G. H. (1975). Moisture availability and crop production. *Transactions of the ASAE*, 18, 980–984.
- Kumar, P., Singh, R., Joshi, P.C., Pal, P.K. (2011). Impact of Additional Surface Observation Network on Short Range Weather Forecast during Summer Monsoon 2008 over Indian Subcontinent. *Journal of Earth System Sciences*, 120, 2011, 1-12.
- Monteith, J. L. (1964). Evaporation and environment. The state of movement of water in living organisms. *Symposium of the society of experimental biology*. 205–234.
- Monteith, J. L. (1973). Principles of environmental physics. Edward Arnold Press. 241.
- Penman, H. L. (1948), Natural evaporation from open water, bare soil and grass. *Proc. Roy. Sec. (London) A* 193:120- 145.
- Priestley, C. H. B., & Taylor, R. J. (1972). On the assessment of surface heat flux and evaporation using large-scale parameters. *Monthly Weather Review*, 100, 81–92.
- Rigollier, C., Lefevre, M., Wald, L. (2004). The method Heliosat-2 for deriving shortwave solar radiation from satellite images. *Solar Energy* 77 (2), 159–169.
- Rowntree, P. R. (1991). Atmospheric parameterization for evaporation over land: Basic concept and climate modeling aspects. In T. J. Schmugge & J. C. André (Eds.), *Land surface evaporation fluxes: Their measurements and parameterization* (pp. 5–30). New York: Springer-Verlag.
- Singh, R., Kumar, P. and Pal, P. K. (2011). Assimilation of Oceansat-2 Scatterometer Derived Surface Winds in the Weather Research and Forecasting Model. (*IEEE Transactions on Geoscience & Remote Sensing* <http://dx.doi.org/10.1109/TGRS.2011.2164410>
- Skamarock W. C., Klemp J. B., Dudhia J., Gill D.O., Barker D.M., Duda M.G., Huang X.Y., Wang Wand Powers J. G. (2008). A description of the Advanced Research WRF Version 3. NCAR/TN-475 STR; NCAR Technical Note, Mesoscale and Microscale Meteorology Division, National Center of Atmospheric Research, June 2008, 113 pp.
- Thornthwaite, C. W. (1948). An approach towards a rational classification of climate. *Geographical Review*, 38, 55–94.